

Design of a Receiver System for Use in Radio Astronomy

by

Lukas Martin van Vuuren

Thesis presented in partial fulfilment of the requirements for the degree Master of Science in Engineering at Stellenbosch University.



Department of Electric and Electronic Engineering,
University of Stellenbosch,
Private Bag X1, Matieland 7602, South Africa.

Supervisor: Dr Dirk de Villiers

March 2015

Acknowledgements

The following people and organisations must be acknowledged for support and contributions to this project in various ways.

- The financial assistance of the National Research Foundation (NRF) towards this research is hereby acknowledged. Opinions expressed and conclusion arrived at, are those of the author and are not necessarily to be attributed to the NRF.
- Dr Dirk de Villers for his continual and invaluable support. This project would not have been completed without his guidance.
- Wessel Croukamp and his team in the workshop for tirelessly ensuring that all requested items were completed in a timely, professional and expert manner.
- Anneke Bester for her help in setting up important test equipment in the HF laboratory.
- Dewald Botes for help with ADS. This help proved fundamental to the development of the low noise amplifiers and low pass filter.
- Vereese van Tonder for help with the ROACH board. It seemed like a daunting task to get the ROACH board up and running, but thanks to Vereese this task was completed quickly.
- NRF (National Research Foundation) for bursary and funding for this project. Special mention must also be made for the opportunity to travel abroad using the available travel grant.
- Leana Ludik for continual support throughout the past 2 years and always believing in me.
- Lastly, my parents. Without their support and encouragement this would never have been possible.

Declaration

"I, the undersigned, hereby declare that the work contained in this report is my own original work unless indicated otherwise."

Signature:
L.M. van Vuuren

Date:

Copyright © 2015 Stellenbosch University
All rights reserved

Abstract

This project aimed to design and test a radio receiver for use in radio astronomy. To highlight the specific challenges of designing such a receiver, most of the components were designed and manufactured instead of purchased. Components of the system that were designed were the antenna, filters and low noise amplifiers. The parabolic reflector dish available at the E&E Engineering Department was to be used as the receiving dish for the system.

The antenna that was designed and optimised was a circular corrugated horn antenna. It was manufactured and measured at the E&E Department. Inter-digital filters were designed for the required band-pass filters of the receiver. A lumped element low-pass filter was also designed. Appropriate low noise amplifiers were purchased while the PCB's required were designed and simulated.

Radio Frequency Over Fibre was used as an alternative to traditional signal transmission. This was done to evaluate whether or not it can be used successfully for radio astronomy. The required transmitter and receiver was acquired on loan while the fibre optic cable was purchased.

The ROACH board was used for the back-end of the receiver. The ROACH is readily available at the E&E Department and is versatile in terms of its ability to suite various back-end requirements.

Opsomming

Hierdie projek het gemik om 'n radio-ontvanger te ontwerp en toets vir gebruik in radio sterrekunde. Meeste van die komponente is ontwerp en vervaardig in plaas van gekoop om die spesifieke uitdagings van die ontwerp van so 'n ontvanger te beklemtoon. Komponente van die stelsel wat ontwerp was is die antenna, filters en laeruisversterkers. Die paraboliese weerkaatser beskikbaar by die E&E Ingenieurswese Departement was as die weerkaatsantenna vir die stelsel gebruik.

Die antenna wat ge-ontwerp en ge-optimeer was was 'n sirkulêre horing antenna. Dit was vervaardig en gemeet by die E&E Departement. Inter-digitale filters is ontwerp vir die vereiste banddeurlaatfilters van die ontvanger. 'n Laagdeurlaatfilter is ook vervaardig. Toepaslike laeruisversterkers was aangekoop terwyl die nodige stroombaanbord uitgelê en gesimuleer was.

Radio Frekwensie oor Vesel verbindings is gebruik as 'n alternatief vir tradisionele sein oordrag. Dit is gedoen om te evalueer of dit suksesvol kan gebruik word vir radio sterrekunde. Die vereiste sender en ontvanger is op lening ontvang, terwyl die optiese vesel kabel aangekoop was.

Die ROACH bord is gebruik vir die digitale agterkant van die ontvanger. Die ROACH is beskikbaar is by die E&E Departement en is veelsydig in terme van sy vermoë om verskeie digitale agterkant vereistes te pas.

Contents

Acknowledgements	i
Declaration	ii
Abstract	iii
Opsomming	iv
Contents	v
List of Figures	x
List of Tables	xiv
Nomenclature	xv
1 Introduction	1
1.1 Background	1
1.2 Objective	1
1.3 Overview	2
1.4 Thesis Layout	3
2 Radio Astronomy Fundamentals	5
2.1 Introduction	5
2.2 Radio Astronomy Fundamentals	6
2.2.1 Coordinate System	6
2.2.2 Brightness	7
2.2.3 Brightness of Discrete Sources	8
2.2.4 Blackbody Radiation and Planck's Law	10
2.3 Radio Astronomy Observations	11
2.3.1 The Sun and Other Bodies in Our Solar System	11
2.3.2 Emission and Absorption Lines	12
2.3.3 Other Sources	13
2.4 Reflector Antennas	13
2.4.1 Types of Reflector Dishes	13
2.4.2 Geometry of Parabolic Dish	14
2.4.3 Dish Gain	14
2.5 Selection of Operating Band	15
2.5.1 Radio Emissions	15
2.5.2 Radio Astronomy Applications	16

2.5.3	The Sun as a Source	18
2.6	Conclusion	19
3	Antenna Design	20
3.1	Antenna Properties	20
3.2	Feed Efficiency	21
3.2.1	Body Of Revolution	21
3.2.2	Co-Polar and Cross-Polar Unit Vectors	23
3.2.3	Spillover Efficiency	24
3.2.4	Polarisation Efficiency	24
3.2.5	Illumination Efficiency	25
3.2.6	Phase Efficiency	25
3.2.7	Phase Centre	25
3.3	Design of Corrugated Conical Horn Antenna	26
3.3.1	Techniques Used to Reduce Cross Polarisation	26
3.3.2	Initial Design	28
3.3.3	Stepped Corrugated Design	29
3.3.4	Design Procedure	30
3.4	Results	31
3.4.1	Initial Design Results	31
3.4.2	Rough Simulations Results	33
3.4.3	Optimisation Results	34
3.4.4	Final Design	38
3.5	Manufacture	41
3.6	Measurements	41
3.6.1	S-Parameter Measurements	41
3.6.2	Gain Measurements	42
3.6.3	Field Pattern Measurements	46
3.6.4	Efficiencies Calculated from Measurements	49
3.7	Conclusion	51
4	Radio Receiver	52
4.1	Mixers	52
4.1.1	Description	52
4.1.2	Mixing	52
4.1.3	Image Frequency	54
4.1.4	Mixer Properties	55
4.2	Local Oscillator	55
4.2.1	Signal Generator	55
4.2.2	Phase Locked Loop	56
4.2.3	Frequency Synthesizer	56
4.3	Different Types of Receivers	57
4.3.1	Direct Receiver	57
4.3.2	Homodyne Receiver	58
4.3.3	Superheterodyne Receiver	58
4.4	Selection of IF Frequency	60
4.4.1	Conversion Schemes	60
4.4.2	Spurious Signals	62
4.4.3	Final Receiver Design	65

4.5	Receiver Simulation	65
4.5.1	Simulation Set-Up	65
4.5.2	Simulated Results	66
4.6	Conclusion	69
5	Low Noise Amplifiers	70
5.1	Noise in Radio Receivers	70
5.1.1	Noise Power	70
5.1.2	Equivalent Noise Temperature	72
5.1.3	Noise Figure	73
5.1.4	Cascaded Noise Figure	74
5.2	Chosen Low Noise Amplifiers	75
5.2.1	RF Amplifier	75
5.2.2	IF Amplifier	76
5.3	Cascaded Low Noise Amplifiers	77
5.3.1	RF Amplifier	77
5.3.2	IF Amplifier	78
5.4	Impedance Matching	79
5.4.1	RF Amplifier	80
5.4.2	IF Amplifier	81
5.5	ADS PCB Layout	81
5.5.1	RF Amplifier	82
5.5.2	IF Amplifier	82
5.6	Manufacture	83
5.7	Measurements	84
5.7.1	RF Amplifier	84
5.7.2	IF Amplifier	85
5.8	Conclusion	86
6	Filters	87
6.1	Role of Filters in the Receiver Chain	87
6.1.1	Low-Pass Filter	87
6.1.2	RF Band-Pass Filter	87
6.1.3	IF Band-Pass Filter	87
6.2	Low-Pass Filter	88
6.2.1	Low-Pass Filter Prototype	88
6.2.2	Low-Pass Filter Design	89
6.2.3	Manufacture	93
6.2.4	Measurements	94
6.3	Band-Pass Filters	95
6.3.1	Band-Pass Transformation	95
6.3.2	Coupled Resonators	96
6.3.3	Quality Factor	98
6.4	Inter-digital Filter	100
6.4.1	Properties	100
6.4.2	Two Parallel Unsymmetrical Coupled Lines	100
6.4.3	Array of Parallel Unsymmetrical Coupled Lines	105
6.4.4	Design for Narrow to Moderate Bandwidth	106
6.4.5	Tuners	106

6.5	Design	107
6.5.1	Design Parameters	107
6.5.2	Design Procedure	109
6.5.3	Final Results	109
6.6	Measurements	111
6.6.1	Setup	111
6.6.2	Method	111
6.6.3	Results	111
6.7	Conclusion	113
7	RF Over Fibre	114
7.1	Introduction	114
7.1.1	Brief Description	114
7.1.2	Advantages	114
7.1.3	Disadvantages	115
7.1.4	Use in the SKA	116
7.2	How RF Over Fibre Works	116
7.2.1	Basic Functioning	116
7.2.2	Modulation Techniques	117
7.3	Fibre Optics Cable	118
7.3.1	Construction	118
7.3.2	Transmission of Light	119
7.3.3	Multimode and Single Mode	120
7.3.4	Fibre Loss	122
7.3.5	Repeaters and Amplifiers	123
7.4	Testing and Implementation	124
7.4.1	Equipment	124
7.4.2	Testing and Characterisation	125
7.5	Conclusion	127
8	Digital Back-End	128
8.1	Back-End Options	128
8.1.1	Simple Microprocessor	128
8.1.2	Arduino Board	128
8.1.3	ROACH Board	128
8.2	ROACH Board	129
8.2.1	Overview	129
8.2.2	KAT-7 ADC	129
8.3	Spectrometry	130
8.4	ROACH Testing	130
8.4.1	Overview	130
8.4.2	"Tutorial 3 - Wideband Spectrometer"	130
8.4.3	Python Script	131
8.4.4	Setting the KAT-7 ADC	131
8.5	Conclusion	132
9	Measurements and Conclusion	133
9.1	Receiver Measurements	133
9.1.1	RF Stage	133

<i>CONTENTS</i>	ix
9.1.2 IF Stage	135
9.1.3 Full Receiver	137
9.2 Summary	139
9.3 Future Work	141
A Additional Equations	I
A.0.1 Equations Used for Calculation of Phase Centre	I
A.0.2 Equations Used for Narrowband Inter-digital Filter Design	II
B Matlab and CST	IV
C Complete Set of Optimisation Results	VII
C.1 Efficiency Optimisation	VII
C.2 Pattern Optimisation	IX
C.3 Γ Optimisation	X
C.4 Cross Polarisation Optimisation	XII
D TraX Specifications	XIV
E Components and PCB Layouts	XV
E.1 Low-Pass Filter	XV
E.2 IF LNA	XVI
E.3 RF LNA	XVII
F Photos	XVIII
Bibliography	XXIII

List of Figures

1.1	Receiver to be Used for Project	2
2.1	Celestial Sphere [1]	6
2.2	Brightness From a Element of Solid Angle $d\Omega$ [2]	7
2.3	Power Pattern of Effective Aperture [2]	8
2.4	Flux Densities of Some Radio Sources [3]	12
2.5	Parabolic Reflector Dishes	13
2.6	Geometry of Front Fed Parabolic Reflector	14
2.7	Atmospheric Absorption [4]	17
2.8	Estimated Expected Power to be Received from the Sun	19
3.1	Examples of BOR_0 and BOR_1 Antennas	21
3.2	Phase Centre Reference Points [5]	26
3.3	Standard Corrugated Horn [6]	26
3.4	Axially Corrugated Horn [6]	27
3.5	Potter Horn Principle [7]	28
3.6	Generation of TM_{11} Mode	28
3.7	Choke-Ring Waveguide [8]	28
3.8	Stepped Corrugated Conical Horn Antenna	29
3.9	Design Process of Antenna	30
3.10	Initial Design Efficiency Bandwidth	31
3.11	Initial Design Field Pattern Simulated Result	32
3.12	Initial Design Reflection Coefficient Simulated Result	32
3.13	Initial Design Cross Polarisation Simulated Result	33
3.14	Aperture Efficiency and Γ Results of Rough Simulations	34
3.15	Bandwidth of Efficiencies for Efficiency Optimised Antenna	35
3.16	Field Pattern for Field Pattern Optimised Antenna	36
3.17	Γ for Γ Optimised Antenna	37
3.18	Cross Polarisation for Cross Polarisation Optimised Antenna	38
3.19	Field Pattern for Final Simulated Antenna	39
3.20	Cross Polarisation for Final Simulated Antenna	39
3.21	Reflection Coefficient for Final Simulated Antenna	40
3.22	Efficiencies Bandwidth for Final Simulated Antenna	40
3.23	Phase Centre δ for Final Simulated Antenna	41
3.24	Reflection Coefficient of Conical Horn Antenna	42
3.25	Basic Calibration Set-Up	42
3.26	S_{21} of 8 m Cable Representing Cable Losses	43
3.27	Calculated Gains of Conical Horn, H1 and H2 Antennas	45
3.28	Expected and Measured Gains	45

3.29	Measured and Simulated Co-Polarisation E -Field Patterns at 7.5 GHz . . .	46
3.30	Measured and Simulated Cross Polarisation E -Field Patterns at 7.5 GHz	47
3.31	Measured and Simulated Co-Polarisation H -Field Patterns at 7.5 GHz . . .	47
3.32	Measured and Simulated Cross Polarisation H -Field Patterns at 7.5 GHz	48
3.33	Measured E - and H -Plane Radiation Pattern	49
3.34	Calculated Efficiencies from Measured Data	50
3.35	Calculated Phase Centre Reference Points from Measured Data	50
4.1	Up-Conversion Spectrum Example [9] with f_{IF} as Incoming Frequency . . .	53
4.2	Down-Conversion Spectrum Example [9] with f_{RF} as Incoming Frequency . . .	54
4.3	Image Frequency Spectrum Example [9]	54
4.4	Direct Receiver System Using RF Power Detector	57
4.5	Homodyne (Direct Conversion) Receiver Architecture	58
4.6	Basic Single Heterodyne Receiver	59
4.7	Basic Double Heterodyne Receiver	59
4.8	Frequency Ranges of First Down Conversion in Proposed Receiver	60
4.9	Frequency Ranges of Second Down Conversion in Proposed Receiver	61
4.10	Proposed Frequency Spectrum of Receiver	62
4.11	Spurious Signals of First Down Conversion up to $m, n = 5$, $RF = 7.5$ GHz, $IF = 3.5$ GHz, $LO = 4$ GHz	64
4.12	Spurious Signals of Second Down Conversion up to $m, n = 5$, $RF = 3.5$ GHz, $IF = 0.375$ GHz, $LO = 3.125$ GHz	64
4.13	Final Receiver Design	65
4.14	RF Stage of Simulated Receiver Chain	66
4.15	IF Stage of Simulated Receiver Chain	67
4.16	Output Stage of Simulated Receiver Chain Before LPF Has Been Added . . .	67
4.17	Output Stage of Simulated Receiver Chain After LPF Has Been Added . . .	69
5.1	Resistor at Temperature T	71
5.2	Equivalent Thevenin Circuit for Noisy Resistor at Temperature T	71
5.3	White Noise Source Modelled as a Resistor at Equivalent Temperature T_e . .	72
5.4	Noises in a Receiver Component	73
5.5	Cascaded Components	74
5.6	Overall System of Cascaded Components	75
5.7	VMMK-3803 Biasing Circuit for Normal Mode of Operation [10]	76
5.8	ADL5602 Biasing Circuit for Normal Mode of Operation [11]	77
5.9	Basic RF LNA Cascaded Simulated Circuit	78
5.10	RF LNA Cascaded Circuit Simulation in ADS	78
5.11	Basic IF LNA Cascaded Simulated Circuit	79
5.12	IF LNA Cascaded Circuit Simulation in ADS	79
5.13	RF Cascaded Circuit With Simulated Input and Output Coplanar Waveg- uides	80
5.14	RF LNA Results with Tuned Coplanar Waveguides	80
5.15	IF Cascaded Circuit With Simulated Input and Output Coplanar Waveguides	81
5.16	IF LNA Matched and Tuned Coplanar Waveguides	81
5.17	RF LNA Simulated with PCB Layout in ADS	82
5.18	IF LNA Simulated with PCB Layout in ADS	82
5.19	S_{21} of Metallic Enclosure - RF LNA Resonance Check in CST	83
5.20	S_{21} of Metallic Enclosure - IF LNA Resonance Check in CST	84

5.21	Measured Results of IF Low Noise Amplifier	85
6.1	Low-Pass Prototype Filters	88
6.2	Ideal Simulated LPF Circuit	90
6.3	Ideal LPF Response Simulated in ADS	91
6.4	Compromised and Matched Simulated LPF	91
6.5	LPF Response with Non-Ideal Components	92
6.6	Final Simulated LPF Response With PCB	93
6.7	LPF S_{21} Metallic Enclosure Resonance Check	94
6.8	Measurement of LPF on Network Analyser	94
6.9	K -Inverter Equivalents	96
6.10	J -Inverter Equivalents	97
6.11	BPF Prototype	97
6.12	BPF Equivalent Prototype	97
6.13	BPF Coupled Resonator	98
6.14	Two Unsymmetrical Coupled Lines [12]	100
6.15	Coupled Lines Capacitances	101
6.16	Even and Odd Mode Capacitances	101
6.17	Mutual and Even-Mode Fringing Capacitances for Coupled Resonator Bars [13]	103
6.18	Odd-Mode Fringing Capacitances for Coupled Resonator Bar [13]	103
6.19	Fringing Capacitances for Isolated Resonator Bar [13]	104
6.20	Array of Parallel Coupled Lines [12]	105
6.21	Temex Ceramics Microwave Tuning Element [14]	107
6.22	Top View of Odd Inter-Digital Filter	108
6.23	Side View of Inter-Digital Filter	108
6.24	Final Simulation of RF-BPF at 7.5 GHz	110
6.25	Final Simulation of IF-BPF at 3.5 GHz	110
6.26	Measurement of BPF at 7.5 GHz	111
6.27	Measurement of BPF at 3.5 GHz	112
7.1	Simple Block Diagram of RFoF	114
7.2	Block Diagram of RFoF	116
7.3	Intensity Modulation - Direct Detection Without External Modulator	117
7.4	Intensity Modulation - Direct Detection With External Mach-Zehnder Modulator	117
7.5	Construction Diagram of a Fibre Optics Cable [15]	118
7.6	Example of Total Internal Reflection	120
7.7	Total Internal Reflection in a Fibre Optics Cable	120
7.8	Single-Mode Graded Index Fibre [16]	121
7.9	Multi-Mode Step Index Fibre [16]	121
7.10	Multi-Mode Graded Index Fibre [16]	121
7.11	Modal Dispersion in Multi-Mode Step Index Fibre [16]	122
7.12	Modal Dispersion in Multi-Mode Graded Index Fibre [16]	122
7.13	Chromatic Dispersion [16]	123
7.14	Output Power Over Frequency for RFoF Link	125
7.15	Input Signal Power and Harmonics for RFoF Link Test	126
7.16	Output Signal Power and Harmonics for RFoF Link Test	127

8.1	ROACH Tutorial 3 Test Signal at 200 MHz	131
9.1	Configuration for the RF Stage Measurement	133
9.2	Measurement Results of RF Stage	134
9.3	Configuration for the RF Stage with RFoF Measurement	134
9.4	Measurement Results of RF Stage with Addition of RFoF Link	135
9.5	Configuration for the IF Stage Measurement	135
9.6	Measurement Results of IF Stage	136
9.7	Configuration for the IF Stage with LPF Measurement	136
9.8	Measurement Results of IF Stage with Addition of LPF	137
9.9	Configuration for the Full Receiver Measurement	137
9.10	Measurement Results of Full Receiver	138
9.11	Configuration for the Full Receiver with LPF Measurement	138
9.12	Measurement Results of Full Receiver with Addition of LPF	139
B.1	Basic MATLAB-CST Program	VI
C.1	Efficiencies of Efficiency Optimised Antenna	VII
C.2	Field Pattern of Efficiency Optimised Antenna	VIII
C.3	Cross Polarisation of Efficiency Optimised Antenna	VIII
C.4	Γ of Efficiency Optimised Antenna	VIII
C.5	Efficiencies of Field Pattern Optimised Antenna	IX
C.6	Field Pattern of Field Pattern Optimised Antenna	IX
C.7	Cross Polarisation of Field Pattern Optimised Antenna	X
C.8	Γ of Field Pattern Optimised Antenna	X
C.9	Efficiencies of Γ Optimised Antenna	XI
C.10	Field Pattern of Γ Optimised Antenna	XI
C.11	Cross Polarisation of Γ Optimised Antenna	XI
C.12	Γ of Γ Optimised Antenna	XII
C.13	Efficiencies of Cross Polarisation Optimised Antenna	XII
C.14	Field Pattern of Cross Polarisation Optimised Antenna	XIII
C.15	Cross Polarisation of Cross Polarisation Optimised Antenna	XIII
C.16	Γ of Cross Polarisation Optimised Antenna	XIII
E.1	Lumped Element Low Pass Filter PCB Design in ADS	XV
E.2	PCB of IF Low Noise Amplifier Designed in ADS	XVI
E.3	PCB of RF Low Noise Amplifier Designed in ADS	XVII
F.1	Photos of Conical Corrugated Horn Antenna	XVIII
F.2	Photo of Mixers	XIX
F.3	Photo of Valon Frequency Synthesizer	XIX
F.4	Photo of Low-Pass Filter	XIX
F.5	Photo of RF Band-Pass Filter	XX
F.6	Photo of IF Band-Pass Filter	XX
F.7	Photo of RF Low Noise Amplifier	XXI
F.8	Photo of IF Low Noise Amplifier	XXI
F.9	Photos of Radio Frequency Over Fibre Link	XXII
F.10	Photo of 30 m Fibre Optics Cable	XXII
F.11	Photo of ROACH Board with Clock Synthesizer	XXII

List of Tables

2.1	Solar Properties	11
2.2	Use of the Radio Band in South Africa [17]	16
2.3	Radio Astronomy Applications [18] [19]	17
3.1	Initial Model Design [8]	29
3.2	Model Parameter Descriptions	30
3.3	Starting Values for Optimisations	34
3.4	Optimised a and d for Efficiency	35
3.5	Optimised a, b and d for Pattern Symmetry	37
3.6	Optimised a and d for Γ	37
3.7	Optimised a, b and d for Cross Polarisation	38
3.8	Summary of Measurements	43
3.9	Summary of Measurements	46
4.1	RF and IF Mixer Properties	55
4.2	Valon Frequency Synthesizer Characteristics	57
4.3	Frequency Ranges of Receiver Components	60
4.4	Third Order Intermodulation Products of Proposed Receiver	63
4.5	Description of LO Leakage Signals and Intermodulation Products in Output of Simulated Receiver	68
5.1	VMMK-3803 RF Low Noise Amplifier Characteristics	76
5.2	ADL5602 IF Low Noise Amplifier Characteristics	77
6.1	Design Parameters for LPF	90
6.2	Design Values Used for Calculation of Order of BPF's	108
6.3	Model Parameter Descriptions	109
6.4	Filter Results	109
6.5	Filter Results	112
7.1	IEEE Fibre Standards [15]	119
7.2	Miteq RFoF Link Properties [15]	124
7.3	Dartcom Fibre Optics Properties [15]	125
D.1	TraX PCB Specifications	XIV
E.1	Low Pass Filter Ideal and Compromised Component Values	XV
E.2	IF LNA Component Values	XVI
E.3	RF LNA Component Values	XVII

Nomenclature

Constants

$$\pi = 3.141\,592\,654\dots$$

$$c_0 = 3 \times 10^8 \text{ m/s} \quad - \text{ Speed of Light}$$

$$h = 6.63 \times 10^{-34} \quad - \text{ Planck's Number}$$

$$k = 1.38 \times 10^{-23} \quad - \text{ Boltzman's Constant}$$

$$T_0 = 290 \text{ }^\circ\text{K} \quad - \text{ Room Temperature}$$

Variables

θ Polar Angle

θ_0 Subtended Angle of Parabolic Dish

θ_c Critical Angle for Total Internal Reflection

θ_i Incident Angle of Parabolic Dish

ϕ Azimuth Angle

ϵ_{ap} Feed Efficiency

Ω_s Solid Angle Subtended by Source

δ Phase Centre Offset

λ Wavelength

B	Brightness of Source
C_f	Fringing Capacitance for Isolated Bar
C_{fe}	Even-Mode Fringing Capacitance for Coupled Bar
C_{fo}	Odd-Mode Fringing Capacitance for Coupled Bar
C_k	Self Capacitance
$C_{k,k+1}$	Coupling Capacitances
T	Temperature

Abbreviations

ADC	- Analogue to Digital Converter
ADS	- Advanced Design Systems
BPF	- Band-Pass Filter
BOR	- Body of Revolution
CASPER	- Collaboration for Astronomy Signals Processing and Electronics Research
CO	- Co-Polarization
CST	- Computer System Technology
CW	- Continuous Wave
DAC	- Digital to Analogue Converter
DDS	- Direct Digital Synthesis
DFT	- Discrete Fourier Transform
E&E	- Electrical and Electronic
EM	- Electromagnetic
EMI	- Electromagnetic Interference

- EU - European Union
- FPGA - Field-Programmable Gate Array
- GPS - Global Positioning System
- GSM - Global System for Mobile Communication
- ICASA - Independent Communications Authority of South Africa
- IDE - Integrated Development Environment
- IEEE - Institute of Electrical and Electronic Engineers
- IF - Intermediate Frequency
- IL - Insertion Loss
- IM-DD - Intensity Modulation - Direct Detection
- ITU - International Telecommunication Union
- LAN - Local Area Network
- LED - Light Emitting Diodes
- LNA - Low Noise Amplifier
- LO - Local Oscillator
- LPF - Low-Pass Filter
- NATO - North Atlantic Treaty Organisation
- NF - Noise Figure
- PCB - Printed Circuit Board
- PEC - Perfect Electrical Conductor
- PSD - Power Spectral Density
- PTP - Point to Point
- RADAR - Radio Detection and Ranging

- RF - Radio Frequency
- RFI - Radio Frequency Interference
- RFoF - Radio Frequency Over Fibre
- RMS - Root Mean Square
- ROACH - Reconfigurable Open Architecture Computing Hardware
- RX - Receiver
- SKA - Square Kilometre Array
- SNR - Signal to Noise Ratio
- TE - Transverse Electric
- TEM - Transverse Electromagnetic
- THD - Total Harmonic Distortion
- TM - Transverse Magnetic
- TX - Transmitter
- UHF - Ultra High Frequency
- VBA - Visual Basic
- VCO - Voltage Controlled Oscillator
- VLBI - Very Long Baseline Interferometry
- WLAN - Wireless Local Area Network
- XP - Cross Polarization

Chapter 1

Introduction

1.1 Background

With the advent of the Square Kilometre Array (SKA) interest in radio astronomy has grown tremendously, not only for the general public, but within the engineering community as well. With two dedicated sites and the largest collecting area of any telescope ever made, the SKA provides many engineering challenges. The sensitivity requirements of such a telescope means that new and better versions of current technology is needed.

The South African bid for the SKA has lead to several innovations within the South African engineering and radio astronomy communities, through ongoing research and collaborations. The SKA is also a source for development of tertiary education in surrounding African countries, helping to make the SKA a truly global project.

The completed SKA telescope is estimated to have a field of view 50 times that of the Hubble Space Telescope. The telescope will be able to survey large areas of the sky in a fraction of the time of current systems. This immense telescope will be used to answer fundamental questions that we as a species have about the universe.

The SKA has the potential to be the defining scientific endeavour of the 21st century.

1.2 Objective

The purpose of this project was to design and implement a receiver system appropriate for radio astronomy at the E&E Engineering Department at Stellenbosch University. The Department has a parabolic reflector dish that can be used for the project.

It is possible to purchase most of the required components off the shelf, but it was decided to design as much of the receiver as possible to highlight the specific challenges that may be encountered during the design of the different components. This includes the design of the antenna, filters and low-noise amplifiers. It was also decided to use Radio Frequency Over Fibre (RFoF) to determine its viability for use in radio astronomy. To ultimately test the system a measurement of the Sun will be carried out. Other strong sources of radio frequency emissions, such as Jupiter, could also possibly be detected.

1.3 Overview

The antenna that was designed for this project is a corrugated conical horn antenna. The antenna was optimised using MATLAB Version R2010a [20] and the full wave electromagnetic simulation program CST 2013 [21]. A step discontinuity was added to the waveguide section of the antenna to generate higher order modes so that spillover and cross polarisation can be reduced. The antenna was manufactured and measured at the E&E Department.

The chosen receiver architecture for this project was the double super-heterodyne receiver. This was mainly chosen due to the lack of viable options for the other receiver types that were considered. Using this type of receiver comes with certain problem areas and the intermediate frequency must be chosen carefully. The presence of possible spurious signals was checked by plotting spur charts. Microwave Office [22] was used to simulate the receiver. Figure 1.1 shows the overall receiver system.

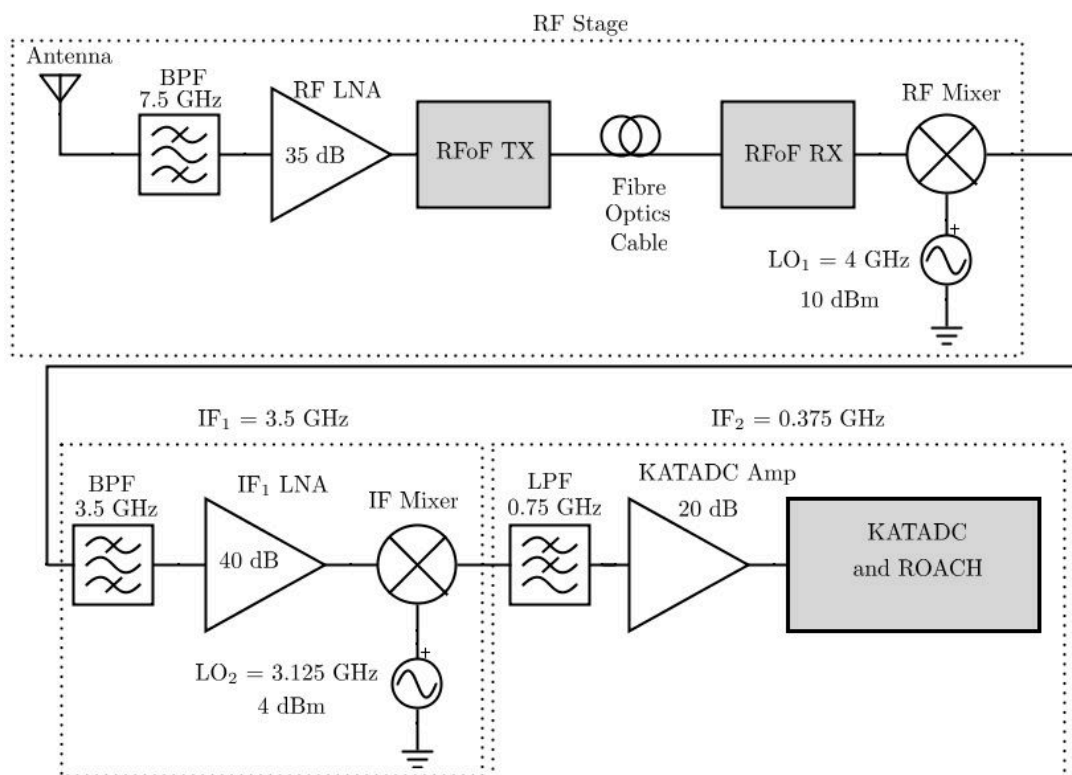


Figure 1.1: Receiver to be Used for Project

Inter-digital waveguide filters were used for the required band-pass filters, while a lumped element design was used for the required low-pass filter. Both designs use a Chebyshev low-pass prototype. The inter-digital design filter is realised as a coupled resonator structure, and physical dimensions are initialised from tabulated data in the literature and finally optimised in CST. The low-pass filter was designed in ADS 2013 [23]. All filters were manufactured and measured at the E&E Department.

A simple design for the low-noise amplifiers was desired. Appropriate off the shelf amplifiers were chosen and the required biasing circuits were simulated in ADS. The Printed Circuit Board (PCB) layout was also simulated in ADS and incorporated with the biasing circuit. Both the low-noise amplifiers were manufactured and measured at the E&E Department.

RFoF was used as an alternative to traditional signal transmission. RFoF uses fibre optics to transmit a signal over long distances with low loss by converting the signal to the optical domain. A RFoF transmitter and receiver was obtained on loan from Accutronics (Pty) Ltd. The RFoF link was tested separately and later added to the receiver chain.

The back-end that was used was the ROACH board. The ROACH board is versatile and can be programmed to perform many different tasks. The board was used as a spectrometer, essentially showing the frequency spectrum of the incoming signal. Existing software available for the board was edited and used.

Final measurements of the receiver were performed in the High Frequency Laboratory at the E&E Department.

1.4 Thesis Layout

Chapter 2 of this thesis will discuss the fundamentals of radio astronomy relevant to this project. Much of the information presented in Chapter 2 was found in the classic textbook by Krauss [2]. The Chapter introduces the fundamental concepts of brightness and blackbody radiation, and then also discusses the dish that is to be used as well as identifying possible bands of operation.

Chapter 3 focusses on the design of the antenna. Techniques that are used to reduce spillover and cross polarisation are discussed, as well as the feed efficiency and the importance of the rotational symmetry of the antenna. The design of the antenna is presented from the initial design, through the optimisation process to the final design. The measurement process is described and the measured results shown.

Chapter 4 describes the design of the receiver. The components of the receiver are briefly discussed and the basic functioning of the receiver is explained. Different types of receivers are identified and the receiver architecture that was used is presented. The selection of the intermediate frequency is shown by identifying spurious signals while a simulation was performed to validate the selection.

Chapter 5 covers the design of the Low Noise Amplifiers (LNA's). Noise in receiver systems is discussed. The design of the LNA's is then presented. The design includes the design of the PCB layouts.

Chapter 6 presents the design, simulation and measurements of the low-pass filter and the band-pass filters. The properties and principles of the inter-digital filter (used for the band-pass filter) is explained.

Chapter 7 introduces the idea of RFoF transmission by explaining the basic functioning

as well as the benefits and limitations of using RFoF. Properties of a fibre optics cable, such as the transmission of light, are also explored. Some basic measurements are also shown.

Chapter 8 is about the back-end of the receiver. Some possible back-end options are explored. The ROACH board is then introduced and its use as a spectrometer is explained. Work done on the ROACH is shown.

Chapter 9 presents the final measurements that were performed for the project. The measurements were done for each individual stage of the receiver as well as a total system measurement.

Chapter 2

Radio Astronomy Fundamentals

2.1 Introduction

Radio astronomy is the study of astronomical sources in the radio frequency band. These sources are studied in the radio band due to the favourable properties of atmospheric absorption at RF. Using other bands of operation, excluding the optical band, is not possible from the surface of the earth. Optical astronomy involves studying the same sources in the optical band. The Hubble Space Telescope is a well known optical telescope.

The primary goal of radio astronomy as a whole is to study the universe. Many objects in the universe emit radio waves [24]. Studying these objects at different frequencies allows astronomers to make important deductions about processes that go on in the universe.

While optical astronomy has been conducted since man first looked up at the stars, radio astronomy is a relatively young field. Karl Jansky is considered as one of the founding figures of radio astronomy. In 1931 he built an antenna designed to receive radio waves. Jansky's goal was to detect interference in the radio band that was affecting Atlantic radio transmissions [25]. After months of investigations Jansky identified 3 sources of interference; nearby thunderstorms, distant thunderstorms and an unidentified source. Eventually Jansky identified the source as the Milky Way and radio astronomy was born.

Many types of radio telescopes exist. A well-known type of radio telescope is the parabolic reflector antenna, which requires a reflector, an antenna feed and a receiver. The dish is usually a front-fed type dish or a Cassegrain dish. Radio waves from astronomical sources are collected by the reflector and directed to the feed. The receiver amplifies and processes the signal so that it can be analysed digitally.

Radio sources produce either continuum radiation or line radiation [26]. Continuum radiation can be detected at various frequencies while line radiation is only detectable at a certain frequency. For example, the Sun is a continuum source since it radiates across the radio band. Continuum radiation can be due to thermal or non-thermal radiation. Radio gas emissions, which occur at specific frequencies, are examples of line radiation. The study of Hydrogen is of particular interest because it is the most abundant element in the universe.

The Square Kilometre Array (SKA) is currently at the cutting edge of radio astronomy. The completed project is estimated to be 50 times more sensitive and 10 000 times faster than radio astronomy system in operation today [27]. The project uses an array to create an effective observation area of 1 square kilometre. Some major applications for the SKA are the study of the formations of stars and galaxies, how they evolve and even possibly the search for life elsewhere in the universe.

2.2 Radio Astronomy Fundamentals

2.2.1 Coordinate System

To be able to observe astronomical sources one must know where to point the appropriate telescopes. Astronomers use what is known as the right ascension and declination system [24]. A "*Celestial Sphere*" is defined as a 2D projection of the sky on a sphere concentric with the earth. This sphere also defines a "*Celestial Equator*". The celestial equator is parallel to earth's equator, and as such, defines the point of 0 declination. At the north and south poles the angle of declination would be 90° and -90° respectively.

To determine the equivalent latitudinal position, a hour circle is defined as a circle on the celestial sphere that passes through both poles. Measuring westward from the local meridian to the hour circle passing through the source will give the required hour angle. Figure 2.1 shows how the celestial sphere uses right ascension and declination.

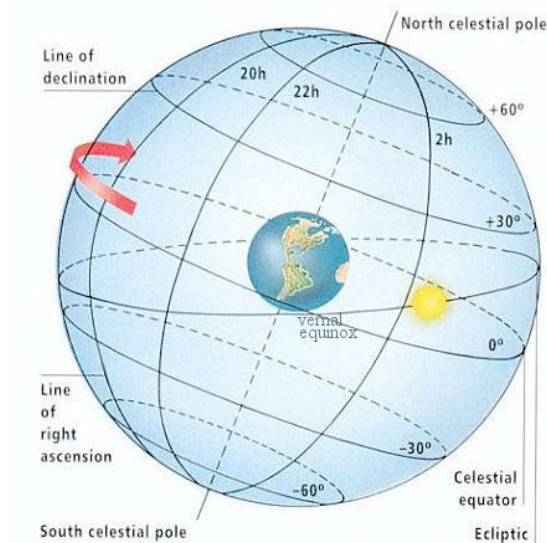


Figure 2.1: Celestial Sphere [1]

An alternate, observation bases system, is the horizon system, defined as follows. The zenith is defined as the point directly above the observer. The azimuth angle ϕ is defined as the polar angle along the ground in the $x - y$ plane while θ is defined as the angle from the z -axis to the source. Figure 2.2 shows this spherical coordinate system.

2.2.2 Brightness

Brightness is one of the most fundamental concepts of radio astronomy. Brightness is essentially a measure of power received per unit area per solid angle per unit bandwidth [2]. Per unit area refers to the collecting area of the dish or effective antenna area. Per solid angle refers to the area of our sky. Per unit bandwidth refers to the bandwidth of operation. The infinitesimal power is defined as

$$dW = B(\theta, \phi) \cos \theta d\Omega dA dv \quad (2.2.1)$$

where

dW = infinitesimal power, [W]

B = brightness, $\left[\frac{\text{W}}{\text{m}^2 \text{ Hz rad}^2}\right]$

$d\Omega$ = infinitesimal solid angle, $[\text{rad}^2]$

θ = angle between $d\Omega$ and zenith, [rad]

dA = infinitesimal area of surface, $[\text{m}^2]$

dv = infinitesimal element of bandwidth, [Hz].

It is important to note that when radio astronomers talk about frequency they use the notation ν as shown in (2.2.1). Engineers use f to note frequency. This Chapter will conform to the astronomers convention. However, the rest of this thesis will use the engineering norm.

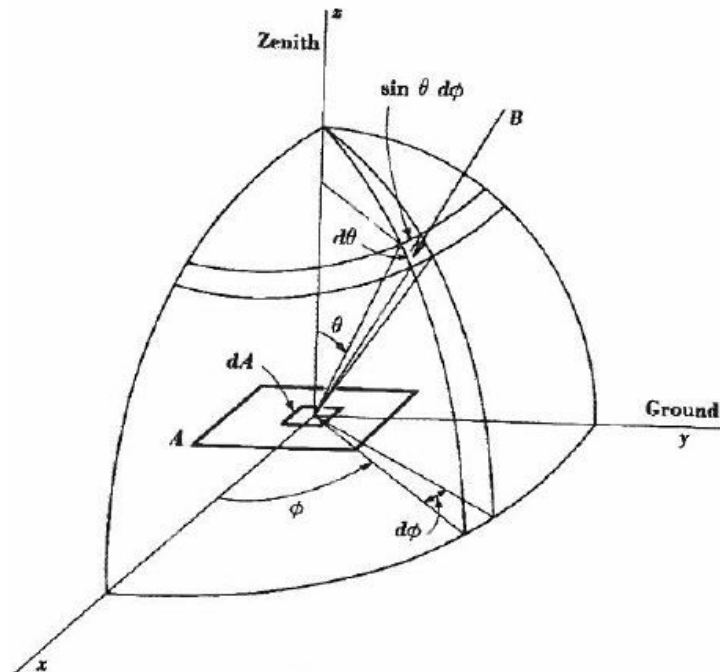


Figure 2.2: Brightness From a Element of Solid Angle $d\Omega$ [2]

If the received infinitesimal power dW is independent of the position of dA on the surface, as shown in Figure 2.2, (2.2.1) becomes

$$W = A \int_v^{v+\Delta v} \iint_{\Omega} B(\theta, \phi) \cos \theta d\Omega dv. \quad (2.2.2)$$

Antennas used in radio astronomy are often mathematically replaced by an effective aperture (A_e). This effective aperture is a horizontal surface with a power pattern $P_n(\theta, \phi)$ directed towards the zenith [2], as shown in Figure 2.3. The power pattern is dimensionless and normalised. This means that for a general case where brightness varies with position and frequency a new equation can be set up. The fraction $\frac{1}{2}$ in (2.2.3) accounts for antennas only receiving power from one polarisation from the source. Received power can then be defined as

$$W = \frac{1}{2} A_e \int_v^{v+\Delta v} \iint_{\Omega} B(\theta, \phi) P_n(\theta, \phi) d\theta dv. \quad (2.2.3)$$

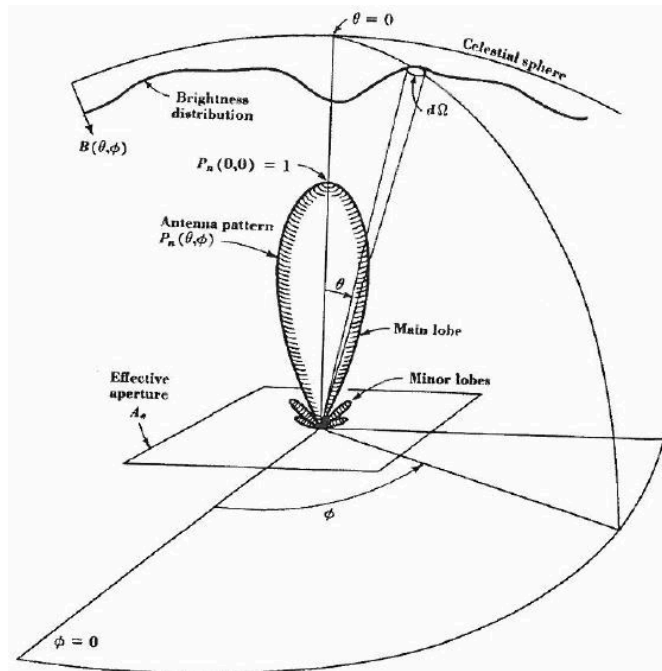


Figure 2.3: Power Pattern of Effective Aperture [2]

2.2.3 Brightness of Discrete Sources

Discrete radio sources are those sources that can be defined as distinct or separate [2]. Discrete radio sources can be classified into 3 categories.

- Point Source
- Localized Source
- Extended Source

A point source is an idealization that subtends an infinitesimal solid angle. Sources of small extent are sometimes regraded as point sources. The distinction between localized source and extended source is somewhat arbitrary. Both are sources with finite subtended angles. Common practice dictates that sources with a diameter less than 1° are considered localized sources while those with a diameter of more than 1° are extended sources [2].

The brightness of a source across the sky may differ. For any discrete source, integrating the brightness over the source will result in the flux density. The flux density of a source is defined as the power received from that source from a specific solid angle in the sky. The unit is the jansky (Jy) and is expressed as S with units $[10^{-26} \times \frac{\text{W}}{\text{m}^2 \text{ Hz}}]$ as

$$S = \iint_{\text{source}} B(\theta, \phi) d\Omega. \quad (2.2.4)$$

When flux density is observed with an antenna with power pattern $P_n(\theta, \phi)$, S_o can be defined as

$$S_o = \iint_{\text{source}} B(\theta, \phi) P_n(\theta, \phi) d\Omega. \quad (2.2.5)$$

From this it follows that (2.2.3) can be rewritten as

$$W = \frac{1}{2} A_e \int_v^{v+\Delta v} S_o dv. \quad (2.2.6)$$

If it is assumed that the flux density of a source is constant over a certain bandwidth Δv (2.2.6) can be expressed as

$$W = \frac{1}{2} A_e S_o \Delta v \quad (2.2.7)$$

where S_o can be determined by assuming either a sufficiently small or large source.

The antenna pattern acts as a weighing function [2] and as such the observed flux density will never be equal to the true flux density shown in (2.2.4). There are however two cases to aid in determining the flux density. If the source is sufficiently small so that $P_n(\theta, \phi) \simeq 1$ over the source (2.2.5) will be very close to the real flux density. In a separate case, if the source is large enough to be considered constant over the main lobe of the antenna (2.2.5) will reduce to

$$S_o = B(\theta, \phi) \iint P_n(\theta, \phi) d\Omega \simeq B(\theta, \phi) \Omega_M \quad (2.2.8)$$

where $\Omega_M =$ main-lobe solid angle, [28].

2.2.4 Blackbody Radiation and Planck's Law

All objects which have a temperature above absolute zero radiate energy using electromagnetic waves [2]. These object also absorb and/or reflect electromagnetic energy. A good absorber of this energy is also a good radiator of this energy. A perfect radiator/absorber is known as a *blackbody*. Sources of blackbody radiation absorb radiation at all frequencies, as well as radiating energy that is only a function of temperature and frequency. No such ideal source exists, but many sources act like blackbodies over a range of frequencies.

Max Planck formulated an equation for the brightness of a blackbody source shown here

$$B = \frac{2hv^3}{c^2} \frac{1}{e^{\frac{hv}{kT}} - 1} \quad (2.2.9)$$

where

B = brightness, [W]

h = Planck's constant = 6.63×10^{-34} , [Joule · sec]

v = frequency, [Hz]

c = speed of light = 3×10^8 , [m/s]

k = Boltzmann's constant = 1.38×10^{-23} , [Joule/°K]

T = temperature, [°K].

Maximum brightness shifts to higher frequencies as the temperature becomes greater. For higher frequencies where $hv \gg kT$ Wien's Displacement Law can be used as an approximate equivalent to Planck's Radiation Law. At lower frequencies where $hv \ll kT$ the Rayleigh-Jeans Approximation can be used.

If a source is discrete and radiating at a constant temperature Planck's Law can be used to find the flux density. It is assumed that the temperature, and brightness as a result, are constant over the source,

$$S = \frac{2hv^3\Omega_s}{c^2} \frac{1}{e^{\frac{hv}{kT}} - 1} = B\Omega_s = B\pi \left(\frac{a}{R}\right)^2 \quad (2.2.10)$$

where

Ω_s = solid angle subtended by source, [rad²]

a = radius of source

R = distance from source to observation point.

Noise in a receiver system is inherent and a consequence of blackbody radiation. The so-called Johnson-Nyquist Noise Power can be defined as

$$P = kTB. \quad (2.2.11)$$

This noise is Gaussian in nature and usually a result of background noise received by the receiver. Section 5.1 goes into more detail about receiver noise and equivalent temperatures.

2.3 Radio Astronomy Observations

2.3.1 The Sun and Other Bodies in Our Solar System

The Sun is by far the strongest and brightest radio astronomical source observable from earth. Radio frequency activity from the Sun can be classified as 3 separate types of phenomena [24], namely

- quiet Sun component which is always present
- slowly varying component
- active Sun component caused by sunspots and flare activity

The quiet Sun emissions are due to the thermal emissions from hot ionized gas [24]. The other emission components are due to sunspot activity. Areas above sunspots have a much higher electron density and the blackbody temperature in these regions can up to 2 million °K. The slowly varying component is a thermal component that is a result of these high temperature regions. Table 2.1 lists some solar properties.

Parameters	Value
Age	4.6 billion years
Distance to Earth	149.6 million km
Radius	695,800 km
Mass	1.989×10^{30} kg
Surface Temperature	5778° K

Table 2.1: Solar Properties

The Sun is an example of a continuum source. It emits electromagnetic energy across the radio frequency band. Figure 2.4 shows flux densities of the active and quiet Sun as well some other well known radio astronomical sources.

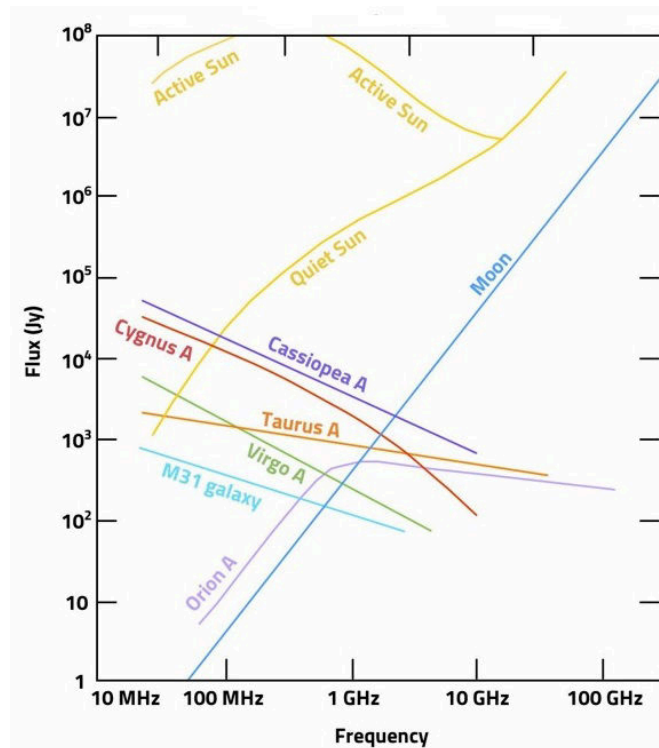


Figure 2.4: Flux Densities of Some Radio Sources [3]

Other celestial bodies in our solar system are visible in the optical spectrum thanks to reflected light from the Sun. At radio frequencies however these bodies emit their own radiation. This is dominated by thermal emission [24].

The Jovian planets, known as the gas giants, are Jupiter, Saturn, Uranus and Neptune. These planets are much colder than other planets in the solar system due to their distance from the Sun and will therefore not be bright sources of thermal radiation. However, Jupiter is known as a strong radio emitter [24]. The source of these emissions have been found to be non-thermal synchrotron emissions from magnetic fields of the planet and non-thermal cyclotron emissions from electrons spinning in this magnetic field.

2.3.2 Emission and Absorption Lines

Spectral lines, comprised of emission and absorption lines, occur only at specific frequencies. The source of these lines are generally atoms and small molecules or molecular ions in gaseous form [24].

Emission lines are a result of a warm gas cloud with a relatively cold background. Much more power will be received at the line frequency than frequencies around the line frequency.

Absorption lines are a result of colder gas with a relatively warmer background. The gas cloud absorbs the radiation from the warmer background at a certain frequency. The power received at the line frequency will be less than the power received at the frequencies around the line frequency.

As mentioned before, Hydrogen is an element of particular interest. Hydrogen emits electromagnetic radiation at 1420.4 MHz. This is called the Hydrogen Line and is due to a change in energy state of neutral hydrogen atoms.

2.3.3 Other Sources

There are many other sources of interest to radio astronomers. These include, but are not limited to, radio galaxies, supermassive black holes, supernova remnants, pulsars, star forming regions and primordial black holes.

2.4 Reflector Antennas

2.4.1 Types of Reflector Dishes

There are various types of reflector dishes used in the antenna systems. These include the plane reflector, the corner reflector and the parabolic reflector. Radio astronomy uses the parabolic reflector dish due to its large effective area. The parabolic reflector dish can be fed in many ways, but the most popular types used in radio astronomy are the front type feed or the Cassegrain type feed. Figure 2.5 shows the difference in these types of feeds.

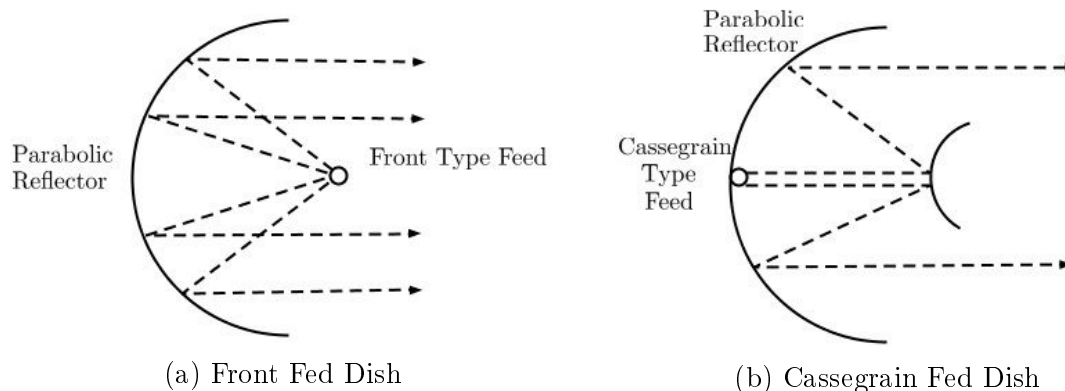


Figure 2.5: Parabolic Reflector Dishes

Plane waves that are incident on the front fed dish are reflected by the dish to a focal point where the antenna is mounted. The Cassegrain dish reflects the plane waves onto a sub-reflector which then reflects the waves to the antenna. The Cassegrain dish has some advantages over the front fed dish. Since the antenna aperture is mounted on the surface of the dish, the rest of the receiver can easily be mounted behind the dish. Also, since the antenna is pointed away from the ground, any spillover past the sub-reflector radiates outward away from the ground. In a front-fed dish spillover will be reflected by the ground and "*ground noise*" may increase the noise temperature of the antenna.

The dish available at the E&E Department is a front fed type dish. Designs in this project are specifically for that dish. This fact becomes most prominent in Chapter 3 when the antenna design is performed with the feed efficiencies in mind. The feed efficiencies depend on the dish used.

2.4.2 Geometry of Parabolic Dish

Figure 2.6 shows the geometry of a front fed type parabolic reflector dish, the type that will be used in this project. These dishes are often characterised by their f/d , which is the distance from the focal point f divided by the diameter of the aperture d .

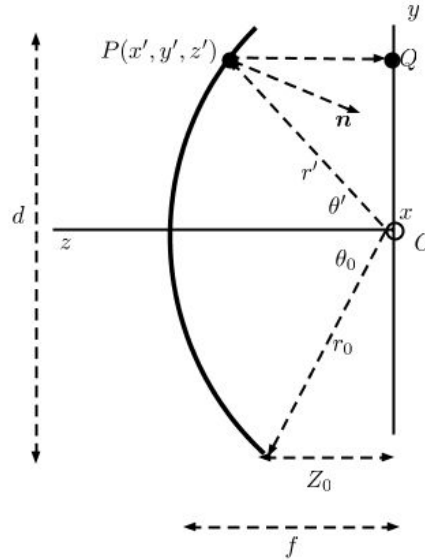


Figure 2.6: Geometry of Front Fed Parabolic Reflector

An important part of the geometry is the subtended angle θ_0 . This is the angle from the focal point to the edge of the dish. Section 3.2 describes the importance of the parameter. It can be calculated using as

$$\theta_0 = \tan^{-1} \left| \frac{\frac{1}{2} \frac{f}{d}}{\left(\frac{f}{d}\right)^2 - \frac{1}{16}} \right|. \quad (2.4.1)$$

The f/d of the available dish is 0.36 with $f = 4.6$ m. The subtended angle is $\theta_0 = 69.56^\circ$.

2.4.3 Dish Gain

The directive properties of a dish antenna can be described by its gain. The gain is the ratio of received power along the beam axis to power received by an isotropic source. The maximum gain can be expressed in terms of the aperture as

$$G_{max} = \frac{4\pi}{\lambda^2} A. \quad (2.4.2)$$

However, the actual gain of the dish antenna will be related to the effective aperture. The effective aperture is the product of the aperture area and feed efficiency ϵ_{ap} . This

efficiency is described in much more detail in Section 3.2 and incorporated into the gain equation

$$G = \epsilon_{ap} \frac{4\pi}{\lambda^2} A. \quad (2.4.3)$$

For the frequency of interest (discussed in the next Section), and assuming a typical $\epsilon_{ap} = 0.65$, the expected gain of the available dish is

$$G = 10 \log \left\{ 0.65 \times \frac{4\pi}{\left(\frac{3 \times 10^8}{7.5 \times 10^9}\right)^2} \times \left[\pi \left(\frac{d}{2}\right)^2 \right] \right\} = 49.4 \text{ dB}. \quad (2.4.4)$$

This is a typical value for parabolic dish antennas.

2.5 Selection of Operating Band

2.5.1 Radio Emissions

Radio frequency signals and optical light are both part of the electromagnetic (EM) spectrum. This spectrum is used in telecommunications and the use of parts of the spectrum are closely regulated. The International Telecommunications Union (ITU) is the regulating body recognised by most of the countries in the world. The ITU has divided the world into different regions. Each region has its own allocation of the spectrum. South Africa is in region 1.

Other organisations such as the Institute of Electrical and Electronics Engineers (IEEE), the European Union (EU) and the North Atlantic Treaty Organisation (NATO) have their own classifications of the EM spectrum.

The radio frequency part of the spectrum is generally considered to be from 3 kHz - 300 GHz. Some of the strongest signals in this band are television broadcasts, radio broadcasts, mobile communication, WiFi, Global Positioning System (GPS) and satellite communication. Table 2.2 gives a brief overview of these and other prominent radio signals in South Africa. The bands shown may have been allocated more applications but only the major applications are presented here.

Frequency (MHz)	Allocated	Used in SA
87-108	Broadcasting	Commercial Radio Broadcasting
470-862	Broadcasting	UHF Commercial TV Broadcasting
900/1800	Fixed Mobile	GSM
1600	Radio-navigation	GPS
2100	3G	3G
2400-2500	WLAN	WLAN
5700-7000	Satellite Communication	Satellite Communication and PTP Links
7000-9000	Satellite Communication	PTP Links
9000-10000	Radio-navigation	RADAR and Radio-Navigation

Table 2.2: Use of the Radio Band in South Africa [17]

As can be seen the spectrum is quite busy. Any unwanted signals are referred to as Radio Frequency Interference (RFI). The challenge for radio astronomers is to find a frequency band that has limited RFI, is practically realisable and has astronomical value. The locations of the proposed SKA sites highlight the need to reduce RFI.

The Independent Communications Authority of South Africa (ICASA) is in charge of spectrum allocation in South Africa. Since South Africa is in region 1 of the ITU allocation, ICASA's main objective is to enforce and regulate this allocation. Upon review of ICASA's general notice it was found that from 7 - 9 GHz there was only one application used in South Africa [17]. This part of the spectrum is allocated for mostly satellite communication and aeronautical/maritime navigation. However, South African applications in this part of the spectrum is only used for point-to-point (PTP) links.

Examples of PTP links include telephone calls, leased lines, microwave relays, two way radio and fixed wireless. Fixed wireless is communication between two fixed points. The antennas are usually highly directional since the transmitting and receiving points are fixed. Due to the position and direction of the available reflector dish, no PTP or fixed wireless signals are expected to be received.

Below 7 GHz satellite communication occurs and above 9 GHz aeronautical and maritime navigation as well as RADAR is used. This means that the 7 - 9 GHz band would be relatively free of RFI for radio astronomical purposes.

2.5.2 Radio Astronomy Applications

The proposed band of operation mentioned in Section 2.5.1 does not contain many traditional areas of interest for radio astronomy. Table 2.3 list radio astronomy applications in and around the proposed band. As can be seen, the only radio astronomy application in the band is the detection of the spectral line of Ionized Helium Isotope at 8.665 GHz.

Frequency (GHz)	Applications
5 - 5.03	VLBI
6.65 - 6.67	Methanol (CH ₂ OH)
8.665	Ionized Helium Isotope (³ HeII)
10.6 - 10.68	VLBI and Continuum Measurements

Table 2.3: Radio Astronomy Applications [18] [19]

In choosing a frequency of operation, the atmospheric absorption must be taken into account. The atmosphere of the earth is not transparent across the entire electromagnetic spectrum. The atmosphere is transparent in the optical band as well as a large section of the radio frequency band. This is one of the main reason why observations of the universe are made at radio frequencies. Figure 2.7 shows the atmosphere's transparency. The atmosphere becomes opaque at about 30 GHz. This means that the proposed band of 7 - 9 GHz is in the transparent part of the spectrum.

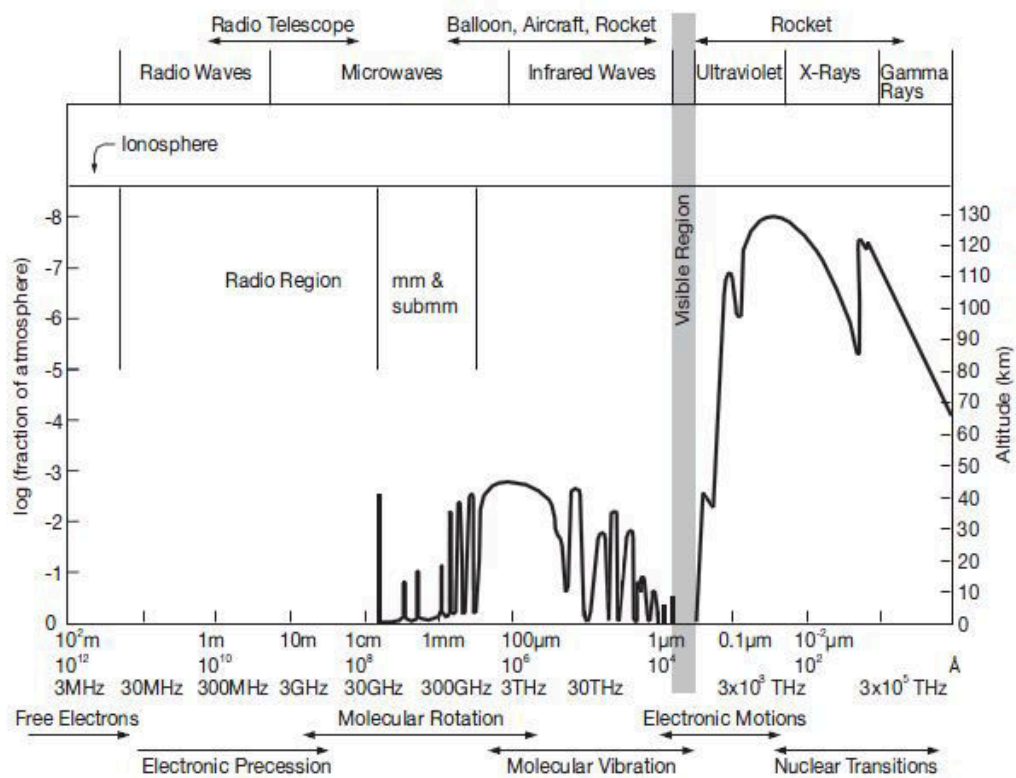


Figure 2.7: Atmospheric Absorption [4]

As highlighted in Section 1.2, the purpose of the project requires measurement of the Sun. Therefore 7.5 GHz was chosen as the operating frequency. This ensures minimum RFI and a high gain for the parabolic reflector. A relatively narrow bandwidth is preferred for the purpose of this project, but also limits received power. This will help to keep the noise floor low. The initial bandwidth will be determined by the antenna and the RF-stage band-pass filter (RF-BPF) of the receiver.

2.5.3 The Sun as a Source

To determine the expected power radiated from the Sun at the desired frequency Planck's Law (Equation 2.2.9) was used and it was found that

$$B = 9.96674 \times 10^{-27} \frac{\text{W}}{\text{m}^2 \text{rad}^2 \text{Hz}}. \quad (2.5.1)$$

As defined in Section 2.2.3, the flux density of a discrete source can be defined by (2.2.10) which states $S = \Omega_s B$. Ω_s is the subtended angle of the source and is defined as

$$\Omega_s = \pi \left(\frac{a}{R} \right)^2 = 6.8783261 \times 10^{-5} \text{ rad}^2 \quad (2.5.2)$$

where

$a = \text{radius of sun} = 6.955 \times 10^8 \text{ m}$

$R = \text{distance from earth to Sun} = 149.6 \times 10^9 \text{ m}.$

The expected flux density of the Sun at 7.5 GHz is then $S = 6.6495 \times 10^5 \text{ Jy}$, which is consistent with Figure 2.4. If it is assumed that the flux density of a source is constant over a certain bandwidth, (2.2.7) can be used to determine the received power. This is an estimation used to gain some idea of the expected power levels. The narrower the bandwidth, the more accurate this estimation will be.

Equation 2.2.7 requires the effective area of the antenna which is calculated as

$$A_e = \frac{G\lambda^2}{4\pi} = 10.8 \text{ m}^2. \quad (2.5.3)$$

Using these calculations, an estimate of the expected power level is plotted against receiver bandwidth.

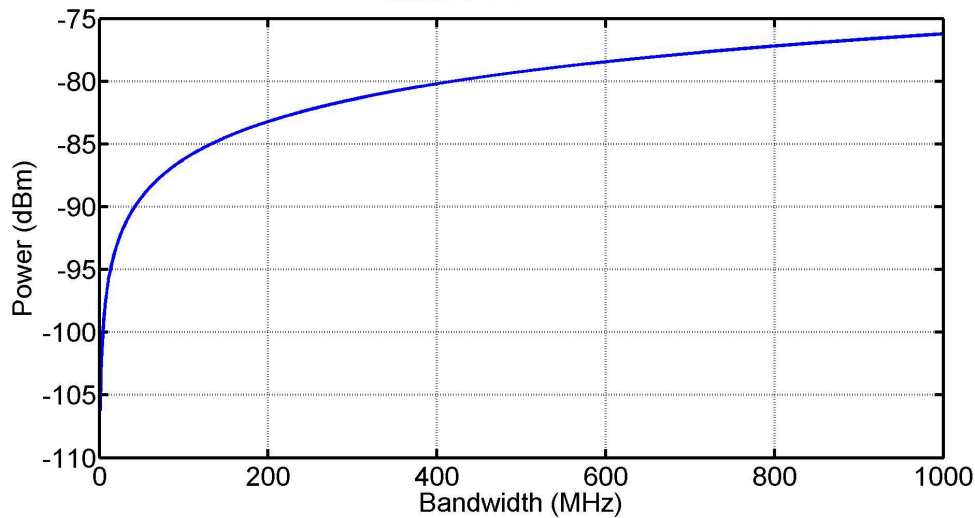


Figure 2.8: Estimated Expected Power to be Received from the Sun

Since the Sun is seen as a blackbody, it will generate Gaussian white noise in the receiver. This signal will be larger than other noise sources and this will be above the noise level of the receiver.

A single observation of the Sun will simply look like Gaussian white noise. To make a valid observation the Sun will be observed for a certain period of time by taking a finite number of measurements. As the sun passes over the receiving beam of the antenna the received "noise" will be greater than previous observations. Once the Sun passes past the receiving beam the signal will not be as powerful. If each observation is digitized, the power at a specific frequency can be found for each observation. The end result will be the normalised received power from the Sun plotted against the angle from the zenith to the Sun.

2.6 Conclusion

This Chapter provided a brief overview of radio astronomy sources, observations and instruments. The fundamental concepts of brightness and flux density were introduced. These can be used to determine the expected received power from a source as well as the noise level in a receiver.

Typical radio astronomy applications were presented. The frequency band of operation for this project was also chosen and an estimate of the expected power was made. A brief overview of how the Sun will be measured was also discussed.

Chapter 3

Antenna Design

This Chapter discusses the antenna that was used for the project. Section 3.1 starts off by describing some basic antenna properties while Section 3.2 defines the feed efficiency. The design of the antenna is then presented along with the simulated and measured results.

3.1 Antenna Properties

The S_{11} of an antenna, which will be known in this thesis as the reflection coefficient Γ , is one of the most important properties of any antenna. The input impedance of an antenna is also important since it has a direct relation to Γ .

The radiation patterns describes how the radiated power of an antenna varies as a function of either angle in the far-field. Radiation patterns are often normalised and expressed in decibels.

Polarisation is another important property. EM plane waves propagating in the \hat{z} - direction can have a \hat{x} component, a \hat{y} component or a combination of \hat{x} and \hat{y} components. If a wave consists of just one component, eg: $\mathbf{E} = \cos(2\pi f(t - \frac{z}{c}))\hat{x}$ then traces of the wave drawn at a particular position in space for varying times would be linear since there is only one component. This is referred to as the polarisation of the wave. Elliptical and circular polarisation occurs when both components are present and increase and decrease out of phase[29].

Cross polarisation refers to undesired components orthogonal to the desired components. Antennas that are ideally polarised cannot received any power from orthogonal polarisations. However, no antenna is ideally polarised and measurements must be taken to determine cross polarisation radiation patterns.

For a transmitting antenna gain is described as a measure of how well the antenna can convert input power into radio waves for a specific direction [30]. Similarly, for a receiving antenna it is described as a measure of how well the antenna can convert incoming radio waves from a specific direction into electrical power. When no direction is specified maximum gain is assumed. Gain can also be thought of as how much power is transmitted in the direction of peak radiation to that of an isotropic source [31]. An isotropic source is a hypothetical lossless antenna that radiates power equally well in all directions.

Gain is also related to directivity, which describes how well the antenna radiates in a certain direction. Radiation efficiency is used to obtain gain from directivity. It is important to note that this radiation efficiency is not the same as the feed efficiency described later on in this Chapter. Gain and directivity are related by

$$G(\theta, \phi) = \epsilon_{antenna} D(\theta, \phi). \quad (3.1.1)$$

3.2 Feed Efficiency

This Section describes the feed efficiency and how it is calculated. It is important to note the difference between the feed efficiency and the radiation efficiency. Feed, or aperture, efficiency is a measure of how well an antenna receives power entering the physical aperture. The feed efficiency ignores possible losses due to aperture blockage and feed scattering [32]. The aperture efficiency can be described as

$$\epsilon_{ap} = \frac{A_{eff}}{A_{phys}} = \frac{\lambda^2/4\pi}{A_{phys}}. \quad (3.2.1)$$

The radiation efficiency is related to the gain and the directivity of an antenna as described in Section 3.1.

The feed efficiency of a reflector system is an important indicator of the quality of the system. This is determined by many different sub-efficiencies as

$$\epsilon_{ap} = e_{BOR1} e_{sp} e_{ill} e_{\phi} e_{pol}. \quad (3.2.2)$$

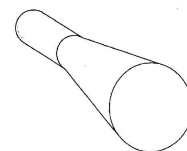
These sub-efficiencies in (3.2.2) are discussed later in Section 3.2.

3.2.1 Body Of Revolution

Body of Revolution (BOR) antennas are structures that are rotationally symmetric around an axis. Rotationally symmetric antennas, such as conical horn antennas, can be used to generate a main beam in the direction of symmetry [33]. These are excited by a TE_{11} mode. A circular main lobe around the axis of symmetry with a null on axis can be produced by a bi-conical antenna excited by a TE_{01} or TM_{01} mode. The former is referred to as a BOR_1 antenna and the latter is referred to as a BOR_0 antenna.



(a) Bi-Conical BOR_0 Antenna [33]



(b) Conical BOR_1 Antenna [33]

Figure 3.1: Examples of BOR_0 and BOR_1 Antennas

Any farfield pattern, such as

$$\mathbf{G}(\theta, \phi) = G_\theta(\theta, \phi)\hat{\theta} + G_\phi(\theta, \phi)\hat{\phi} \quad (3.2.3)$$

can be expressed in terms of a Fourier series because ϕ is periodic with period 2π [34]. The Fourier expansion defines $\mathbf{G}_\theta(\theta, \phi)$ and $\mathbf{G}_\phi(\theta, \phi)$ as

$$\mathbf{G}_\theta(\theta, \phi) = \sum_{n=0}^{\infty} [A_n(\theta) \sin(n\phi) + B_n(\theta) \cos(n\phi)] \quad (3.2.4)$$

$$\mathbf{G}_\phi(\theta, \phi) = \sum_{n=0}^{\infty} [C_n(\theta) \cos(n\phi) - D_n(\theta) \sin(n\phi)]. \quad (3.2.5)$$

We can also write

$$\mathbf{G}(\theta, \phi) = \mathbf{G}_s(\theta, \phi) + \mathbf{G}_i(\theta, \phi) \quad (3.2.6)$$

where $\mathbf{G}_s(\theta, \phi)$ is due to source currents and $\mathbf{G}_i(\theta, \phi)$ is due to induced currents on the antenna structure. These can also be expanded using Fourier series. For any *BOR* antenna the Fourier coefficients of $\mathbf{G}_s(\theta, \phi)$ will be proportional to $\mathbf{G}_i(\theta, \phi)$ because of the symmetry. Rotationally symmetric antennas cannot excite modes of higher order with ϕ variation other than those introduced by the source [33].

As an example, a BOR antenna fed by an infinitesimal electric dipole with a magnitude of Il is considered. The dipole is located on and normal to the symmetry axis and it is assumed that it is y -polarised. A radiation field function shown as (3.2.7) can be used to describe the associated $\mathbf{G}_s(\theta, \phi)$ as

$$\mathbf{G}_{s-y}(\theta, \phi) = -j \frac{k}{4\pi} \left[\cos \theta \sin \phi \hat{\theta} + \cos \phi \hat{\phi} \right] \eta Il. \quad (3.2.7)$$

Since the induced coefficients must be proportional to the source coefficients and since $\mathbf{G}(\theta, \phi) = \mathbf{G}_\theta(\theta, \phi) + \mathbf{G}_\phi(\theta, \phi) = \mathbf{G}_s(\theta, \phi) + \mathbf{G}_i(\theta, \phi)$, it can be concluded, by comparing (3.2.7) and (3.2.4)-(3.2.5), that for the case described only $A_1(\theta)$ and $C_1(\theta)$ are excited and that

$$A_1(\theta) = -j \frac{k}{4\pi} \eta Il \cos \theta \quad (3.2.8)$$

$$C_1(\theta) = -j \frac{k}{4\pi} \eta Il \quad (3.2.9)$$

where A_1 and C_1 are the E - and H -plane radiation patterns respectively.

For the infinitesimal dipole case, all the radiated power is due to A_1 and C_1 . No power exists in the higher order modes. For the practical dipole case, power radiated in the higher order modes represent power lost to the sidelobes. The ratio of BOR_1 power to total power $\left(\frac{P_{BOR_1}}{P_{total}}\right)$ can be defined as

$$e_{BOR_1} = \frac{\int_0^{2\pi} \int_0^\pi [|G_{\theta 1}|^2 + |G_{\phi 1}|^2] \sin \theta d\theta d\phi}{\int_0^{2\pi} \int_0^\pi [|G_\theta(\theta, \phi)|^2 + |G_\phi(\theta, \phi)|^2] \sin \theta d\theta d\phi} \quad (3.2.10)$$

while the Fourier expansion of BOR_1 power is

$$\int_0^{2\pi} \int_0^\pi [|G_{\theta 1}|^2 + |G_{\phi 1}|^2] \sin \theta d\theta d\phi = \pi \int_0^\pi [|A_1(\theta)|^2 + |B_1(\theta)|^2 + |C_1(\theta)|^2 + |D_1(\theta)|^2] \sin \theta d\theta. \quad (3.2.11)$$

Since only A_1 and C_1 contribute towards the antenna gain (3.2.4)-(3.2.5) can be used to determine the field patterns for all values of ϕ . The entire field pattern can be constructed from knowing only these components. This is thanks to the rotational symmetry of the BOR_1 antenna.

3.2.2 Co-Polar and Cross-Polar Unit Vectors

Given that $\mathbf{G}(\theta, \phi) = G_{CO}(\theta, \phi) \hat{\mathbf{a}}_{CO} + G_{XP}(\theta, \phi) \hat{\mathbf{a}}_{XP}$ and using Ludwig's third definition [32] we can define CO and XP . CO and XP are the co- and cross-polar patterns in the $\phi = 45^\circ$ plane. It is useful to define CO and XP because the mathematical formulations of the feed sub-efficiencies becomes simpler if CO and XP are used.

The unit vectors can be described as

$$\hat{\mathbf{a}}_{CO} = \hat{\mathbf{a}}_\theta + \hat{\mathbf{a}}_\phi = \sin(\phi) \hat{\boldsymbol{\theta}} + \cos(\phi) \hat{\boldsymbol{\phi}} \quad (3.2.12)$$

$$\hat{\mathbf{a}}_{XP} = \hat{\mathbf{a}}_\theta - \hat{\mathbf{a}}_\phi = \cos(\phi) \hat{\boldsymbol{\theta}} - \sin(\phi) \hat{\boldsymbol{\phi}}. \quad (3.2.13)$$

Therefore we can define \mathbf{G}_{CO} and \mathbf{G}_{XP} as

$$G_{CO} = \mathbf{G}(\theta, \phi) \cdot \hat{\mathbf{a}}_{CO} = CO(\theta, \phi) - XP(\theta, \phi) \cos(2\phi) \quad (3.2.14)$$

$$G_{XP} = \mathbf{G}(\theta, \phi) \cdot \hat{\mathbf{a}}_{XP} = XP(\theta, \phi) \sin(2\phi) \quad (3.2.15)$$

where CO and XP can be defined as

$$CO(\theta) = [A(\theta) + C(\theta)] / 2 \quad (3.2.16)$$

$$XP(\theta) = [A(\theta) - C(\theta)] / 2. \quad (3.2.17)$$

The total *BOR* power radiated can be expressed in terms of the ϕ -components as

$$P = \pi \int_0^\pi [|A(\theta)|^2 + |C(\theta)|^2] \sin \theta d\theta \quad (3.2.18)$$

or by the co- and cross-polar functions as

$$P = 2\pi \int_0^\pi [|CO(\theta)|^2 + |XP(\theta)|^2] \sin \theta d\theta. \quad (3.2.19)$$

The power radiated by both the co- and cross-polar functions can also be individually expressed as

$$P_{CO} = 2\pi \int_0^\pi \left[|CO(\theta)|^2 + \frac{1}{2} |XP(\theta)|^2 \right] \sin \theta d\theta \quad (3.2.20)$$

$$P_{XP} = \pi \int_0^\pi |XP(\theta)|^2 \sin \theta d\theta. \quad (3.2.21)$$

3.2.3 Spillover Efficiency

The efficiencies described in Sections 3.2.3 - 3.2.6 apply to all reflector antennas.

Spillover efficiency describes how much of the radiated power is lost because it is radiated past the reflector dish. It is defined as the total power within the subtended angle θ_0 to the total radiated power as

$$e_{sp} = \frac{\int_0^{\theta_0} [|CO(\theta)|^2 + |XP(\theta)|^2] \sin \theta d\theta}{\int_0^\pi [|CO(\theta)|^2 + |XP(\theta)|^2] \sin \theta d\theta}. \quad (3.2.22)$$

3.2.4 Polarisation Efficiency

The polarisation efficiency describes how effectively the field is polarised and is defined as the co-polar power within the subtended angle to the total power within the subtended angle as

$$e_{pol} = \frac{\int_0^{\theta_0} [|CO(\theta)|^2 + \frac{1}{2} |XP(\theta)|^2] \sin \theta d\theta}{\int_0^{\theta_0} [|CO(\theta)|^2 + |XP(\theta)|^2] \sin \theta d\theta}. \quad (3.2.23)$$

3.2.5 Illumination Efficiency

Illumination efficiency is derived from the polarisation efficiency. It describes how effectively the reflector dish is used (illuminated) and is defined as

$$e_{ill} = 2 \cot^2(\theta_0/2) \frac{\left[\int_0^{\theta_0} |CO(\theta)| \tan(\theta/2) d\theta \right]^2}{\int_0^{\theta_0} \left[|CO(\theta)|^2 + \frac{1}{2} |XP(\theta)|^2 \right] \sin \theta d\theta}. \quad (3.2.24)$$

It is important to note that e_{sp} and e_{ill} are complementary. There is a maximum that the product of the efficiencies can obtain. This optimum taper is often quoted as 80%. As more of the reflector is illuminated more of the radiated power will be radiated past the reflector. As e_{ill} increases, so e_{sp} decreases. Sharper field patterns result in higher e_{sp} , while wider patterns result in higher e_{ill} . A middle-ground between high e_{sp} and e_{ill} can be obtained.

3.2.6 Phase Efficiency

The phase efficiency describes phase errors in the co-polar field. This efficiency is dependent on the position of the feed relative to the focal point of the reflector. Section 3.2.7 discusses phase centre calculation and maximum phase efficiency. The phase efficiency is defined as

$$e_{\phi} = \frac{\left| \int_0^{\theta_0} CO(\theta) \tan(\theta/2) \right|^2}{\left[\int_0^{\theta_0} |CO(\theta)| \tan(\theta/2) \right]^2}. \quad (3.2.25)$$

3.2.7 Phase Centre

The phase centre of an antenna is the point from which all EM radiation spreads out spherically with the phase of the signal being equal at any point on the sphere. A horn antenna has what is known as an apparent phase centre. The apparent phase centre is defined as the apparent source of radiation [35] and is generally placed at the focal point of the parabolic reflector antenna.

Kildal presents a mathematical formulation for the calculation of δ , shown in Figure 3.2. Positioning the feed antenna so that point P is located at the focal point will maximise the phase efficiency of the system. δ is the distance from the apparent phase centre of the feed antenna to the focal point.

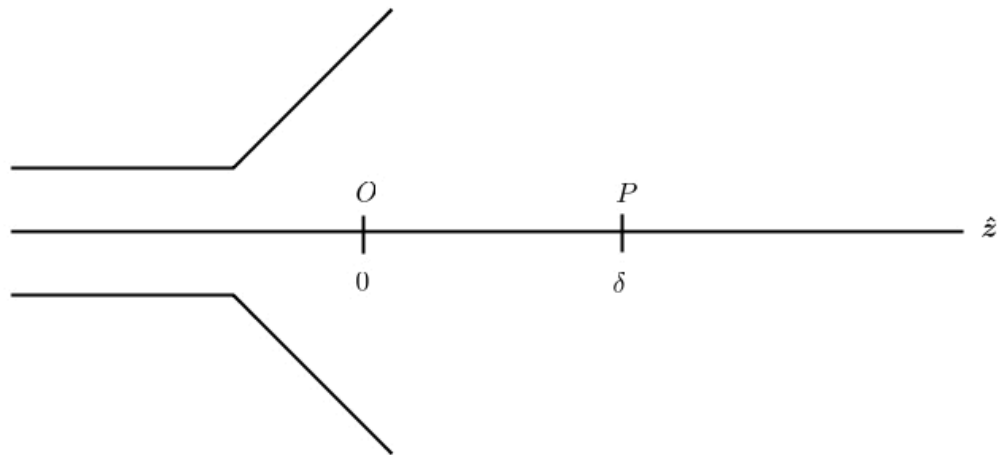


Figure 3.2: Phase Centre Reference Points [5]

Kildal presents a very thorough calculation of the phase centre [5] briefly shown here as

$$\delta = \frac{b}{a} = \frac{I_w I_{w\phi c} - I_{w\phi} I_{wc}}{I_{wc} I_w - (I_{wc})^2}. \quad (3.2.26)$$

The equations for the terms in (3.2.26) are shown in Appendix A.

3.3 Design of Corrugated Conical Horn Antenna

This Section introduces concepts used to reduce cross polarisation. The design of the antenna is then presented.

3.3.1 Techniques Used to Reduce Cross Polarisation

3.3.1.1 Corrugations at Antenna Aperture

Corrugated horns can radiate fields with a high degree of axial symmetry. This makes them ideal as feed antennas for reflector systems [36]. Corrugated horn antennas can improve aperture efficiency from around 50-60% to 75-80% [37].

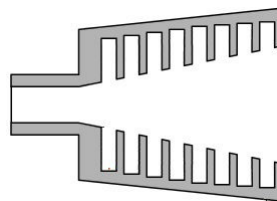


Figure 3.3: Standard Corrugated Horn [6]

In a waveguide with no corrugations, the E - and H -plane patterns will differ. This is because the electric and magnetic fields have different boundary conditions on the walls of the waveguide [36]. The tangential electric field will experience a short circuit on the walls of the waveguide while the tangential magnetic field will experience an open circuit. This results in curved field lines which can be made unidirectional by means of corrugating the surface of the waveguide with slots a quarter of a wavelength deep, covering it with dielectrics or inserting strips. This results in low cross polarisation.

Adding many corrugations on the wall surface of the waveguide will change the surface impedance so that the tangential electric field experiences an open circuit [36]. This is accomplished by the radial transmission line formed by the corrugations. The transformation only has a second-order effect on the transverse magnetic field. Pattern symmetry, low cross polarisation and low side-lobes are all results of adding corrugations.

The corrugation of Figure 3.3 can be difficult to manufacture. Axially corrugated horns, as shown in Figure 3.4, are easy to manufacture and follow the same basic principles.

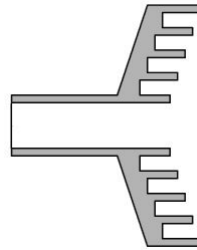


Figure 3.4: Axially Corrugated Horn [6]

The corrugation depth is also set to approximately a quarter wavelength. The corrugations therefore act as a transmission line and are seen by the axial currents as an open circuit instead of a short circuit. This ensures no axial current flow and therefore no "curved" modes at the aperture [37].

3.3.1.2 Modal Conversion Using Step Discontinuity

Another method used to reduce cross polarisation is to use modal conversion. The Potter horn was the first horn to use this technique to generate higher order modes for side-lobe suppression, better cross polarisation and rotational symmetry.

The horn's fundamental mode is the TE_{11} mode. The generation of the higher order mode TM_{11} allows for side-lobe cancellation. Side-lobes are any lobes present in the radiation pattern of an antenna outside of the main beam. Side-lobe cancellation is desirable since as much of the power as possible should be radiated in the main beam. Side-lobe cancellation is a consequence of the higher order mode generation.

Potter presents a mathematical formulation, but a qualitative approach is shown in Figure 3.5. From this it can be seen that cross polarisation will be very low since the radiating

electric field is (ideally) perfectly linearly polarised. The curved parts of the fundamental TE_{11} mode are cancelled by the higher order TM_{11} mode that is generated.

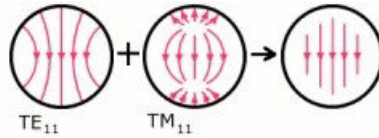


Figure 3.5: Potter Horn Principle [7]

The TM_{11} mode can be generated in a number of ways. Three popular techniques used in circular waveguides are the iris, groove and step discontinuity. The modes need to be in phase. This happens over the length of the horn [36].

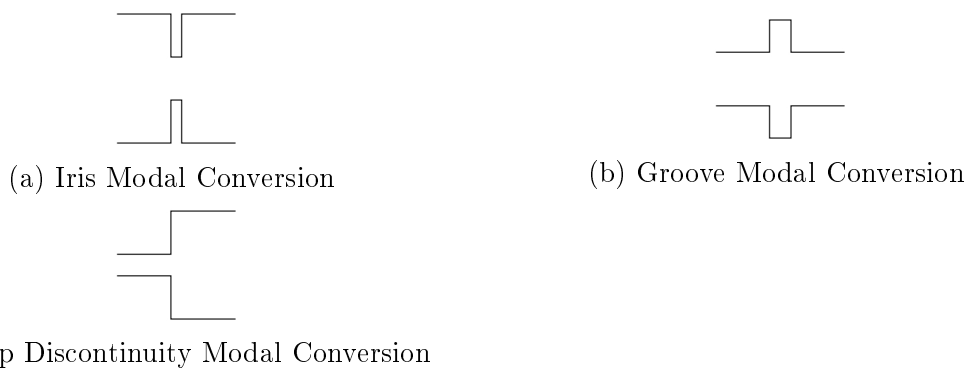


Figure 3.6: Generation of TM_{11} Mode

3.3.2 Initial Design

As a starting point, the design presented by Balanis was used. The design is shown in Figure 3.7 with the initial design equations shown in Table 3.1 [8]. Balanis refers to this as a single choke-ring waveguide, which is mostly used in reflector systems with a $F/D < 0.5$. The F/D of the dish used is 0.36.

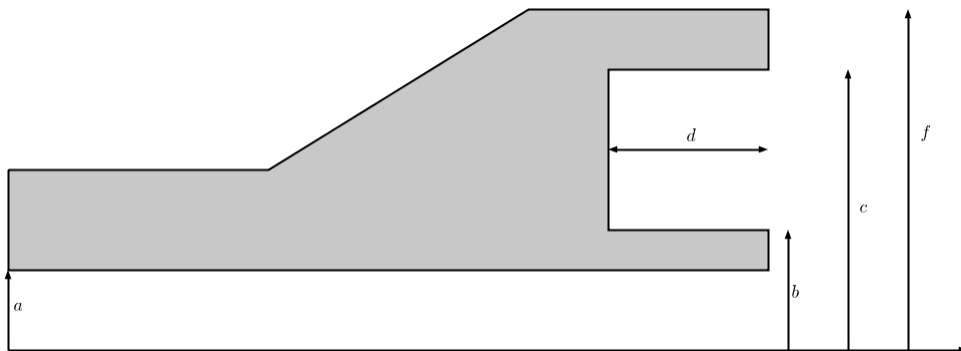


Figure 3.7: Choke-Ring Waveguide [8]

Design Parameter	Design Value	Parameter Value (mm) ($\lambda = 40mm$)
$a(\lambda)$	0.55	22
$b(\lambda)$	0.575	23
$c(\lambda)$	0.675	27
$d(\lambda)$	0.25	10
$f(\lambda)$	0.7375	29.5

Table 3.1: Initial Model Design [8]

The values shown in Table 3.1 were used as a starting point. The antenna shown in Figure 3.7 was simulated in CST to get a feel for antenna. The initial results for this design are shown in Section 3.4.1.

Upon review of the initial design results it was decided to add a step to the horn to improve pattern symmetry and cross polarisation as discussed in the introduction to this Section.

3.3.3 Stepped Corrugated Design

The chosen design can be seen in Figure 3.8 with parameter names included in Table 3.2.

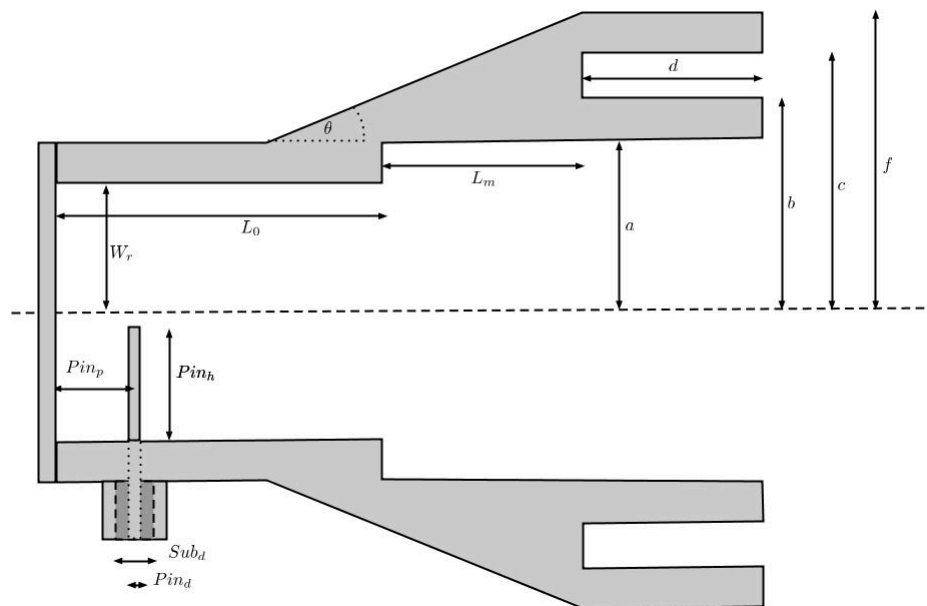


Figure 3.8: Stepped Corrugated Conical Horn Antenna

Design Parameter	Description
a	Inner radius of aperture
b	Outer radius of inner choke
c	Inner radius of outer choke
d	Choke length
f	Outer radius of outer choke
L_0	Length of antenna from back-wall to step
L_m	Length of matching section
θ	Flare angle
Pin_p	Position of feed from back-wall
Pin_h	Length of pin into antenna
Pin_d	Diameter of pin (standard SMA)
Sub_d	Diameter of substrate (standard SMA)
W_r	Radius of input waveguide

Table 3.2: Model Parameter Descriptions

CST was used to set-up a 3D model of the antenna for simulation. This was done by creating a 2D cut-plane sketch and then sweeping the sketch axially.

3.3.4 Design Procedure

CST was used in conjunction with MATLAB to simulate designs and then evaluate and save the results. CST provides help files so that all the necessary functions can be called and initialised from MATLAB. See Figure B.1 in Appendix B for a brief overview of how this was achieved.

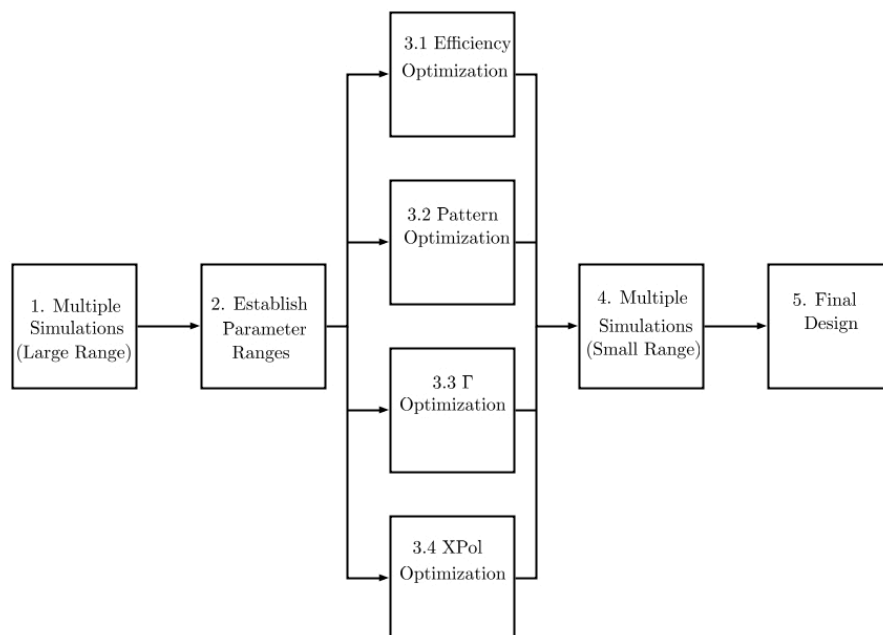


Figure 3.9: Design Process of Antenna

Figure 3.9 shows the simulation plan. First, the parameters of the antenna would all be given a relatively large range of values. The CST-MATLAB scripts would then run many simulations and save the results. This was done to find a range of values that worked well in terms of efficiency, Γ and field patterns.

Once a workable range was found, parameter sweeps of all the parameters were performed. This was done to determine what effect each parameter had on the results, and to what extent. This knowledge allowed the next part of the design to take place, which was to optimise the antenna for Γ , field pattern and efficiency (cross polarisation optimisation was run at a later stage).

By knowing how each parameter affected the desired results, separate optimisations could be run, each with its own error function, each optimising specific parameters for specific results. The error functions and optimised parameters are discussed in more detail in Section 3.4.3.

Once the optimisation was complete, multiple simulations were run once again. This time the range of values was small compared to the simulations run in step 1. The ranges were determined from the optimised parameters. This allowed for a good overall result which was then fine tuned by rounding off all parameter values manually.

3.4 Results

3.4.1 Initial Design Results

Figure 3.10 shows the efficiency results of the initial Balanis design shown in Figure 3.7. For the frequency of interest, 7.5 GHz, the results are unacceptable. In fact, all sub efficiencies are high except e_{BOR1} . This suggests that most of the power is not radiated with axial symmetry. The spillover and illumination efficiencies show that while very little power is radiated past the dish, the dish is not fully utilised.

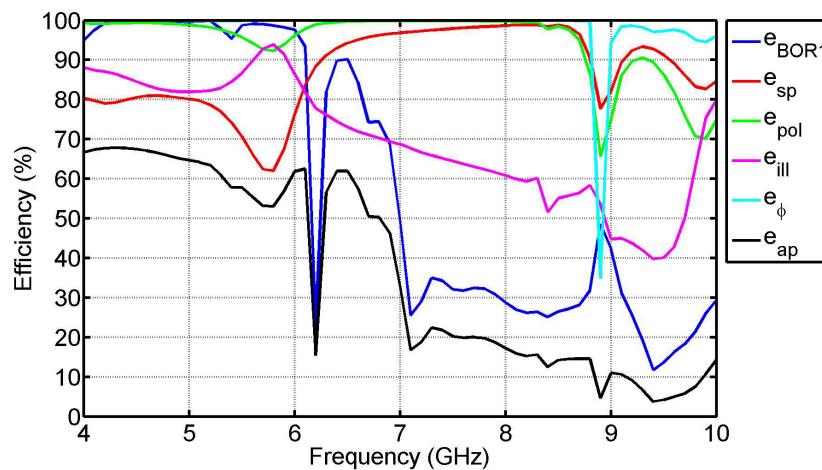


Figure 3.10: Initial Design Efficiency Bandwidth

Figure 3.11 shows the field pattern for the initial design. As can be seen the pattern is not

circular at all. A circular pattern will have the same E - and H -plane patterns. Circular patterns are desirable in reflector systems because they have low cross polarisation when BOR_1 antennas are used. The $\phi = 45^\circ$ plane is shown since it is the CO component described earlier.

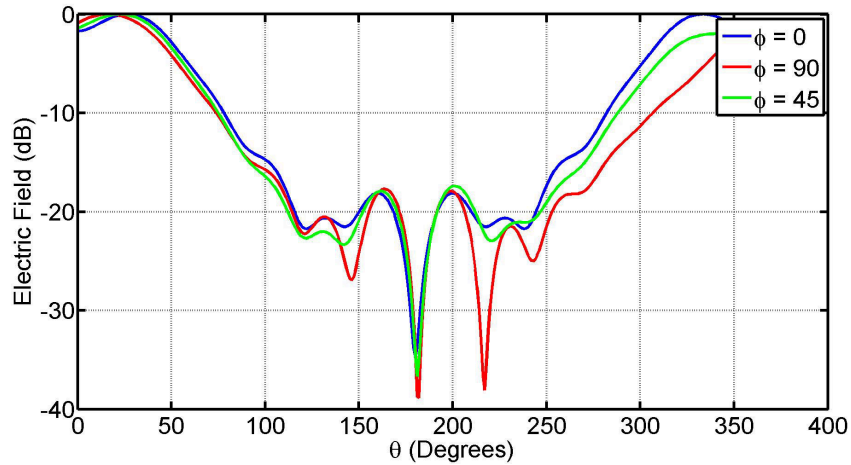


Figure 3.11: Initial Design Field Pattern Simulated Result

Figure 3.12 shows the Γ response of the initial design. The response has a value of -15 dB at 7.5 GHz. The feed is well matched between 7 and 9 GHz.

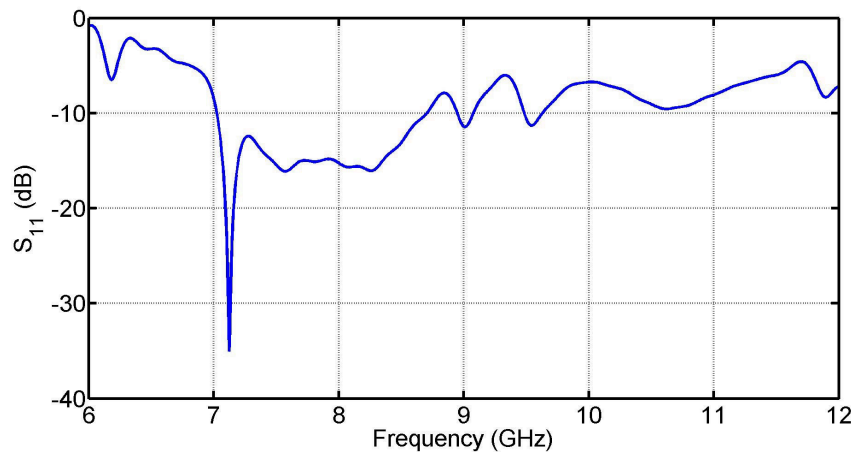


Figure 3.12: Initial Design Reflection Coefficient Simulated Result

Figure 3.13 shows the cross polarisation for the initial design. The pattern in the H -plane ($\phi = 0$) is not desirable. The $\phi = 45^\circ$ plane is shown since it is the XP component described earlier.

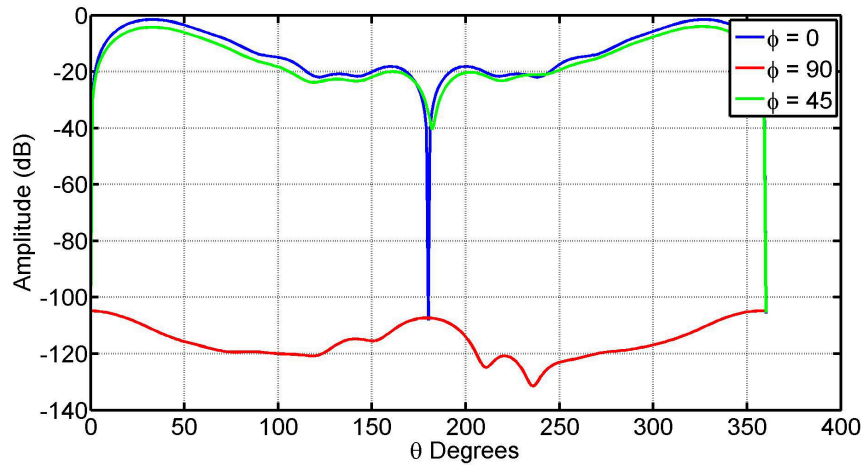


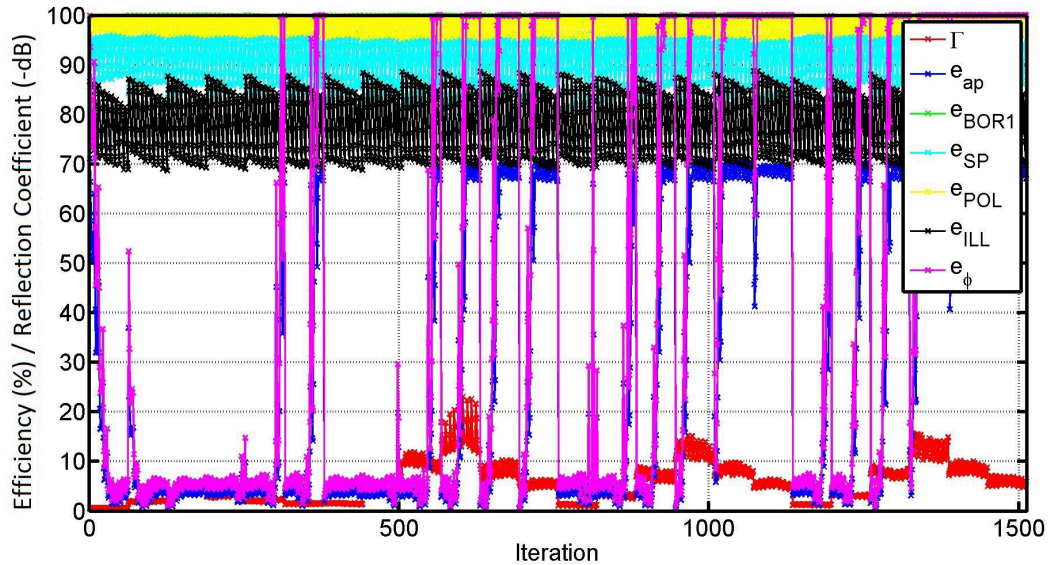
Figure 3.13: Initial Design Cross Polarisation Simulated Result

These results prompted the need for better cross polarisation and field pattern symmetry. Techniques used to improve these are discussed in Section 3.3.1. The design shown in Figure 3.8 was used from this point on.

3.4.2 Rough Simulations Results

The rough simulations were concerned with the reflection coefficient and efficiency of the antenna. High e_{BOR1} and e_{pol} are indicators of axially symmetric field patterns and low cross polarisation pattern. These are therefore desirable results from the rough simulations.

Figure 3.14 shows results for various simulations. Each parameter was given a large range relative to the size of the antenna. The results shown are the individual efficiencies as well as the absolute value of Γ at 7.5 GHz. Around iteration 600 there are many results that have high efficiency and an acceptable Γ response. This represents a good range of parameter values which were used in the optimisation simulations.

Figure 3.14: Aperture Efficiency and Γ Results of Rough Simulations

From these results starting values were chosen for all optimisation simulations. These starting values are shown in Table 3.3 and compared against the initial design values. The initial design values shown in Table 3.3 are the same initial design values found in Balanis, shown in Table 3.1.

Parameter	Design Value	Starting Value for Optimisation	Real Value (mm)
a	$0.55(\lambda)$	$0.4375(\lambda)$	17.5
b	$0.575(\lambda)$	$0.55(\lambda)$	22
c	$0.675(\lambda)$	$0.625(\lambda)$	25
d	$0.25(\lambda)$	$0.23(\lambda)$	9
f	$0.7375(\lambda)$	$0.75(\lambda)$	29.5
L_0	N/A	$1(\lambda)$	40
L_m	N/A	$0.25(\lambda)$	10
pin_p	N/A	$0.25(\lambda)$	10
pin_h	N/A	$0.2(\lambda)$	8

Table 3.3: Starting Values for Optimisations

3.4.3 Optimisation Results

The Section shows the optimised results for certain goals. For example, the efficiency results for the efficiency optimisation is shown. Other results produced by the efficiency optimisation can be found in Appendix C. Field pattern, reflection coefficient and cross polarisation results were also optimised. This multi-objective approach was performed to obtain the best general results for all the parameters.

The goal of the optimisation process was to find various solutions best suited for certain antenna characteristics. From these solutions a final range of parameter values will be

chosen and the final solution will be determined. Once again the CST-MATLAB software combination was used. MATLAB has a built in function called *fminsearch*, which uses the Nelder-Mead Simplex [38], that is used for optimisation purposes. This function receives a value from some other "error" function (in this case user-defined *runCST()*) which returns an "error". The error function must be properly defined as *fminsearch* attempts to minimise the "error-function" by changing the input parameters to the function.

The error function of the efficiency optimisation was simply $1 - \epsilon_{ap}$. This ensured that the optimisation function will maximise ϵ_{ap} .

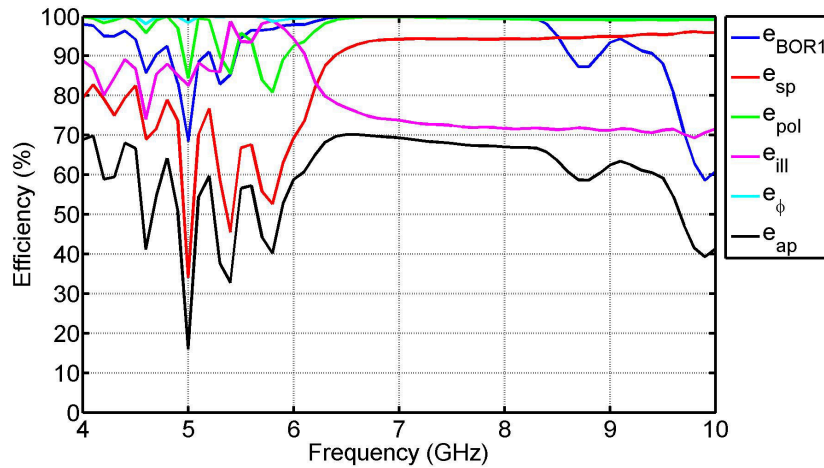


Figure 3.15: Bandwidth of Efficiencies for Efficiency Optimised Antenna

As can be seen in Figure 3.15 the total efficiency at 7.5 GHz is just under 70%. This was achieved by creating a smaller aperture from the initial design (decreasing parameter a) and lowering the choke depth (decreasing d). This suggests that for optimal efficiency the choke depth must be slightly less than $\lambda/4$. Table 3.4 summarizes the results for a and d . e_{BOR1} is also 100% for the range of interest.

Design Parameter	Start Value	Optimised Design Value	Real Value (mm)
a	$0.4375(\lambda)$	$0.3689 (\lambda)$	14.756
d	$0.23(\lambda)$	$0.249 (\lambda)$	9.973

Table 3.4: Optimised a and d for Efficiency

To define an error function for pattern symmetry is slightly less intuitive than defining an error function for the efficiency. While the efficiency can be calculated as a single value and optimised, the radiation pattern has many discrete points, for both $\phi = 0^\circ$ and $\phi = 90^\circ$. Of course the two patterns could be subtracted from each other and the difference could be minimized so that the patterns would eventually be identical (or close to it). However, this would take too long to run and thus a more efficient error function was needed.

For this reason, it was decided that instead of evaluating the two patterns at every point, only the value of the patterns at θ_0 would be evaluated. It was thought that if the patterns were the same at this point, they would be the same for all $|\theta| < |\theta_0|$ due to the directionality of the antenna.

So the difference of the $\phi = 0^\circ$ and $\phi = 90^\circ$ patterns at θ_0 and $-\theta_0$ were found and labelled dif_0 and dif_{90} . The error was then defined as

$$error = |dif_0| + |dif_{90}| \quad (3.4.1)$$

and then minimized by *fminsearch*.

The reason θ_0 was chosen is because most sub-efficiencies (excluding e_{BOR_1}) are evaluated using the power available in the pattern from 0° to θ_0° . So optimising for pattern symmetry will also keep total efficiency high.

Both a and d were again used for parameter optimisation. After some simulations were run independently from the optimisation process it was decided that b was to be added as a optimisation parameter. This was because optimisation for just a and d was over fairly quickly and did not produce desired results.

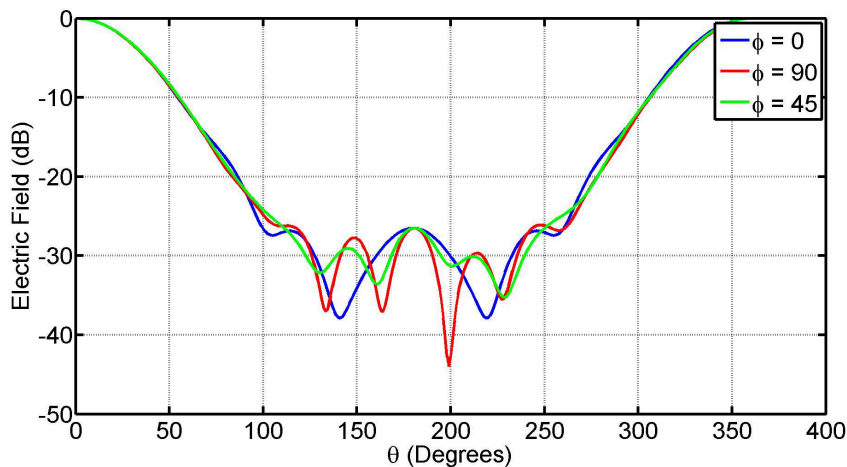


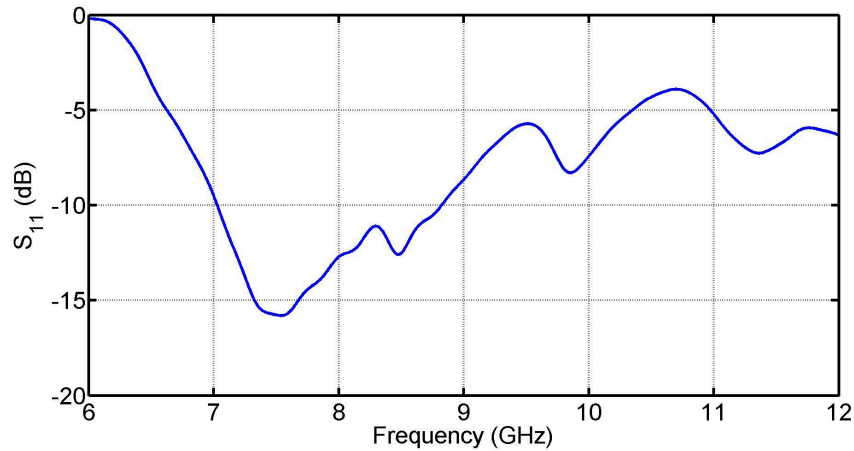
Figure 3.16: Field Pattern for Field Pattern Optimised Antenna

Having a symmetrical pattern means that $A(\theta) = C(\theta)$. From (3.2.17) it is clear that this will result in $XP = 0$ for BOR_1 antennas, which is desirable. As Figure 3.16 shows, the pattern is almost perfectly symmetric in the range $|\theta| < |\theta_0|$, while Figure C.5 shows that the efficiency is still very high. This is a desirable solution. Once again, the parameters are shown in tabular form in Table 3.5.

Design Parameter	Start Value	Optimised Design Value	Real Value (mm)
a	$0.4375(\lambda)$	$0.472(\lambda)$	18.87
b	$0.55(\lambda)$	$0.492(\lambda)$	19.671
d	$0.23(\lambda)$	$0.233(\lambda)$	9.3192

Table 3.5: Optimised a , b and d for Pattern Symmetry

To optimise Γ the value of Γ at 7.5 GHz was found. This value was then directly used for minimization by the *fminsearch* function. The waveguide cut-off frequency is at about 6.5 GHz which justifies only looking at a single point for the Γ optimisation. From the rough simulations it was determined that not much has an effect on Γ . The waveguide radius must simply be large enough to allow propagation of the TE_{11} mode at 7.5 GHz. The parameters that have the largest effect on Γ are the feed parameters (pin_h and pin_p) and the matching length of the antenna (L_m). These can however very simply be changed in the final design to match properly. So it was decided to optimise Γ with a and d instead. This would give a optimised result which could be matched even better if need be. The field pattern, cross polarisation and feed efficiency is relatively unchanged. These results can be seen in Appendix C.

Figure 3.17: Γ for Γ Optimised Antenna

Design Parameter	Start Value	Optimised Design Value	Real Value (mm)
a	$0.4375(\lambda)$	$0.41(\lambda)$	16.82
d	$0.25(\lambda)$	$0.2544(\lambda)$	10.179

Table 3.6: Optimised a and d for Γ

Cross polarisation patterns for $\phi = 0^\circ$, $\phi = 45^\circ$ and $\phi = 90^\circ$ must be taken into account. According to Kildal [32] the cross polarisation is maximum in the $\phi = 45^\circ$ plane. This was however realised after the optimisations were completed. Thus, the optimisations

were run by considering the cross polarisation in the $\phi = 0^\circ$ and $\phi = 90^\circ$ planes. The requirements for cross polarisation is that it must simply be much lower than any significant co-polarisation value. Thus, the error function is simply the maximum value of either of the cross polarisation patterns. The maximum of each pattern is found and then the maximum of those two is the error function value. This is then minimized by the *fminsearch* function. Since the cross polarisation is related to the radiation pattern, the same parameters were used for optimisation.

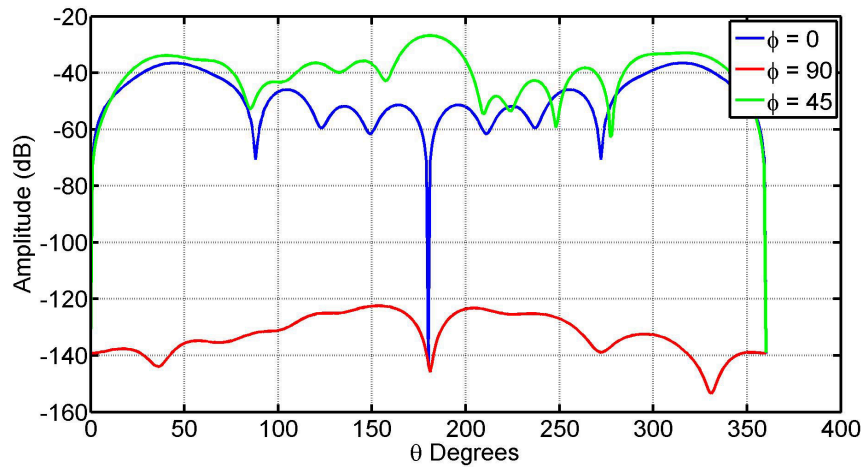


Figure 3.18: Cross Polarisation for Cross Polarisation Optimised Antenna

Figure 3.18 shows the optimised cross polarisation patterns, with a maximum value of around -30 dB for the $\phi = 45^\circ$ plane. The maximum occurs in the back-lobe of the pattern. This is an acceptable result.

Design Parameter	Start Value	Optimised Design Value	Real Value (mm)
a	$0.4375(\lambda)$	$0.484(\lambda)$	19.33
b	$0.55(\lambda)$	$0.498(\lambda)$	19.935
d	$0.23(\lambda)$	$0.235(\lambda)$	9.4

Table 3.7: Optimised a , b and d for Cross Polarisation

3.4.4 Final Design

The final design was based primarily on the optimisation of the field pattern. Another large simulation was run, but this time with much smaller parameter ranges. These ranges were determined from the optimisation results.

However, at the time of final design there was a bug in the MATLAB code that did not consider the value of the patterns at $\theta = -\theta_0$ for the pattern optimisation. The bug was eventually identified and found after the manufacture of the antenna had been completed. Due to lack of time the process could not be repeated. This meant that the final design pattern is not entirely symmetrical.

From the optimisation results, the goals of the final design were determined. A (nearly) symmetric field pattern, with Γ at 7.5 GHz around -15 dB and an efficiency of at least 65% is required. A specific value for the cross polarisation is not necessary. The only requirement is that it is low compared to the field pattern.

Figure 3.19 shows the asymmetrical radiation patterns. Even though they are not perfectly symmetrical, they are very nearly symmetrical, especially in the range $-\theta_0$ to θ_0 , which is main lobe and most important part of the radiation pattern.

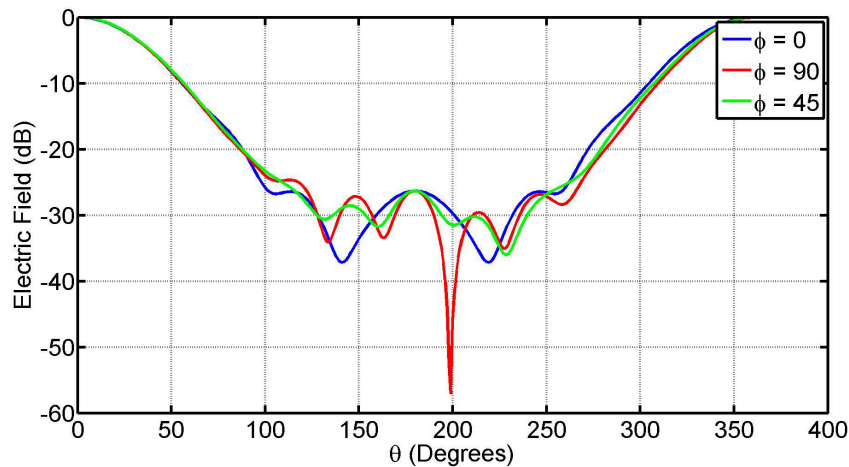


Figure 3.19: Field Pattern for Final Simulated Antenna

The maximum cross polarisation in the $\phi = 45^\circ$ plane shown in 3.20 has a maximum of about -27 dB for the back-lobe of the pattern. This is an acceptable result.

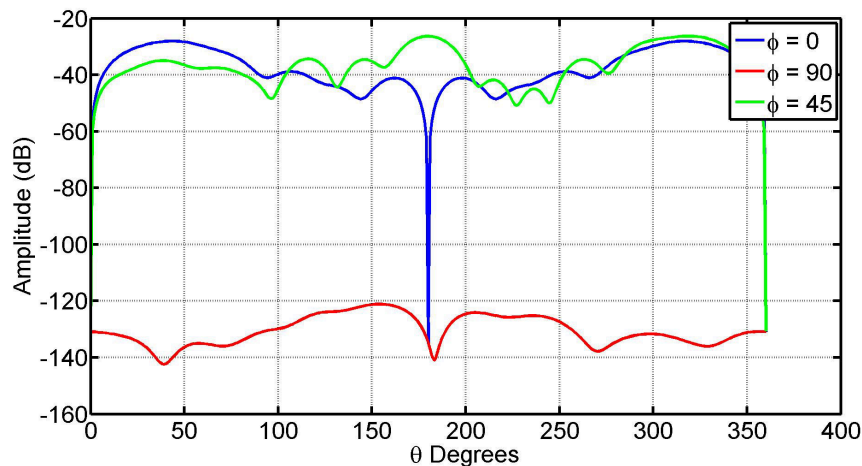


Figure 3.20: Cross Polarisation for Final Simulated Antenna

The Γ in Figure 3.21 is acceptable. Most of the power that the antenna will receive will be at 7.5 GHz and nothing below 6 GHz will be received by the antenna. This is good because it eliminates most of the possible RFI.

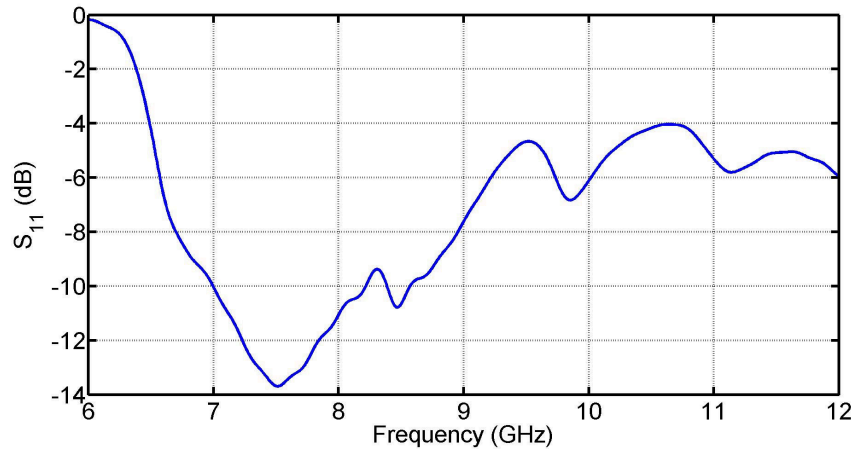


Figure 3.21: Reflection Coefficient for Final Simulated Antenna

The efficiencies shown in Figure 3.22 for the final design are also acceptable, with a total efficiency very close to 70% at 7.5 GHz. The phase centre reference δ is shown in Figure 3.23.

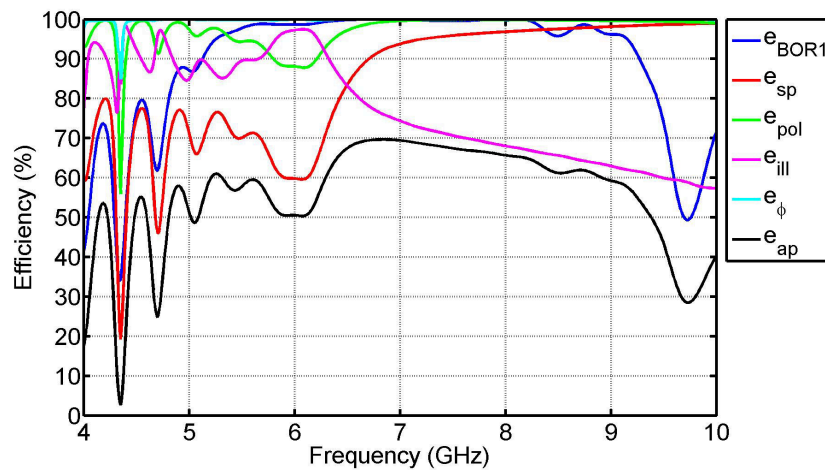


Figure 3.22: Efficiencies Bandwidth for Final Simulated Antenna

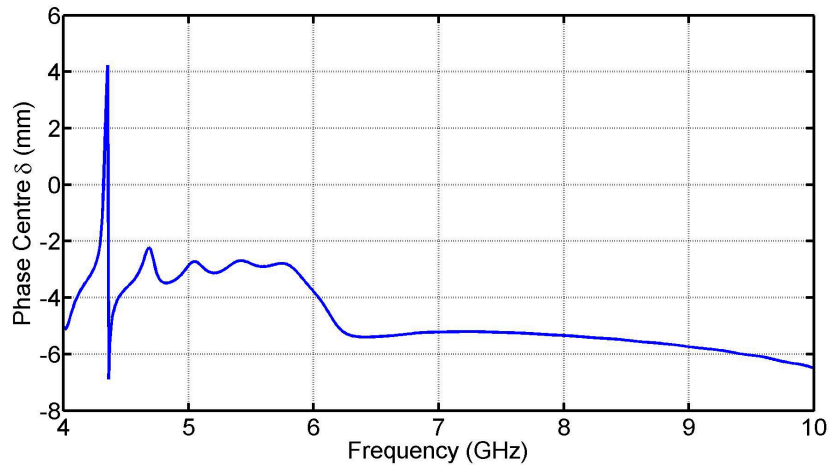


Figure 3.23: Phase Centre δ for Final Simulated Antenna

3.5 Manufacture

The antenna was manufactured at the workshop in the E&E Department with the help of Wessel Croukamp and Lincoln Saunders. The lathe was used hollow out a piece of aluminium to the desired specifications. Photos of the antenna can be seen in Appendix F.

The antenna was also alodined. This helps to retain conductivity and prevent corrosion.

3.6 Measurements

Once the antenna was manufactured measurements were taken in the High Frequency Laboratory at the E&E Department. These measurements included S-Parameter, gain and field pattern measurements. The measurements were done with the help of Anneke Bester.

3.6.1 S-Parameter Measurements

The S-Parameters of the antenna were measured on the Agilent PNA-X Network Analyser. A frequency range of 6-12 GHz was chosen. The N4691-60004 ECal was used to electronically calibrate the measurement set-up.

The response, shown in Figure 3.24, compares well with the simulated response. The pin height was in fact slightly longer than what it was supposed to be. Correcting this mistake ran the risk of shortening the pin too much, so it was decided to leave the pin as is.

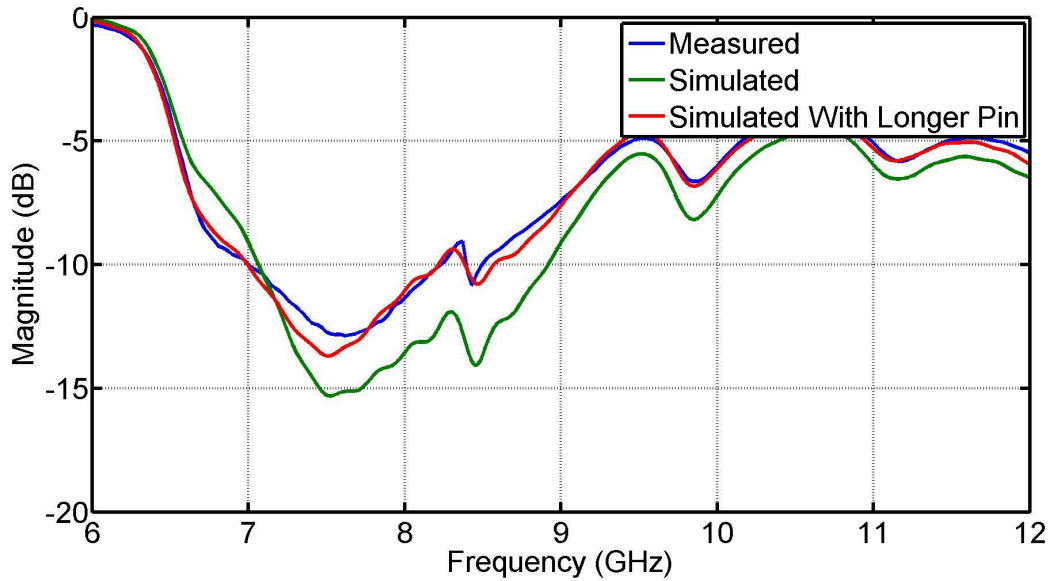


Figure 3.24: Reflection Coefficient of Conical Horn Antenna

3.6.2 Gain Measurements

To measure the gain and field pattern the anechoic chamber was used in conjunction with the Hewlett Packard 8530A Microwave Receiver. Before any measurements could be taken the system had to be calibrated. The set-up is shown in Figure 3.25. The calibration is necessary to eliminate losses or gains that might occur in the set-up so that accurate measurements can be taken.

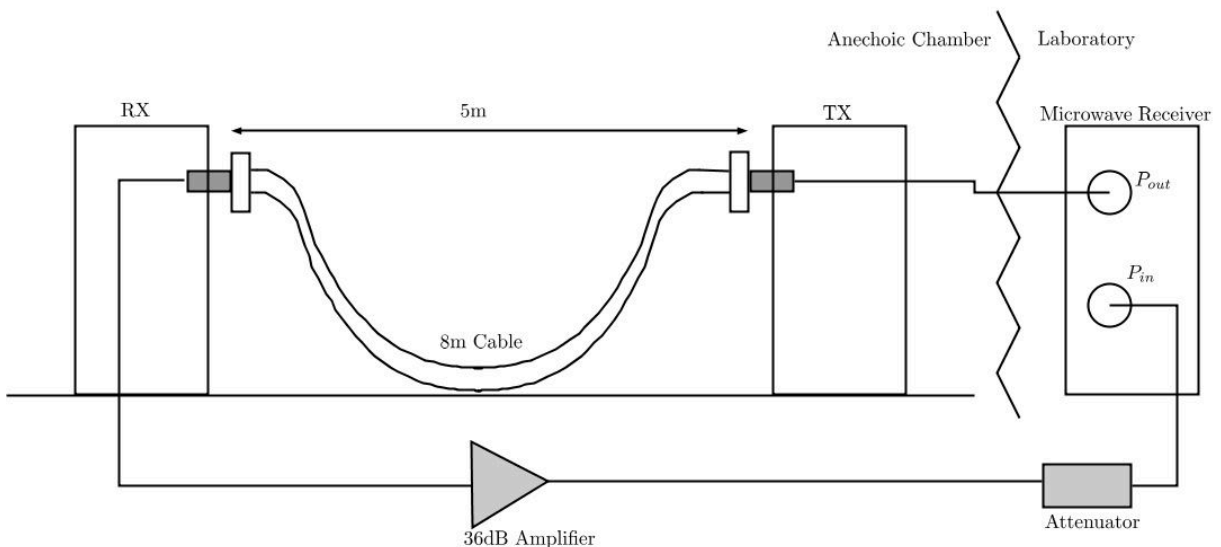


Figure 3.25: Basic Calibration Set-Up

A 8m cable was used for the through calibration. This cable is not present in the measurements of the antennas and must therefore be taken into account at a later stage. This is done by measuring the losses in the cable and then adding those losses to any

measurements taken. The losses were measured on the PNA-X in the same way described in Section 3.6.1, except that 2 ports were used. These losses can be seen in Figure 3.26.

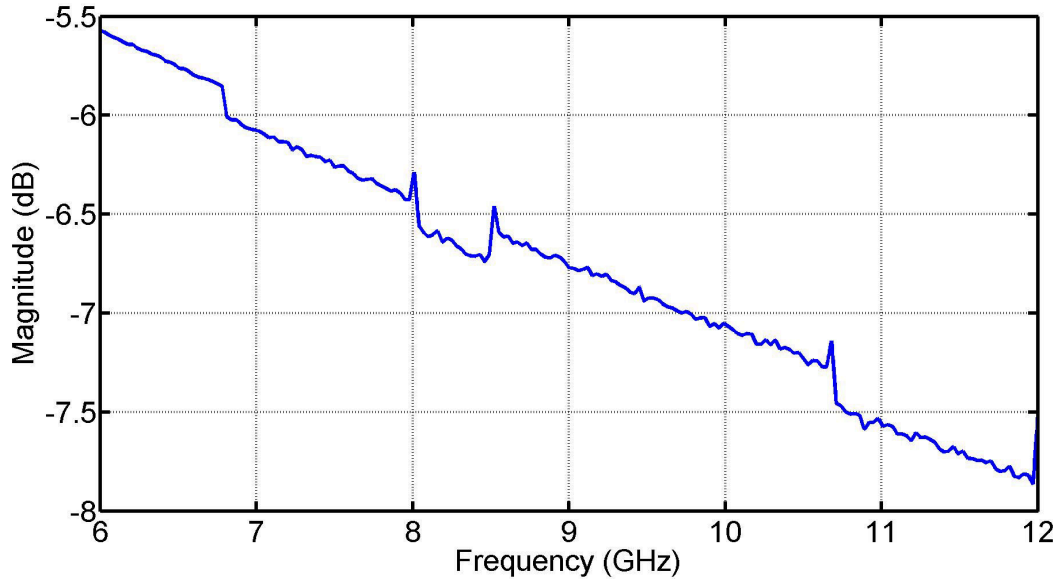


Figure 3.26: S_{21} of 8 m Cable Representing Cable Losses

Three gain measurements were done using the designed conical corrugated horn and two pyramidal horn antennas available in the laboratory. These are designated H_1 and H_2 while the conical horn is designated H_C . Table 3.8 described how the measurements were taken.

Measurement	Transmit	Receive
1	H_2	H_1
2	H_C	H_1
3	H_C	H_2

Table 3.8: Summary of Measurements

Using Frii's Transmission Equation we can see that we have three unknowns and three separate measurements, or equations. This means that we can solve for the gains of each antenna used. Frii's Equation is defined as

$$\frac{P_r}{P_t} = G_t G_r \left(\frac{\lambda}{4\pi R} \right)^2 \quad (3.6.1)$$

where

P_r = received power

P_t = transmitted power

G_t = transmit antenna gain

G_r = receive antenna gain
 $\left(\frac{\lambda}{4\pi R}\right)^2$ = free-space path loss
 R = distance between antennas
 λ = wavelength.

The free-space path loss represents the attenuation through the air. $\frac{P_r}{P_t}$ is the ratio of received power to transmitted power. This ratio is the result of the gain measurement for a pair of antennas.

Care must be taken to include the cable losses in these calculations. The calibration included these losses but all measurements excluded the losses. The measurement equipment has calibrated for losses no longer in the system. Equation (3.6.2) shows that the measured response is the actual response with the calibration added,

$$\left(\frac{P_r}{P_t}\right)_{measured} = \left(\frac{P_r}{P_t}\right)_{real} + \text{system calibration.} \quad (3.6.2)$$

The calibration that the systems adds to the measurement is the negative of the losses and/or gains experienced during calibration. Thus, (3.6.2) becomes

$$\left(\frac{P_r}{P_t}\right)_{measured} = \left(\frac{P_r}{P_t}\right)_{real} - \text{cable losses.} \quad (3.6.3)$$

Now we can substitute the real power ratio in (3.6.3) with the equivalent Frii's Transmission Equation for gain in dB. Equation (3.6.3) becomes

$$\left(\frac{P_r}{P_t}\right)_{measured} = G_t + G_r + 20 \log_{10} \left(\frac{\lambda}{4\pi R}\right) - \text{cable losses.} \quad (3.6.4)$$

Equations (3.6.5) to (3.6.7) can now be set-up.

$$G_{H1} + G_{H2} = \left(\frac{P_{r1}}{P_{t1}}\right)_{measured} - 20 \log_{10} \left(\frac{\lambda}{4\pi R}\right) + \text{cable losses} \quad (3.6.5)$$

$$G_{H1} + G_{HC} = \left(\frac{P_{r2}}{P_{t2}}\right)_{measured} - 20 \log_{10} \left(\frac{\lambda}{4\pi R}\right) + \text{cable losses} \quad (3.6.6)$$

$$G_{H2} + G_{HC} = \left(\frac{P_{r3}}{P_{t3}}\right)_{measured} - 20 \log_{10} \left(\frac{\lambda}{4\pi R}\right) + \text{cable losses} \quad (3.6.7)$$

This leaves 3 equations with 3 unknowns, and Matrix theory can be used to solve for the gains.

$$\begin{bmatrix} G_{H1} & G_{H2} & G_C \end{bmatrix} * \begin{bmatrix} 1 & 1 & 0 \\ 1 & 0 & 1 \\ 0 & 1 & 1 \end{bmatrix} = \begin{bmatrix} G_{H1} + G_{H2}, & G_{H1} + G_C, & G_{H2} + G_C \end{bmatrix}^T$$

$$\begin{bmatrix} G_{H1} \\ G_{H2} \\ G_C \end{bmatrix} = \begin{bmatrix} 1 & 1 & 0 \\ 1 & 0 & 1 \\ 0 & 1 & 1 \end{bmatrix}^{-1} * [G_{H1} + G_{H2}, G_{H1} + G_C, G_{H2} + G_C]^T$$

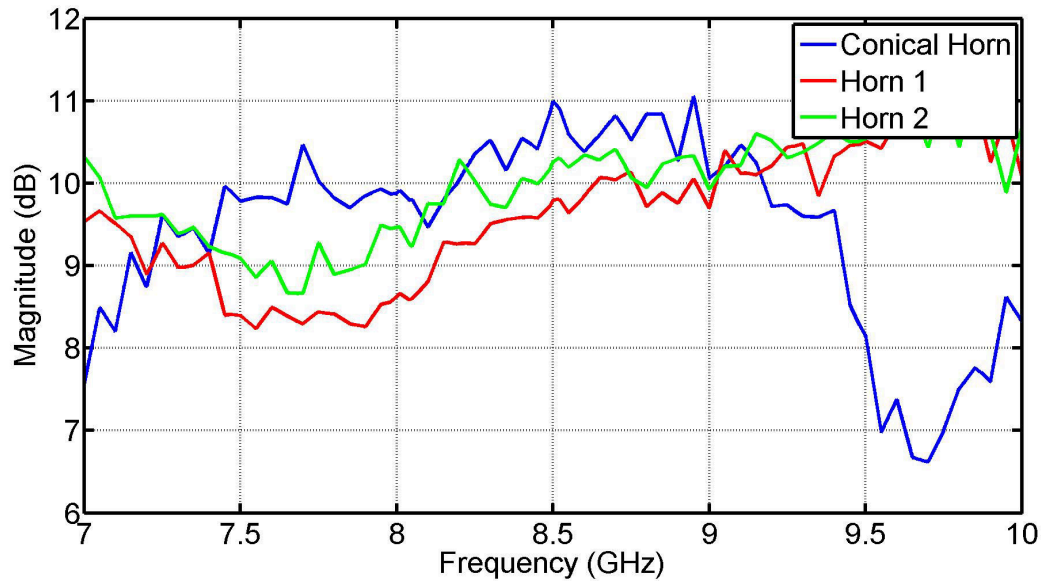


Figure 3.27: Calculated Gains of Conical Horn, H1 and H2 Antennas

Figure 3.27 shows the gains of the antennas. The H_1 and H_2 calculated gains corresponded to known gain values for the antennas. Figure 3.28 compares the measured calculated gain to the realised gain simulated in CST. The measured gain is slightly lower than the simulated gain but it is clear that they follow the same trend. Differences could be due to conduction losses since the CST model was simulated as a PEC model.

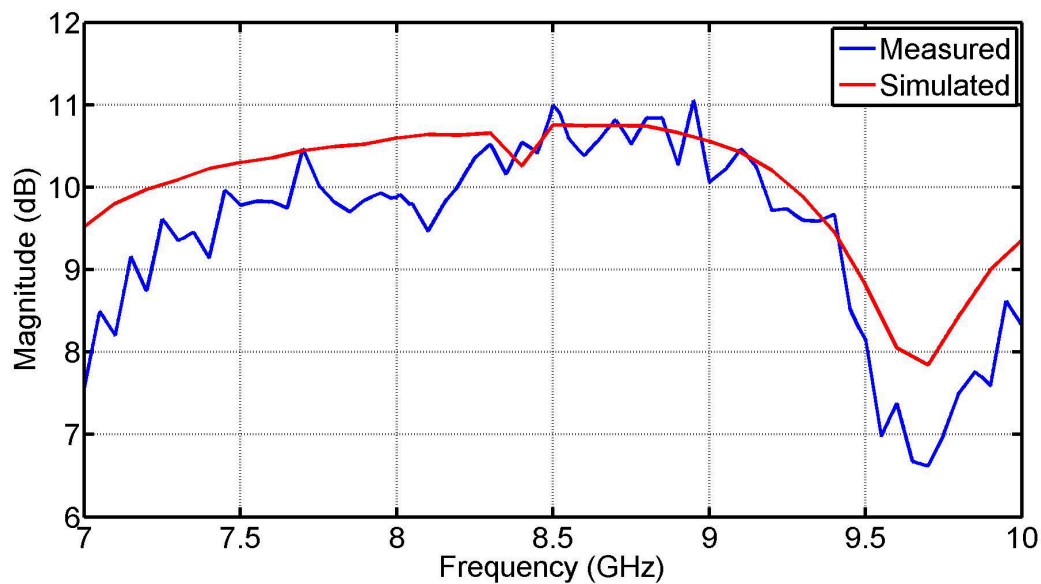


Figure 3.28: Expected and Measured Gains

3.6.3 Field Pattern Measurements

Field pattern measurements were taken by transmitting from the designed antenna and receiving with a pyramidal horn antenna. The θ angle of the transmitting antenna was changed in increments of 3° . The orientation of the feed was also changed to measure the polarisations described in Table 3.9.

Measurement	Transmit	Receive
<i>E</i>-Plane		
Co-Pol	H_C Vertical	H_1 Vertical
XPol	H_C Vertical	H_1 Horizontal
<i>H</i>-Plane		
Co-Pol	H_C Horizontal	H_1 Horizontal
XPol	H_C Horizontal	H_1 Vertical

Table 3.9: Summary of Measurements

Figures 3.29 and 3.30 show the *E*-plane measurements and simulations. As can be seen there is a slight difference in the field patterns for the vertically polarised case. The difference is very slight and the pattern is otherwise symmetric. For the angles of particular interest ($-\theta_0 \leq \theta \leq \theta_0$) the pattern is almost exactly what is required. There is a very clear main lobe with very little power received outside of it.

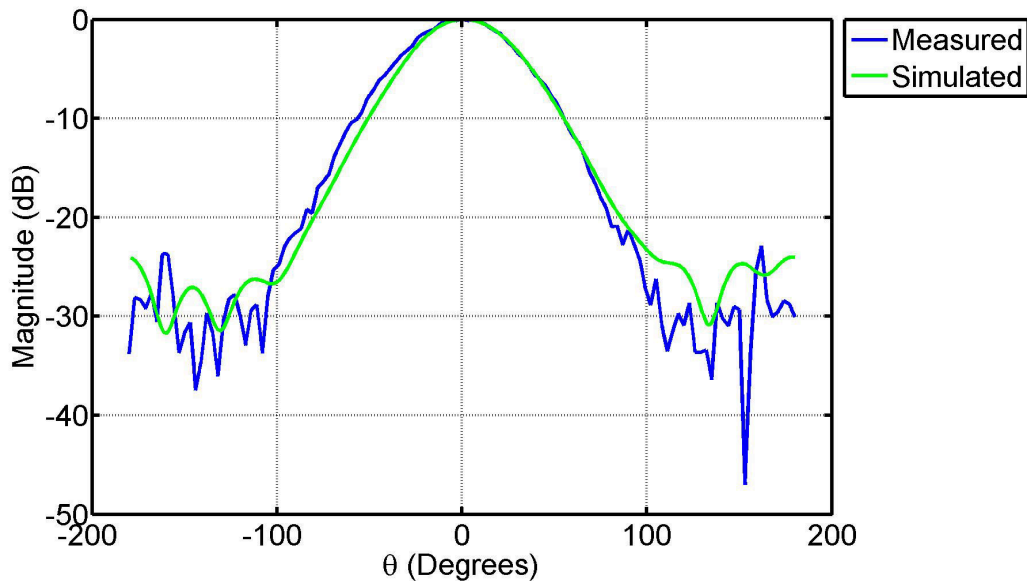


Figure 3.29: Measured and Simulated Co-Polarisation *E*-Field Patterns at 7.5 GHz

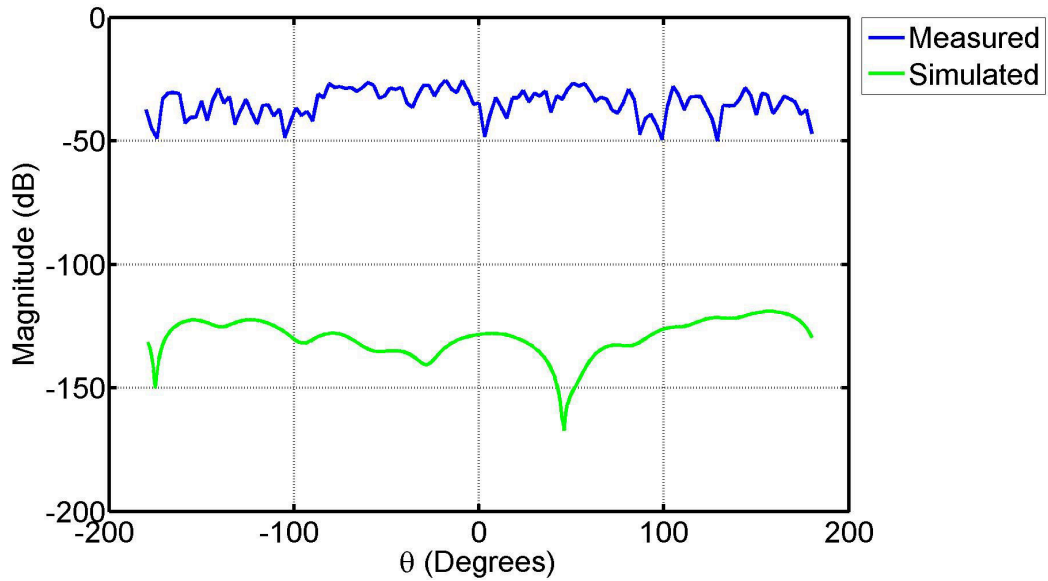


Figure 3.30: Measured and Simulated Cross Polarisation E -Field Patterns at 7.5 GHz

Figures 3.31 and 3.32 show the H -plane measurements and simulations. This result is even better than the E -plane result, with the measured pattern corresponding exactly with the simulated result for $-\theta_0 \leq \theta \leq \theta_0$. Once again there is an obvious main lobe with very little power received outside of it.

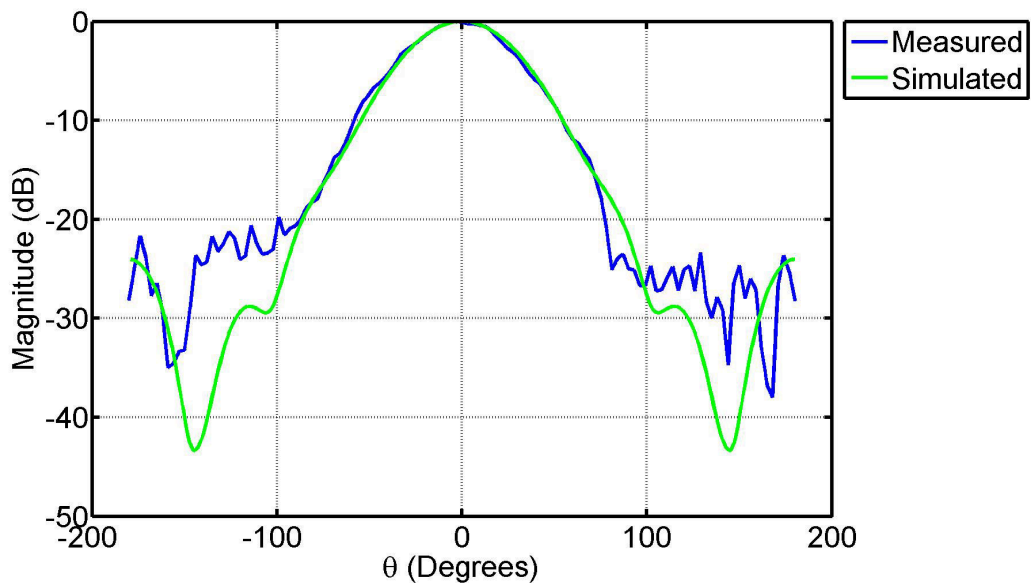


Figure 3.31: Measured and Simulated Co-Polarisation H -Field Patterns at 7.5 GHz

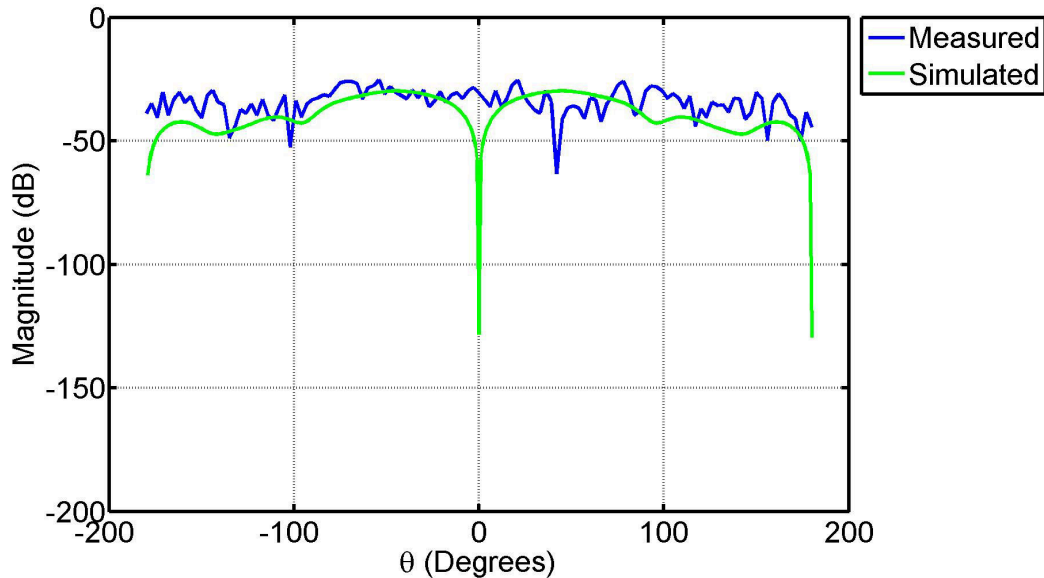
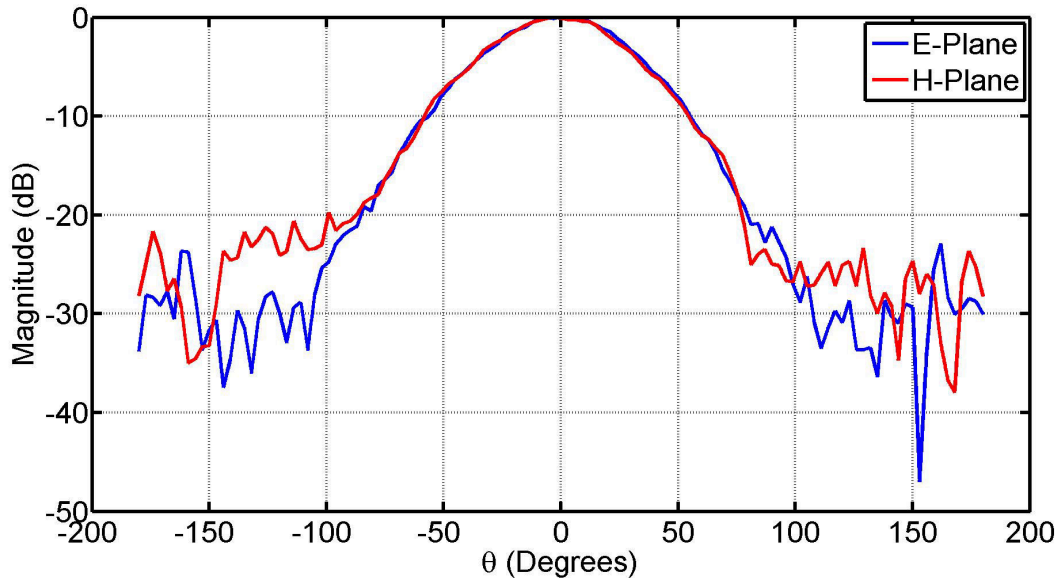


Figure 3.32: Measured and Simulated Cross Polarisation H -Field Patterns at 7.5 GHz

The cross polarised results shown in Figures 3.30 and 3.32 show patterns with low cross polarisation. Virtually no power is received when the polarisations do not match. Figure 3.30 shows a vast difference between the measured and simulated results. The simulated cross polarisation is very low, so any slight error in manufacturing would produce some cross polarisation. Thus these results are not surprising. Comparing the measured cross polarised results of Figures 3.30 and 3.32 we see that they are on the same level. The cross polarisation of Figure 3.32 might seem like it follows the simulated result quite well, but at 0° there is an obvious difference, which could once again be due to small imperfections.

Figure 3.33 shows the E - and H -plane results. They are exactly the same for $-\theta_0 \leq \theta \leq \theta_0$ which is better than what was expected. Figure 3.19 shows that the expected result should differ slightly. This result means that high efficiencies are expected. These are shown in Section 3.6.4.

Figure 3.33: Measured E - and H -Plane Radiation Pattern

3.6.4 Efficiencies Calculated from Measurements

Figure 3.34 shows the calculated efficiencies from the measured patterns. Section 3.2.1 explains why only the E - and H -plane patterns were needed for these calculations. The only sub-efficiency that could not be calculated was the e_{BOR1} efficiency. Equation (3.2.10) shows that the entire field at every point must be known to calculate e_{BOR1} . It can be shown that for an infinitesimal dipole feed with a BOR_1 antenna, e_{BOR1} is 100% [33], and thus it was assumed to be 100%.

The calculated efficiencies show desirable results. Polarisation efficiency is high due to the cross polarisation measured in Section 3.6.3. The spillover efficiency is also high and is expected due to the field patterns being identical in the $-\theta_0 \leq \theta \leq \theta_0$ range. The illumination efficiency is lower than the polarisation and spillover, but spillover and illumination are a trade off, and a value of 70% at the frequency of interest is still an acceptable result. Once the phase data was corrected as it was in Section 3.2.7 the phase efficiency is near 100%.

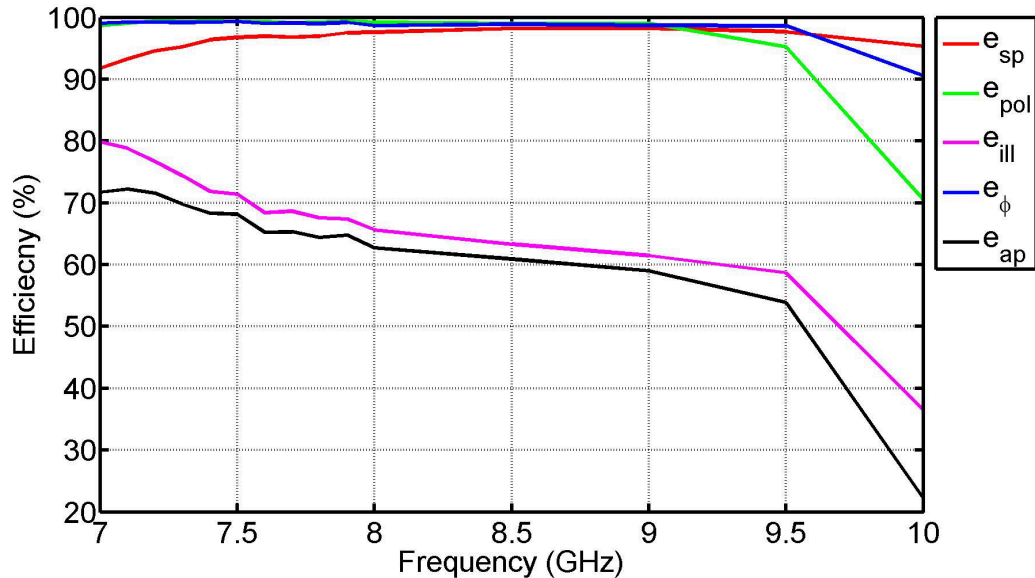


Figure 3.34: Calculated Efficiencies from Measured Data

The efficiencies from measured results compares very well with the efficiencies calculated from simulated data shown in Figure 3.22. The measured spillover efficiency is slightly higher, but this is expected due to the field patterns being better than expected.

Figure 3.35 shows the measured and simulated phase centre δ discussed in Section 3.2.7 that would result in a maximum phase efficiency. There is a vast difference between the two sets of results. This is because δ is measured from different planes of reference for the simulated (CST) and measured results (in the anechoic chamber). Due to time constraints, further investigation of this phenomenon could not be performed.

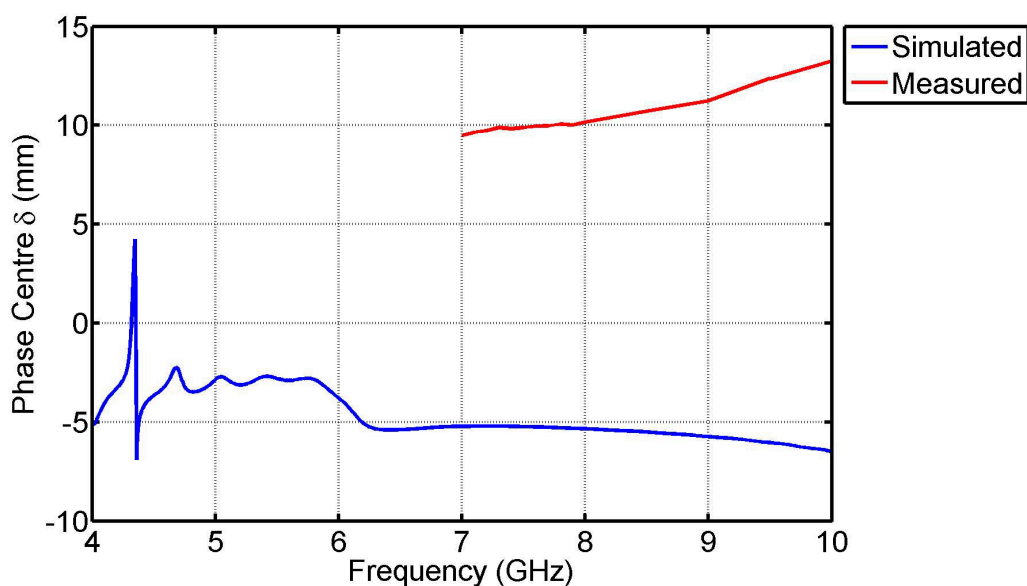


Figure 3.35: Calculated Phase Centre Reference Points from Measured Data

3.7 Conclusion

This Chapter started by briefly describing some antenna properties including Γ , gain and polarisation. The feed efficiency of a parabolic reflector antenna was then defined.

The feed efficiency of a reflector system was described as a product of various sub-efficiencies. These efficiencies can easily be calculated from measured data since only the E - and H -plane measurements are necessary. This is due to the rotational symmetry of the conical horn antenna. This makes it a BOR_1 antenna.

BOR_1 antennas are rotationally symmetric and only radiate power in A_1 and C_1 , known as the BOR_1 components. These components equate to the E - and H -plane field patterns. Thanks to (3.2.3) and (3.2.4) these components can be used to completely describe the field pattern of the antenna.

The design of the antenna was also included. This included an initial design, a rough simulation, an optimisation process and finally the final design. The summarised results of the optimisations is shown, while the full set of results is available in Appendix C.

The measured results were also included. The results generally show expected results and are considered to be successful measurements. From this it can be concluded that the conical horn antenna with corrugations and modal conversion is ideal for this radio astronomy application.

Chapter 4

Radio Receiver

This Chapter aims to describe the receiver system design, as well as components of the receiver systems not described elsewhere in this thesis. The benefits and limitations of some receiver types will be discussed while receiver simulations will be performed.

4.1 Mixers

4.1.1 Description

Mixers play a pivotal role in any receiver system. As the name implies, they mix the incoming frequency of a signal to a different output frequency. This is done by using a Local Oscillator (LO) which is discussed in Section 4.2. The LO synthesizes a frequency which determines the output frequency. The mixers will be specified for a certain LO input power, usually in dBm. Depending on the requirements of the receiver, the desired output can be either the mixed-up or mixed-down signal.

4.1.2 Mixing

Mixers will have a certain frequency range for its inputs and output. Due to the non-linearity of the device many unwanted harmonics can be produced during the mixing stage [9]. A conversion loss is also associated with mixers. This is simply the loss of power of the original signal and is denoted as K .

Up-Conversion

Up-Conversion occurs when the incoming frequency, f_{IF} in this case, is lower than the local oscillating frequency ($f_{IF} < f_{LO}$). Mixing is represented as convolution in the frequency domain and multiplication in the time domain. Thus, we can represent the mixing process as follows:

$$v_{LO} = \cos(2\pi f_{LO}t) \quad (4.1.1)$$

$$v_{IF} = \cos(2\pi f_{IF}t) \quad (4.1.2)$$

$$\begin{aligned}
v_{RF} &= K v_{LO} v_{IF} & (4.1.3) \\
&= K \cos(2\pi f_{LO} t) \cos(2\pi f_{IF} t) \\
&= \frac{K}{2} [\cos(2\pi[f_{LO} - f_{IF}]) + \cos(2\pi[f_{LO} + f_{IF}])]
\end{aligned}$$

where v_{LO} and v_{IF} represent the input frequencies and v_{RF} represents the output frequency. From this we can deduce that $f_{RF} = f_{LO} \pm f_{IF}$ [9].

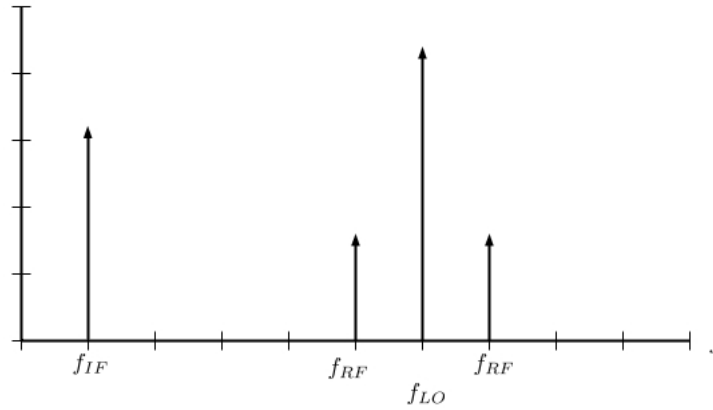


Figure 4.1: Up-Conversion Spectrum Example [9] with f_{IF} as Incoming Frequency

Down-Conversion

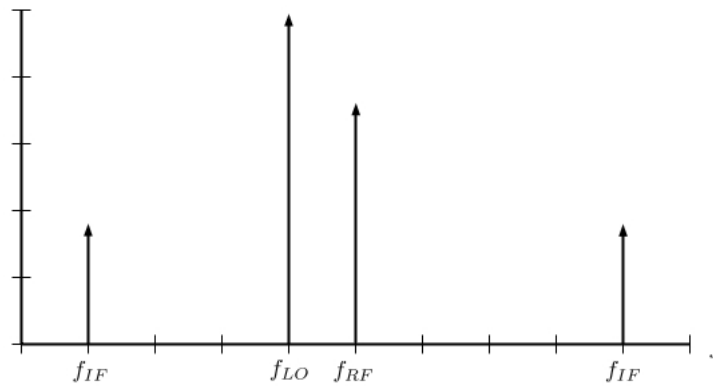
Down-Conversion occurs when the incoming frequency, f_{RF} in this case, is higher than the LO oscillating frequency ($f_{RF} > f_{LO}$). We can represent the mixing process as follows:

$$v_{RF} = \cos(2\pi f_{RF} t) \quad (4.1.4)$$

$$v_{LO} = \cos(2\pi f_{LO} t) \quad (4.1.5)$$

$$\begin{aligned}
v_{IF} &= K v_{RF} v_{LO} & (4.1.6) \\
&= K \cos(2\pi f_{RF} t) \cos(2\pi f_{LO} t) \\
&= \frac{K}{2} [\cos(2\pi[f_{RF} - f_{LO}]) + \cos(2\pi[f_{RF} + f_{LO}])]
\end{aligned}$$

where v_{RF} and v_{LO} represent the input frequencies and v_{IF} represents the output frequency. From this we can deduce that $f_{IF} = f_{RF} \pm f_{LO}$ [9].

Figure 4.2: Down-Conversion Spectrum Example [9] with f_{RF} as Incoming Frequency

4.1.3 Image Frequency

Image frequencies can be a major problem in receiver systems. Consider a down-conversion set-up. According to (4.1.6) the output frequency is $f_{IF} = f_{RF} \pm f_{LO}$. For certain applications we are only interested in $f_{IF} = f_{RF} - f_{LO}$, the lower side-band.

There exists another signal that would result in the same f_{IF} . This is called the image frequency, denoted by f_{IM} . Care must be taken to ensure that the image is filtered out - this is done by using an image rejection filter. If f_{IM} is close to f_{RF} the image rejection filter should be designed with a very sharp cut-off. The image frequency in Figure 4.3 will be mixed down to the same f_{IF} as f_{RF} .

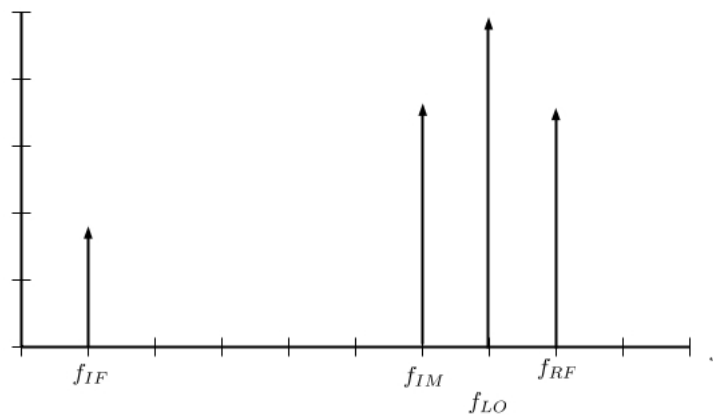


Figure 4.3: Image Frequency Spectrum Example [9]

If the image frequency is not properly filtered out, the unwanted signal will be mixed into the f_{IF} operating band that would interfere with the desired signal. It can be seen from Figure 4.3 that

$$f_{IM} = f_{LO} - f_{IF} \quad (4.1.7)$$

since $f_{IF} = f_{LO} - f_{IM} = f_{RF} - f_{LO}$.

It must be noted here that "negative frequencies" that may arise from these calculations are mathematically identical to their absolute value. This is because the Fourier spectrum of any real signal is symmetric about zero frequency, and thus contains both negative and positive frequencies [9].

4.1.4 Mixer Properties

Later in this Chapter the type of receiver used, selection of IF and baseband frequency are explained. The IF frequency is 3.5 GHz. This is a consequence of both the available mixers and low noise amplifiers. Thus two mixers were purchased. They will be referred to as the RF mixer at 7.5 GHz and the IF mixer at 3.5 GHz.

The mixers were purchased from mini-circuits. Table 4.1 provides a summary of their properties. The RF mixer requires more power from the LO. This is however the only mixer available for a reasonable price. The LO leakage eventually presents a problem in the receiver, as highlighted in Section 4.5.

Parameter	RF	IF
Name	ZX05-153LH+	ZX05-73L+
Frequency Range	3.2-15 GHz	2.4-7 GHz
IF Bandwidth	DC-4 GHz	DC-3 GHz
Max Input Power	17 dBm	17 dBm
Required LO Power	10 dBm	4 dBm
L-I Isolation	18 dBm	26 dBm
1db Compression	2 dBm	1 dBm
IP3	15 dBm	12 dBm

Table 4.1: RF and IF Mixer Properties

Once the mixers were received they were tested to ensure they performed as required. From the measurements it was determined that they performed as expected.

4.2 Local Oscillator

A Local Oscillator, as briefly discussed in Section 4.1, is used in conjunction with a mixer to up- or down-convert a signal. The LO is ideally a signal of a single frequency. Varying the LO frequency will vary the output frequency of the mixer.

4.2.1 Signal Generator

The simplest way to generate the required signal is to use a signal generator. The required frequency and power output can easily be set. This is easily applicable in this thesis because of the use RFoF, which is discussed in Chapter 7. Without the use of RFoF,

the LO signals would need to be applied at the antenna or generated there using a more appropriate method.

4.2.2 Phase Locked Loop

A phase locked loop (PLL) can also be used to generate the required signal. The required circuitry is complicated however and still needs a reference oscillator, possibly Direct Digital Synthesis (DDS).

The PLL works by detecting the phase difference between the reference signal and the output signal. A constant phase difference implies that the frequencies of the signals are the same while a change in phase difference implies a change in frequency of the output signal [39]. A phase detector is used to determine the phase difference.

The phase detector provides an output proportional to the phase difference. A loop filter then attenuates the signal to help improve the phase noise characteristics and supply a voltage for the voltage controlled oscillator (VCO). The VCO provides the output signal that is tested against the original input signal. Eventually the output frequency will be the same as the input frequency.

By adding a programmable divider after the VCO feedback and before the phase detector a different frequency can be provided by the VCO output. The VCO frequency will be divided by the division ratio of the divider, known as n [39]. This means that the output signal frequency of the VCO will be n times larger than the input reference signal. By changing the value of n the PLL can be used as a frequency synthesizer. Analogue PLL use a mixer instead of a programmable divider.

While a PLL will provide the required signals, they can be difficult to design and manufacture and still require a reference signal. It was decided not to use a PLL.

4.2.3 Frequency Synthesizer

A Valon Frequency Synthesizer can also be used. The output frequency and output power can be set via a USB interface. The synthesizer uses FLASH memory and does not require a USB connection to deliver the output signal. This means that the synthesizer can be mounted anywhere in the receiver system. The synthesizers can however be expensive.

The synthesizer is set-up to use an internal 10 MHz reference signal. If required an external reference can be applied. The synthesizer can also supply two independent output signals. This makes the synthesizer very versatile. The generated frequencies are synthesized by two separate PLL's.

Table 4.2 provides a summary of the synthesizer characteristics.

Parameter	Value
Name	5008 Dual Valon Frequency Synthesizer
Output Frequency Range	137.5 to 4400 MHz
Output Power	-1 to 9 dBm
Synthesizer Output Isolation	-60 dB
Required DC Input Power	5 V
RF Connectors	SMA Female
Size	67.7 x 91.7 x 13.2 mm

Table 4.2: Valon Frequency Synthesizer Characteristics

The Valon Frequency Synthesizer is a very dynamic and versatile device that fulfils all of the requirements for the local oscillators. Since a comparison between the RFoF system and conventional system is required, the Valon Frequency Synthesizers present the ideal solution for the LO's. They can easily be used in the lab as well as easily mounted along with the rest of the receiver system at the dish. For these reasons it was decided that the Valon Frequency Synthesizer would be used for the LO's.

4.3 Different Types of Receivers

Different types of receivers were considered for this project. Each type discussed here has its own benefits and limitations.

4.3.1 Direct Receiver

The receiver architecture described here is not strictly a receiver type, but its has been used by the writer before. Figure 4.4 shows a simple system consisting of a LNA and a band-pass filter as part of the RF stage. After this the signal is transmitted to a RF Power Detector, which is a IC device that receives a RF signal as input and outputs a DC voltage proportional to the power received.

This receiver type is appropriate for the goals outlined in this thesis and would allow the back-end of the system to be very simple. Unfortunately there are no appropriate RF Power Detectors available at the required frequency of operation.

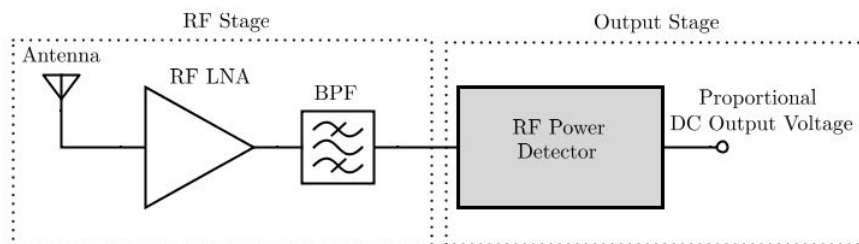


Figure 4.4: Direct Receiver System Using RF Power Detector

4.3.2 Homodyne Receiver

Homodyne receivers, also known as direct conversion receivers, are a very popular type of receiver. Figure 4.5 shows the architecture of such a receiver. The incoming RF signal is filtered, amplified and then mixed down to baseband. The signal is mixed down to baseband in one step by allowing the LO frequency to be the same as (or very close to) the carrier frequency of the signal. Once the signal has reached the baseband it undergoes demodulation. For frequency and phase modulated signals quadrature outputs must be included in the down conversion to ensure no information is lost [40].

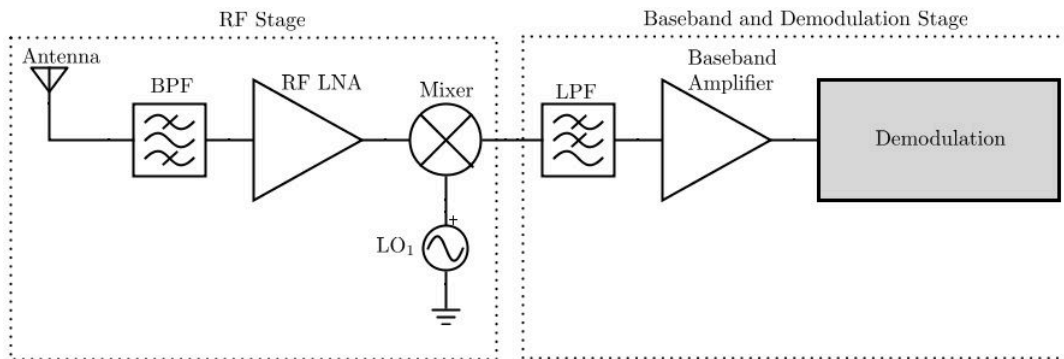


Figure 4.5: Homodyne (Direct Conversion) Receiver Architecture

This receiver has less hardware than the popular superheterodyne receiver and does not suffer from image rejection issues since the LO frequency is the same as the carrier. LO leakage into the antenna can be a problem since the LO frequency is the same as the receiving signal [40]. Also, the RF components can become expensive at higher frequencies.

With an appropriate back-end this receiver would be suitable for the goals of this thesis. However, the desired frequency of operation, 7.5 GHz, is quite high. Only one mixer was found that would be able to mix such a high frequency signal down to baseband. Also, no frequency synthesizers were found that could generate such a frequency for the LO. This means that this type of receiver would need either a PLL or a signal generator for the LO.

4.3.3 Superheterodyne Receiver

The superheterodyne receiver is by far the most popular type of receiver used in modern radio communications. As highlighted in Section 4.1, the result of mixing two signal together is the sum and difference frequencies, $f_{IF} = f_{RF} \pm f_{LO}$. Figure 4.6 shows the architecture of a superheterodyne receiver.

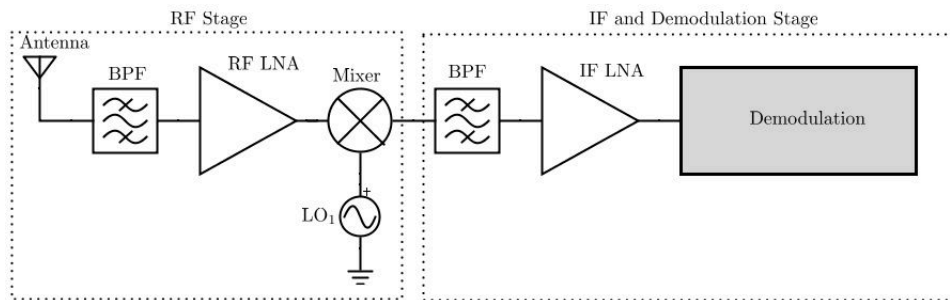


Figure 4.6: Basic Single Heterodyne Receiver

Mixing down to an IF allows operation at a more manageable frequency. This means components such as filters and amplifiers can be bought off the shelf instead of being designed and manufactured. Having fixed IF's can also allow components at those frequencies to be optimised and made less expensive [41]. Depending on the values of the RF and LO signals, image frequencies might become a problem. This is however most prevalent in double superheterodyne systems.

Like the homodyne receiver, this system meets all the requirements for this thesis assuming an appropriate back-end. Unfortunately, also like the homodyne receiver, it is not practically realisable for the same reasons. A back-end like the ROACH board requires input in the band 0 - 400 MHz (or 0 - 750 MHz if a maximum clock is applied). A mixer was found that could perform the required mixing, but the image frequency would have been very close to the desired signal. There was also no frequency synthesizer that could supply the necessary LO. Therefore a double superheterodyne system was considered.

Figure 4.7 shows the architecture of a double superheterodyne receiver. The addition of the second IF stage allows higher frequencies to be mixed down to the appropriate frequency. This allows a high IF_1 which means the first image frequency can be easily filtered out and a low IF_2 which means that high performance components at low costs can be used [42].

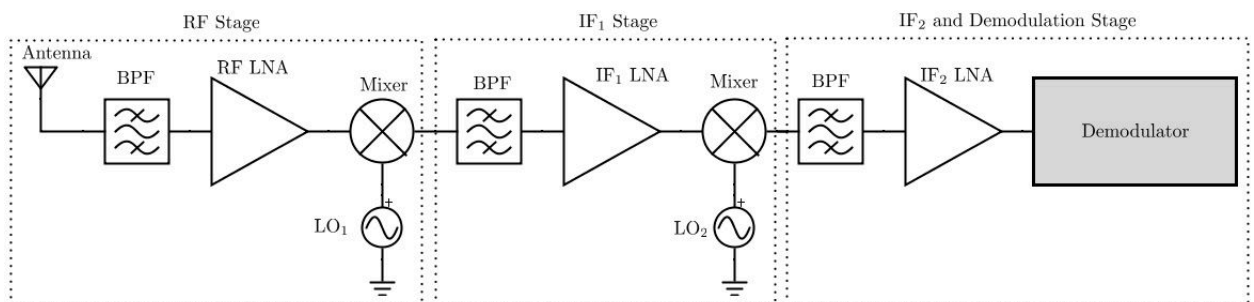


Figure 4.7: Basic Double Heterodyne Receiver

It was decided to use this receiver architecture due to the lack of available components for the other suggested systems. The next Section will describe how the double superheterodyne receiver will be implemented.

4.4 Selection of IF Frequency

Once the receiver type was chosen the IF frequencies had to be chosen. To do this, the receiving band for the back-end had to be determined. It was at this stage that it was decided to use the ROACH board available at the faculty as the back-end. Using the thesis "The Design of a Two-Element Correlation Interferometer Operating at L-Band" [43] by JP Jansen van Rensburg as a reference, as well as documentation on the ROACH board, 375 MHz was chosen as the final operating frequency of the receiver.

4.4.1 Conversion Schemes

One of the most important design considerations of the superheterodyne receiver is the image frequency rejection. Figures 4.8 and 4.9 shows the possible ranges for IF_1 given the choice of 375 MHz for IF_2 , the relevant LO frequency synthesizer ranges and the mixer ranges. These are briefly summarised in Table 4.3.

Component	Range (GHz)
LO	0.137-4.4
Mixer ₁ RF	3.2-15
Mixer ₁ IF	DC-4
Mixer ₂ RF	2.4-7
Mixer ₂ IF	DC-4
IF ₂	0.375

Table 4.3: Frequency Ranges of Receiver Components

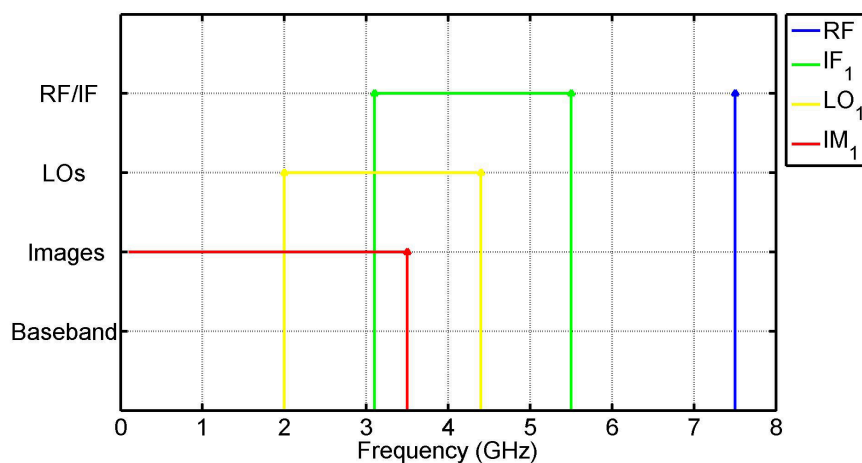


Figure 4.8: Frequency Ranges of First Down Conversion in Proposed Receiver

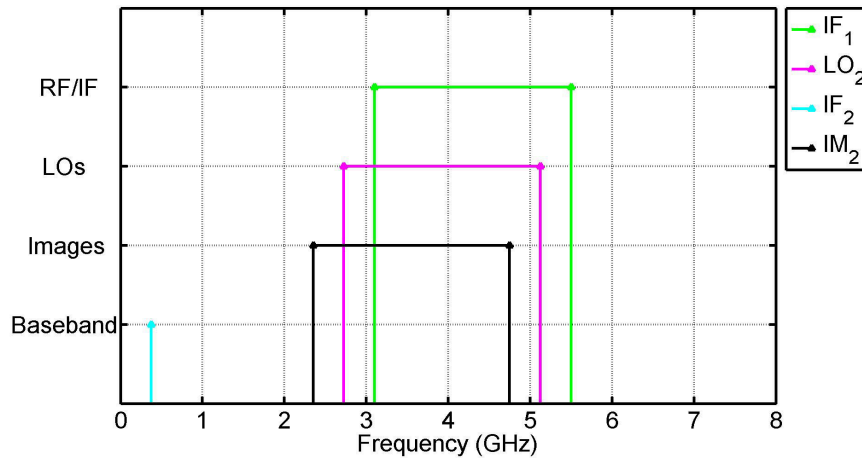


Figure 4.9: Frequency Ranges of Second Down Conversion in Proposed Receiver

Figures 4.8 and 4.9 were produced by allowing a LO range of 2-4.4 GHz. The upper limit is because of the maximum frequency the frequency synthesizer can generate. The lower limit was chosen arbitrarily to try and keep IF_1 somewhere in the middle between the incoming RF signal and IF_2 .

As can be seen in Figure 4.8 the image frequency is far away from the incoming RF signal and can be easily filtered out. The image frequency in Figure 4.9 is much closer to the IF_1 frequency. This means that a filter with sharp cut-off will be required in the IF_2 stage for image rejection. The image range must be mentioned here. The range in Figure 4.8 is much larger than the image range in Figure 4.9. This is because the IF_1 in Figure 4.8 is a range as well, but IF_2 in Figure 4.9 is a fixed value.

From Figures 4.8 and 4.9 many possible down conversion schemes were made possible. To ultimately decide what IF_1 should be, possible amplifiers in the IF_1 band were reviewed. It was then decided that IF_1 should be 3.5 GHz. This allows a LO_1 of 4 GHz with the first image at 0.5 GHz. The second image frequency would then be at 2.75 GHz with a LO_2 of 3.125 GHz. Figure 4.10 describes this case.

Figure 4.10 also includes the leakage from LO_1 , LOM_1 , mixed down. This was observed during the receiver simulation stages and added to Figure 4.10 at a later stage. Once mixed down the leakage is very close to the band of operation and must be filtered out appropriately.

Figure 4.10 shows all the signals of interest in the proposed receiver. The passbands of the two mixing stages are highlighted by the dotted lines which represent the need for image rejection filters.

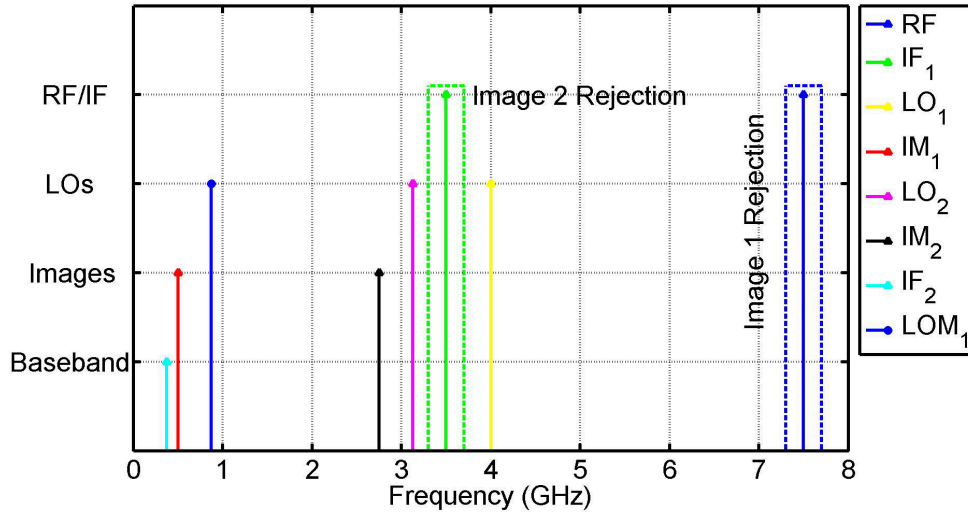


Figure 4.10: Proposed Frequency Spectrum of Receiver

4.4.2 Spurious Signals

Once the IF has been chosen, the proposed receiver must be checked for spurious signals, also known as spurs. The non-linear properties of mixers allow for the sum and difference frequencies that are used [9]. Along with these frequencies intermodulation products also contribute signals at certain frequencies with less power. Some of these frequencies may fall within the receiver passband and are unwanted.

Intermodulation products are the results of non-linearities in a component. The output of a general non-linear network can be expanded by using a Taylor series in terms of the input voltage signal v_i [44],

$$v_0 = a_0 + a_1 v_i + a_2 v_i^2 + a_3 v_i^3 + \dots \quad (4.4.1)$$

$$a_0 = v_0(0) \quad (\text{DC Output}) \quad (4.4.2)$$

$$a_1 = \left. \frac{dv_0}{dv_i} \right|_{v_i=0} \quad (\text{Linear Output}) \quad (4.4.3)$$

$$a_2 = \left. \frac{d^2 v_0}{dv_i^2} \right|_{v_i=0} \quad (\text{Squared Output}) \quad (4.4.4)$$

$$\vdots$$

where the a_0 coefficient represents the DC component, the a_1 represents a linear attenuator or amplifier and a_2 represents the mixed products. The other higher order coefficients are generally unwanted but are always present in any practical system. Considering the case when two frequencies are applied to a general non-linear network, the following equations can be set up:

$$\begin{aligned}
v_i &= A(\cos w_1 t + \cos w_2 t) & (4.4.5) \\
v_0 &= a_0 + a_1 A(\cos w_1 t + \cos w_2 t) + a_2 A^2 (\cos w_1 t + \cos w_2 t)^2 + \dots \\
&= a_0 + a_1 v_0 \cos w_1 t + a_1 A \cos w_2 t + \frac{1}{2} a_2 A^2 (1 + \cos 2w_1 t) + \frac{1}{2} \dots
\end{aligned}$$

It is clear that the output v_0 consists of harmonics. These harmonics are of the form $mw_1 + nw_2$, where m and n are integers. The term is defined as $|n| + |m|$. The second order terms are used in mixers to mix two signals together. The other products are generally out of the band of operation, with the notable exception of the third order products. This is well known and interference from these products is known as third order intermodulation distortion. Table 4.4 provides the third order products for the chosen RF and IF frequencies.

Product	First Down Conversion (GHz)	Second Down Conversion (GHz)
$3w_1$	22.5	10.5
$3w_2$	12	9.375
$2w_1 + w_2$	19	10.125
$w_1 + 2w_2$	15.5	9.75
$2w_1 - w_2$	11	3.875
$2w_2 - w_1$	0.5	2.75

Table 4.4: Third Order Intermodulation Products of Proposed Receiver

All this means that (4.4.6) can be used to determine the frequencies of the spurious signals, given that m and n are integers,

$$f = mf_1 + nf_2 \quad (4.4.6)$$

$$m, n = 0, \pm 1, \pm 2, \pm 3, \dots \quad (4.4.7)$$

Instead of calculating all the intermodulation products and seeing which are within the passband, a MATLAB script was written to graphically display the required information. Figures 4.11 and 4.12 were produced by calculating the mixer output given a value for f_{RF} . Both the f_{RF} and f_{IF} values are normalised by f_{LO} . This was done for values of m and n up to 5. The green line represents the desired output where $m = n = 1$. The blue lines are varying degrees of intermodulation products. The red boxes represent the chosen bands of operation. It is required that almost no intermodulation products exist in the box. Higher order products in the box may be acceptable due to their low power levels.

lowers the impact that they might have on the system. Figure 4.12 also validates the choice of $f_{IF1} = 3.5$ GHz and $f_{IF2} = 0.375$ GHz.

4.4.3 Final Receiver Design

The final receiver architecture can now be seen in Figure 4.13. The required gains of the amplifiers will be discussed in Chapter 5 as well as briefly in the next Section.

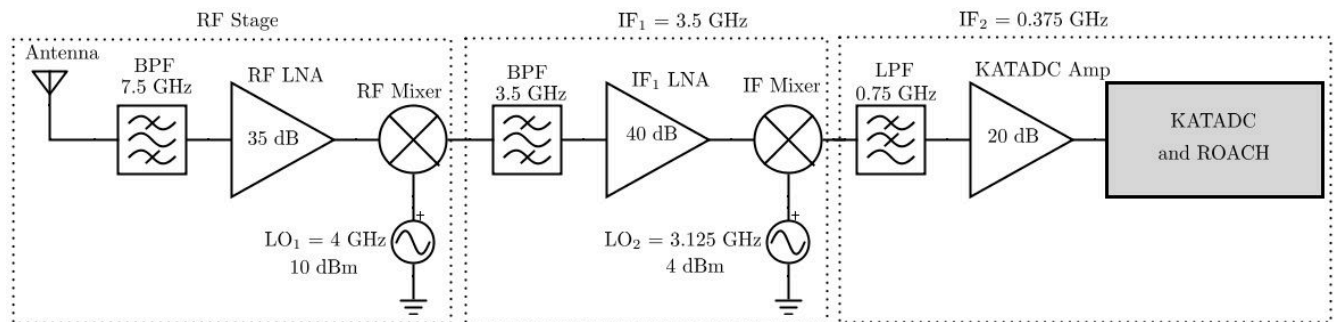


Figure 4.13: Final Receiver Design

The architecture is slightly different to that of Figure 4.7. The BPF in the IF_2 stage has been replaced by a Low-Pass Filter (LPF). The following Section will discuss this and show that while a filter is required, a LPF is more convenient. It is also important to note that the Radio Frequency Over Fibre has not yet been included. In this Figure it would appear just after the RF LNA and before the RF Mixer.

4.5 Receiver Simulation

To test the feasibility of the proposed receiver a simulation was performed in Microwave Office (MWO). This simulation served as a rough indicator of how the receiver performs.

4.5.1 Simulation Set-Up

The receiver shown in Figure 4.13 was simulated in MWO. Certain elements were however omitted from the simulation design. These included the antenna and the KAT-7 ADC/ROACH components. The KAT-7 ADC amplifier was however included. Initially the LPF was omitted as well.

The band-pass filters used are the simulated inter-digital filters that are described in Chapter 6. The S-parameters were imported into MWO. The low noise amplifiers were the simulated amplifiers described in Chapter 5. Both the RF and IF amplifiers have a cascaded design for more gain.

The mixers used were general mixers available in the MWO library. Parameters like 1 dB compression point, IP3 and isolation values were set to match the parameters of the ZX05-153LH+ and ZX05-73L+ mixers. The local oscillators were simply signals set to the correct frequency and power.

4.5.2 Simulated Results

As shown in Chapter 2 the power from the sun will be between -100 dBm and -75 dBm for receiver bandwidths from 0 - 1 GHz. The simulated results use an input signal of -80 dBm at 7.5 GHz to represent the desired signal. Two signals at 6 and 9 GHz were also applied to the input to represent signals out of band.

Figure 4.14 shows the applied signals as well as the effect of the RF BPF and RF LNA. The input signals are idealised signals. The cascaded LNA provided about 32 dB of gain. The desired signal is now at -47 dBm. The unwanted signals have been attenuated to -120 dBm. The "RF_{in} Amplified" signals are the input to the RF mixer in the receiver. These signals will be mixed with a LO of 4 GHz.

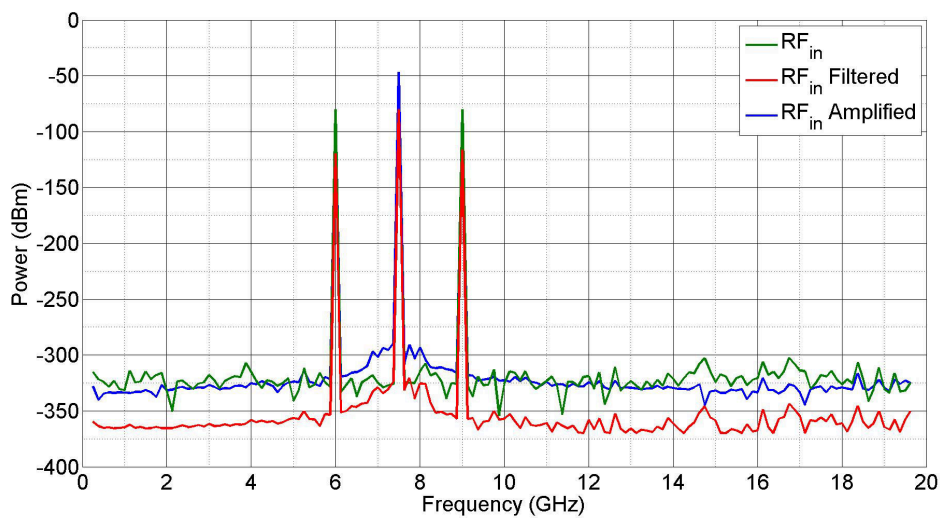


Figure 4.14: RF Stage of Simulated Receiver Chain

Figure 4.15 shows the IF stage of the receiver. "IF_{in}" represent the mixed down signal from the RF stage (the output of the RF mixer). The desired signal is present at 3.5 GHz, but there are many other unwanted signals. At 4 GHz a very strong signal is present. This is the leakage from LO₁. This was not initially considered and means that the IF BPF should have a sharp cut-off. Fortunately this was already a requirement due to potential image frequencies. At 11.5 GHz the up-converted signal from the mixer is visible and can be easily filtered out. There is also some leakage from the input signal at 7.5 GHz which is also easily filtered out. The signal at 4.5 GHz was unexpected. Investigation revealed that it must be the 4th order intermodulation product defined by $7.5 - 3 \times 4 = 4.5$ GHz.

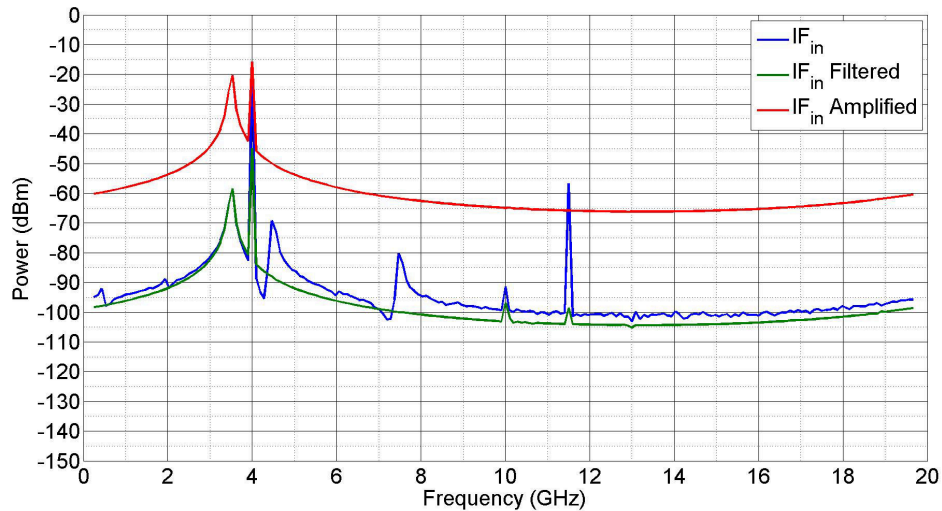


Figure 4.15: IF Stage of Simulated Receiver Chain

"IF_{in} Amplified" is the signal that will be applied to the IF mixer. The desired signal at 3.5 GHz has been amplified to -20 dBm. The rest of the signal is clear except for the presence of the LO₁ leakage. Even after filtering the signal is still strong. This means that it will be mixed down by the mixer just like the desired signal.

Figure 4.16 shows the output stage of the receiver. Before a LPF was applied the leakage signals and intermodulation products were scattered across the spectrum. The most troublesome of these is the signal at 875 MHz which is denoted as 1 on the Figure. The signal denoted as 1 is the LO₁ leakage that has been mixed down through the IF mixer. All of the signals mentioned in Table 4.5 could cause problems with the KAT-7 ADC or ROACH board and thus it was decided to add a LPF to the receiver. The LPF that has been added to the simulation is an ideal LPF available in the MWO library.

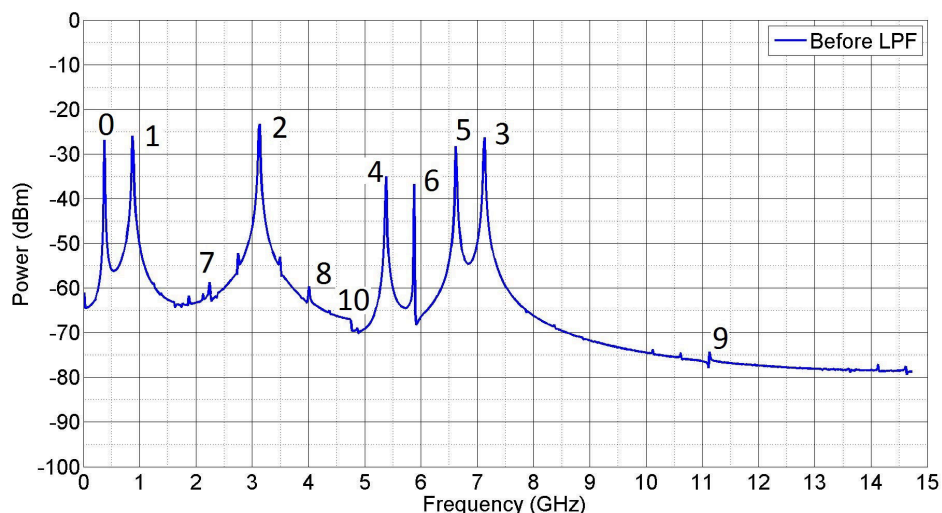


Figure 4.16: Output Stage of Simulated Receiver Chain Before LPF Has Been Added

Signal	Description	Frequency (GHz)
0	Desired Signal at IF ₂	0.375
1	LO ₁ Leakage Mixed Down by IF Mixer	$4 - 3.125 = 0.875$
2	LO ₂ Leakage	3.125
3	LO ₁ Leakage Mixed Up by IF Mixer	$4 + 3.125 = 7.125$
4	LO ₁ Leakage Mixed Down 4th Order Harmonic	$4 - 3 \times 3.125 = 5.375$
5	Desired Signal Mixed Up	$3.5 + 3.125 = 6.625$
6	Desired Signal Mixed Down 4th Order Harmonic	$3.5 - 3 \times 3.125 = 5.875$
7	LO ₁ Leakage Mixed Down 3rd Order Harmonic	$4 - 2 \times 3.125 = 2.25$
8	LO ₁ Leakage from IF Stage Leaking Through IF Mixer	4
9	LO ₁ Leakage Mixed Up 3rd Order Harmonic	$2 \times 4 + 3.125 = 11.125$
10	LO ₁ Leakage Mixed Down 3rd Order Harmonic	$2 \times 4 - 3.125 = 4.875$

Table 4.5: Description of LO Leakage Signals and Intermodulation Products in Output of Simulated Receiver

Figure 4.16 shows many signals in the output stage. The prevalence of the LO leakage was unexpected, as was the presence of 4th order intermodulation products. The 3rd order products that are present have much less power than the 4th order. The mixer models in MWO have an option to enter the IP3 for each mixer. It seems that while 3rd order products are attenuated appropriately thanks to the IP3 information, higher order products are not. This was confirmed by running simple MWO simulations and taking note of 3rd order and 4th order products. It must be noted that the intermodulation products in Figure 4.16 are mostly a result of the leakage signals. Intermodulation from the desired signals are not nearly as prevalent as the leakage intermodulation.

Figure 4.17 shows the output after the LPF has been added. The use of the LPF allows for a clean signal at 375 MHz to be applied to the KAT-7 ADC and ROACH board. This simulation has the signal at -8 dBm. The KAT-7 ADC has a maximum input of -27 dBm before the signal starts to saturate. The KAT-7 ADC also has a 31.5 dB variable attenuator that can be programmed and used. The gain of the KAT-7 ADC can also be disabled.

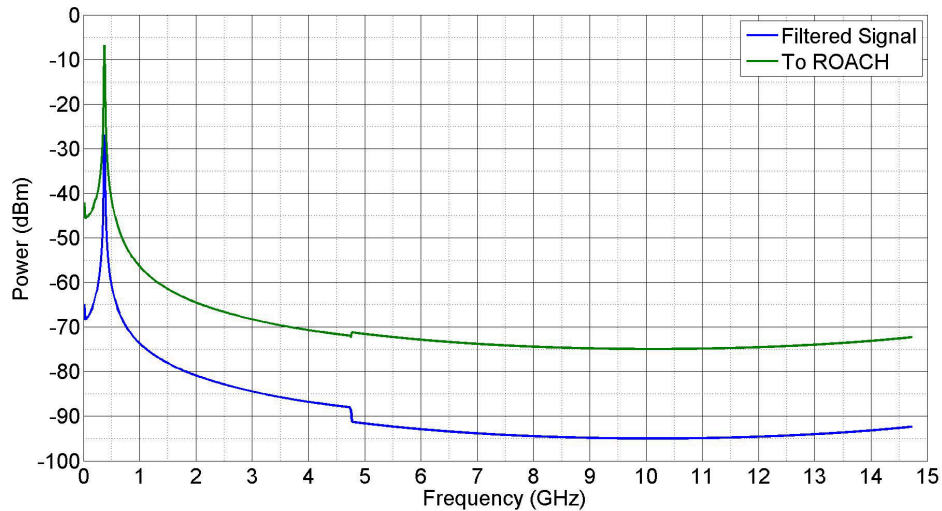


Figure 4.17: Output Stage of Simulated Receiver Chain After LPF Has Been Added

4.6 Conclusion

Mixers were briefly discussed. Their operation was shown and the potential problems areas were identified as image frequencies and third order intermodulations products. The chosen mixers were measured to ensure they were in working condition. Several possibilities for the local oscillator were also discussed. The Valon Frequency synthesizer was chosen because of its ability to generate two independent signals at the required frequencies.

Different receiver architectures were discussed. The benefits and shortcomings of each type were identified. It was decided to use the double super-heterodyne receiver for this project because of the high frequency of the input signal and the low frequency requirement of the back-end. To check whether or not this receiver could work spurious signals were defined. Spur charts were plotted for each down conversion and it was found that the proposed receiver had minimal spurious interference.

To validate the choice of receiver even more simulations was performed in Microwave Office. This produced the desired results as well as some unexpected ones. The LO leakage was identified as a problem and a LPF was introduced to the final stage before the KAT-7 ADC to eliminate all LO leakage signals and intermodulation signals. The result was a clean signal at 375 MHz for the KAT-7 ADC and ROACH board.

Chapter 5

Low Noise Amplifiers

A Low Noise Amplifier is required at various stages in an RF system to amplify small signals. Signals can be weak so ideally no noise must be introduced into the system.

5.1 Noise in Radio Receivers

Noise is a very important characteristics of any radio receiver system as it ultimately determines the performance of the system. This is because the minimum detectable signal level is determined by the noise. In radio astronomy this is even more important because the expected signals are typically low; anything from -130 dBm to -80 dBm.

Noise can be introduced to a system through a variety of sources. These include thermal noise generated by RF components, noise generated by atmosphere, cosmic background radiation [45], and man made noise [9]. Fluctuations in the system can more specifically be attributed to random refraction of light due to atmospheric turbulence, statistical and physical processes and bad electrical connections [46].

5.1.1 Noise Power

This Section aims to briefly explain noise power and implications that come with it. The most common type of noise in radio receivers is thermal noise. Thermal noise is generated in any lossy passive circuit element by the random motion of charge carriers.

Consider the resistor in Figure 5.1. The resistor operates at a temperature T in degrees Kelvin. At any temperature above absolute zero the temperature causes random motion of the electrons in the resistor. The degree of these small fluctuations is proportional to the temperature and causes small voltages to appear across the terminals [9].

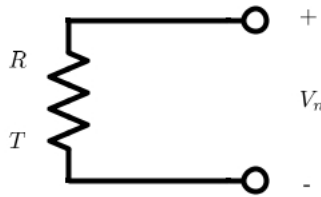


Figure 5.1: Resistor at Temperature T

The fluctuations in voltage and current will always be about zero [46]. The time average for the voltage $\langle V \rangle = \int v(t)dt = 0$. The average rms voltage however is not 0. The mean square voltage due to thermal processes is

$$\langle V_n^2 \rangle = 4kTRB \quad (5.1.1)$$

where

k = Boltzmann's Constant = 1.380×10^{-23} , [J/°K]

T = temperature, [°K]

B = bandwidth, [Hz]

R = resistance, [Ω]

$\langle \rangle$ indicate a time average.

This is known as Thermal or Johnson-Nyquist Noise. Thermal electron motion in a resistor gives rise to additional fluctuating voltages that are independent of the current through the resistor.

To now calculate the noise power a Thevenin equivalent circuit can be constructed as a voltage source of V_n and a noiseless resistor R . The worst case scenario, when the output load is conjugately matched to the source load resulting in maximum power transfer, is considered.

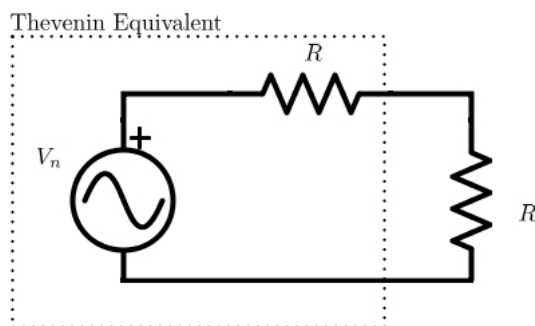


Figure 5.2: Equivalent Thevenin Circuit for Noisy Resistor at Temperature T

The power is found to be

$$\begin{aligned}
 P_R &= \langle v_R i_R \rangle \\
 &= \frac{\langle v_R^2 \rangle}{R} \\
 &= \frac{1}{R} \langle \left(\frac{V_n}{2} \right)^2 \rangle \\
 &= \frac{\langle V_n^2 \rangle}{4R} \\
 &= kTB.
 \end{aligned} \tag{5.1.2}$$

The thermodynamic quantity of temperature is related to the electrical quantity of voltage and power by this theorem [4]. This result is important because it shows that the noise power is dependent upon bandwidth and temperature and independent of the resistance value. The noise can be thought of as Gaussian white noise at frequencies below 80 GHz. The Johnson Noise is present due to the blackbody radiation within the conductor [47].

5.1.2 Equivalent Noise Temperature

An arbitrary white noise source can be modelled as a resistor with a equivalent temperature T_e so that the resulting output noise is the same. This is useful because antennas can be modelled in a receiver system as a resistor at an equivalent temperature.

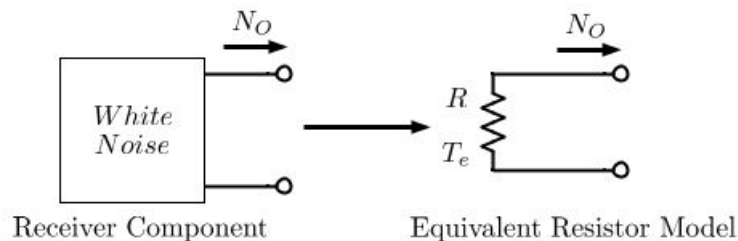


Figure 5.3: White Noise Source Modelled as a Resistor at Equivalent Temperature T_e

If the noise power from the white noise source is defined as N_O , the equivalent temperature can be defined as

$$T_e = \frac{N_O}{kB}. \tag{5.1.3}$$

Noisy amplifiers can also be modelled as an equivalent resistor and noiseless amplifier that produce the same results. The equivalent temperature is then found to be

$$T_e = \frac{N_O}{GkB} \tag{5.1.4}$$

where G is the gain of the amplifier converted from decibels.

Figure 5.4 shows an arbitrary component with a gain G and the various noise powers associated with it. Both the incoming noise N_i and noise added by the component N_{added} are multiplied by the gain G of the component.

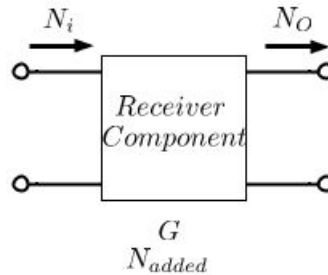


Figure 5.4: Noises in a Receiver Component

The total output noise N_O can then be written as

$$\begin{aligned}
 N_O &= G(N_i + N_{added}) \\
 &= G(kT_i B + kT_{added} B) \\
 &= kB G(T_i + T_{added}).
 \end{aligned} \tag{5.1.5}$$

5.1.3 Noise Figure

The most common manner to express the merit of noise of a component or receiver system is to use the noise figure. The noise figure is a measure of degradation of the Signal-to-Noise Ratio (SNR) from the input to the output of the component or system in question [9].

A noiseless network will amplify or attenuate both the desired signal and the noise by the same amount. When the system becomes noisy, noise is added and the SNR of the output signal is less than the SNR of the input signal. The noise figure can be defined as

$$NF = \frac{SNR_i}{SNR_o} \tag{5.1.6}$$

where $SNR_i = \frac{S_i}{N_i}$ is the SNR of the input and $SNR_o = \frac{S_o}{N_o}$ is the SNR of the output.

By definition the input noise power must be from a matched load at temperature $T_O = 290K$. This means that $N_i = kT_O B$ [9]. Noise figure is mostly expressed in term of decibels,

$$NF_{dB} = 10 \log(NF). \tag{5.1.7}$$

Pozar presents an equation to express equivalent noise temperature in terms of the noise figure [9]. Note this equation uses NF not NF_{dB} ,

$$T_e = (NF - 1) T_O. \quad (5.1.8)$$

For lossy components Pozar presents an equation that expresses the noise figure of the component in terms of its loss. L represents the fraction of power loss due to attenuation [45]. Considering that the component loss $L = \frac{1}{G}$, the noise figure can be defined as

$$NF = 1 + (L - 1) \frac{T}{T_O} \quad (5.1.9)$$

where T is the operating temperature. Two special cases of operation can be deduced from (5.1.9). Firstly, at absolute zero ($T = 0$) the component will be lossless. This means that $NF = 1 = 0dB$. The second special case is at room temperature where $T = T_O$ and the noise figure becomes $NF = L$. This means that a component with x dB attenuation will have a noise figure of x dB at room temperature.

5.1.4 Cascaded Noise Figure

An important characteristic of receiver systems is the fact that the components that are first in the system dominate the noise figure of the receiver. Amplifiers later in the chain need not have especially low noise figures. This means that the design of the first component is critical in terms of noise.

Once again Pozar presents a solution for the calculation of cascaded noise figures. Consider the network in Figure 5.5.

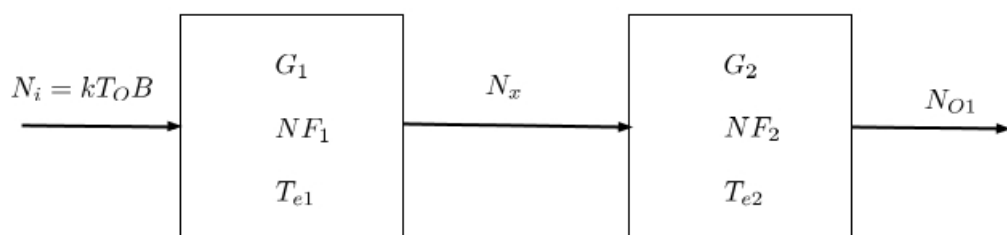


Figure 5.5: Cascaded Components

N_x is the noise power after the first stage. It can be written as

$$N_x = G_1 k T_O B + G_1 k T_{e1} B \quad (5.1.10)$$

while the output noise power N_{O1} can be written as

$$N_{O1} = G_2 N_x + G_2 k T_{e2} B = G_1 G_2 k B \left(T_O + T_{e1} + \frac{T_{e2}}{G_1} \right). \quad (5.1.11)$$

This can be compared to the overall system

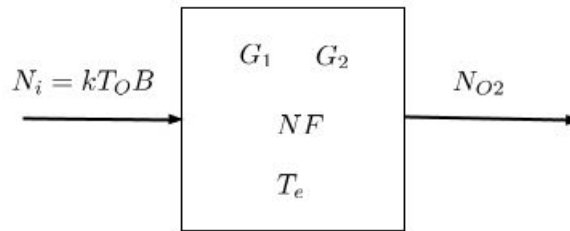


Figure 5.6: Overall System of Cascaded Components

where $N_{O2} = G_1 G_2 k B (T_e + T_O)$. Comparing N_{O1} and N_{O2} allows the noise figure of the system to be written as

$$NF = NF_1 + \frac{NF_2 - 1}{G_1}. \quad (5.1.12)$$

This result can be generalised as follows

$$NF = NF_1 + \frac{NF_2 - 1}{G_1} + \frac{NF_3 - 1}{G_1 G_2} + \frac{NF_4 - 1}{G_1 G_2 G_3} + \dots \quad (5.1.13)$$

It is obvious that the first term will dominate the noise figure calculation if the gains are positive and $\gg 1$.

5.2 Chosen Low Noise Amplifiers

In Section 4.4.1 it was mentioned that the LNA's were chosen during the process of selecting an IF frequency. The available LNA options helped to determine the IF frequency. Simple designs were required to attempt to streamline the design process as much as possible. The LNA's that were chosen for the RF and IF stages are described in the following sections.

5.2.1 RF Amplifier

The signal at the RF stage of the receiver is at 7.5 GHz. This limits the choice in LNA's somewhat since very few off the shelf devices are available at these frequencies. However, a suitable device was found. Needing only a biasing network and appropriate PCB the Avago VMMK-3803 LNA typically provides 18 dB gain with a noise figure of 1.5 dB (this figure is unavoidable since these are not cooled LNA's).

Figure 5.7 shows the biasing circuit needed for the VMMK-3803. There are many modes of operation pertaining to the values of the supply voltages, but it was decided to let $V_{pd} = V_{dd} = 3$ V for simplicity.

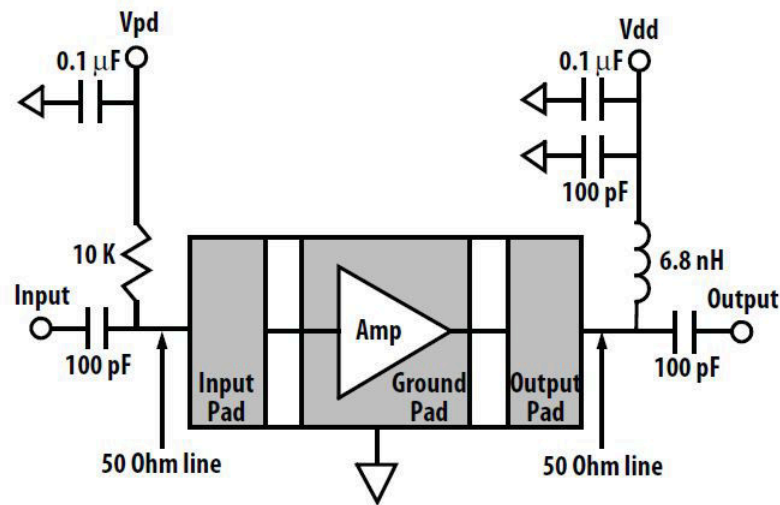


Figure 5.7: VMMK-3803 Biasing Circuit for Normal Mode of Operation [10]

Table 5.1 shows some important parameters of the VMMK-3803 LNA. All values are rated at 7.5 GHz.

Parameter	Value
Supply Voltage	3 V
Max Input Power	15 dBm
Gain	18 dB
Input Return Loss	15 dB
Input Return Loss	9 dB
NF	1.65 dB
NF_{min}	1.5 dB
Output 1dB Compression Point	6 dB
Input IP3	2 dB

Table 5.1: VMMK-3803 RF Low Noise Amplifier Characteristics

5.2.2 IF Amplifier

There were many more options for the IF amplifier since the frequency of operation is lower and the noise figure is not as important as for the RF LNA. Upon review of all the available options, an amplifier from Analog Devices was chosen. It has a typical gain of 20 dB and a typical noise figure of 3.3 dB.

Figure 5.8 shows the biasing circuit needed for the ADL5602.

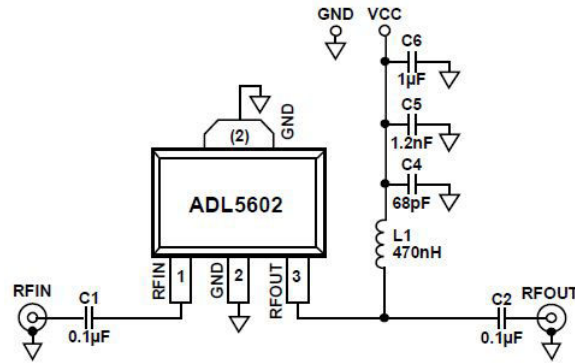


Figure 5.8: ADL5602 Biasing Circuit for Normal Mode of Operation [11]

Table 5.2 shows some important parameters of the ADL5602 amplifier. All values are rated at 3.5 GHz.

Parameter	Value
Supply Voltage	5 V
Max Input Power	16 dBm
Gain	19.3 dB
NF	3.8 dB
Output 1dB Compression Point	17.4 dB
Output IP3	31.5 dB

Table 5.2: ADL5602 IF Low Noise Amplifier Characteristics

5.3 Cascaded Low Noise Amplifiers

To provide more gain in the receiver, it was decided to use cascaded LNA's. Section 5.1.4 highlighted the fact that the noise figure of cascaded components is dominated by the first component.

5.3.1 RF Amplifier

Equation (5.3.1) is used to determine the noise figure of the cascaded LNA's. The equation requires linear values instead of logarithmic values. The noise figure is

$$NF = NF_1 + \frac{NF_2 - 1}{G_1} \quad (5.3.1)$$

$$NF_{RFdB} = 10 \log \left(1.462 + \frac{1.462 - 1}{63.09} \right) = 1.6711 \text{ dB}. \quad (5.3.2)$$

The noise figure of the cascaded configuration is 0.02 dB higher than the single LNA. Figure 5.9 shows the circuit that was simulated in ADS to gauge whether or not the

cascaded LNA's provided a noise figure as low as the noise figure calculated. The rest of the biasing circuit was omitted since the S-parameters provided did not require it.

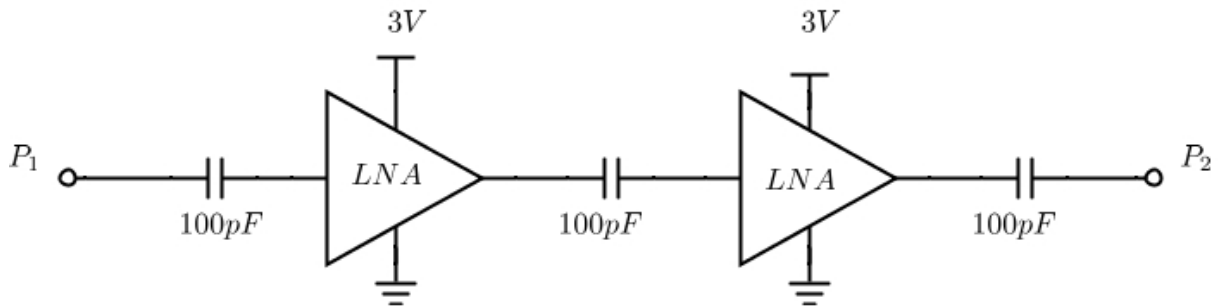


Figure 5.9: Basic RF LNA Cascaded Simulated Circuit

ADS was used to simulate the circuit. The result is shown in Figure 5.10. The gain is as expected and the Γ response is excellent at 7.5 GHz. The noise figure is also low across the entire band. The cascaded circuit is therefore appropriate for use in the proposed receiver.

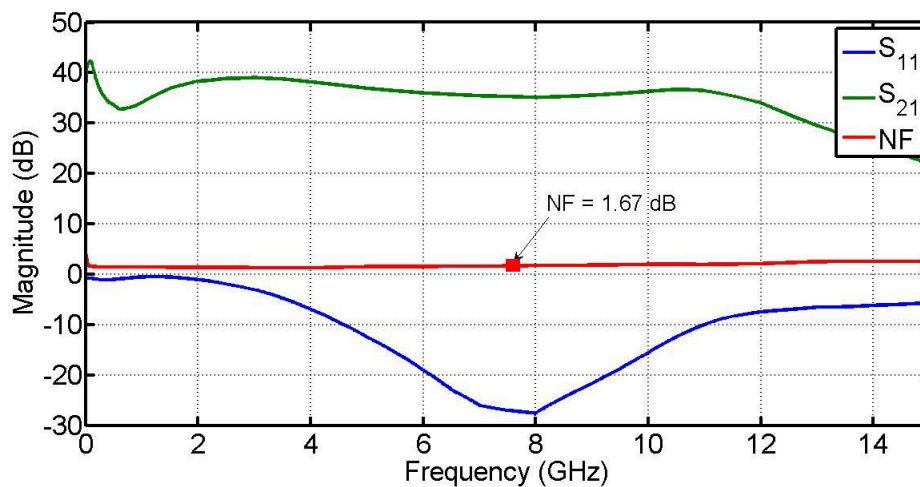


Figure 5.10: RF LNA Cascaded Circuit Simulation in ADS

5.3.2 IF Amplifier

Once again (5.3.1) is used to determine the noise figure of the cascaded LNA's. The equation requires linear values instead of logarithmic values. The noise figure is

$$NF_{IFdB} = 10 \log \left(2.4 + \frac{2.4 - 1}{85.11} \right) = 3.83 \text{ dB}. \quad (5.3.3)$$

The noise figure of the cascaded configuration is 0.03 dB higher than the single LNA. Figure 5.11 shows the circuit that was simulated in ADS to gauge whether or not the cascaded LNA's performed as expected. This is, however, only done for completeness.

Because of the IF LNA's position in the receiver system, any noise that the IF LNA contributes will have minimal effect on receiver performance.

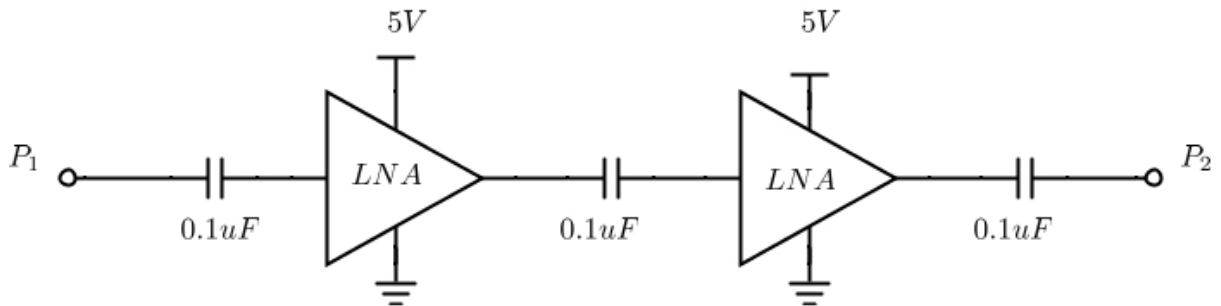


Figure 5.11: Basic IF LNA Cascaded Simulated Circuit

ADS was used to simulate the circuit. The result is shown in Figure 5.12. The gain is as expected and while Γ is not well matched to 3.5 GHz, this can be improved by changing the impedance of the input and output tracks that will be added later. There is unfortunately no noise information available for the ADL5602, so no noise simulation could be performed. However, the noise contributions of this amplifier are less important and thus the cascaded circuit is deemed appropriate for use in the proposed receiver.

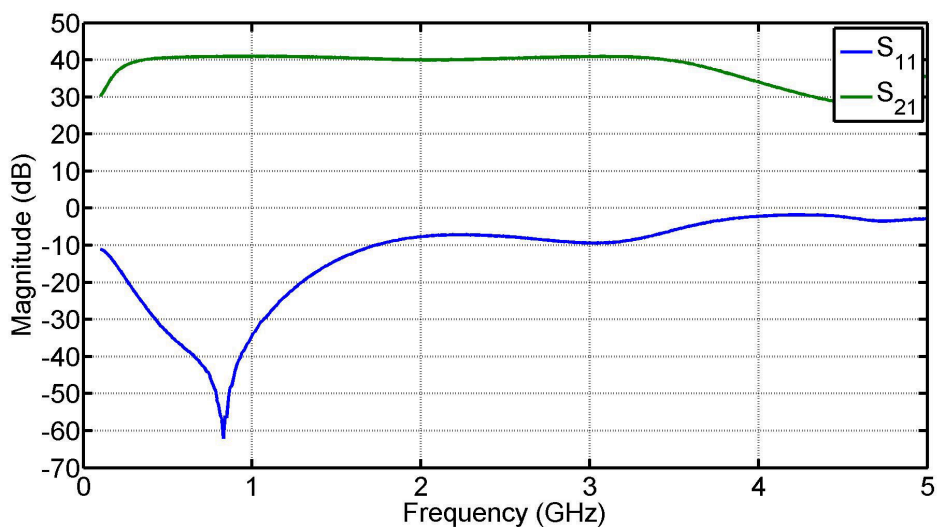


Figure 5.12: IF LNA Cascaded Circuit Simulation in ADS

5.4 Impedance Matching

The first step in the design of the LNA's was to match the input and output impedances of the components. This was done in ADS by simulating the basic chain of the cascaded amplifiers. The input and output impedances were plotted as their real and imaginary parts. The Smith [48] program was then used to transform these impedances to $50\ \Omega$ to ensure minimum noise figure in the case of the RF amplifier, and maximum power

transfer in the case of the IF amplifier. The datasheets for both amplifiers specified $50\ \Omega$ input and output tracks.

5.4.1 RF Amplifier

The RF LNA is required to be matched so that noise figure of the amplifier is minimized. F_{min} occurs very close to $50\ \Omega$ so a decision was taken to match the LNA to $50\ \Omega$. The datasheet also specifies the input and output impedance as $50\ \Omega$. TXLine 2003 [49] was then used to find the dimensions of input and output tracks of $50\ \Omega$. These dimensions were applied in ADS to the circuit shown in Figure 5.9. Ports P_1 and P_2 are $50\ \Omega$ ports. The substrate parameters are those of the Rogers RO4003C board.

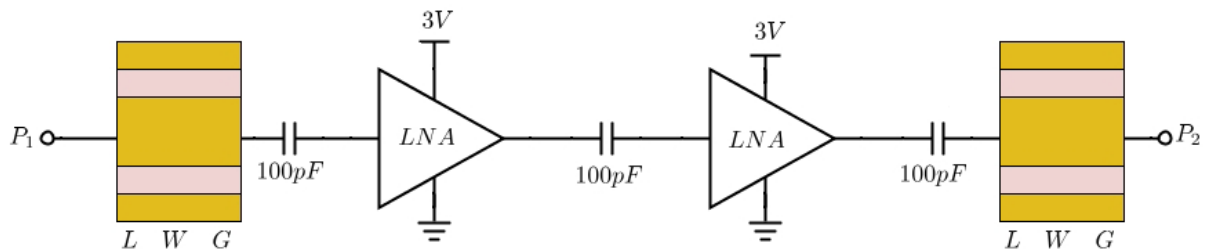


Figure 5.13: RF Cascaded Circuit With Simulated Input and Output Coplanar Waveguides

The length and width of the tracks were slightly tuned in ADS. The results are shown in Figure 5.14. The gain, return loss and noise figure are all acceptable.

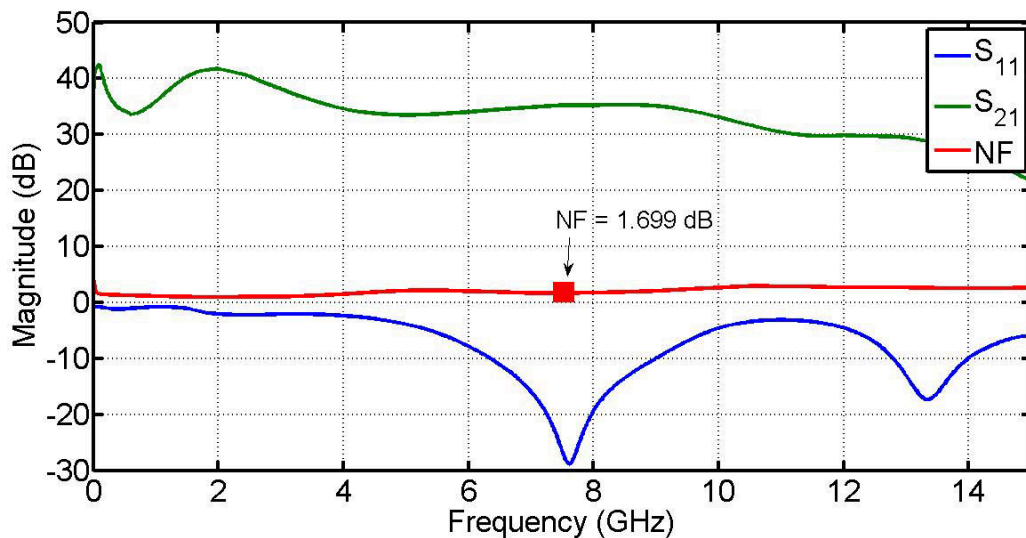


Figure 5.14: RF LNA Results with Tuned Coplanar Waveguides

5.4.2 IF Amplifier

Since this amplifier does not add a significant amount of noise to the system the LNA would simply be matched to $50\ \Omega$. Once again TXLine was used. Figure 5.15 shows the circuit that was simulated in ADS.

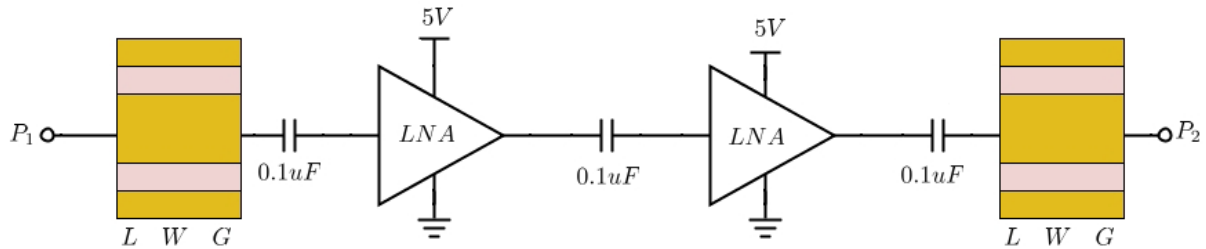


Figure 5.15: IF Cascaded Circuit With Simulated Input and Output Coplanar Waveguides

Once again the tracks were slightly tuned in ADS. Figure 5.16 shows these results which are acceptable.

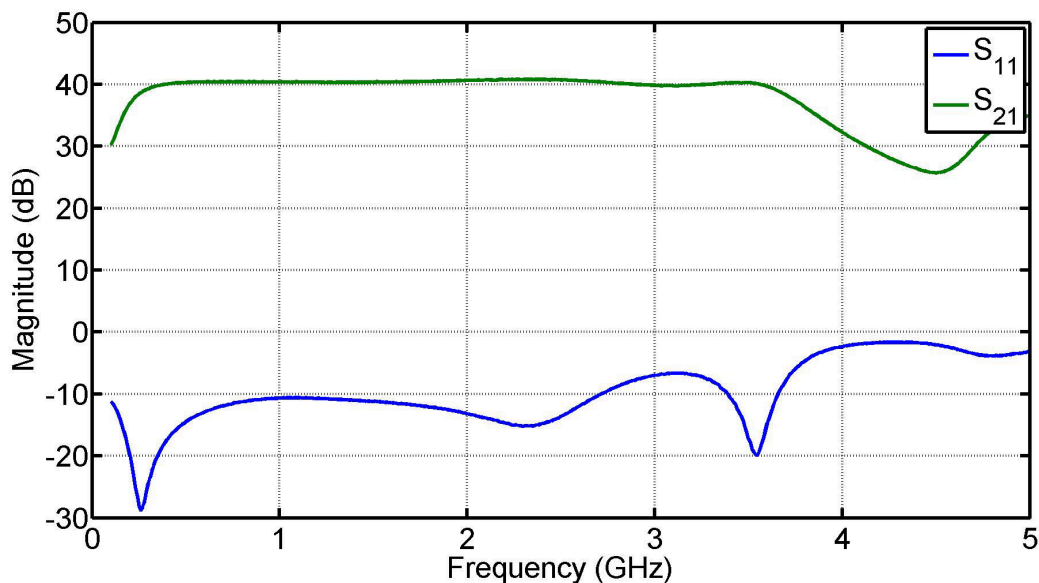


Figure 5.16: IF LNA Matched and Tuned Coplanar Waveguides

5.5 ADS PCB Layout

The next step in the design process was to design the PCB layouts for the LNA's. Many software packages are able to do this, but ADS allows an option to simulate the physical layout. The simulation includes many ports which allow devices to be added to the simulated PCB. Essentially the effect of the PCB on the rest of the LNA circuit is brought into account. The PCB layouts as well as the final LNA circuits can be found in Appendix E.

5.5.1 RF Amplifier

Figure 5.17 shows the RF LNA simulated with its PCB layout. The gain is slightly less than it is in Figure 5.14 but Γ is well matched at 7.5 GHz and the noise figure is low across the band.

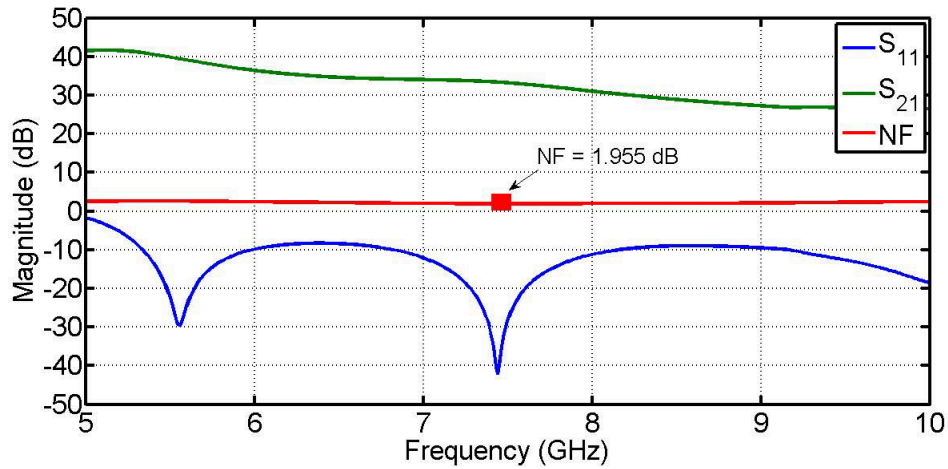


Figure 5.17: RF LNA Simulated with PCB Layout in ADS

5.5.2 IF Amplifier

Figure 5.18 shows the IF LNA simulated with its PCB layout. Once again the gain is slightly less than the previous simulation in Figure 5.16. It proved challenging to tune the input and output tracks of the PCB layout to obtain a match for Γ . It is not as well matched as in Figure 5.16 but the results in Figure 5.18 were the best obtained at 3.5 GHz.

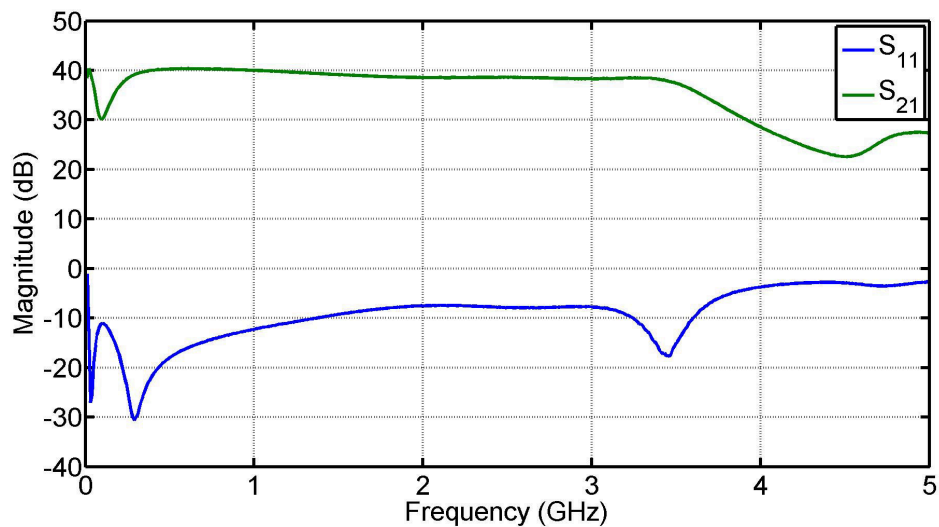


Figure 5.18: IF LNA Simulated with PCB Layout in ADS

5.6 Manufacture

It was decided to use the local PCB printing company TraX to print the PCB's. The substrate that was used in all PCB simulations is Rogers RO4003C with a height of 0.5 mm. This is a high quality substrate commonly used in microwave applications and a one that TraX has in stock. This substrate was also mentioned in both LNA datasheets as the preferred substrate for the biasing circuit. Before the PCB's could be fabricated the designs needed to meet all of TraX's specifications. See Appendix D for a brief description of TraX specifications.

The LNA's are to be placed inside a metallic enclosure to ensure a solid grounding for the LNA's as well to provide protection from the environment. The input and output of the metallic enclosures are standard female SMA connectors. As is done in Section 6.2.3 for the low-pass filter the enclosures had to be checked for resonances. The substrate as well as the input and output tracks were added to the enclosure. This was done in CST.

Figure 5.19 shows the resonance check of the enclosure to be used for the RF LNA. There is some activity just below 7 GHz but none in the 7 - 8 GHz range. The enclosure can therefore be used.

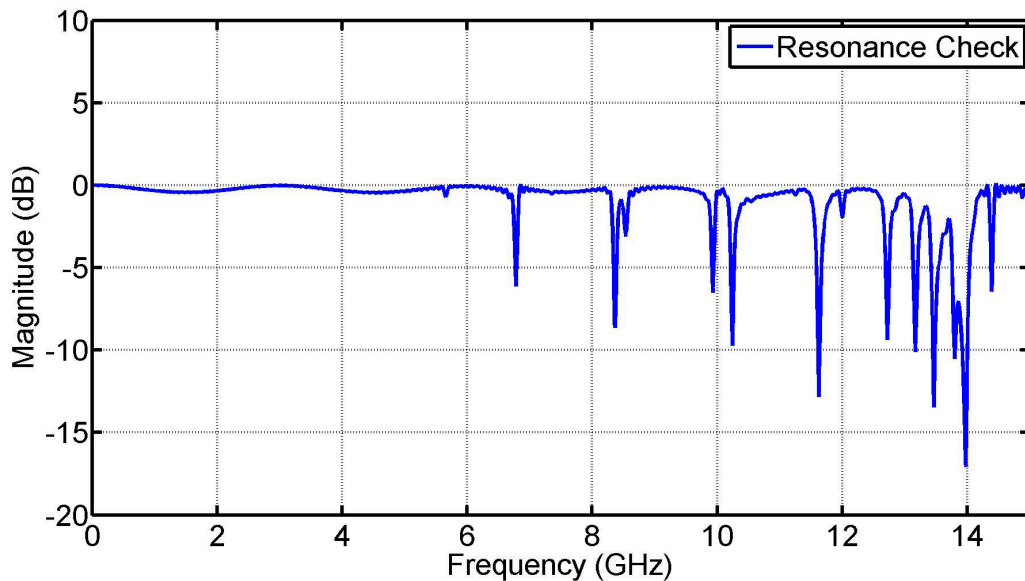


Figure 5.19: S_{21} of Metallic Enclosure - RF LNA Resonance Check in CST

Figure 5.20 shows the resonance check of the enclosure to be used for the IF LNA. There is no activity from DC up to 7 GHz. The enclosure can be used.

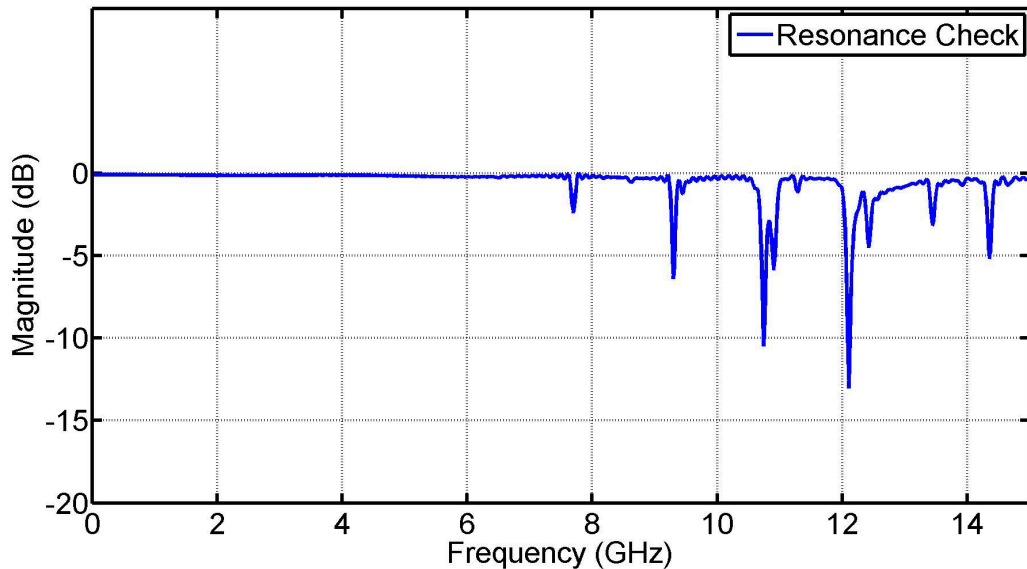


Figure 5.20: S_{21} of Metallic Enclosure - IF LNA Resonance Check in CST

The enclosures were manufactured at the E&E Department workshop and all the components were placed on the PCB's. Voltage regulators were used for the supply voltages of the LNA's.

5.7 Measurements

The Low Noise Amplifiers were measured at the E&E Department on the PNA-X Network Analyser. Initial measurements provided undesirable results. There was no gain for the IF LNA and no response at all for the RF LNA. An attempt was then made to isolate and repair the issues.

5.7.1 RF Amplifier

The RF LNA did not have the expected response. The lid of the metallic enclosure was removed to test if resonances were a problem. It was found that they were not. Upon investigation of the biasing circuit, it was found that the PCB track providing the supply voltages was shorted to ground. It was suspected that the first of the cascaded LNA's was faulty. The LNA component was replaced but the short remained. The voltage regulator was then replaced and the short circuit was no more. The result was an undesired S-parameter response with no gain, indicating that there was still an issue.

It was decided to test the DC characteristics of the circuit. It was thought that the voltage regulator might not supply enough current for both the LNA's and so 3 V was applied directly to the supply voltage track and to the input of the regulator to compare how much current is drawn in both situations. There was no difference in the amount of current drawn; 40 mA was expected and notable current could be measured. Other DC measurements showed expected results.

The output of the LNA was then displayed on a spectrum analyser without any RF input. The results showed that the LNA was oscillating. Before an accurate measurement of the oscillations could be taken, the oscillations disappeared. It can be concluded that the first LNA component is once again faulty. It is suspected that there is not enough isolation between the two cascaded LNA components. The undesired feedback causes the first LNA to be unstable and it eventually malfunctions. Thus there was no S-parameter response that could be measured after the malfunction of the LNA.

5.7.2 IF Amplifier

Figure 5.21 shows the measured results of the IF LNA. While S_{11} looks somewhat like simulated results with a value of -5 dB at the frequency of operation, there is no gain. S_{21} is below -20 dB across the band.

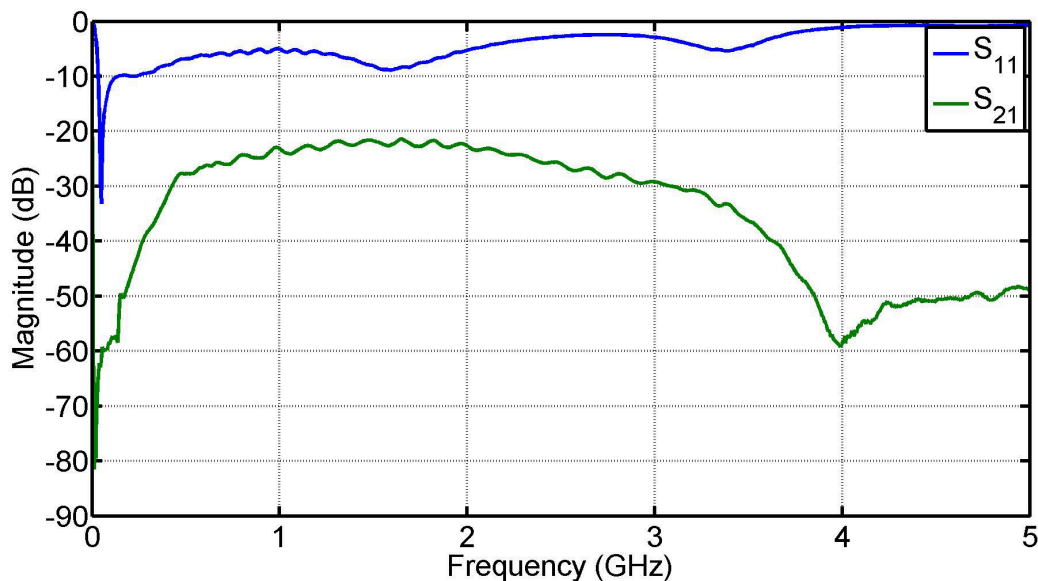


Figure 5.21: Measured Results of IF Low Noise Amplifier

Once again, the lid of the enclosure was removed and DC tests were performed. No short circuits were found and the same amount of current was drawn by using the regulator or directly applying the supply voltage; 178 mA is expected and 60 mA was drawn. Once again, the DC voltage at the input of the first LNA component was higher than it was expected to be. It was measured as 3 V. Since there is no supply voltage track on that side of the component it implies that once again isolation of the cascaded components is a problem. The first LNA component was replaced and measured on the spectrum analyser without an input. No oscillations were found, but the same DC problem persisted.

Ideally the next step would be to manufacture single LNA's instead of cascaded LNA's to determine if the isolation is indeed the issue. However, the LNA's completed manufacturing near the end of the project and it would not be feasible to design new PCB layouts and manufacture new enclosures due to time constraints. Unfortunately this means that a full scale measurement of the Sun cannot be performed. Chapter 9 describes the measurements that were taken instead.

5.8 Conclusion

This Chapter started by introducing the concept of noise in receiver systems. The noise figure of a device was defined and it was made clear that the earlier a device is in the receiver, the more that device contributed to the noise added in the receiver. This made it possible to consider cascaded LNA's.

The design of the RF and IF low noise amplifiers was described. This started by checking that the cascaded design did not contribute significantly to the noise figure. It was found that the cascaded designs added significant gain and added almost no additional noise. It was decided to use the cascaded designs.

The input and output tracks were then added in an ADS simulation and tuned until desirable results were obtained. The PCB tracks for the LNA's were then designed in ADS because ADS allows a simulation of the physical PCB layout. The layout simulation was then combined with the LNA's as well as models for the passive components used. The PCB tracks were edited until acceptable results were found.

Resonance checks were performed on the metallic enclosures to be used for the LNA's. The PCB's were fabricated at TraX and the enclosures were manufactured at the E&E Department.

The measurement of the LNA's revealed a major issue with the cascaded biasing circuits. Even though simulations in ADS showed acceptable results, the isolation between the two components was poor. The LNA's could not be used for amplification in the proposed receiver.

Chapter 6

Filters

Various filters are required in the proposed receiver architecture. Figure 4.13 shows two band-pass filters, one each in the RF and IF stages of the receiver. A low-pass filter is also shown in the final stage of the receiver.

6.1 Role of Filters in the Receiver Chain

6.1.1 Low-Pass Filter

Even if the IF band-pass filter has an excellent response, LO_1 leakage will still exist because of the amount of power needed for the mixer (10 dBm). This means that the leaked signal will also be down-converted by the second mixer. The main objective of the LPF is to eliminate this mixed down leakage at 875 MHz.

The secondary objective for the LPF is to eliminate all the intermodulation products that are common in a super-heterodyne system. These needs can be justified by Figures 4.14 and 4.15.

6.1.2 RF Band-Pass Filter

The main objective of the RF filter is to set the bandwidth of the incoming signal and thus eliminating any possible RFI. As noted in Chapter 2 the frequency of interest is 7.5 GHz. A design bandwidth of 800 MHz was chosen. This ensured a wide enough band for significant power expected from the sun (around -80 dBm) as well as narrow enough to eliminate any significant RFI. Bandwidth can also be limited by the digitizers of the back-end ROACH board.

6.1.3 IF Band-Pass Filter

The IF filter has primary objectives which can be justified by Figure 4.10. Firstly, as identified in Section 4.1.3, the image frequency of the second down-converted stage in a super-heterodyne receiver is usually close to the passband of the IF stage. The IF filter needs a sharp cut-off to ensure that the image frequency stays well outside the passband.

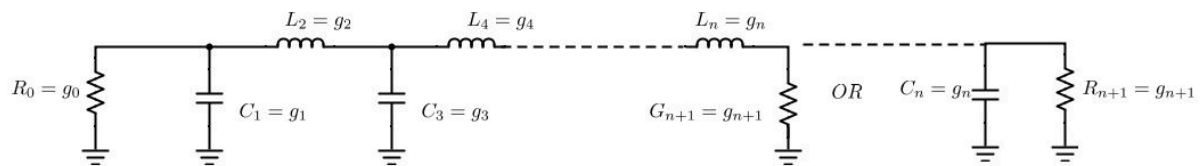
Secondly, the first local oscillator has what is known as LO leakage. The power used for LO_1 leaks through the IF output of the mixer and is present in the receiver system. The

IF filter must therefore have a sharp cut-off to ensure that this leakage is also outside the passband. Because of all this a bandwidth of 500 MHz was chosen.

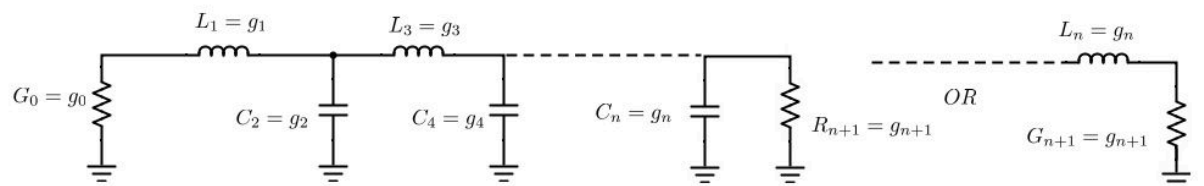
6.2 Low-Pass Filter

6.2.1 Low-Pass Filter Prototype

The Chebyshev low-pass filter design is known to have a sharper cut-off than the equivalent Butterworth design and is used for all filters in this project. The starting point for all designs described in this Chapter is the LC-ladder prototype seen in Figure 6.1a and 6.1b.



(a) LC Ladder - Capacitor First



(b) LC Ladder - Inductor First

Figure 6.1: Low-Pass Prototype Filters

To calculate the values of the passive elements

$$C'_k = \frac{g_k}{w_c} \quad (6.2.1)$$

$$L'_k = \frac{g_k}{w_c} \quad (6.2.2)$$

can be used. Equations (6.2.1) and (6.2.2) provide values for the impedance normalised filter prototype.

These equations require $g_0 \dots g_{n+1}$, also known as the Chebyshev Coefficients. Many tables are available for a quick look-up, but it was decided to calculate the values explicitly. Equations (6.2.3) to (6.2.8) were presented by Susan Maas [50] in her thesis and were used to calculate the necessary coefficients for both the LPF design as well as the BPF design. To calculate these coefficients \mathbf{a} and \mathbf{b} coefficients were also calculated.

For a $g_0 = 1$, the following equations are valid.

Calculation of Chebyshev Coefficients

$$g_1 = \frac{2a_1}{\sinh \left\{ \frac{\ln [\coth (\frac{L_{ar}}{17.37})]}{2n} \right\}} \quad (6.2.3)$$

$$g_k = \frac{4a_{k-1}a_k}{b_{k-1}g_{k-1}}, \quad k = 2, 3, \dots n \quad (6.2.4)$$

$$g_{n+1} = \coth^2 \left\{ \frac{\ln [\coth (\frac{L_{ar}}{17.37})]}{4} \right\}, \quad n = \text{even} \quad (6.2.5)$$

$$g_{n+1} = 1, \quad n = \text{odd} \quad (6.2.6)$$

a and b Coefficients

$$a_k = \sin \left\{ \frac{(2k-1)\pi}{2n} \right\}, \quad k = 1, 2, \dots n \quad (6.2.7)$$

$$b_k = \sinh^2 \left\{ \frac{\ln [\coth (\frac{L_{ar}}{17.37})]}{2n} \right\} + \sin^2 \left(\frac{k\pi}{n} \right), \quad k = 1, 2, \dots n \quad (6.2.8)$$

where

L_{ar} = passband ripple, [dB]

n = number of components in filter

k = component number

These equations were implemented in MATLAB and compared against known tabular values. The values corresponded exactly.

6.2.2 Low-Pass Filter Design

As described in Section 4.5 a LPF is needed to allow only the desired signal through to the KAT-7 ADC. The Chebyshev design is chosen for its sharp cut-off due to the signals shown in Figure 4.10. The approach to calculate the prototype coefficients discussed in the previous Section is followed.

An additional step is added to allow for impedance scaling of the impedance normalised values.

$$C_k = \frac{C'_k}{R_0} \quad (6.2.9)$$

$$L_k = L'_k R_0 \quad (6.2.10)$$

where $R_0 = 50 \Omega$.

From Figure 4.10 a cut-off of 750 MHz was chosen and the initial design parameters were set. The pass-band ripple was chosen to be low in an attempt to obtain a flat S_{21} .

Parameter	Value	Description
L_{ar}	0.001 dB	Pass-band Ripple
R_0	50 Ω	Input Impedance
R_{n+1}	50 Ω	Load Impedance
n	11	Number of Components
f	750 MHz	Cut-off Frequency

Table 6.1: Design Parameters for LPF

This resulted in ideal values for $C_1, L_1 \dots C_3, L_3$. The circuit shown in Figure 6.2 was simulated in ADS using ideal circuit components. The resulting S-parameters can be seen in Figure 6.3. The parameter values can be seen in Appendix E in Table E.1.

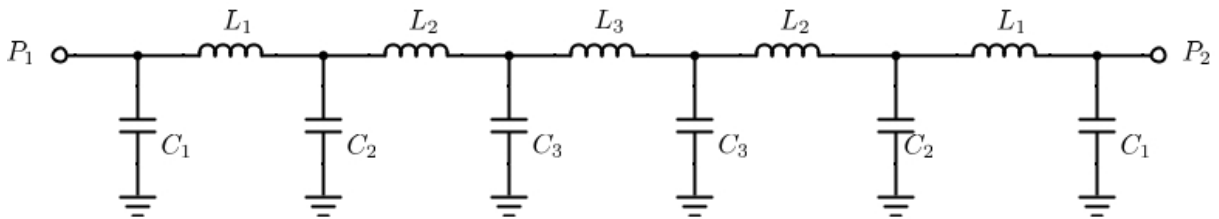


Figure 6.2: Ideal Simulated LPF Circuit

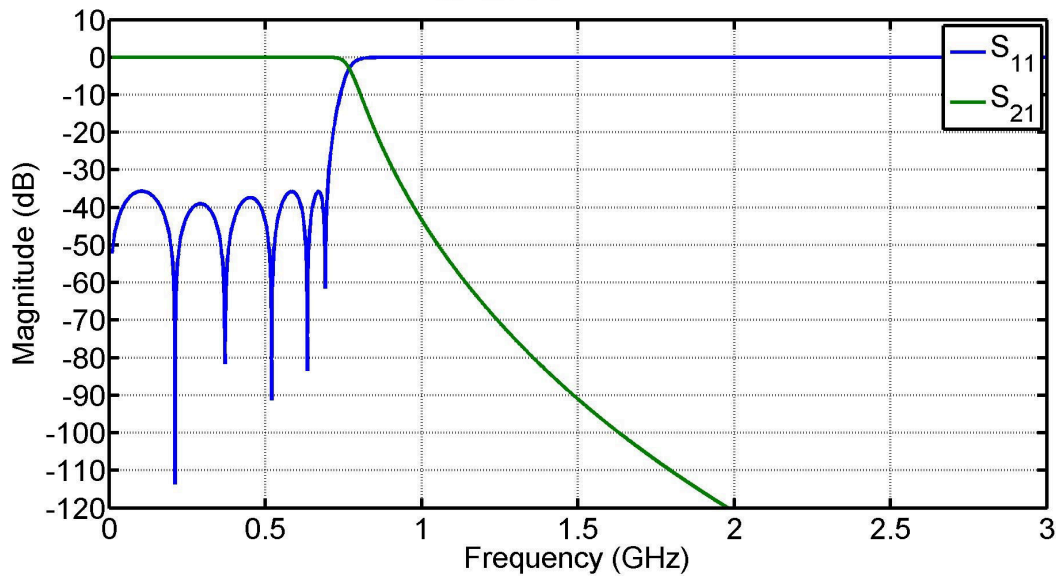


Figure 6.3: Ideal LPF Response Simulated in ADS

This response is exactly what is required. The next step was to simulate the same circuit with models of real passive components (lumped element) that will be used. Unfortunately, not all calculated values exist as real components or as models in ADS. Slight compromises had to be made in terms of element values for components applicable to the desired frequency range. The compromised component values can be seen in Table E.1.

The input and output tracks were also added here to see the effect of a physical PCB track line. The impedance of the line was designed to be $50\ \Omega$. The dimensions were found using TXLine, which is a transmission line calculator. Tuning of the dimensions were then performed in ADS. Figure 6.4 shows this set-up. L , W , and G in the Figure are the length, width and gap dimensions of the input and output tracks.

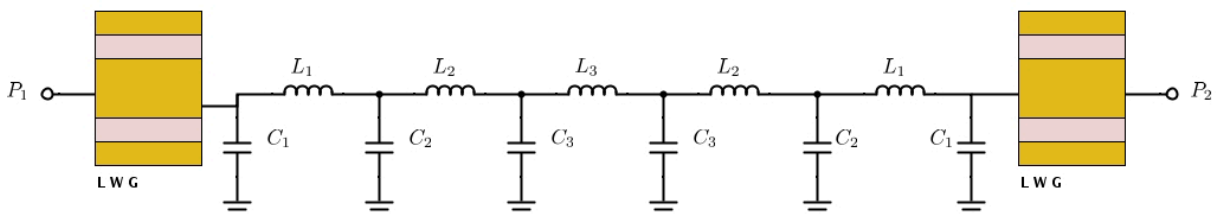


Figure 6.4: Compromised and Matched Simulated LPF

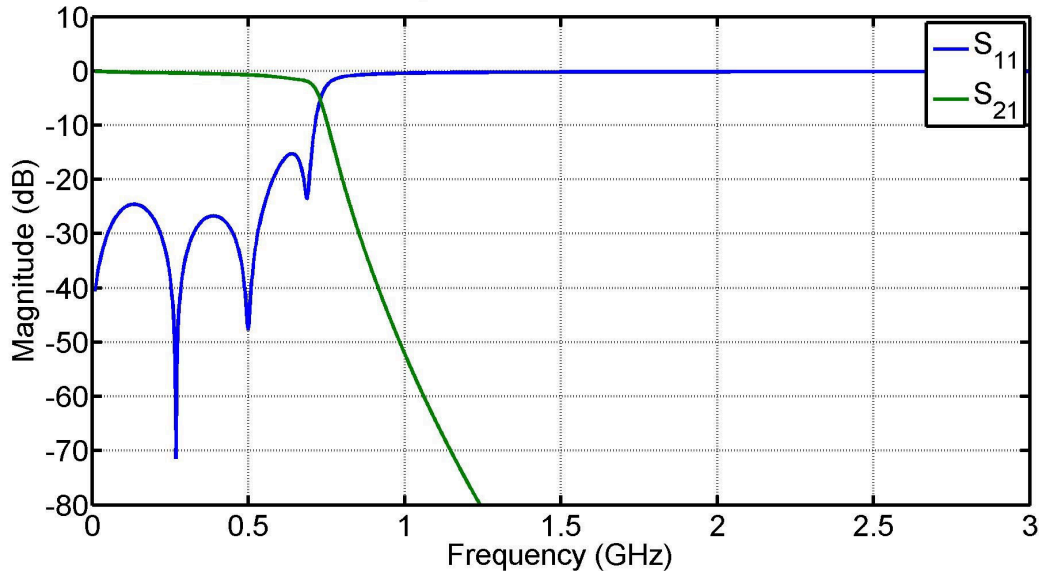


Figure 6.5: LPF Response with Non-Ideal Components

As can be seen in Figure 6.5 the compromised component values had a large effect on the desired response. This could be because of the low-pass band ripple specification. The compromised response does however still meet all requirements and is deemed as acceptable.

ADS was then used to design the PCB board for the filter. The input and output connectors are the same 50Ω co-planar SMA's mentioned in Chapter 5. This restricted the widths of the input and output tracks as well as the gaps between the tracks and the adjacent ground plane. The lengths of the tracks were first calculated using TXLine and then tuned so that the filter behaved as required.

The next step is to design the board layout. This layout can be seen in Appendix E. The same substrate that was used for the LNA's was used here. The layout (without components) was simulated using the ADS EM solver to account for any losses that may occur. The modelled circuit elements were then added to the simulation results and simulated again. This resulted in the S-parameters shown in Figure 6.6.

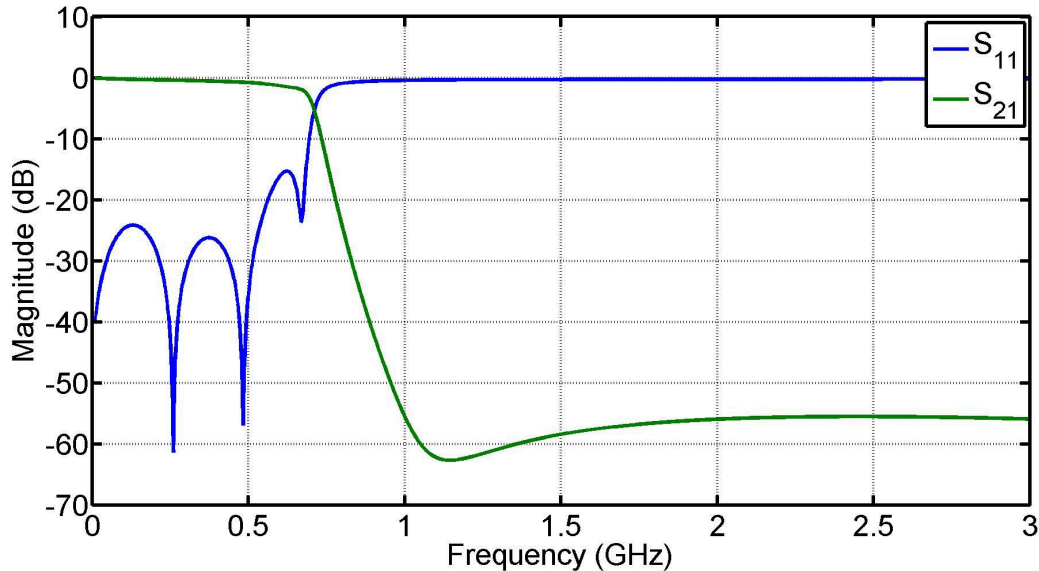


Figure 6.6: Final Simulated LPF Response With PCB

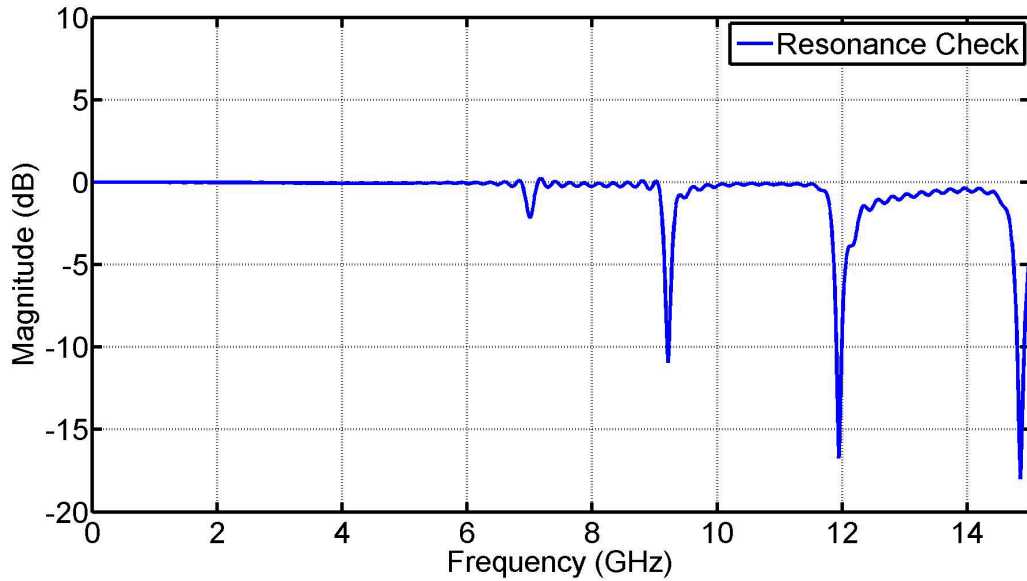
This final results meets all the requirements for the LPF. The next step is the manufacture of the LPF PCB and metallic box.

6.2.3 Manufacture

The PCB design is shown as Figure E.1 in Appendix E. Once the design was complete it was to be manufactured by TraX. It was ensured that the design met all TraX specifications.

The next part of the process is to manufacture the metallic enclosure of the LPF PCB. This was done at the E&E Department workshop with the help of AutoDesk Inventor designs. As with the LNA's, 2-hole panel mount flange SMA's were used to couple into and out of the enclosure. Before the enclosure can be manufactured however a resonance check must be performed.

In metallic enclosures energy could be coupled in at a resonant frequency, meaning that that energy is never coupled out. A metallic enclosure was created in CST with a coaxial input and output, as well as the substrate in question. Figure 6.7 shows the resonant frequencies of the enclosure. There are no resonances near the band of operation so therefore the enclosure need not be changed and is acceptable.

Figure 6.7: LPF S_{21} Metallic Enclosure Resonance Check

6.2.4 Measurements

The LPF was measured on the same PNA-X network analyser used for the antenna S-parameter measurements. A two port measurement was performed. The resulting S-parameters can be seen in Figure 6.8. While S_{11} does not correspond exactly to the simulated LPF the passband is exactly what is required. While the simulated results had most of the passband below -20 dB, the measured results has most of the passband below -15 dB. Considering that this band of operation is notorious for being difficult to work with using lumped element filters, this is an acceptable result. The measured cut-off frequency is just below 700 MHz.

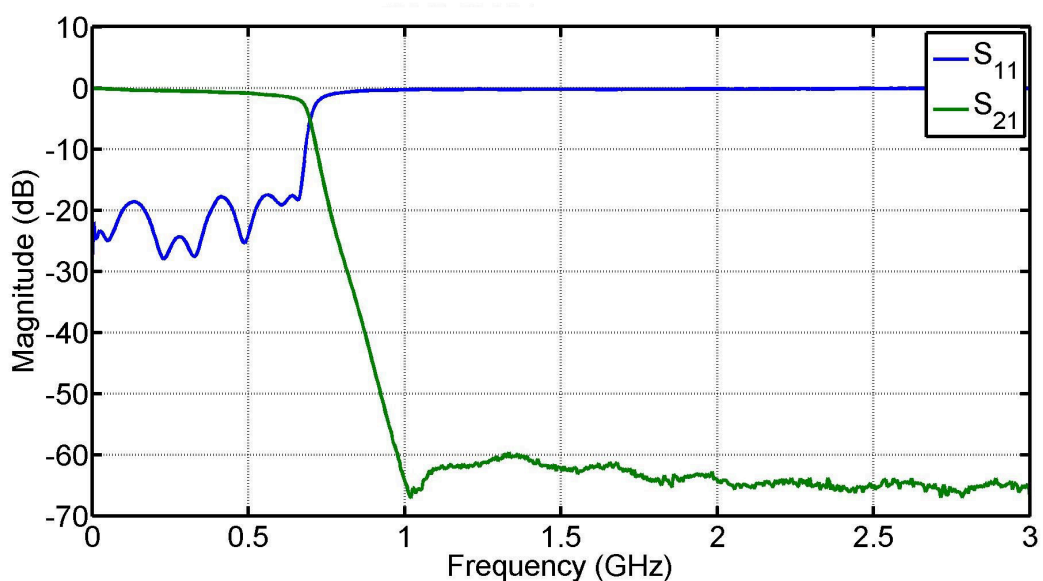


Figure 6.8: Measurement of LPF on Network Analyser

6.3 Band-Pass Filters

6.3.1 Band-Pass Transformation

A BPF transformation from a LPF prototype can be performed by substituting (6.3.1) [44] into w_c of (6.2.1) and (6.2.2). This is achieved by using

$$\frac{1}{\Delta} \left(\frac{w}{w_0} - \frac{w_0}{w} \right) \longrightarrow w_c \quad (6.3.1)$$

where Δ is the fractional bandwidth

$$\Delta = \frac{w_2 - w_1}{w_0} \quad (6.3.2)$$

and w_0 is the geometric mean,

$$w_0 = \sqrt{w_1 w_2} \quad (6.3.3)$$

of the w_1 and w_2 which are the edges of the passband.

This mapping allows a new set of equations for the lumped element prototype shown here as

$$\begin{aligned} L_k &\longrightarrow L'_k = \frac{L_k}{\Delta w_0} \\ &\longrightarrow C'_k = \frac{\Delta}{w_0 L_k} \end{aligned} \quad (6.3.4)$$

$$\begin{aligned} C_k &\longrightarrow L'_k = \frac{\Delta}{w_0 C_k} \\ &\longrightarrow C'_k = \frac{C_k}{\Delta w_0}. \end{aligned} \quad (6.3.5)$$

These equations mean that in Figure 6.1a, all capacitors will be replaced by series LC resonators while all inductors will be replaced by shunt LC resonators. While this is a valid method for obtaining a BPF, the resulting component values are often difficult to realise in microwave structures [50]. This is typical for such high frequency applications when it comes to LC circuits. The main issue is the low Q of the inductors. LC circuits can however be avoided by using coupled resonators.

6.3.2 Coupled Resonators

Coupled resonators consist of either shunt or series resonators that are coupled to each other through the use of admittance or impedance inverters. Admittance or impedance inverters are used in coupled resonators to convert the LPF prototype to a equivalent low-pass design that only uses one type of reactive element. This equivalent design can then be transformed to a BPF design using the appropriate transformation. The lumped elements resonators can then be replaced by any type of appropriate resonator.

Impedance inverters are represented by $K_{n,n+1}$ and each inverter can be replaced by an equivalent T-network of capacitors or a quarter-wavelength transmission line with a characteristics impedance of $Z_0 = K$ as shown in Figure 6.9.

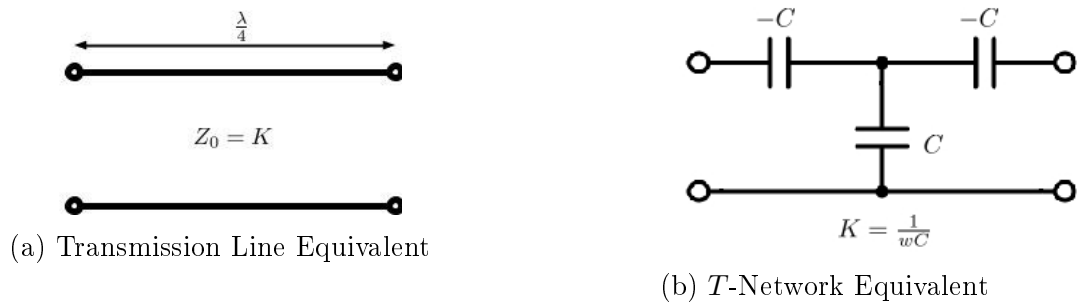


Figure 6.9: K -Inverter Equivalents

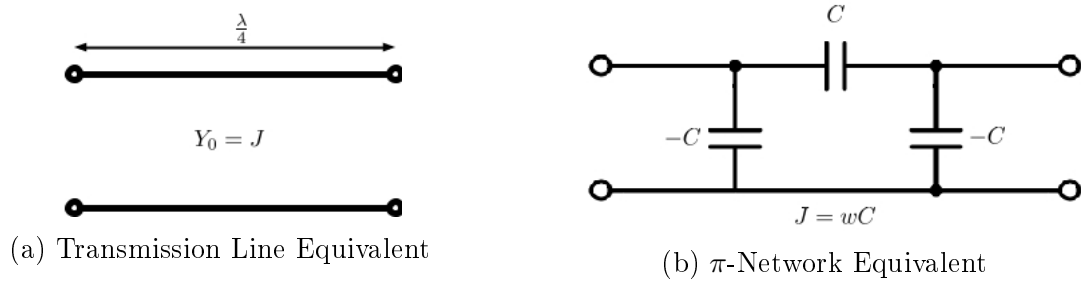
The input impedance of the T -Network with a load Z_L can be found as follows:

$$Z_{in} = (-Z_C + Z_L) // Z_C - Z_C \quad (6.3.6)$$

where $Z_C = \frac{1}{j\omega C}$, so that the impedance becomes the known input impedance of a equivalent transmission line which is

$$Z_{in} = \frac{K^2}{Z_L}. \quad (6.3.7)$$

Admittance inverters are represented by $J_{n,n+1}$ and each inverter can be replaced by an equivalent π -network of capacitors or a quarter-wavelength transmission line with a characteristic admittance of $Y_0 = J$ as shown in Figure 6.10.


 Figure 6.10: J -Inverter Equivalents

A similar approach to (6.3.6) can be used to determine the input admittance of the π -Network with a load admittance of Y_L . It is the same as the known admittance for the transmission line equivalent which is

$$Y_{in} = \frac{J^2}{Y_L}. \quad (6.3.8)$$

Considering shunt resonators, adding admittance inverters to Figure 6.1a and applying the appropriate transformations the circuit in Figure 6.11 can be used to represent a coupled BPF prototype.

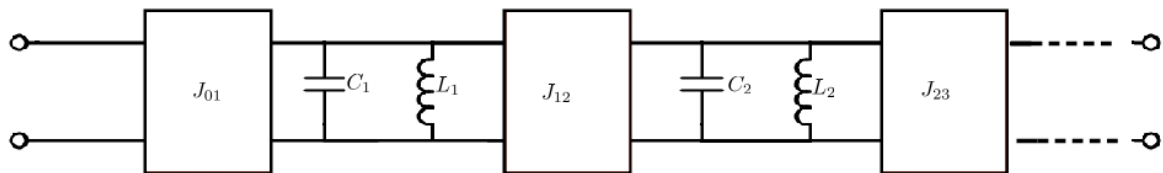


Figure 6.11: BPF Prototype

By inserting the equivalent π model the circuit can then be simplified into the circuit shown in Figure 6.12. The $C_{n,n+1}$ capacitors are known as the coupling capacitances.

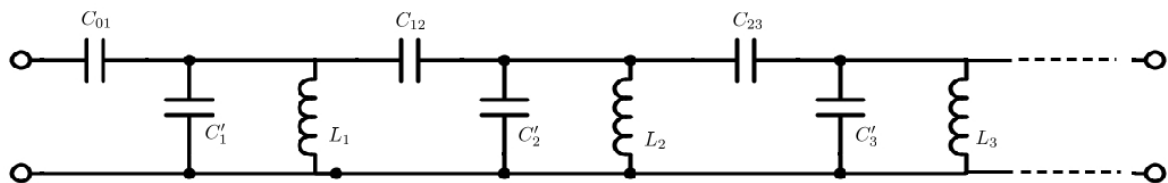


Figure 6.12: BPF Equivalent Prototype

Since some capacitance has now been added to the resonator capacitor a change in capacitance for each resonator can be defined as

$$\Delta C_n = -C_{n-1,n} - C_{n,n+1}. \quad (6.3.9)$$

Finally the LC resonators can be replaced by transmission line equivalent stubs. Figure 6.13 represents a coupled BPF prototype. Each resonator is coupled to neighbouring resonators through some kind of capacitance.

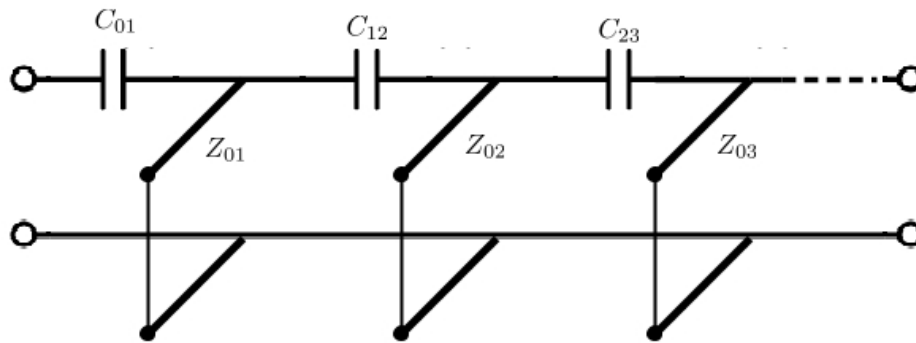


Figure 6.13: BPF Coupled Resonator

It is important to note that the resonant frequency of each stub has changed slightly and is no longer w_c . The capacitance value of each resonator has been changed by some capacitance as defined by (6.3.9). The change in capacitance is negative for shunt resonators using admittance inverters. This implies that the length of the resonator stubs will be less than $\frac{\lambda}{4}$ at w_c [44].

Section 6.4 describes how these coupling capacitances and admittance values are used to determine the physical dimensions of an inter-digital filter using "*Getsinger's Charts*" [13]. Section 6.4 also describes what an inter-digital filter is.

6.3.3 Quality Factor

The term Q , or Quality Factor, can be used in many applications in a variety of contexts. Some of these include component quality (inductors and capacitors), filter pole quality factor and band-pass filter quality factor.

Essentially the Q factor characterizes the bandwidth of a resonator relative to its resonant frequency, which follows from the fundamental definition of $\frac{\text{energy stored}}{\text{energy lost}}$. A high Q indicates a lower rate of energy loss relative to the stored energy; simply put, any oscillations in the system take longer to die out. Equation (6.3.10) is a general equation for any Q [44], and is defined as

$$Q = 2\pi \frac{\text{maximum energy stored during cycle}}{\text{average energy dissipated per cycle}}. \quad (6.3.10)$$

For resonant circuits, the Q is a measure of loss. These losses may be a result of conductor losses, dielectric losses or radiation losses. Any external circuitry added to the resonator, such as a network analyser, may introduce additional losses.

Because of this external circuitry lowering the Q of the resonator, three different Q 's have been defined, Q_U , Q_E and Q_L . Q_U is the unloaded Q , the quality factor of just the resonator. Q_E is the Q of any external circuitry that is used to measure the Q . Q_L is the Q that can be measured and is referred to as the loaded quality factor. These different Q 's can be related as follows:

$$\frac{1}{Q_L} = \frac{1}{Q_E} + \frac{1}{Q_U} = \frac{1}{Q_U} \left(1 + \frac{Q_U}{Q_E} \right) = \frac{1}{Q_U} (1 + k) \quad (6.3.11)$$

$$Q_U = (1 + k)Q_L \quad (6.3.12)$$

where $k = \frac{Q_U}{Q_E}$ is defined as coupling coefficient between the external circuitry and the resonator. It is the ratio of power dissipated in the external circuitry to the power dissipated in the resonator [51]. When $k = 1$ the power dissipated in the external circuitry and the resonator is the same and the coupling is referred to as critical.

The loaded Q can be estimated from the S_{21} measurements of the resonator,

$$Q_L \approx \frac{f_0}{f_2 - f_1} \quad (6.3.13)$$

where f_1 and f_2 are the frequencies at which half the power is transmitted around centre frequency f_0 .

The coupling coefficient k is related to the insertion loss, IL , by

$$k = \frac{IL}{1 - IL} \quad (6.3.14)$$

$$IL = 10^{\frac{IL_{dB}}{20}}. \quad (6.3.15)$$

The insertion loss is simply the value of S_{21} at the centre frequency.

$$IL_{dB} = S_{21}(f_0)_{dB} \quad (6.3.16)$$

To find the Q_U of a resonant circuit, first an S-parameter measurement is performed. This technique uses the 2-port measurement, but there are other techniques that use only a 1-port measurement. Once the measurement is complete, (6.3.16) is used to find the

insertion loss. This is then used to determine the coupling coefficient k using (6.3.14). The loaded Q is also determined from the S_{21} measurement using (6.3.13). Equation (6.3.12) is then used to determine the unloaded Q .

6.4 Inter-digital Filter

6.4.1 Properties

An inter-digital filter consists of TEM-mode resonators with a length of $\frac{\lambda}{4}$ [50]. Each element is short-circuited on alternating sides while the other end of the element is open-circuited. The input and output connections will be on the same side if the number of resonators is uneven and will be on opposite sides if the number of resonators is even (see Figure 6.22). All the resonators (including input and output couplers) are housed in a metallic box between two parallel ground planes above and below the resonators.

Inter-resonator coupling is achieved by the fringing fields between the adjacent resonators. Each line segment acts as a resonator, the exception being the input and output couplers. They have impedance matching functions [12].

Matthaei lists several advantages of inter-digital filters which are summarized here [12].

- They are compact.
- The second resonant passband is located at 3 times the desired centre frequency of the first passband.
- The form of the filters allows for self-supporting structures which means no dielectrics are needed, and therefore dielectric loss is not an issue.

6.4.2 Two Parallel Unsymmetrical Coupled Lines

This Section explains the existence of the self and mutual capacitances that exists within an inter-digital filter in the case of 2 unsymmetrical resonators. These capacitances are used in conjunction with "*Getsinger's charts*" [13] to determine the widths of the resonators, spacings between them and the height of the ground planes above and below. Section 6.4.3 expands this idea to an array of resonators.

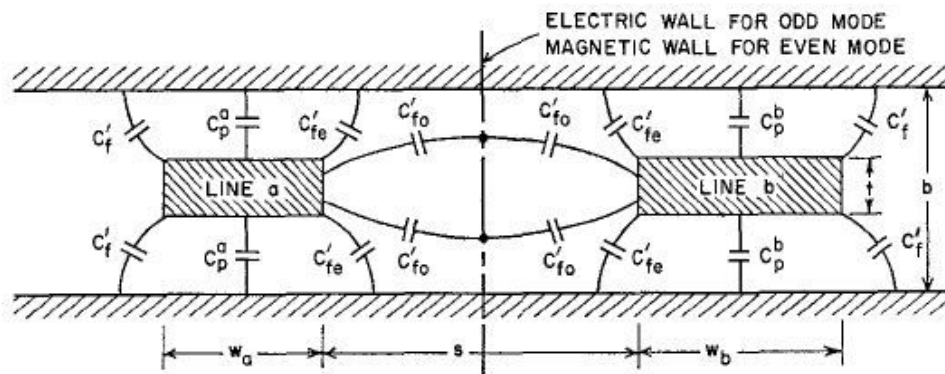


Figure 6.14: Two Unsymmetrical Coupled Lines [12]

Coupled transmission lines can be split using the superposition principle into even and odd modes. Figure 6.15 is the circuit model for per unit length coupled lines [52] and Figure 6.16 represents the even and odd mode cases. Equations (6.4.1) to (6.4.4) can be used to describe the even and odd mode admittances.

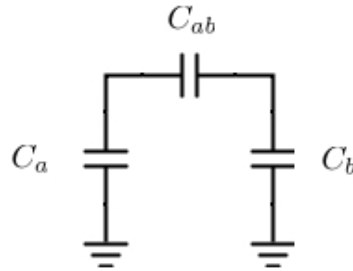


Figure 6.15: Coupled Lines Capacitances

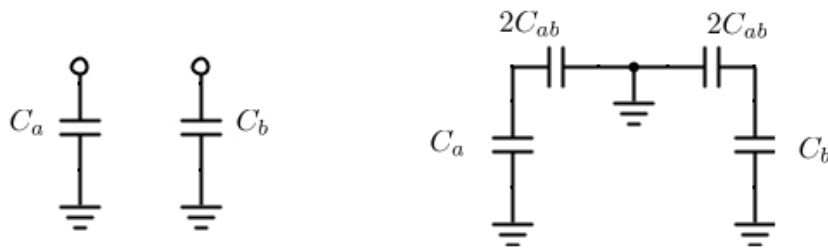


Figure 6.16: Even and Odd Mode Capacitances

For the unsymmetrical case $C_a \neq C_b$. This means that the two lines will have different even and odd mode admittances. These admittances can be expressed [12, 52] as

Even Mode Admittances for Lines a and b

$$Y_{0e}^a = v_e C_a \quad (6.4.1)$$

$$Y_{0e}^b = v_e C_b \quad (6.4.2)$$

Odd Mode Admittances for Lines a and b

$$Y_{0o}^a = v_o [C_a + 2C_{ab}] \quad (6.4.3)$$

$$Y_{0o}^b = v_o [C_b + 2C_{ab}] \quad (6.4.4)$$

where $v_e = v_o = c_0 = 3 \times 10^8$ m/s, v not to be confused with frequency v in Chapter 2.

Equations (6.4.1) to (6.4.4) are needed when using "*Getsinger's charts*".

When dealing with symmetrical parallel coupled lines the impedances of the lines are known to be simply the inverse of the admittances. This is not true for cases of unsymmetrical lines [52]. This ultimately leads to a set of equations for the impedances of the lines [12].

Even Mode Impedances

$$Z_{0e}^a = \frac{C_b + 2C_{ab}}{vF} \quad (6.4.5)$$

$$Z_{0e}^b = \frac{C_a + 2C_{ab}}{vF} \quad (6.4.6)$$

Odd Mode Impedances

$$Z_{0o}^a = \frac{C_b}{vF} \quad (6.4.7)$$

$$Z_{0o}^b = \frac{C_a}{vF} \quad (6.4.8)$$

where

$$F = C_a C_b + C_a C_{ab} + C_b C_{ab}. \quad (6.4.9)$$

Equations (6.4.5) to (6.4.8) are not strictly needed here but are included for completeness.

To use "*Getsinger's charts*" we need to calculate the self and mutual capacitances per unit length. Matthaei presents these formulas for that purpose [12]:

Self Capacitances Per Unit Length

$$\frac{C_a}{\epsilon} = \frac{\eta_0 Y_{0e}^a}{\sqrt{\epsilon_r}} \quad (6.4.10)$$

$$\frac{C_b}{\epsilon} = \frac{\eta_0 Y_{0e}^b}{\sqrt{\epsilon_r}} \quad (6.4.11)$$

Mutual Capacitances Per Unit Length

$$\frac{C_{ab}}{\epsilon} = \frac{\eta_0}{\sqrt{\epsilon_r}} \left(\frac{Y_{0o}^a - Y_{0e}^a}{2} \right) = \frac{\eta_0}{\sqrt{\epsilon_r}} \left(\frac{Y_{0o}^b - Y_{0e}^b}{2} \right) \quad (6.4.12)$$

The mutual capacitances $\frac{C_{ab}}{\epsilon}$ equates to $\frac{\Delta C}{\epsilon}$ as described by Getsinger in his article [13]. Now using this value an appropriate $\frac{t}{b}$ value can be chosen and from that a $\frac{s}{b}$ value can be determined. From this $\frac{C'_{fe}}{\epsilon}$, $\frac{C'_{fo}}{\epsilon}$ and $\frac{C_f}{\epsilon}$ can also be determined. This is illustrated in Figures 6.17, 6.18 and 6.19.

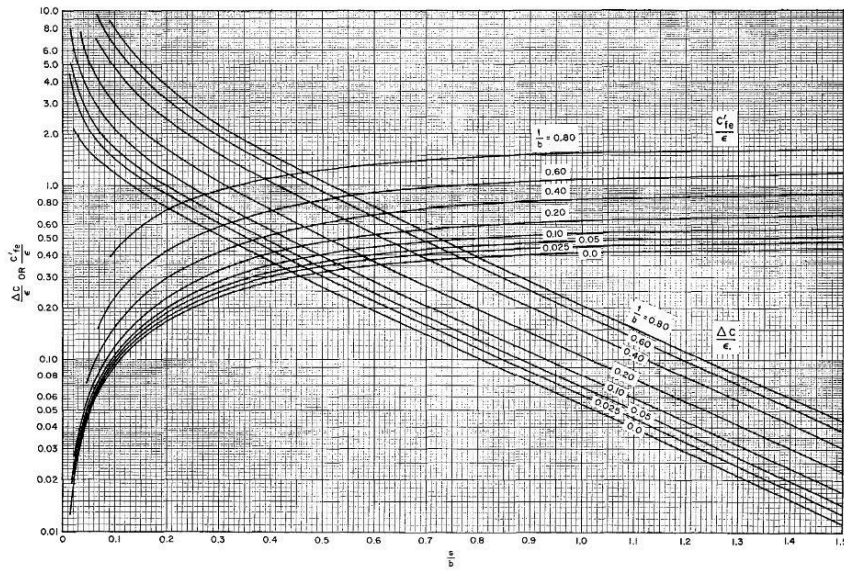


Figure 6.17: Mutual and Even-Mode Fringing Capacitances for Coupled Resonator Bars [13]

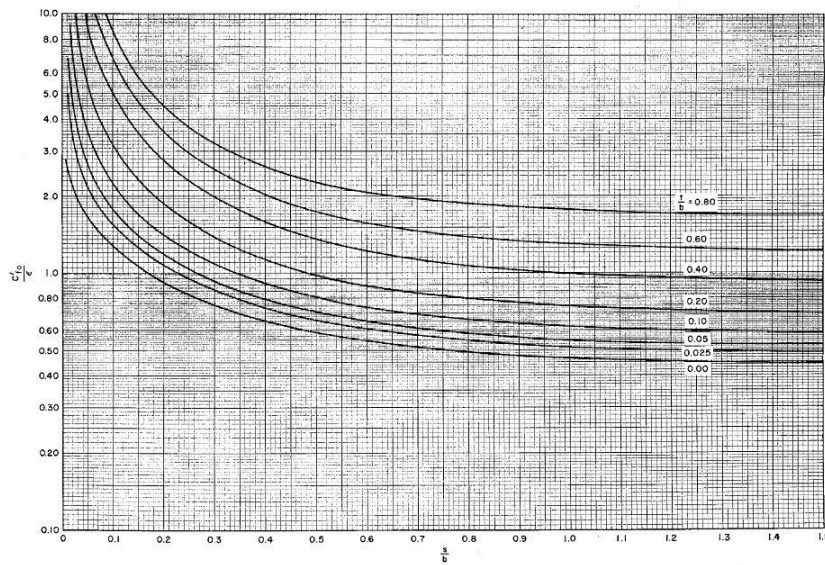


Figure 6.18: Odd-Mode Fringing Capacitances for Coupled Resonator Bar [13]

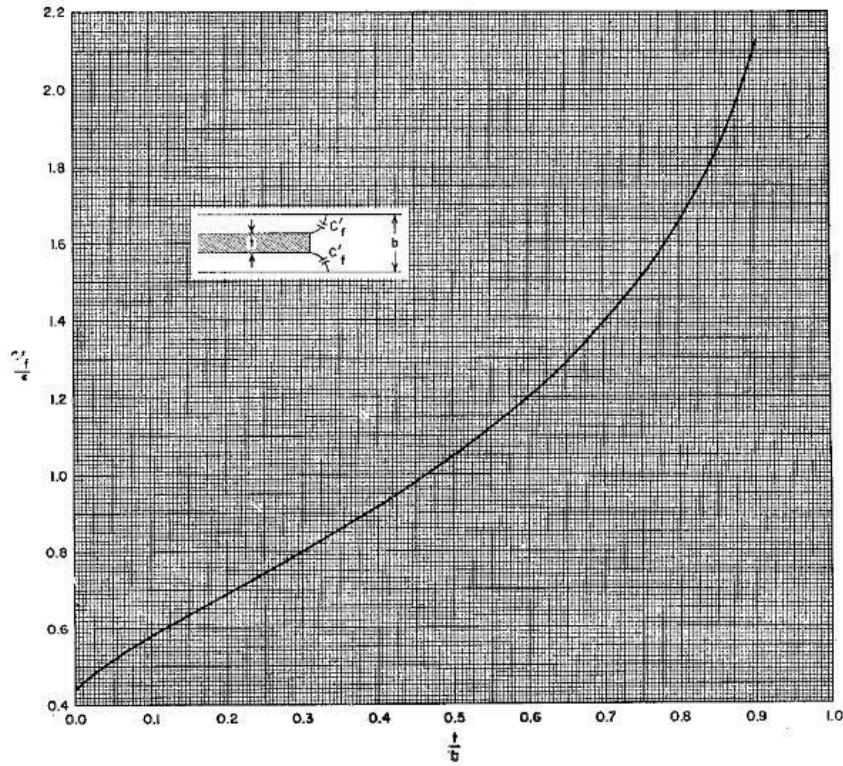


Figure 6.19: Fringing Capacitances for Isolated Resonator Bar [13]

Once all the necessary values have been obtained the final step is to calculate the widths of the resonators. The spacing has already been obtained since $\frac{s}{b}$ has been determined. To determine the widths Matthaei presents these equations,

$$\frac{w_a}{b} = \frac{1}{2} \left(1 - \frac{t}{b} \right) \left[\frac{1}{2} \left(\frac{C_a}{\epsilon} \right) - \frac{C'_{fe}}{\epsilon} - \frac{C'f}{\epsilon} \right] \quad (6.4.13)$$

$$\frac{w_b}{b} = \frac{1}{2} \left(1 - \frac{t}{b} \right) \left[\frac{1}{2} \left(\frac{C_b}{\epsilon} \right) - \frac{C'_{fe}}{\epsilon} - \frac{C'f}{\epsilon} \right] \quad (6.4.14)$$

where b is the height of the cavity of the filter, t is thickness of the vertical thickness of the resonators and ϵ is the dielectric constant of the material in the filter. Figure 6.14 describes t and b .

These equations are valid as long as both $\frac{w_a}{b}$ and $\frac{w_b}{b}$ are more than $0.35 \left(1 - \frac{t}{b} \right)$. If either is less than this value a different approximate formula can be used. This corrected formula is useful when the resonators are relatively narrow and interaction of the fringing fields occur:

$$\frac{w'}{b} = \frac{0.07 \left(1 - \frac{t}{b} \right) + \frac{w}{b}}{1.2} \quad (6.4.15)$$

given that

$$0.1 < \frac{w'}{b} < 0.35. \quad (6.4.16)$$

6.4.3 Array of Parallel Unsymmetrical Coupled Lines

Section 6.4.2 showed how Getsinger's charts, along with the appropriate equations, can be used to find the widths of two unsymmetrical resonators as well as the spacing between them. This Section extends this formulation to n unsymmetrical resonators.

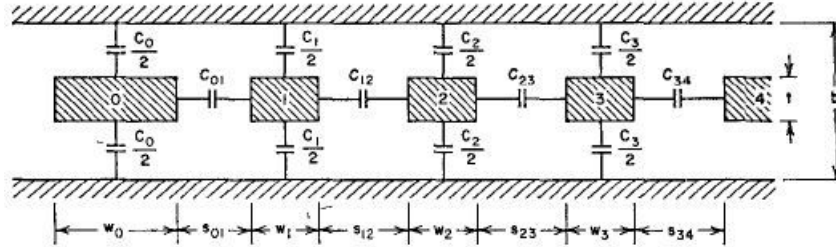


Figure 6.20: Array of Parallel Coupled Lines [12]

All the same formulations of the previous Section apply. The self capacitances are now defined as C_k and the mutual capacitances are defined as $C_{k,k+1}$ where k is the resonator number. There is also now an array of spacings defined as $s_{k,k+1}$. An equation for the width of the k_{th} resonator can be set up as

$$\frac{w_k}{b} = \frac{1}{2} \left(1 - \frac{t}{b} \right) \left[\frac{1}{2} \left(\frac{C_k}{\epsilon} \right) - \frac{(C'_{fe})_{k-1,k}}{\epsilon} - \frac{(C'_{fe})_{k,k+1}}{\epsilon} \right]. \quad (6.4.17)$$

The width of the input and output couplers can also be calculated using (6.4.17). The associated fringing capacitances must however be altered since $(C'_{fe})_{k-1,k}$ and $(C'_{fe})_{k,k+1}$ cannot be applied to the input and output couplers. This is because there is no resonators before or after the respective couplers so C'_f must be used as a substitute. See the 0th resonator in Figure 6.20 as an example. The relevant fringing capacitances are replaced by the fringing capacitances of an isolated resonator bar, shown as

$$\frac{w_0}{b} = \frac{1}{2} \left(1 - \frac{t}{b} \right) \left[\frac{1}{2} \left(\frac{C_0}{\epsilon} \right) - \frac{C'_f}{\epsilon} - \frac{(C'_{fe})_{0,1}}{\epsilon} \right] \quad (6.4.18)$$

$$\frac{w_{n+1}}{b} = \frac{1}{2} \left(1 - \frac{t}{b} \right) \left[\frac{1}{2} \left(\frac{C_{n+1}}{\epsilon} \right) - \frac{(C'_{fe})_{k-1,k}}{\epsilon} - \frac{C'_f}{\epsilon} \right]. \quad (6.4.19)$$

The condition $(0.35(1 - \frac{t}{b}))$ introduced in Section 6.4.2 as well as the correction still holds. See (6.4.15) and (6.4.16).

6.4.4 Design for Narrow to Moderate Bandwidth

Matthaei presents a step-by-step guide for calculating the necessary self and mutual capacitances [12] required by "*Getsinger's Charts*". These equations have components such as θ , J , N , h and M which are all defined in Appendix A. ϵ is the dielectric constant and ϵ_r is the relative dielectric constant in the medium of propagation.

Self Capacitances per Unit Length

$$\frac{C_0}{\epsilon} = \frac{376.7}{\sqrt{\epsilon_r}} [2Y_A - M_1] \quad (6.4.20)$$

$$\frac{C_1}{\epsilon} = \frac{376.7}{\sqrt{\epsilon_r}} \left[Y_A - M_1 + hY_A \left[\frac{\tan \theta_1}{2} + \left(\frac{J_{01}}{Y_A} \right)^2 + N_{12} - \frac{J_{12}}{Y_A} \right] \right] \quad (6.4.21)$$

$$\frac{C_k}{\epsilon} = \frac{376.7}{\sqrt{\epsilon_r}} hY_A \left[N_{k-1,k} + N_{k,k+1} - \frac{J_{k-1,k}}{Y_A} - \frac{J_{k,k+1}}{Y_A} \right] \quad (6.4.22)$$

$$\frac{C_n}{\epsilon} = \frac{376.7}{\sqrt{\epsilon_r}} \left[Y_A - M_n + hY_A \left[\frac{\tan \theta_1}{2} + \left(\frac{J_{n,n+1}}{Y_A} \right)^2 + N_{n-1,n} - \frac{J_{n-1,n}}{Y_A} \right] \right] \quad (6.4.23)$$

$$\frac{C_{n+1}}{\epsilon} = \frac{376.7}{\sqrt{\epsilon_r}} [2Y_A - M_n] \quad (6.4.24)$$

Coupling Capacitances per Unit Length

$$\frac{C_{01}}{\epsilon} = \frac{376.7}{\sqrt{\epsilon_r}} [M_1 - Y_A] \quad (6.4.25)$$

$$\frac{C_{k,k+1}}{\epsilon} = \frac{376.7}{\sqrt{\epsilon_r}} \left(\frac{J_{k,k+1}}{Y_A} \right) \quad (6.4.26)$$

$$\frac{C_{n,n+1}}{\epsilon} = \frac{376.7}{\sqrt{\epsilon_r}} [M_n - Y_A] \quad (6.4.27)$$

6.4.5 Tuners

Many microwave filters require the use of tuners to fine tune the response of the filter. The tuners that are applicable to the inter-digital filters used are mechanical tuners. They are alternatives to other traditional methods, such as using screws.

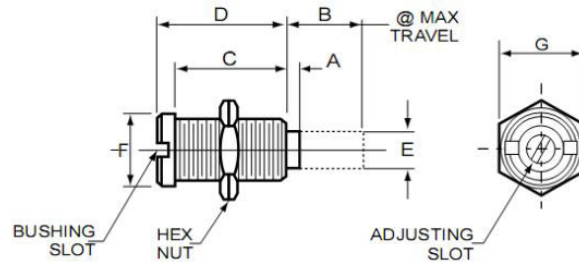


Figure 6.21: Temex Ceramics Microwave Tuning Element [14]

A tuner will be placed opposite each resonator so that the capacitances associated with each resonator can be altered.

6.5 Design

6.5.1 Design Parameters

To determine the order n , an equation presented by Matthaei [53] is used. This calculation was performed for the IF filter, since it has the greatest need for sharp cut-off. It was decided to allow the RF filter to have the same n for simplicity in design flow. The order was determined by

$$n = \frac{\cosh^{-1} \left[\sqrt{\frac{10^{\frac{L(f_a)}{10}} - 1}{10^{\frac{\Gamma_{dB}}{10}} - 1}} \right]}{\cosh^{-1} (\Delta f_n)} \quad (6.5.1)$$

where

$L(f_a)$ = attenuation required at specific rejection frequency, [dB]

Γ_{dB} = passband ripple, [dB]

$\Delta f_n = \frac{2|f_a - f_0|}{\Delta f}$ = normalised bandwidth at rejection frequency

f_a = rejection frequency, [Hz]

f_0 = centre frequency, [Hz]

Δf = bandwidth, [Hz].

Using (6.5.1) and the values in Table 6.2 the order was found to be $n = 5$. The values in Table 6.2 were chosen to ensure that the image frequency of the IF stage of the receiver at 2.75 GHz is attenuated.

Variable Name	Value
$L(f_n)$	40 dB
Γ_{dB}	0.1 dB
Δf	0.6 GHz
f_a	2.75 GHz

Table 6.2: Design Values Used for Calculation of Order of BPF's

Figure 6.22 shows the top view of the odd numbered inter-digital filter with $n = 5$, while Figure 6.23 shows the side view.

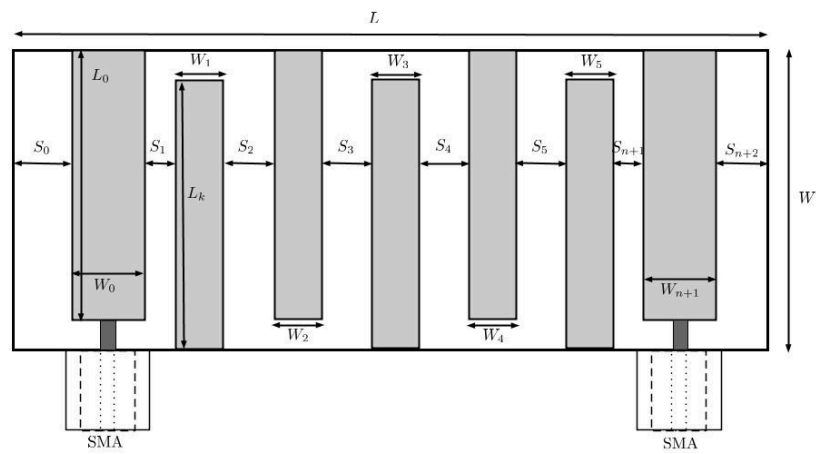


Figure 6.22: Top View of Odd Inter-Digital Filter

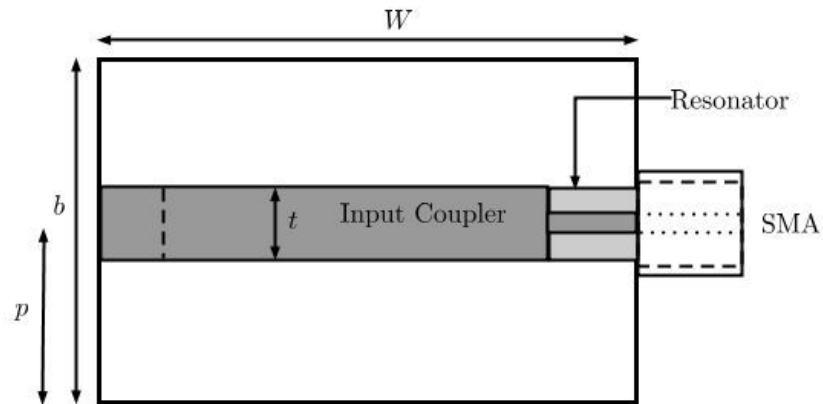


Figure 6.23: Side View of Inter-Digital Filter

The parameter p is chosen so that the resonators and couplers are centred with regards to position along the side walls. Table 6.3 shows the parameters of the inter-digital filter.

Variable Name	Description
L	Length of filter
W	Width of filter
W_x	Width of resonator x
S_x	Spacing between resonator $x - 1$ and x
L_k	Resonator length
L_0	Input coupler length
$b(EPs)$	Earth plane spacing (height)
t	Thickness of resonators and input couplers
p	Position of resonators and input couplers

Table 6.3: Model Parameter Descriptions

6.5.2 Design Procedure

The design presented by Matthaei and described in Section 6.4 was used to design both the filters required. The purpose of both the inter-digital filters is briefly summarized in Section 6.1. From here on the filters will be described as the RF filter ($f_0 = 7.5$ GHz) and IF filter ($f_0 = 3.5$ GHz).

All the equations described in Section 6.4 were calculated using MATLAB for a RF filter design and an IF filter design. Once the design variables were found CST was once again used to simulate the designed filters. First of all CST models had to be created so that the variables could simply be changed by MATLAB, instead of creating brand new models for each simulation, which could become complicated and prone to bugs.

Once the MATLAB-CST hybrid program was up and running initial simulations were performed. Table 6.4 shows the initial results.

Filter	Design Value		Simulated Value	
	$f_0(GHz)$	$BW(GHz)$	$f_0(GHz)$	$BW(GHz)$
RF	7.5	0.8	7.9	0.9
IF	3.5	0.6	3.45	0.6

Table 6.4: Filter Results

As can be seen, the RF results are not desirable while in contrast, the IF results are acceptable. To fix the centre frequency of the RF filter the resonator lengths were changed until a desirable result was found. It can be concluded that the design of Matthaei works well. However adjustments to the design must be made at higher frequencies.

6.5.3 Final Results

A rule of thumb requirement for filter design is for the S_{11} across the passband to be below -20 dB. The results of the filters after the resonator lengths of the RF filter was shortened were promising. Metallic tuners were added to both simulated filters in an

attempt to get as much of the S_{11} in the passband below -20 dB. This was also done to ensure that adding tuners would indeed have an effect on the S-parameter response of the filters. The tuners increase the self-capacitance of the resonators when they are screwed towards the resonator. This decreases the resonant frequency.

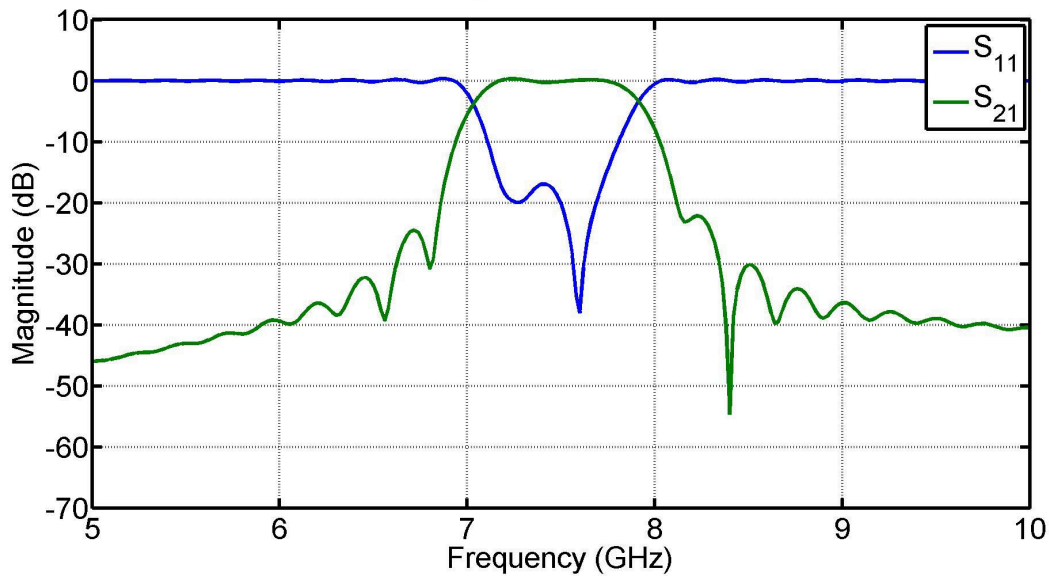


Figure 6.24: Final Simulation of RF-BPF at 7.5 GHz

The RF filter S_{11} response in Figure 6.24 and the IF filter S_{11} response in Figure 6.25 is almost entirely below -20 dB in the passband. Both filters also have sharp cut-off's which is essential in radio receiver systems. These results satisfy the design parameters.

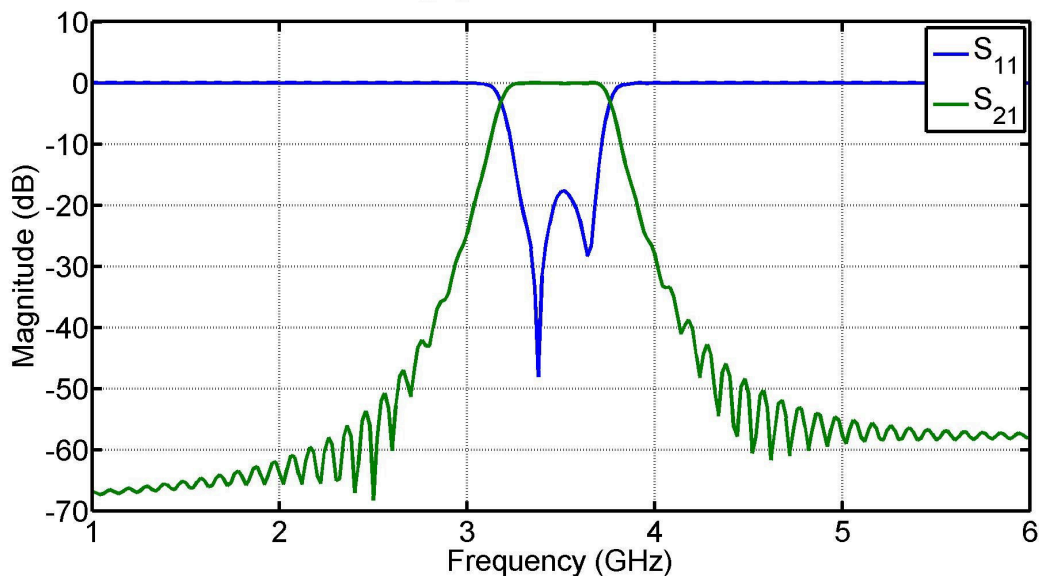


Figure 6.25: Final Simulation of IF-BPF at 3.5 GHz

6.6 Measurements

6.6.1 Setup

The filters were measured on the same Agilent PNA-X network analyser that was used for the antenna. The network analyser was once again calibrated using the N4691-60004 ECal. Both port 1 and port 2 were used for this measurement.

6.6.2 Method

Various measurement techniques can be used to tune the tuners appropriately. It was decided to first try manual tuning to get a feel for the tuning process. It was found that the filters were easily tunable and thus no further tuning techniques were attempted.

6.6.3 Results

The major concern from both measurements was that the responses were shifted in frequency. The RF filter in Figure 6.26 has been slightly shifted by 0.13 GHz and has slightly less bandwidth (0.1 GHz). This is not a major problem as the desired signal at 7.5 GHz is still in the passband and because of the band chosen, no RFI is present in the passband.

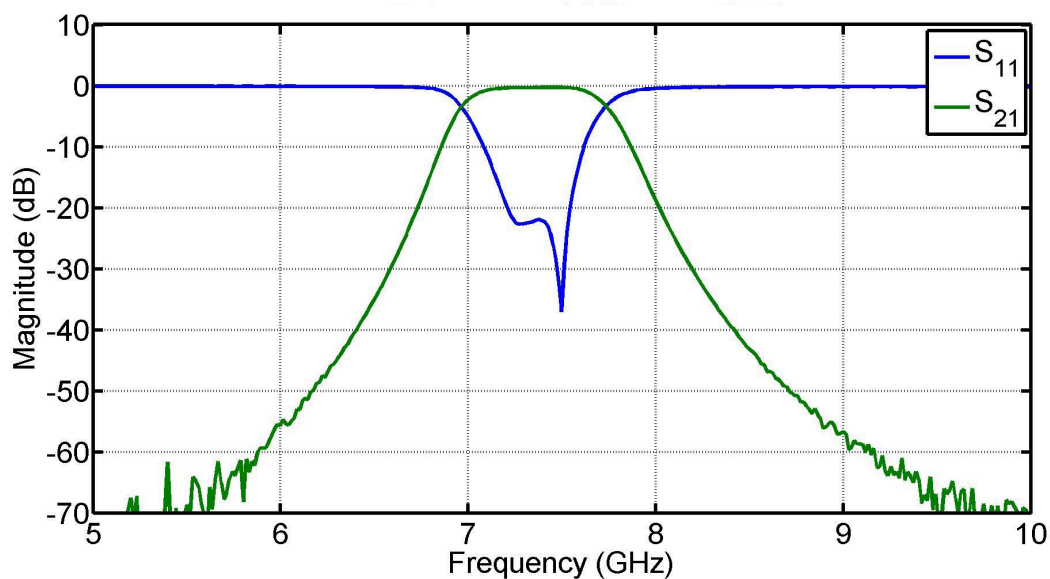


Figure 6.26: Measurement of BPF at 7.5 GHz

The IF filter was shifted about 0.14 GHz. The bandwidth however remained more or less the same. This means that 3.5 GHz (the intermediate frequency) is still in the passband. The major concerns are whether or not the image frequency of the second mixing stage and the mixed down LO_1 leakage is in the passband. Referring to Figure 4.10 it is determined that these signals are outside the passband.

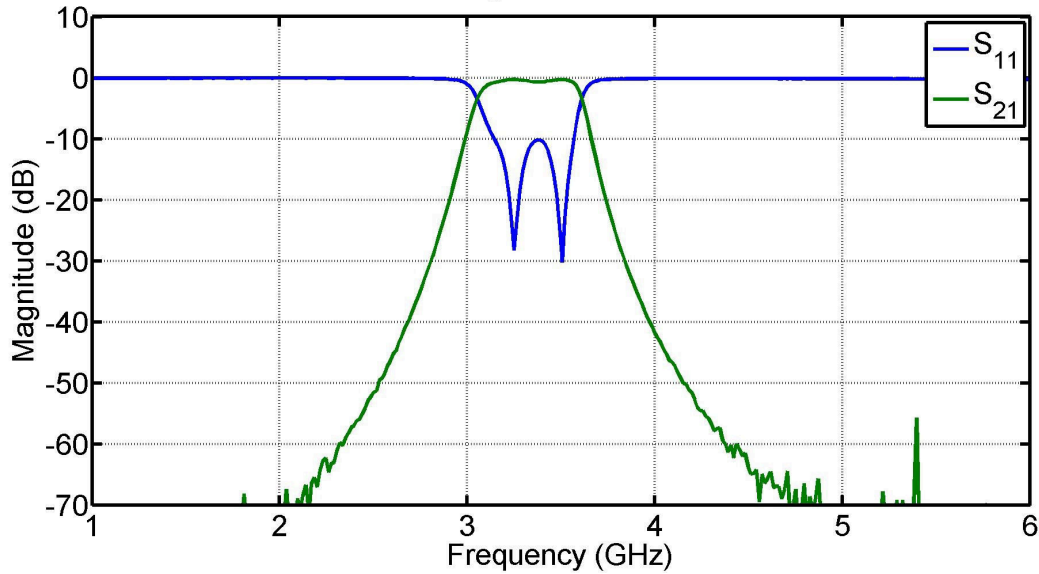


Figure 6.27: Measurement of BPF at 3.5 GHz

The RF filter has a much better overall response compared to the IF filter. Most of the passband is below -20 dB. The initial IF filter response was similar to the RF filter response, but because of the shift, the minimum S_{11} value was less than 3.5 GHz. The filter was then tuned so that a local minimum of -30 dB occurred at 3.5 GHz.

Table 6.5 summarizes the results of the RF and IF filter measurements. The Q 's of both are significantly lower than the simulated Q 's. This is mostly because of conduction losses as the simulations were performed with PEC structures.

Filter	Simulated				Measured			
	f_0 (GHz)	BW(GHz)	Q	IL(dB)	f_0 (GHz)	BW(GHz)	Q	IL(dB)
RF	7.4775	0.853	555.08	-0.14	7.35	0.75	308.81	-0.28
IF	3.47	0.58	654.03	-0.08	3.33	0.55	129.87	-0.4

Table 6.5: Filter Results

The filters are considered a success even though the responses were slightly shifted in frequency. The reason for this could be resonators that are slightly too long. Simulation of longer resonators for both RF and IF filters revealed that longer resonators do indeed decrease the centre frequency as expected. At these high frequencies the filter response is sensitive to small inaccuracies, so a resonator that is slightly too long will decrease the resonant frequency.

6.7 Conclusion

This Chapter described the need for certain filters in the receiver system. The RF BPF is needed to reject RFI and image frequencies. The IF BPF is needed to ensure leaked LO_1 power and second image frequencies are not in the pass-band. The LPF is needed to ensure leaked LO_1 that is mixed down is not sent to the ADC as well as elimination of intermodulation products.

The LPF filter design started with a Chebyshev LPF prototype. From this ideal component values were obtained. ADS was then used to determine the response of an ideal filter and a compromised filter. The compromised filter used real ADS models for the components. Simulated results were promising and the filter was then manufactured. The measured results met all specifications and corresponded well to the final simulations.

BPF transformations for microwave structures at high frequencies can yield difficult component values because of the low Q of inductors that need to be used. This is why a coupled resonator filter type was chosen. The use of admittance inverters to get one type of component in the prototype was explained. From this prototype BPF transformation can be applied. Using equivalent circuits for the inverters a BPF equivalent circuit with transmission line resonators and coupling capacitances can be set up.

A design by Matthaei was used in conjunction with "*Getsinger's Charts*" to determine the physical dimensions of the filters from the self- and coupling capacitances. The RF and IF filters were then simulated in CST and were found to have acceptable responses.

The filters were then built and measured. The measured results were slightly shifted in frequency but not by a significant amount. It was found that the metallic tuners can be used to tune the filters quite well.

Chapter 7

RF Over Fibre

7.1 Introduction

7.1.1 Brief Description

Radio Frequency Over Fibre (RFoF) is an alternative to conventional high frequency coaxial signal transmission. A RF signal is received and converted from the electrical domain to the optical domain and transmitted over a fibre optics cable. The signal is then converted back to the electrical domain. This allows high frequency analogue signals to be transmitted over long distances with negligible attenuation.

The RFoF link consists of a transmitter to convert the RF signal, a fibre optics cable (possibly with repeaters in the case of very large distances) and a receiver to convert the light back into RF. The transmitter and receiver will also often have low noise amplifiers to give gain to the overall RFoF link.

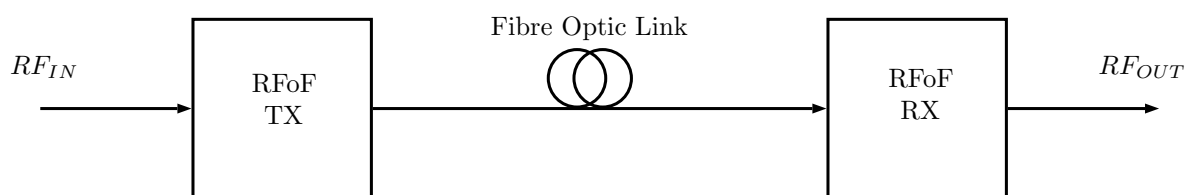


Figure 7.1: Simple Block Diagram of RFoF

7.1.2 Advantages

7.1.2.1 Centralisation

With appropriate transmitters and receivers, a fibre optics cable can transmit any RF signal of practical use. This allows a high frequency signal to be transmitted over long distances without the need to be down- or up-converted. Currently high frequency signals are down-converted to lower frequencies before transmission because of the unacceptable attenuation.

RFoF technology allows certain front-end components, such as mixers and local oscillators, to no longer be mounted near or at the antenna. This frees up some design requirements as most of the front-end will now be in a lab or base station.

This centralised signal processing allows for equipment sharing, dynamic resource allocation and simplified system operation [54]. This can reduce costs of the overall system and make maintenance of the system more efficient.

7.1.2.2 Low Attenuation

Fibre optic cables are known for very low losses. This eliminates the need for repeaters at most distances. Losses are known to be around 0.3 dB/km for 1550 nm optical wavelength, and 0.5 dB/km for 1310 nm. This does not include the loss or gain of the transmitters or receivers, which may have a conversion loss and a low noise amplifier gain.

Due to this low attenuation repeaters are not necessary except for very long cables. Generally cables up to 80 km long do not require repeaters or optical amplifiers.

This low attenuation is highly desirable in sensitive communication systems.

7.1.2.3 Adaptability

Due to the large bandwidth and speed of a fibre optics system, future technologies that require high-speed connections will be able to use any existing optical fibre infrastructure with minimal effort. In contrast, existing coaxial infrastructure could be a limiting factor in future technologies.

7.1.2.4 Bandwidth

Optical fibre has a practically infinite bandwidth (about 50 THz), meaning that the bandwidth of the link is determined by the transmitter and receiver [55]. This can be anything from 12 GHz to 50 GHz.

7.1.2.5 Interference

Since the signal is being transmitted as light, the signal is not susceptible to any kind of EMI. This includes RFI and lightning strikes. Fibre optics is also immune to possible signal theft.

7.1.2.6 Phase Stability

The phase stability of the fibre optics cable over temperature is a major advantage of RFoF over coaxial cable transmission. Coaxial cables are sensitive to temperature and in highly sensitive systems this can cause problems.

7.1.3 Disadvantages

7.1.3.1 Noise and Distortion

RFoF is fundamentally an analogue transmission. This leaves it open to noise and distortion [55]. This can be caused by non-linear elements in the system, namely the laser (used

in transmitter) and the photo-detector (used in receiver). This limits the noise figure and dynamic range of the system.

Chromatic dispersion in the cable, explained in Section 7.3.4, can also lead to RF carrier phase noise.

7.1.3.2 Cost

Currently transmitter and receiver modules (combined) for RFoF systems can cost anything from R70 000 to R220 000, depending on functionality of the modules. All these modules follow a simple plug-and-play logic, where all that is required is power, RF input and an optical cable.

Optical fibre cabling is known to be somewhat expensive but new breakthroughs are making it more affordable by the day.

7.1.4 Use in the SKA

SKA SA, who have developed KAT-7 and are busy with MeerKAT that will eventually form part of the SKA, do not use RFoF. All the radio telescopes have the front-end receiver located at the dish along with a digitiser. Fibre optics is still relevant to the SKA however, because after the digitiser a vast fibre optics network is used to transmit the digitised signals. Extensive work has been done to implement the current systems, especially the digitizer, so the SKA is unlikely to use RFoF in the future. The exception is SKA-Low, where RFoF may be used at lower frequencies where the costs are not as high.

7.2 How RF Over Fibre Works

7.2.1 Basic Functioning

Given an input RF signal, a receiver will use the electrical signal to modulate the optical source (a laser diode) [55]. The signal is then transmitted across the optical link at a certain wavelength of light. This usually is 1310 nm or 1550 nm.

The receiver then uses a photo-detector. This is a semi-conductor device and may be a p-n junction, p-i-n photo-diode or an avalanche photo-diode [56].

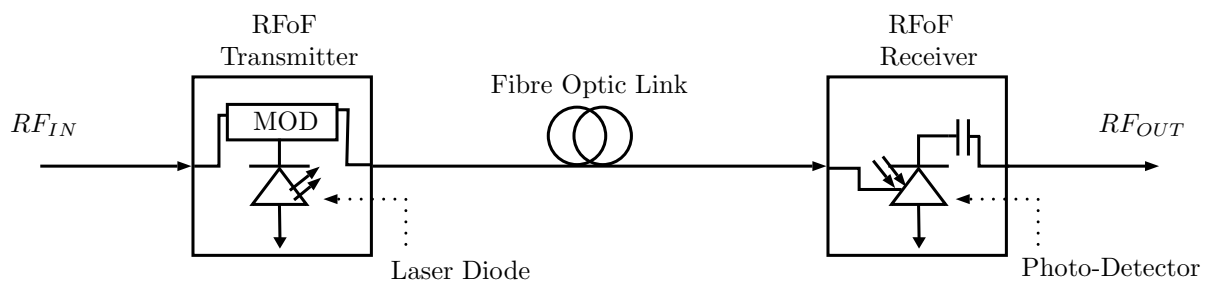


Figure 7.2: Block Diagram of RFoF

7.2.2 Modulation Techniques

There are many techniques that can be used in an RFoF system, but by far the simplest and most widely used is Intensity Modulation-Direct Detection (IM-DD). The RF signal directly modulates the intensity of the laser diode [54].

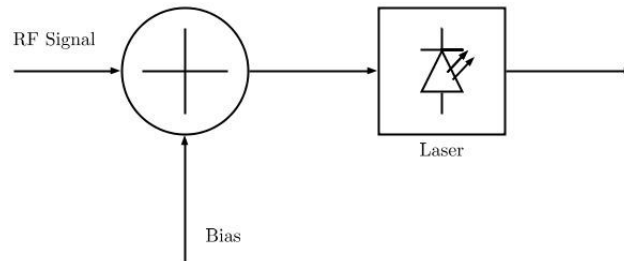


Figure 7.3: Intensity Modulation - Direct Detection Without External Modulator

The laser could also be operated in continuous wave (CW) mode and then intensity modulated using a Mach-Zehnder modulator [55]. A Mach-Zehnder Modulator is an optical device that uses a directional coupler to split the input power of the CW laser into two separate waveguides. The refractive index of one of these waveguides is changed by application of an external voltage. This causes the phase of the light wave passing through that waveguide to change. Another directional coupler combines all the power in the modulator. By combining two signals with different phase change, an amplitude modulated signal can be obtained interferometrically [57].

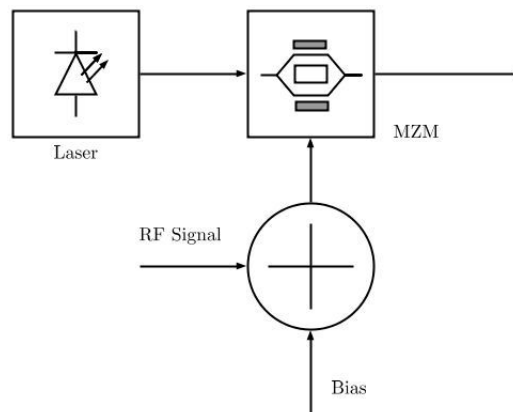


Figure 7.4: Intensity Modulation - Direct Detection With External Mach-Zehnder Modulator

After the signal has been transmitted over the cable, the photo-diode in the RFoF receiver then uses direct detection to recover the electrical signal.

7.3 Fibre Optics Cable

7.3.1 Construction

A fibre optics cable consists of 3 main parts. The inner most narrow strand of high quality glass is called the core. Around the core another layer of glass exists with a slightly different index of refraction (usually 1 or 2% lower than the core) called the cladding. A protective layer made of plastic called the buffer surrounds the cladding.

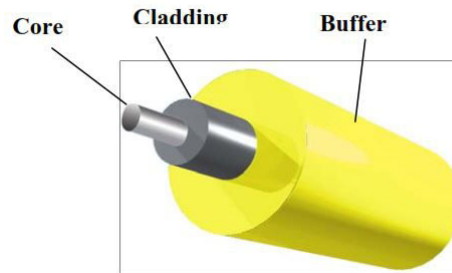


Figure 7.5: Construction Diagram of a Fibre Optics Cable [15]

Two types of cladding exist: step index fibre and graded index fibre. Step index fibre refers to a cable that has a step in the refractive indices at the interface of the core and cladding. Step index fibre is mostly used in single mode operations. Graded index fibre has a gradual change in refractive index from the core to the cladding. The graded index fibre allows for the transmitted light to follow a sinusoidal path along the cable. This helps to eliminate modal dispersion in multi-mode fibre which is discussed later.

Fibre cables are usually characterized by 3 properties, namely diameter of core and cladding, transmission wavelength and mode of fibre. For example, a cable can have specifications of 62.5/125 μm , MM, 850 nm. This means the core is 62.5 μm in diameter, the cladding is 125 μm in diameter, it operates in multi-mode and has a transmission wavelength of 850 nm. The transmission wavelength refers to the wavelength of the light travelling along the cable.

Fibre optics are extensively used and as such the IEEE has set out standards for their use. Most of these are for Ethernet and Local Area Network (LAN) type communication. Table 7.1 summarises IEEE fibre standards.

Standard	Mbps	Cable Type	Max Distance
10Base-FL	10	Multi-mode 850 nm 50/125 μm or 62.5/125 μm	2 km
100Base-FX	100	Multi-mode 1300 nm 50/125 μm or 62.5/125 μm	2 km
100Base-SX ¹	100	Multi-mode 850 nm 50/125 μm or 62.5/125 μm	300 m
100Base-LX	100	Single-mode 1310 nm, 1550 nm 9/125 μm	100 km
1000Base-SX	1000	Multi-mode 850 nm 62.5/125 μm Multi-mode 850 nm 50/125 μm	220 m 550 m
1000Base-LX	1000	Multi-mode 1300 nm 50(62.5)/125 μm Single-mode 1310 nm 9/125 μm	550 m 2 km
1000Base-LH ¹	1000	Single-mode 1310 nm 9/125 μm	70 km

Table 7.1: IEEE Fibre Standards [15]

7.3.2 Transmission of Light

Fibre optics technology is possible because of the transmission of light along a narrow strand of glass named the core. The cladding around the core keeps the light in the core using a phenomenon known as total internal reflection. Refractive index is a dimensionless number describing the propagation properties of a medium and is defined as

$$n = \frac{c}{v} \quad (7.3.1)$$

where $c = 3 \times 10^8$ m/s and $v =$ speed of light in medium. Total internal reflection occurs when a propagating wave strikes a medium boundary with an angle greater than the critical angle and if the second medium has a refractive index lower than the refractive index of the first medium.

¹While these are not formally adopted standards they are still widely used and understood.

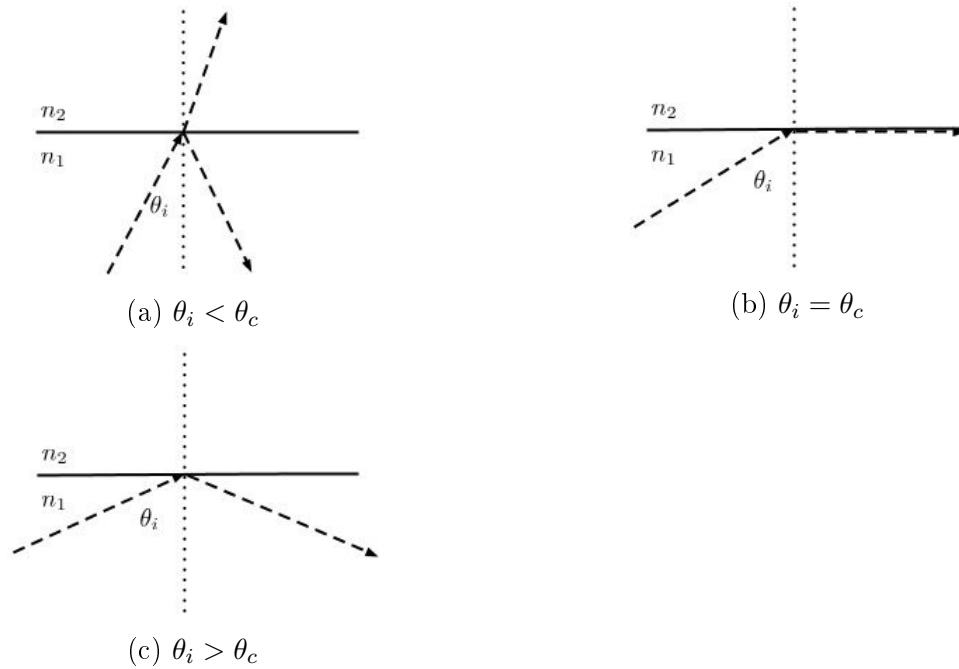


Figure 7.6: Example of Total Internal Reflection

In Figure 7.6a the angle of incidence is smaller than the critical angle. This means that some of the signal is transmitted into the second medium while the rest is reflected back into the first medium. In Figure 7.6b the angle of incidence is equal to the critical angle. The signal is not transmitted into the second medium and propagates along the boundary of the two mediums. In Figure 7.6c the angle of incidence is greater than the critical angle so total internal reflection occurs. The signal is reflected back into the first medium.

Light entering the cable above the critical angle will continually be reflected by the cladding so that it can travel along the core. Since the angle of reflection during total internal reflection is equal to the angle of incidence, the light will be reflected for the entire length of the cable, as shown in Figure 7.7.

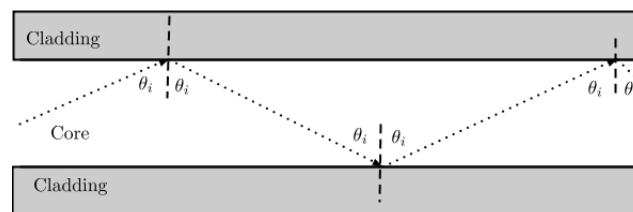


Figure 7.7: Total Internal Reflection in a Fibre Optics Cable

7.3.3 Multimode and Single Mode

Fibre optics cables can operate in either single-mode or multi-mode. The mode determines the path of the transmitted light along the core of the cable. Single-mode light has only one possible path while multi-mode has many possible paths. This is because of the diameters of the different types of cables. Multi-mode cables are much larger in diameter than the single-mode cables (around $62.5 \mu\text{m}$ and $9 \mu\text{m}$ respectively).

Transmitted light along a single-mode fibre cable does not reflect from the cladding as it does in multi-mode cables. The small size of the core only allows the transmission of a path of light parallel to the axis of the core. Single-mode fibre does not suffer from modal dispersion and as such has a theoretically infinite bandwidth [56]. The main bandwidth limitation is chromatic dispersion which is discussed in Section 7.3.4. This is overcome by using 1310 nm for the transmission light. Chromatic dispersion is a function of transmission light wavelength and at 1310 nm is very close to 0.

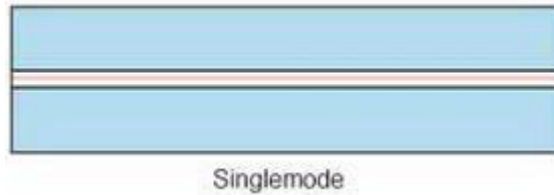


Figure 7.8: Single-Mode Graded Index Fibre [16]

Multi-mode fibre allows multiple paths of light along the core due to its larger diameter. This gives multi-mode fibre a high level of efficiency, but makes it more susceptible to modal dispersion which limits the bandwidth extensively. The problem arises as light on different paths do not travel at the same speeds and therefore arrive at the receiver at slightly different times [58]. This causes the signal to spread out and lose its shape. Some time must then pass before another signal can be sent across the cable. Bandwidth and maximum distance of the cable is therefore limited.

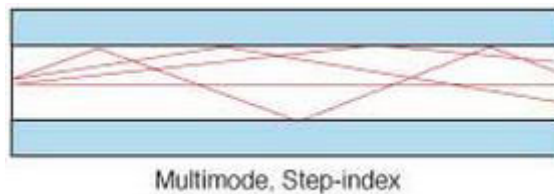


Figure 7.9: Multi-Mode Step Index Fibre [16]

Graded index fibre can vastly improve the bandwidth of multi-mode fibre and the effects of modal dispersion. Since the core gradually changes its refractive index up to the cladding, light not travelling along the core will move more slowly the closer it gets to the cladding. This causes an almost sinusoidal path instead of the straight paths shown in step index multi-mode fibre. This slows down the light and causes it to arrive at the receiver at more or less the same time as the light that travels along the core axis.

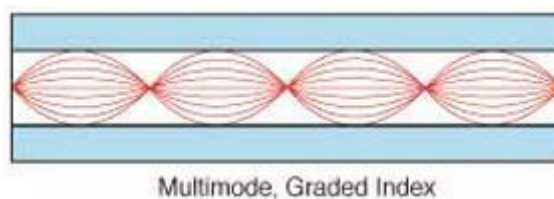


Figure 7.10: Multi-Mode Graded Index Fibre [16]

Multi-mode cables are easier to manufacture and their high efficiency allows for simple LED's to be used to transmit light. This all drives down costs. However, single-mode fibre, which requires a high degree of precision during manufacturing, is becoming more and more affordable. Single-mode fibre is superior in terms of distance and is preferred when it comes to "long haul" applications. The term "long haul" refers to any fibre optic link that covers some non-negligible distance. A RFoF system where the antenna is far away from the front-end receiver would be classified as a "long haul" application.

7.3.4 Fibre Loss

To calculate losses in a cable the different types of losses must first be discussed.

The attenuation of a cable is defined as the loss of the fibre per unit length (dB/km) [16]. This is due to two factors; scattering and absorption.

Absorption is the process of light being converted to heat by certain molecules in the glass. The two main absorbers are residual OH⁺ molecules and the dopants used to change the refractive index of the glass. Absorption due to dopants occurs at discrete wavelengths of transmitted light, unlike the OH⁺ absorption, which occurs at 1000 nm, 1400 nm and above 1600 nm [16].

Scattering is the largest contributor to attenuation. Glass is anisotropic² so when light hits certain individual atoms in the glass it will either be absorbed into the cladding or transmitted back along the core. Scattering is function of transmitted light wavelength and is proportional to the inverse fourth power; i.e. doubling wavelength will reduce scattering by $2^4 = 16$ times [16].

Modal dispersion is only a problem in multi-mode fibre cabling. It is a type of distortion in which the signal is spread out in time. This happens because different modes of light travel at different speeds resulting in a more spread out output signal. Graded index fibre helps to solve this problem.

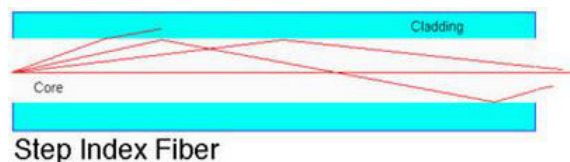


Figure 7.11: Modal Dispersion in Multi-Mode Step Index Fibre [16]

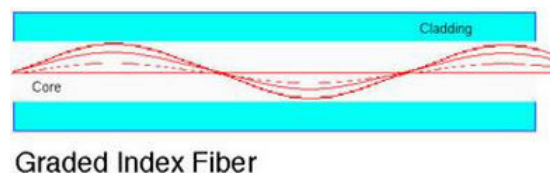


Figure 7.12: Modal Dispersion in Multi-Mode Graded Index Fibre [16]

²object or substance having a physical property which has a different value when measured in different directions. An example is wood, which is stronger along the grain than across it.

Chromatic dispersion is similar to modal dispersion. The transmitted light in a fibre optics cable, like any other light, is made up of various colours. Some colours travel faster than others and therefore arrive earlier [15]. This distorts the signal. Chromatic dispersion is a function of wavelength and the wavelength 1310 nm has very low (virtually 0) chromatic dispersion and is very commonly used among single-mode fibre solutions [56].

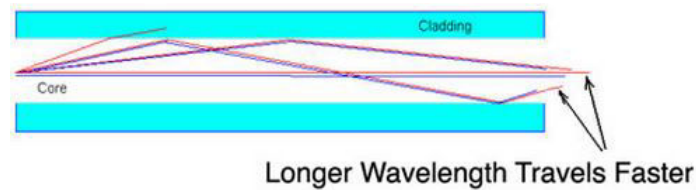


Figure 7.13: Chromatic Dispersion [16]

A splice is a permanent connection between 2 fibre cables. There is no such thing as a perfect splice and any splice can result in about 0.01 dB loss.

Connectors at the cable ends also contribute towards losses. Connectors consist of a rigid cylindrical barrel surrounded by a sleeve. The barrel ensures that the cable is held in place, a requirement for maximum light transfer [56]. Dirt and grime can heavily attenuate the signal. It is common practice to use 0.5 dB per connector for design purposes [15].

It is common in practice to add a safety buffer to account for unforeseen or unmeasurable losses. These might include poor slicing, fibre ageing, humidity and temperature (for non-linear elements during transmitting and receiving of light). Normally 3 dB is used [15].

A power budget can be evaluated to determine the maximum amount of loss that is allowed to occur in a system [15]. The equation uses a "worst case scenario" approach by assuming the transmitted signal level is the lowest it can be.

$$\text{Power Budget}_{dB} = \text{Minimum Launch Power}_{dBm} - \text{Receiver Sensitivity}_{dBm} \quad (7.3.2)$$

By subtracting splice, connector and safety margin losses a net power budget can be found. This can then be used to determine the maximum distance the light can travel before it is no longer receivable by dividing by the specified attenuation for a specific cable.

$$\text{Max Distance} = \frac{\text{Net Power Budget [dB]}}{\text{Fibre Attenuation [dB/km]}} \quad (7.3.3)$$

7.3.5 Repeaters and Amplifiers

Different types of losses have been presented and it has been shown that fibre optics cables have a maximum distance that they can operate before the signal travelling along

them is distorted beyond recognition. If a cable needs to be longer than this repeaters or amplifiers can be used.

Opto-electronic repeaters converts the light signal back to the electrical domain to check whether or not the signal has been distorted. Once the signal has been processed it is converted back to the optical domain and transmitted along the cable [56].

Optical amplifiers are preferred over repeaters for a variety of reasons. They amplify the optical signal without the need for conversion. This is accomplished by using a doped section of fibre cable and illuminating it with a shorter wavelength of light. This amplifies the original signal [56].

7.4 Testing and Implementation

7.4.1 Equipment

As mentioned before, RFoF links are very expensive. Many options were considered but the viability of these options was limited due to the locations of the suppliers of the RFoF products. Eventually a company in Pretoria, Accutronics, agreed to let me use their Miteq RFoF link demo-model.

Table 7.2 summarises some of the important properties of this link.

Parameters	Typical
Operating Frequency	0.1-11 GHz
Gain	22 dB
Noise Figure	8 dB
Max Input Power	10 dBm
Max Saturated Output Power	10 dBm
Input/Output Impedance	50 Ω
RF Connectors	SMA Female
Optical Wavelength	1550 <i>nm</i>

Table 7.2: Miteq RFoF Link Properties [15]

Fibre optics cables are much more accessible. Dartcom offers various fibre solutions. A 30 m single-mode cable was chosen and purchased. Table 7.3 summarises some of the important cable properties.

Parameter	Value
Length	30 m
Type	9/125 μm
Mode	Single-mode
Losses	0.4/0.25 dB/km at 1310/1550 nm
Price	R 240 (including VAT)

Table 7.3: Dartcom Fibre Optics Properties [15]

7.4.2 Testing and Characterisation

The RFoF link and the fibre optics cable were tested in the HF laboratory. Two tests were performed.

First, the link's performance over frequency was determined. As shown in Table 7.2 there is expected gain in the system. Figure 7.14 shows the measured results. As can be seen there is unexpected loss. After some investigation it was thought that the gain in the system is faulty. The link was sent back to Accutronics. They confirmed the faulty gain. However, the link has low loss at the frequency of interest (7.5 GHz) and it was decided to use the link regardless of the faulty gain.

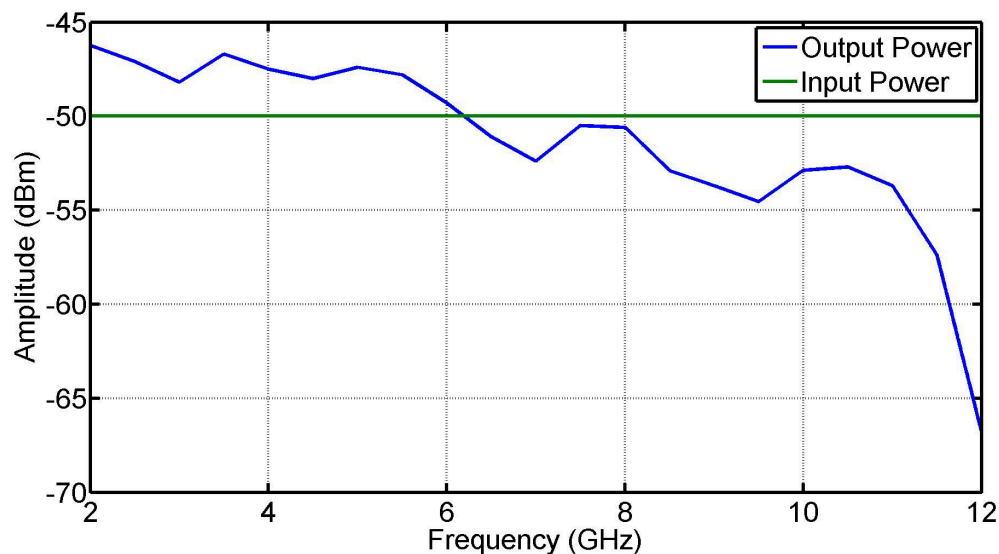


Figure 7.14: Output Power Over Frequency for RFoF Link

Secondly, the linearity of the link was tested as shown in Figure 7.16. This was done by performing a Total Harmonic Distortion (THD) test. The THD of a signal is defined as the ratio of the sum of all harmonic components to the power of the fundamental frequency. Low THD means a "purer" signal with less harmonic components. This is desirable. The THD of a signal can be defined as

$$THD = \frac{\sqrt{V_2^2 + V_3^2 + V_4^2 + \dots}}{V_1} \quad (7.4.1)$$

where V_n refers to the Root Mean Square (RMS) voltage of the n th harmonic.

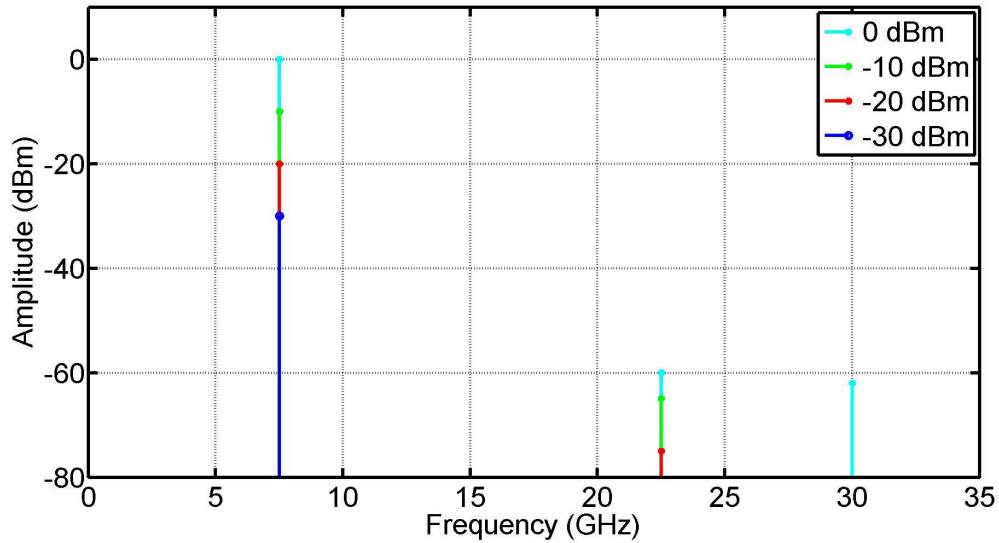


Figure 7.15: Input Signal Power and Harmonics for RFoF Link Test

While some more advanced methods exist with which to measure THD, the general linearity of the link can be tested by applying a pure signal at 7.5 GHz, whose spectrum is seen in Figure 7.15, to the link. An appropriate signal generator was used to generate the 7.5 GHz signal. As can be seen, the signal generator has excellent suppression of the 2nd harmonic at 15 GHz. As the input power is increased, so the power of the higher order harmonics increases.

Figure 7.16 shows the output of the link given the signals in Figure 7.15 as input. Taking the high input power scenario of a 0 dBm input, the THD can be approximated as 0.129. At -50 dBm input power, the higher order harmonics become negligible and the THD can be approximated as 0.

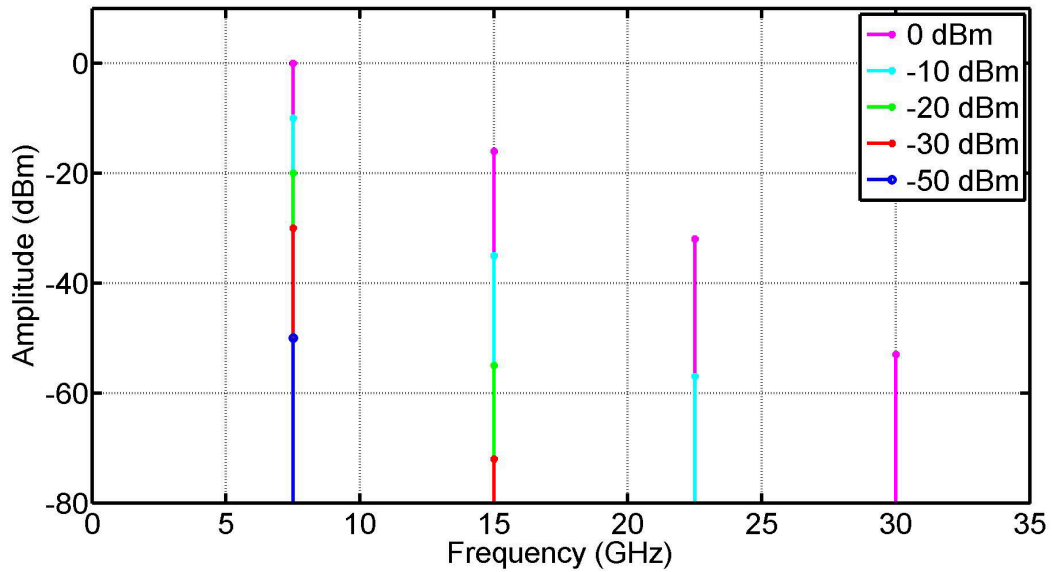


Figure 7.16: Output Signal Power and Harmonics for RFoF Link Test

7.5 Conclusion

This Chapter introduced the use of a RFoF link for signal transmission. The transmitter, receiver and fibre optics cable were each described. The transmitter converts an incoming RF signal to the optical domain. This signal is then transmitted along the fibre optics cable. The receiver then converts the signal back into the electrical domain.

A high frequency RF signal can be transmitted along a fibre optics cable thanks to the low losses associated with the cable. As a result, most of the receiver in a receiver system could be located far away from the antenna. This is one of the main advantages of such a system. One of the main disadvantages is the cost of a RFoF link.

A RFoF link was obtained and tested. A Miteq transmitter and receiver was used along with a 30 m Dartcom fibre optics cable. The link was tested for power loss across frequency and linearity. The gain in the link was found to be faulty, but still usable for this project. It can be concluded that RFoF is a viable technique for signal transmission in a receiver system if the cost can be carried.

Chapter 8

Digital Back-End

This Chapter describes the back-end options that were considered. Implementation of the chosen option is presented.

8.1 Back-End Options

8.1.1 Simple Microprocessor

Section 4.3.1 mentions a direct receiver type that implements a RF Power Detector. The DC output from this detector can be used to characterize the received signal using a microprocessor. This type of back-end was used for the writer's undergraduate thesis. To implement this method is relatively simple, but the RF Power Detectors do not work at the frequency of operation.

8.1.2 Arduino Board

An Arduino board is a single-board micro-controller. The goal of the Arduino board is to provide an inexpensive and easy way for hobbyists, students and professionals to interact with the environment. This is done by sensors and actuators. It comes with a simple Integrated Development Environment (IDE) so that personal computers can be used to program the board using C or C++.

Many open source projects exist that use the Arduino board for ADC and frequency detection. These can be used to digitize the received signal and record observations at specific intervals. The inputs on the Arduino board have 10-bit resolution, which equates to 1024 states [59]. The default reference voltage is 5 V, so the ADC resolution is 48 mV/state. This can be appropriate for receivers systems with high power RF signals, but for radio astronomy this resolution could be too coarse. The internal reference of some boards are 1.1 V and an external reference voltage can also be used.

8.1.3 ROACH Board

The Reconfigurable Open Architecture Computing Hardwareboard (ROACH) is a standalone FPGA processing board developed by the Collaboration for Astronomy Signal Processing and Electronics Research group (CASPER). The main goal of the CASPER team is to streamline and simplify the flow of radio astronomy instrumentation [60].

The E&E Department has ROACH boards available for use. All ROACH software is open-source and there are many tutorials documenting the use of these boards. Python is used as the programming language that controls the board.

Due to the availability of the hardware and software the ROACH board was chosen as the digital back-end of this project. The incoming signals will be digitized by the ADC preceding the board, processed by the board and stored by the controlling PC.

8.2 ROACH Board

8.2.1 Overview

The ROACH is essentially a Xilinx FPGA and a PowerPC which runs Linux separately to control the board. The board has high speed as well as high capacity RAM for the FPGA. The board has two Z-DOK (high performance docking connector) connectors allowing ADC, DAC and other interface cards to be attached to the FPGA [60]. There are also four CX4 connectors allowing ROACH boards to connect to each other at 40 Gbits/second as well as an independent 100 Mbps Ethernet port for independent board control and monitoring.

The FPGA has several clocking options, including on-board and external clocks. When used in conjunction with an ADC clock, the FPGA must be programmed to use a clock that is a quarter of the frequency of the ADC clock. The clock is derived from the ADC clock to ensure there are no timing issues.

8.2.2 KAT-7 ADC

The ROACH board needs a digitizer to convert incoming analogue signals to digital signals. The KAT-7 ADC (or Ratty ADC) is widely used. It takes a clock input (which can also be used by the FPGA) as well as the incoming signal. The maximum clock ratings are 1 dBm at 1.5 GHz.

The signal is digitized using 8-bit binary point numbers between -1 and 1. Two's-complement representation is used. The clock signal determines the bandwidth of the back-end since Nyquist sampling requires that sampling occurs at twice the bandwidth.

The outputs of the KAT-7 ADC are the digitized signal and the digital clock that can be used for the FPGA. The incoming clock signal frequency must be 4 times larger than the digital clock frequency used for the FPGA.

The KAT-7 ADC also has an amplifier attached to its front end. The default amplifier provides about 20 dB gain from 50 - 850 MHz with the option of upgrade to an amplifier with range from 50 - 6000 MHz. An attenuator is also included and can provide attenuation from 0 dB - 31.5 dB in 0.5 dB steps. At about -27 dBm input signal power the amplifier starts to saturate.

8.3 Spectrometry

Spectrometers are by far the most widely used type of back-end used for radio astronomy [61]. Spectrometers are used to measure Power Spectral Density (PSD). Spectrometers therefore convert the incoming signal in the time domain to the frequency domain.

The spectrometer used in this project will simply follow the design presented in Tutorial 3 of the ROACH documentation. This is explained in the next Section. The change of the ADC clock frequency is also explained.

8.4 ROACH Testing

8.4.1 Overview

There are many tutorials available designed to give users understanding and experience with the ROACH board. One of these is named "*Tutorial 3 - Wideband Spectrometer*". The tutorial essentially goes through the process to set-up the ROACH as a spectrometer. The required .bof and .py files are also provided.

Since the ROACH board was designed with versatility and flexibility in mind, it will come as no surprise that programming the board is relatively straightforward. A model file is provided which contains a Simulink design. This design contains the appropriate model blocks for the ADC, PFB, DFT and other important aspects of the ROACH. This is where the design of the back-end takes place. The design is then compiled and saved as a .bof file.

A Python script is also provided. The script communicates with the ROACH, copies the .bof file to it and sets important parameters on the board. The script then sends a command to the ROACH to run the .bof file. The script also receives the output data from the ROACH which can then be saved for further processing.

8.4.2 "Tutorial 3 - Wideband Spectrometer"

Tutorial 3 is designed to show how a spectrometer works. Only one signal is applied to the ADC along with the clock signal. The clock input to the KAT-7 ADC has a frequency of 800 MHz. This will provide a bandwidth of 400 MHz. The provided .bof file has already set-up all the required Simulink blocks. The FPGA clock rate is set to 200 MHz and the ADC attenuation is 0 dB.

A clock signal with 0 dBm input power was applied alongside an input test signal of -30 dBm at 200 MHz. The resulting data was saved at a certain time instance and plotted in Figure 8.1.

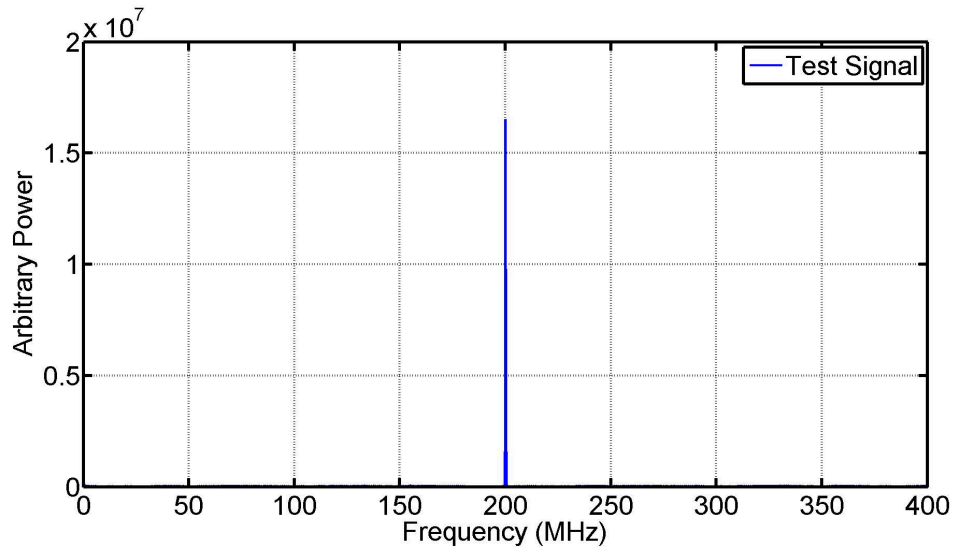


Figure 8.1: ROACH Tutorial 3 Test Signal at 200 MHz

8.4.3 Python Script

Some code was added to the Python script that sends command to the ROACH board. The added code saved the data received from the ROACH and did so at certain intervals. This allowed data to be recorded over a long time. The data is then available to be used later.

8.4.4 Setting the KAT-7 ADC

The bandwidth of the IF BPF mentioned in Section 6.6.3 is 550 MHz centred around 3.3 GHz. Once this has been down-converted by the IF mixer using a LO of 3.125 GHz the baseband bandwidth will be 450 MHz, which is slightly outside the bandwidth of the ROACH board using the default Tutorial 3 settings. Therefore the bandwidth of the ROACH must be set.

In the Simulink design the clock frequency of the ADC and FPGA can be set. Changing these settings may however cause some problems during compilation time. Increasing some of the latencies between the Simulink blocks allowed the compilation to finish. An ADC clock of 900 MHz and a FPGA clock of 225 MHz was applied and the .bof file was successfully created. It takes about 01h:45m for the compilation to be completed.

Unfortunately, none of the compiled model files ran successfully on the ROACH board. This included the provided model file, which was compile without any change. The tests done in Section 8.4.2 were performed with the provided .bof file. It is suspected that there might be compatibility issues since the model files have been updated to work on the ROACH 2 board and the ROACH that was used for testing is a ROACH 1 board. Compatibility issues could also arise with the MATLAB and Simulink versions used as well as the required software that must be downloaded from the CASPER website.

Much time was spent in an attempt to identify the issue, but it was eventually realised that a solution would not be found in time. This meant that the ROACH's bandwidth and KAT-7 ADC's attenuation cannot be set. A possible solution could be to try and

tune the BPF in the IF stage of the receiver so that the high frequency cut-off is slightly less. Physical attenuators can be added to the system if need be.

8.5 Conclusion

Some possible back-end options were considered and the ROACH board was chosen due to its availability and versatility. The available open source software was noted as a decisive advantage of the ROACH board, specifically Tutorial 3 - The Wideband Spectrometer.

Spectrometers were defined as instruments used to measure the PSD of a signal.

Tutorial 3 was implemented and a test signal was applied. The need to increase the bandwidth of the ROACH board was highlighted and the means to do so in the Simulink model file was presented.

While the provided .bof file ran successfully on the ROACH, any model file that was compiled did not run. This included the provided model file that was compiled without any changes. This might be caused by compatibility issues from a variety of sources. Even though the bandwidth and attenuation is not what is required, it was decided to use the successfully tested .bof file for future measurements.

Chapter 9

Measurements and Conclusion

This Chapter contains the final measurements of the project as well as the necessary conclusions. Some insight into possible future work on the project is discussed.

9.1 Receiver Measurements

Unfortunately, due to the faulty LNA's, a measurement of the Sun could not be performed. Any signals from radio astronomical sources are too weak to be detected without the required amplification. It was decided to test the different parts of the receiver without the LNA's in the laboratory.

9.1.1 RF Stage

The RF stage of the receiver was tested with and without the RFoF link. Figures 9.1 and 9.3 describes these two architectures.

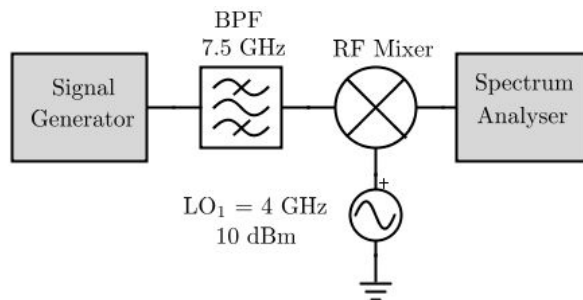


Figure 9.1: Configuration for the RF Stage Measurement

Figure 9.2 shows the input and output signals of the architecture in Figure 9.1. The most notable difference between the measured results and the simulations is the presence of the LO leakage harmonics at 8 GHz and 12 GHz. The output of the RF stage is as expected, with the desired signal at 3.5 GHz,

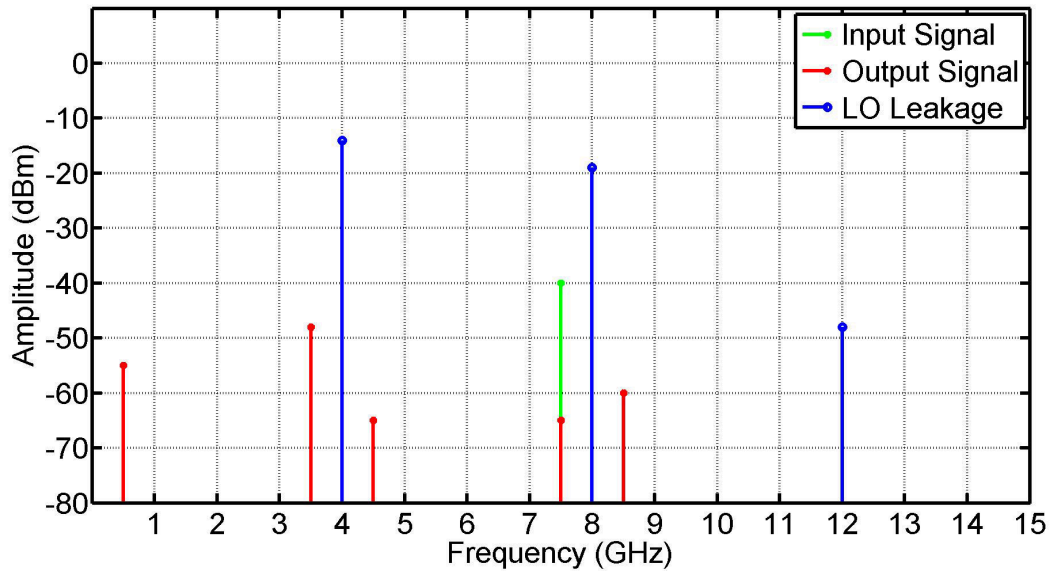


Figure 9.2: Measurement Results of RF Stage

Figure 9.3 shows the addition of the RFoF link.

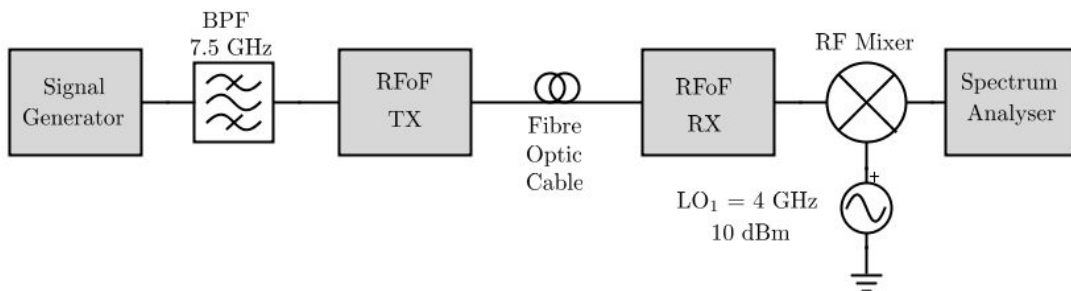


Figure 9.3: Configuration for the RF Stage with RFoF Measurement

Figure 9.4 shows the input and output signals of the architecture in Figure 9.3. Unsurprisingly, the output is almost identical to the output of Figure 9.2.

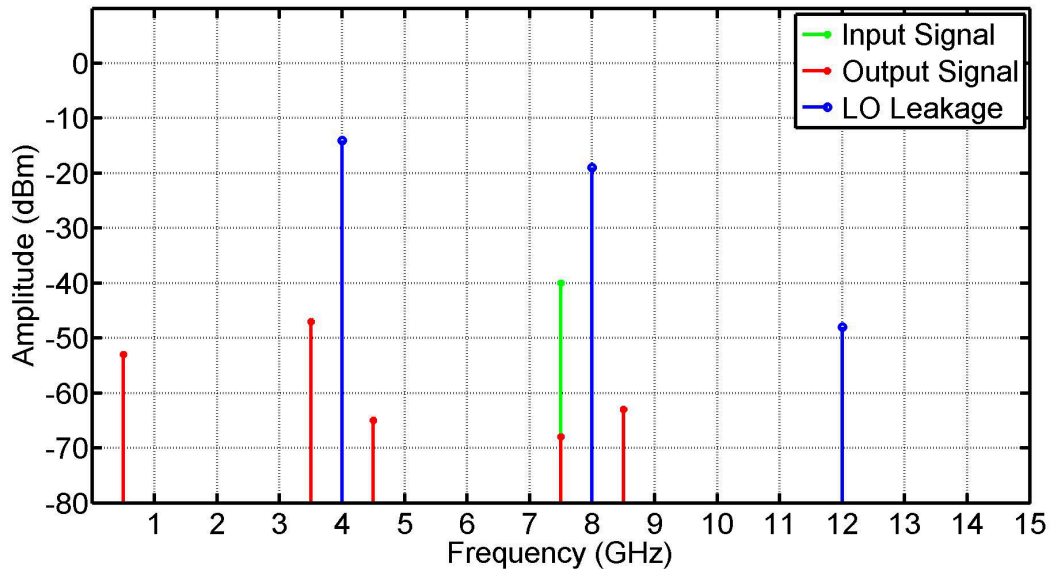


Figure 9.4: Measurement Results of RF Stage with Addition of RFoF Link

9.1.2 IF Stage

The IF stage of the receiver was tested with and without the LPF that was added at the end of the receiver simulations.

Figure 9.5 shows the initial IF stage architecture without the LPF.

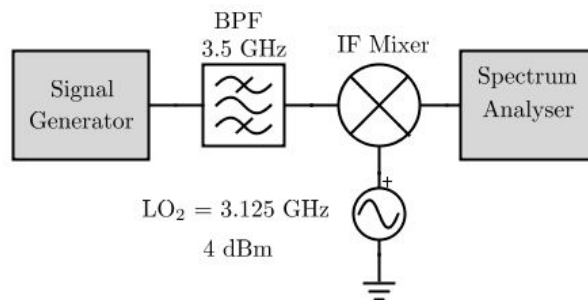


Figure 9.5: Configuration for the IF Stage Measurement

Figure 9.6 shows the input and output signal of the architecture in Figure 9.5. The output is as expected with the desired signal at 0.375 GHz. Once again the presence of the LO leakage and its harmonics are noticeable. There is some input signal leakage at 3.5 GHz and some mixed harmonics. The signal at 0.375 GHz has no nearby harmonics of undesired signals.

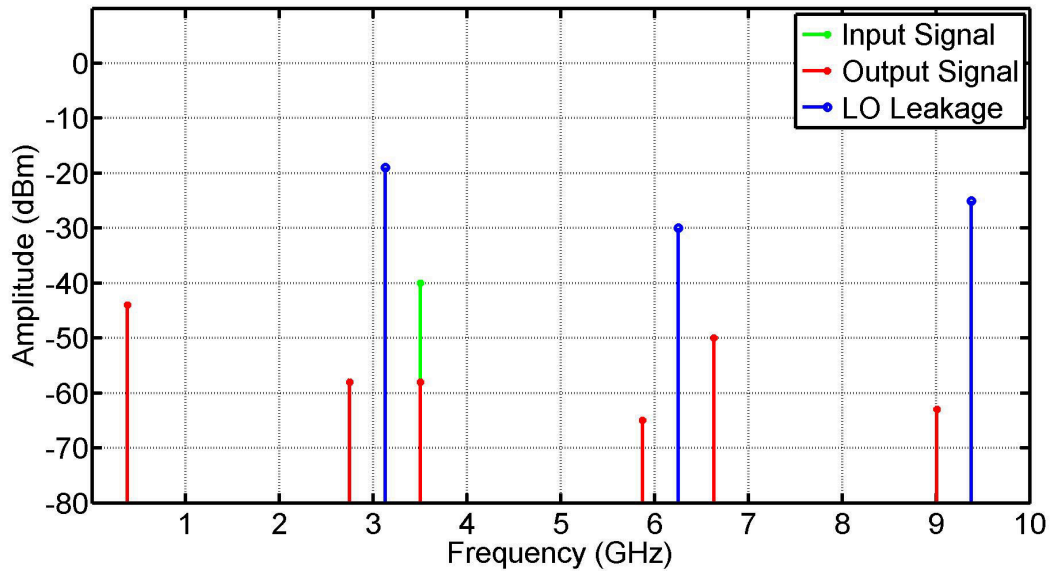


Figure 9.6: Measurement Results of IF Stage

Figure 9.7 shows the addition of the LPF.

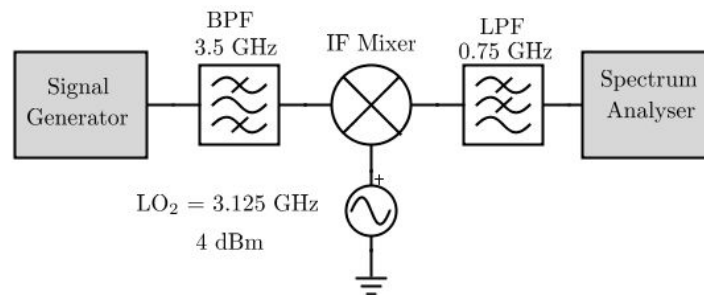


Figure 9.7: Configuration for the IF Stage with LPF Measurement

Figure 9.8 shows the input and output signal of the architecture in Figure 9.7. The addition of the LPF suppressed all the undesired signals, even the powerful LO leakage signals. The result is just the desired baseband signal at 0.375 GHz which will be the input to the ROACH.

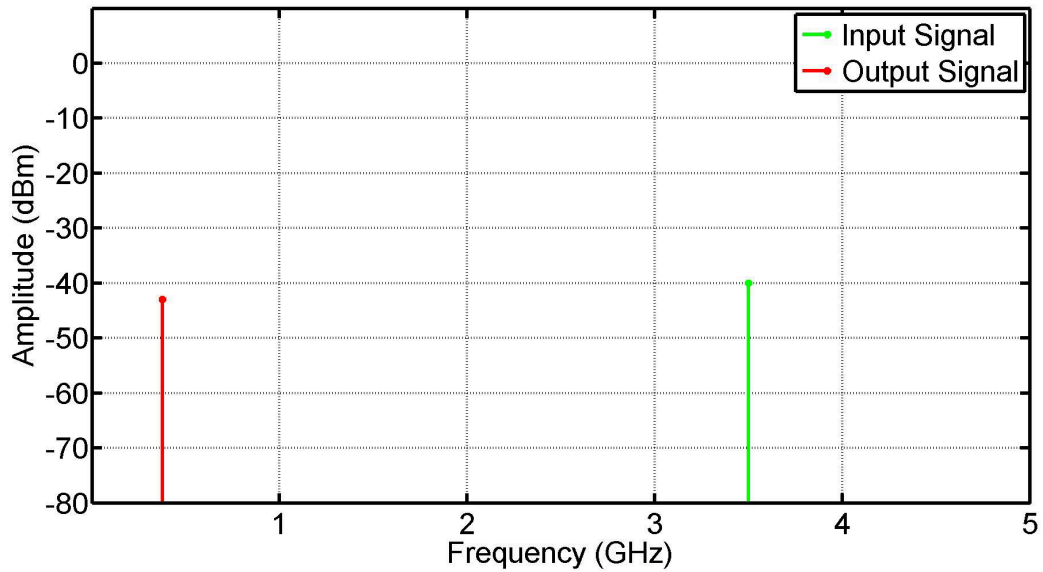


Figure 9.8: Measurement Results of IF Stage with Addition of LPF

9.1.3 Full Receiver

The full receiver was tested with and without the LPF.

Figure 9.9 shows the initial architecture.

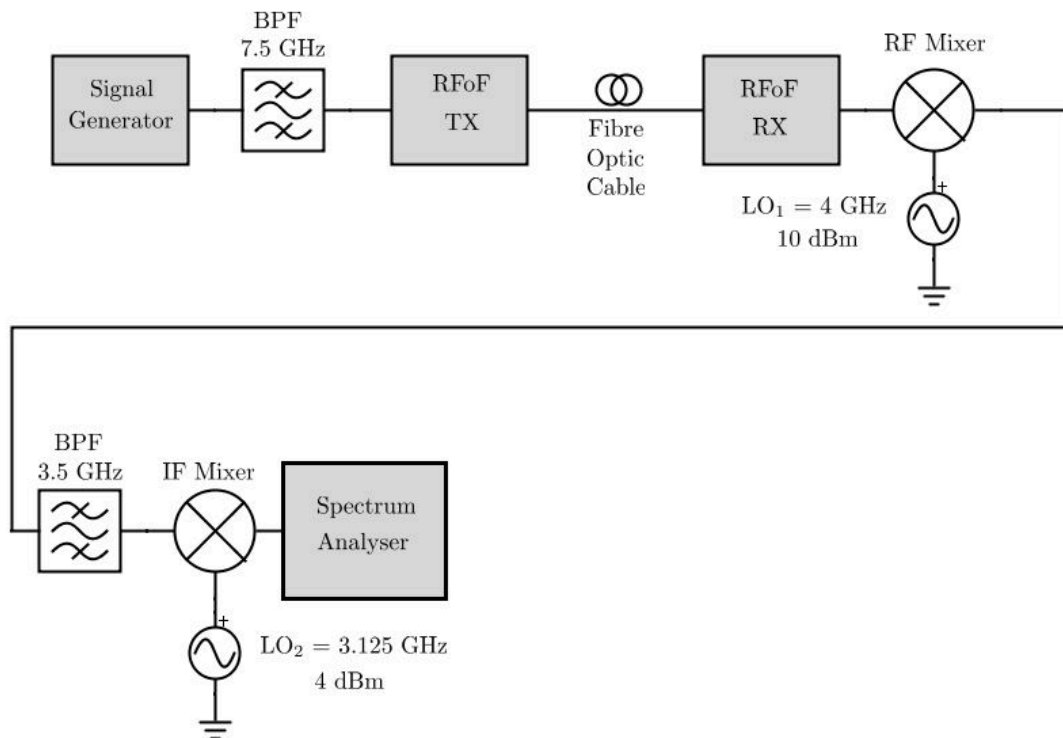


Figure 9.9: Configuration for the Full Receiver Measurement

Figure 9.10 shows the input and output signal of the architecture in Figure 9.9. The measured result compare well to the simulated results. The signal at 0.875 GHz, the LO₁ leakage mixed down by the IF mixer, was identified as a potential problem. This is what prompted the need for the LPF that was added for the next measurement.

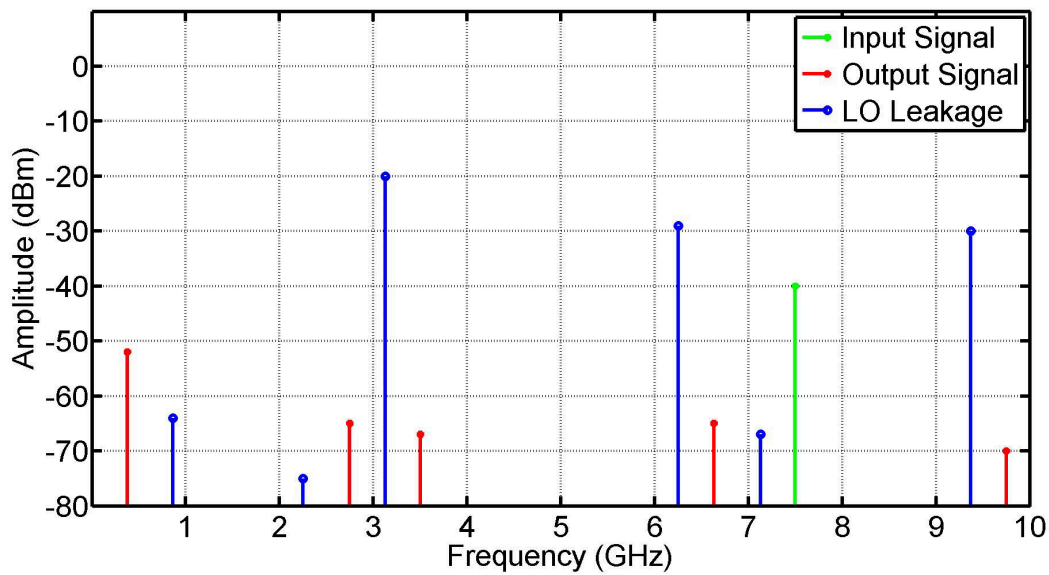


Figure 9.10: Measurement Results of Full Receiver

Figure 9.11 shows the addition of the LPF.

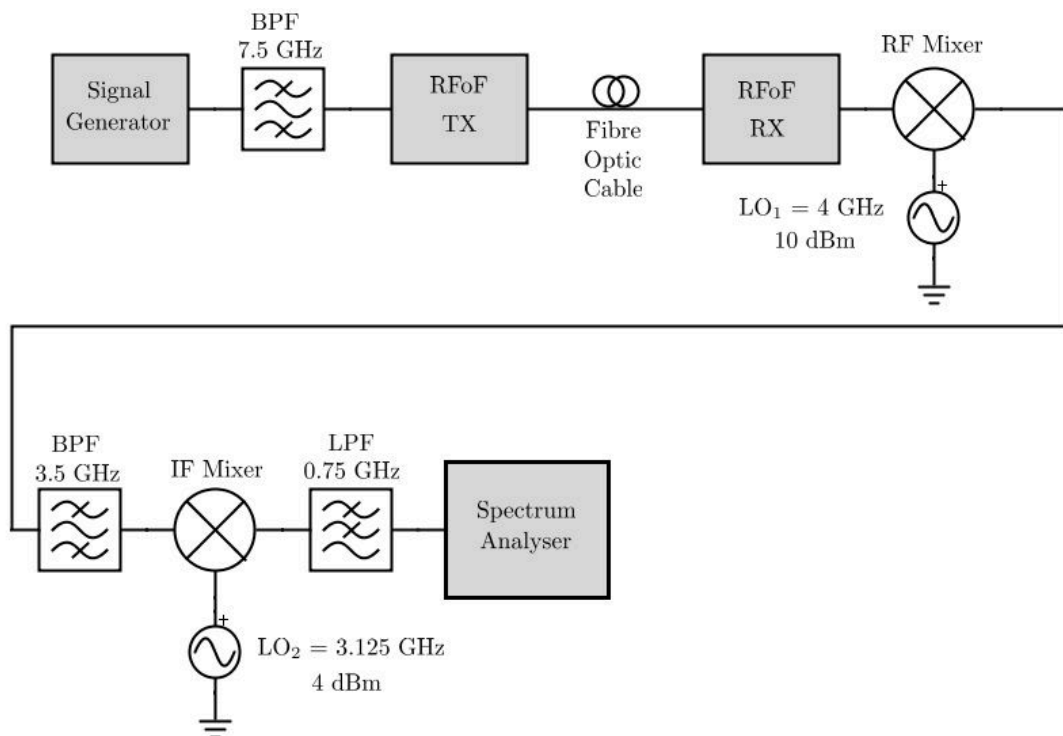


Figure 9.11: Configuration for the Full Receiver with LPF Measurement

Figure 9.12 shows the input and output signal of the architecture in Figure 9.11. Once again the LPF has provided excellent suppression of undesired signals. This validates the use of this type of receiver.

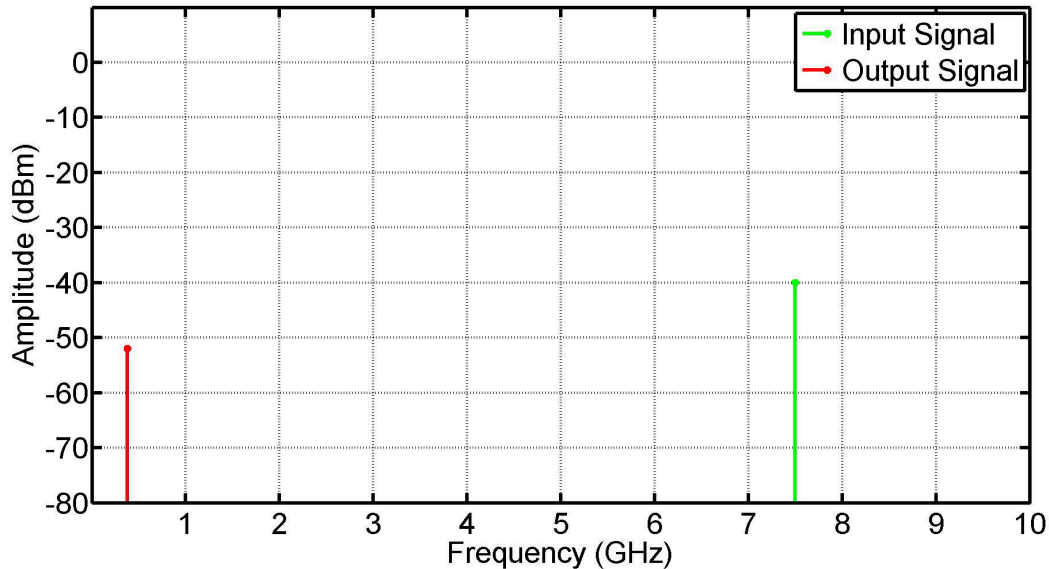


Figure 9.12: Measurement Results of Full Receiver with Addition of LPF

9.2 Summary

This thesis started by highlighting the growth in interest in radio astronomy due to the SKA. Because of the SKA, radio astronomers and engineers in South Africa are at the forefront of radio astronomical innovation. This helped to define the goal of this project - to develop a receiver system suitable for use in radio astronomy so that areas of concern in the design process can be identified. A measurement of the Sun was to be performed as the final measurement.

Some fundamental concepts of radio astronomy were defined. The most fundamental of these being the brightness of a source. The Sun and some other astronomical sources of radio signals were discussed. The frequency of operation was chosen as 7.5 GHz to avoid any RFI. The physical parabolic dish that was to be used was also discussed and the expected power to be received was shown.

The antenna that was to be used is the corrugated conical horn antenna. It is a BOR_1 type antenna, meaning that it is rotationally symmetric, and that only the A_1 and C_1 components of the Fourier expansion of the farfield contribute to the power radiated by the antenna. It also means that A_1 and C_1 fully describe the farfield, thanks to (3.2.3) and (3.2.4). The feed efficiencies of the antenna were defined and methods to reduce cross polarisation were discussed. Adding a step to the waveguide section of the horn was identified as such a method and it was incorporated into the design. The antenna was designed and optimised in CST using MATLAB to control the optimisation process. The antenna was built and measured. The measured results corresponded well to the simulated results.

The basic components of a receiver system were introduced and described. The mixing process as well as the concept of image frequencies were discussed. Local Oscillators were discussed and it was decided to use a Valon Frequency Synthesizer for the receiver. Various receiver architectures were considered and the double superheterodyne receiver was eventually chosen because of the lack of LO's for the other receiver types. Spur plots were performed to decide on an intermediate frequency of 3.5 GHz. Simulations were run in MWO to determine the response of the proposed receiver. It was determined that a LPF should be added before the back-end to suppress any intermodulation products that occur due to LO leakage. It was found that LO leakage was more prevalent than other intermodulation products.

Noise in radio receiver components was described and it was shown that components at the start of the receiver contribute the most to the noise figure of the system. Low noise amplifiers were then chosen based on a low noise requirement and frequency bands defined by the RF and IF receiver stages. Cascaded designs were performed in ADS. The PCB's of the amplifiers were also designed and simulated in ADS. This resulted in a simulation of the biasing networks, amplifiers and PCB's. The input and output tracks were tuned until the desired results were obtained. The LNA's were then manufactured at the E&E Department. The measured results however produced no gain and after some testing it was concluded that the cascaded components did not have adequate isolation between them. Due to time constraints new single stage amplifiers could not be designed and manufactured. The final measurement of the Sun cannot be completed without the required amplification.

The filters that were required for this project were the RF band-pass filter at 7.5 GHz, IF band-pass filter at 3.5 GHz and the LPF at the end of the receiver with a cut-off at 750 MHz. The low-pass Chebyshev prototype that was used for all the filters was described and the LPF required was designed from that prototype. The lumped element design was simulated in ADS using component models. The LPF was measured and it was shown that the measurements compare well to the simulated results. Band-pass filter transformation was then described and the use of admittance inverters and coupled resonators was introduced. Inter-digital filters were then explained and "*Getsinger's Charts*" were used to find the physical dimensions of the filters. The BPF's were simulated in CST and manufactured at the E&E Department. The measured results were slightly shifted in frequency, but still compared well to the simulated results.

Radio Frequency Over Fibre was used as an alternative to traditional signal transmission so that an incoming signal with high frequency could be transmitted without the need to mix down. RFoF essentially modulates an optical source with the incoming RF signal. This is then transmitted across a fibre optics cable. RFoF has many advantages such as low loss, centralisation and immunity to EMI. Such a link is however expensive. The construction of a fibre optics cable as well as the transmission of light along it was discussed. The RFoF link acquired from Accutronics was tested and the harmonics were identified to determine the linearity of the link. With an input of -50 dBm no harmonics could be detected. As expected, the more input power was used, the more power the harmonics had. It was determined that RFoF is a suitable method for signal transmission in radio astronomy.

The ROACH board was chosen as the back-end for this project, with 450 MHz as the

bandwidth of operation. The ROACH and its digitiser, the KAT-7 ADC, were both described. The KAT-7 ADC has a maximum of 1.5 GHz for the input clock frequency. This means that the maximum bandwidth of the unaltered ROACH and KAT-7 ADC is 750 MHz due to Nyquist sampling. It was decided to use the ROACH as a spectrometer, a common instrument used in radio astronomy. A spectrometer essentially displays the frequency response of a signal. The ROACH has open source tutorials that provide the required model files for such a spectrometer. The bandwidth of the tutorial is 400 MHz, while the required bandwidth of the final stage was slightly higher. Attempts were made to increase the bandwidth but these were unsuccessful. It was decided to use the 400 MHz bandwidth. To alter the provided model files or programme the FPGA of the ROACH requires much more time than what was available in this project.

The individual RF and IF stages were measured without the LNA's. Both stages performed as expected when measured. The LPF provided excellent suppression of undesired signals. The receiver is therefore appropriate for use with the ROACH board.

9.3 Future Work

Without the required LNA's a measurement of the Sun could not be taken. The receiver was however tested without the amplification and performed as expected. Possible future work for this project would be to design and manufacture Low Noise Amplifiers suitable for the receiver. If the same components are to be used, the new LNA's should be single-stage amplifiers or the isolation issue should be resolved.

Once the receiver has enough gain in the system measurement of astronomical radio sources can be performed.

Appendix A

Additional Equations

The equations that are listed here are used elsewhere in the thesis but are not essential to understanding the topics that are discussed. Section A.0.1 shows the full set of equations required to calculate the phase centre described in Section 3.2.7. Section A.0.2 shows the equations used by Matthaei [12] to design inter-digital filters, as described in Section 6.4.4.

A.0.1 Equations Used for Calculation of Phase Centre

Components of (3.2.26) Used to Calculate Phase Centre

$$a = \frac{I_{wc}^2}{I_w} - \left(\frac{I_{wc}}{I_w} \right)^2 \quad (\text{A.0.1})$$

$$b = \frac{I_{w\phi c}}{I_w} - \frac{I_{w\phi} I_{wc}}{I_w^2} \quad (\text{A.0.2})$$

$$c = 1 - \frac{I_{w\phi}^2}{I_w} + \left(\frac{I_{w\phi}}{I_w} \right)^2 \quad (\text{A.0.3})$$

Components of (A.0.1), (A.0.2) and (A.0.3)

$$I_w = \int_0^{\theta_0} w(\theta) d\theta \quad (\text{A.0.4})$$

$$I_{w\phi} = \int_0^{\theta_0} w(\theta) [\phi(\theta) - \phi(0)] d\theta \quad (\text{A.0.5})$$

$$I_{w\phi}^2 = \int_0^{\theta_0} w(\theta) [\phi(\theta) - \phi(0)]^2 d\theta \quad (\text{A.0.6})$$

$$I_{wc} = \int_0^{\theta_0} w(\theta) [\cos \theta - 1] d\theta \quad (\text{A.0.7})$$

$$I_{wc2} = \int_0^{\theta_0} w(\theta) [\cos \theta - 1]^2 d\theta \quad (\text{A.0.8})$$

$$I_{w\phi c} = \int_0^{\theta_0} w(\theta) [\cos \theta - 1] [\phi(\theta) - \phi(0)] d\theta \quad (\text{A.0.9})$$

Weighing Function

$$w(\theta) = |A(\theta) + C(\theta)| \tan \theta \quad (\text{A.0.10})$$

Phase of A and C

$$\phi(\theta) = \angle A(\theta) + C(\theta) \quad (\text{A.0.11})$$

A.0.2 Equations Used for Narrowband Inter-digital Filter Design

Calculation of θ_1

$$\theta_1 = \frac{\pi w_1}{2 w_0} \quad (\text{A.0.12})$$

Calculation of J

$J_{k,k+1}$ represents the value of the admittance inverters.

$$\frac{J_{01}}{Y_A} = \frac{1}{\sqrt{g_0 g_1 w'_1}} \quad (\text{A.0.13})$$

$$\frac{J_{k,k+1}}{Y_A} \Big|_{k=1 \text{ to } n-1} = \frac{1}{w'_1 \sqrt{g_k g_{k+1}}} \quad (\text{A.0.14})$$

$$\frac{J_{n,n+1}}{Y_A} = \frac{1}{\sqrt{g_n g_{n+1} w'_1}} \quad (\text{A.0.15})$$

Calculation of N

$N_{k,k+1}$ is simply used as a place-holder equation for (6.4.21) to (6.4.23).

$$N_{k,k+1} \Big|_{k=1 \text{ to } n-1} = \sqrt{\left(\frac{J_{k,k+1}}{Y_A}\right)^2 + \frac{\tan^2 \theta_1}{4}} \quad (\text{A.0.16})$$

Calculation of h

h is a dimensionless scale factor of admittance. It is specified arbitrarily to provide a convenient admittance level in the filter. h should be chosen to make (A.0.17) true [12].

$$\frac{2C_{k,k+1}}{\epsilon} + \frac{C_k}{\epsilon} = \frac{2C_{k,k-1}}{\epsilon} \Big|_{k=\frac{n}{2} \text{ for } n \text{ odd}, k=\frac{n+1}{2} \text{ for } n \text{ odd}} \approx 5.4 \quad (\text{A.0.17})$$

Calculation of M

Similar to $N_{k,k+1}$, M_1 and M_n are used as place-holder equations for (6.4.20), (6.4.21), (6.4.23), (6.4.24), (6.4.25) and (6.4.24).

$$M_1 = Y_A \left[\frac{J_{01}}{Y_A} \sqrt{h} + 1 \right] \quad (\text{A.0.18})$$

$$M_n = Y_A \left[\frac{J_{n,n+1}}{Y_A} \sqrt{h} + 1 \right] \quad (\text{A.0.19})$$

Appendix B

Matlab and CST

A Visual Basic (VBA) script can be used to control tools in the CST STUDIO. This includes CST MWS that was used in this project. It can be used for creation of elements or automation of CST tasks [63]. An interface to OLE automation (a windows inter-process communication mechanism) allows integration to the Windows environment which means certain programs like Microsoft Office, MATLAB, AutoCAD and MathCAD can be used in conjunction with CST.

Figure B.1 shows the flow of a basic MATLAB script that opens a CST model file, changes parameters, runs the solver and stores the results. Some of the script is shown to illustrate how the MATLAB-CST link is achieved.

```
%1. Initializing CST application
cst = actxserver('CSTStudio.application');
```

```
%2. Opening CST application
mws = invoke(cst, 'NewMWS');
invoke(mws, 'OpenFile', path);
```

```
%3. Setting units
units = invoke(mws, 'Units');
invoke(units, 'Geometry', 'mm');
invoke(units, 'Frequency', 'ghz');
invoke(units, 'Time', 'ns');
```

```
%4. Setting parameters
invoke(mws, 'StoreParameter', 'X', x);
invoke(mws, 'Rebuild');
```

```
%5. Invoking solver
solver = invoke(mws, 'Solver');
invoke(solver, 'FrequencyRange', fr1, fr2);
invoke(solver, 'Start');
```

```
%6. Getting S11 Results%
s11_path = strcat(strcat(global_results_path,filename), '_s11_data.txt');
invoke(mws, 'SelectTreeItem', '1D Results\S-Parameters');
s11p = invoke(mws, 'Plot1D');
invoke(s11p, 'GetCurveIndexOfCurveLabel', 'S11');
invoke(s11p, 'Plot');
```

```
%7. Storing Results
export = invoke(mws, 'ASCIIExport');
invoke(export, 'Reset');
invoke(export, 'FileName', s11_path);
invoke(export, 'Mode', 'FixedWidth');
invoke(export, 'Step', 0.1);
invoke(export, 'SetVersion', '2010');
invoke(export, 'Execute');
release(export)
```

```
%8. Saving Model File
invoke(mws, 'Save');
```

```
%9. Quitting CST
invoke(mws, 'Quit');
```

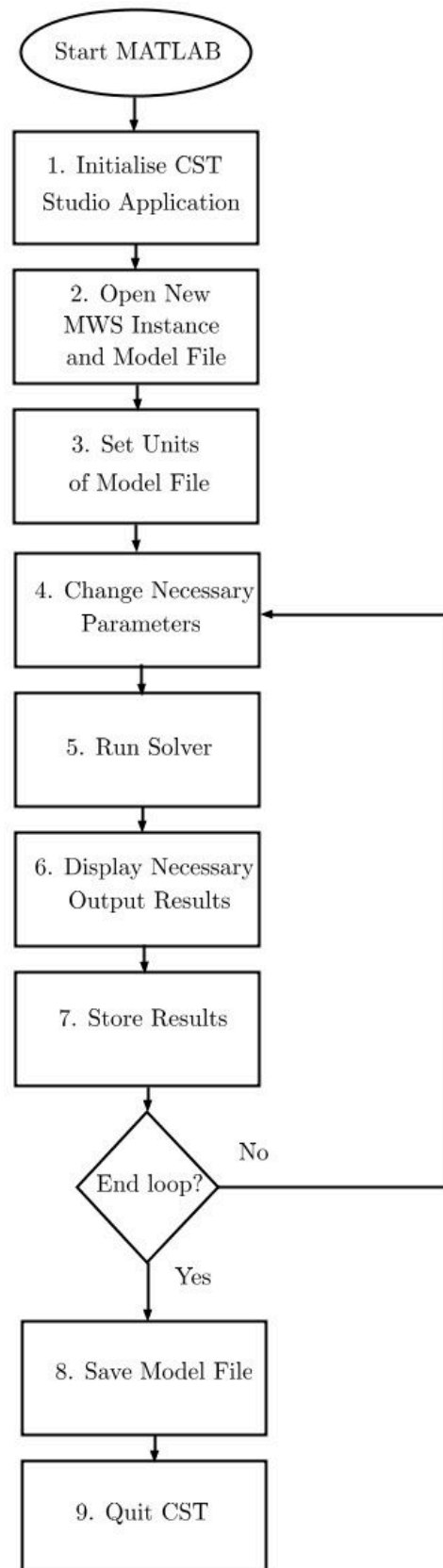


Figure B.1: Basic MATLAB-CST Program

Appendix C

Complete Set of Optimisation Results

The Figures shown here are the complete set of optimisation results. Section 3.4.3 shows the summarised results. Parameters that were optimised include efficiency, field pattern, Γ and cross polarisation. For each optimisation all other results are shown as well.

C.1 Efficiency Optimisation

To optimise efficiency, the error function was defined as $1 - \epsilon$. The optimisation function minimizes this, and thus maximises the efficiency. Optimised maximum efficiency at 7.5 GHz was found to be 68 %. Other results were acceptable.

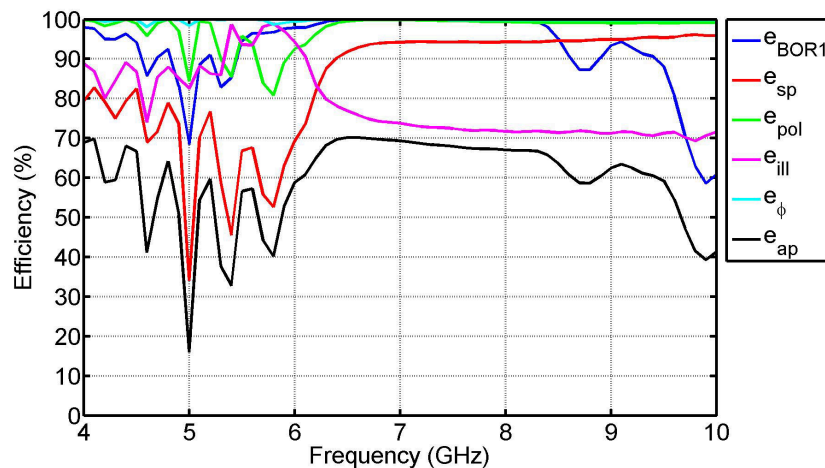


Figure C.1: Efficiencies of Efficiency Optimised Antenna

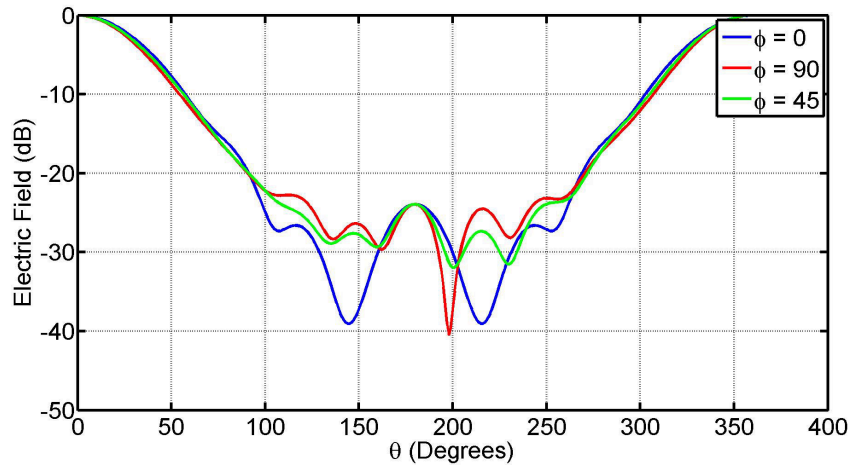


Figure C.2: Field Pattern of Efficiency Optimised Antenna

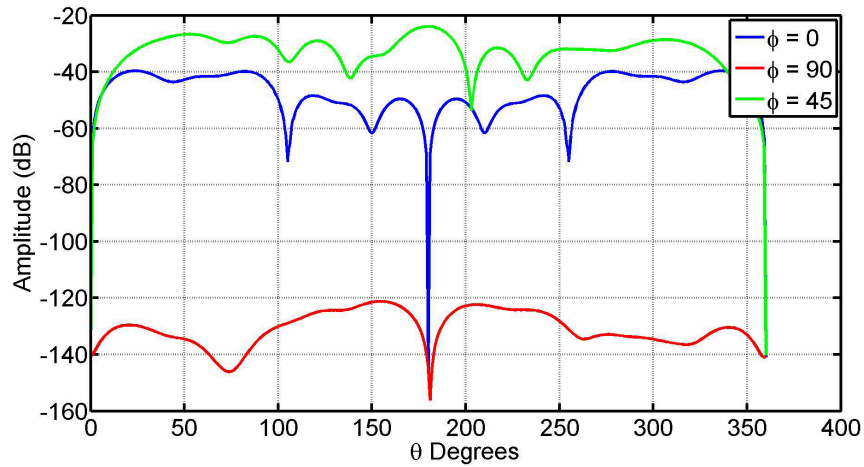
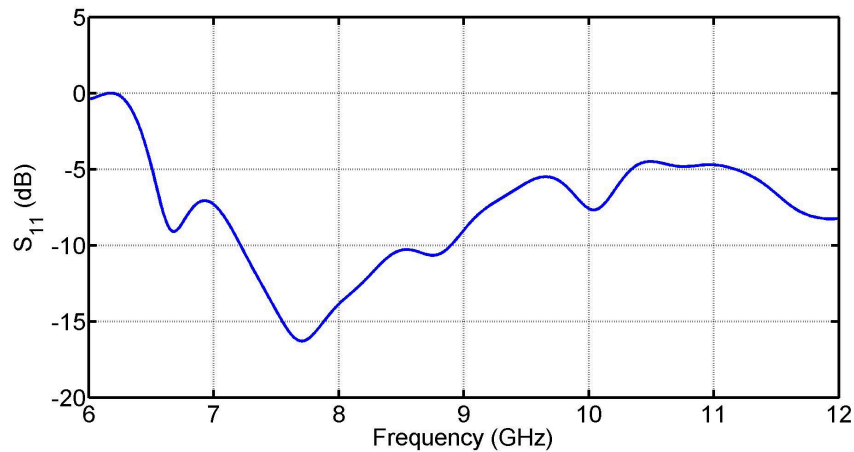


Figure C.3: Cross Polarisation of Efficiency Optimised Antenna

Figure C.4: Γ of Efficiency Optimised Antenna

C.2 Pattern Optimisation

To optimise the field pattern, the error function was defined so that the value of the fields at the subtended angle θ_0 is the same. This was done to ensure a symmetric field within the subtended angle. The optimised field pattern is symmetrical, especially within the subtended angle. The other results are acceptable.

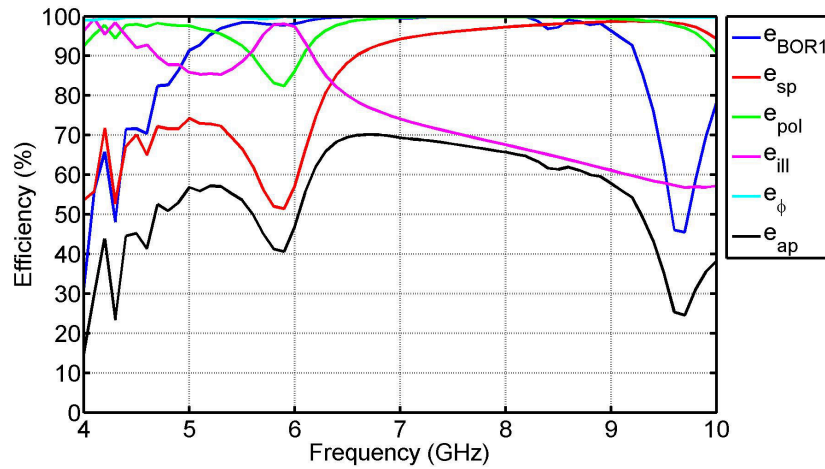


Figure C.5: Efficiencies of Field Pattern Optimised Antenna

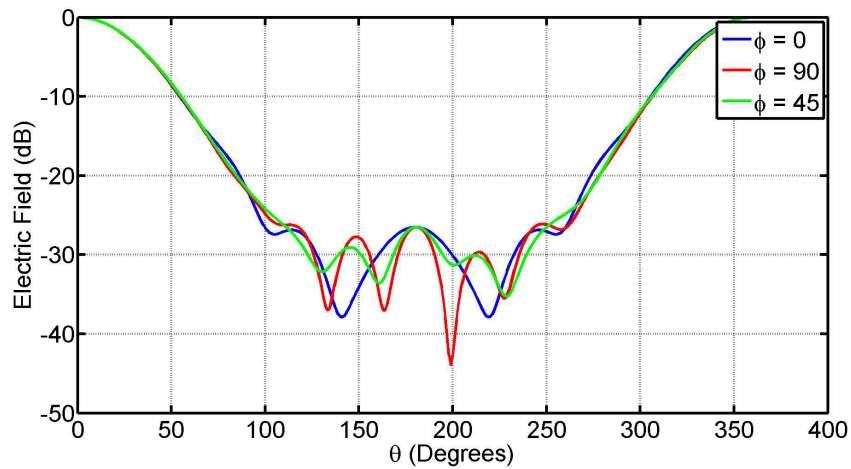


Figure C.6: Field Pattern of Field Pattern Optimised Antenna

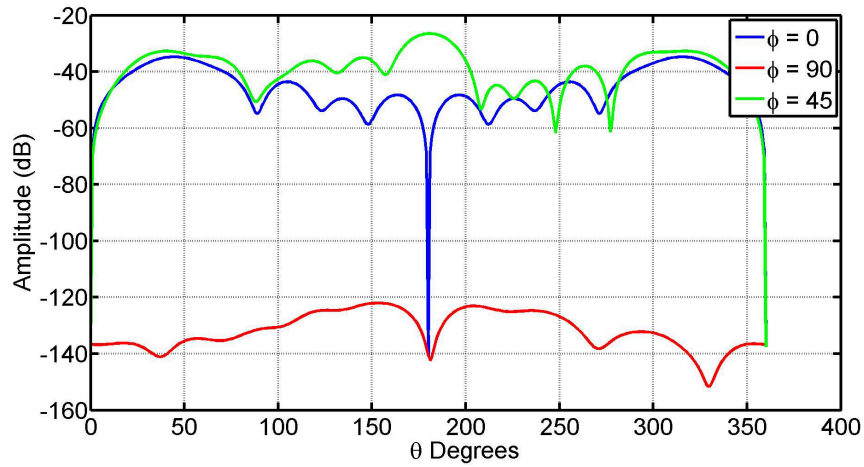
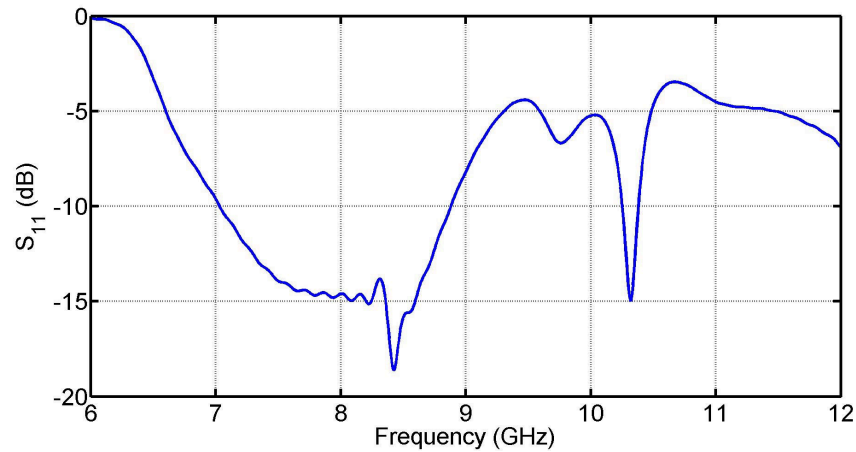


Figure C.7: Cross Polarisation of Field Pattern Optimised Antenna

Figure C.8: Γ of Field Pattern Optimised Antenna

C.3 Γ Optimisation

To optimise Γ , the error function was defined simply as $\Gamma_{7.5GHz}$. The optimisation function then minimises Γ to find the lowest possible value. The optimised Γ was found to be -16 dB at 7.5 GHz. The other results are acceptable.

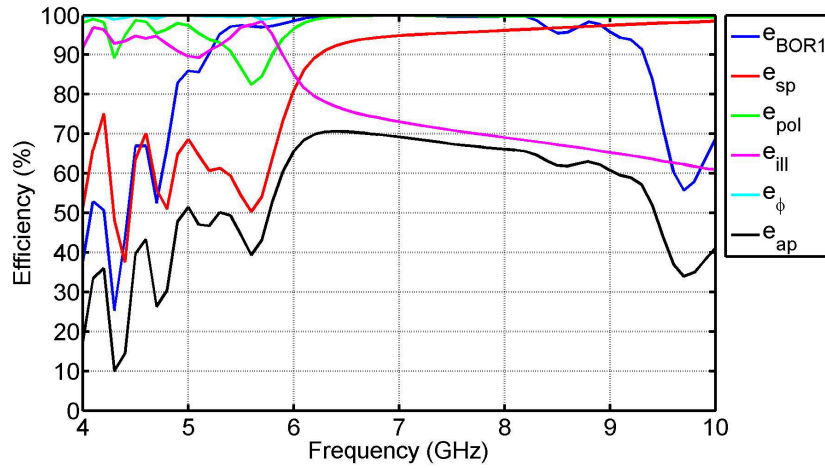


Figure C.9: Efficiencies of Γ Optimised Antenna

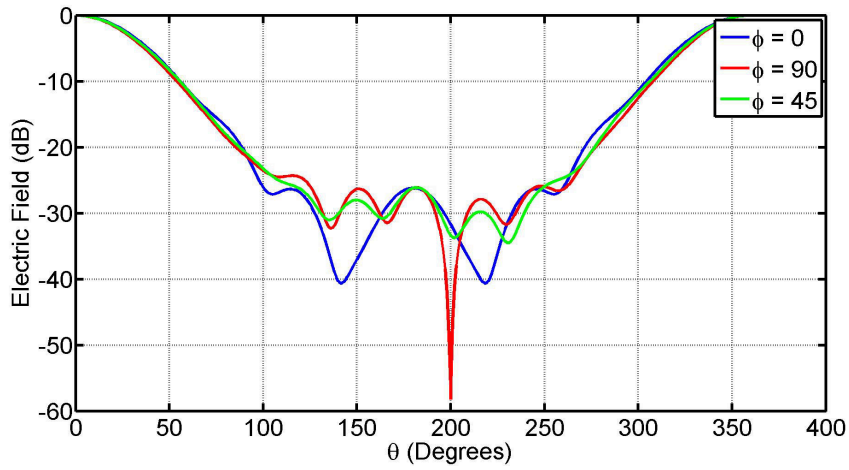


Figure C.10: Field Pattern of Γ Optimised Antenna

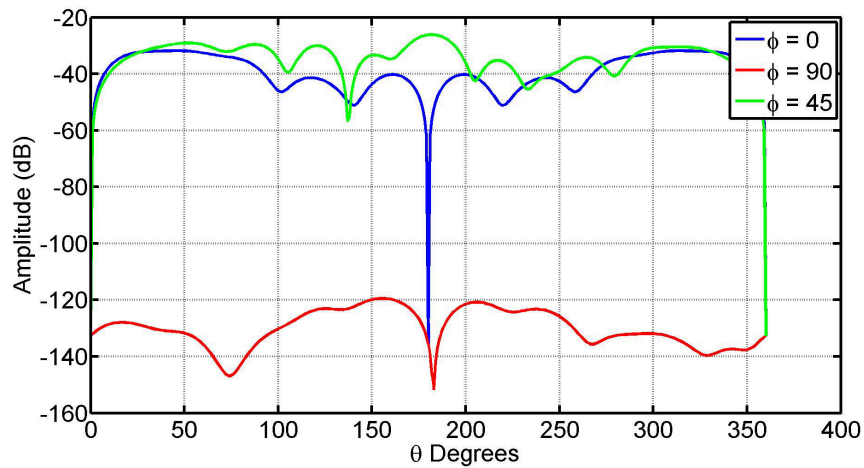
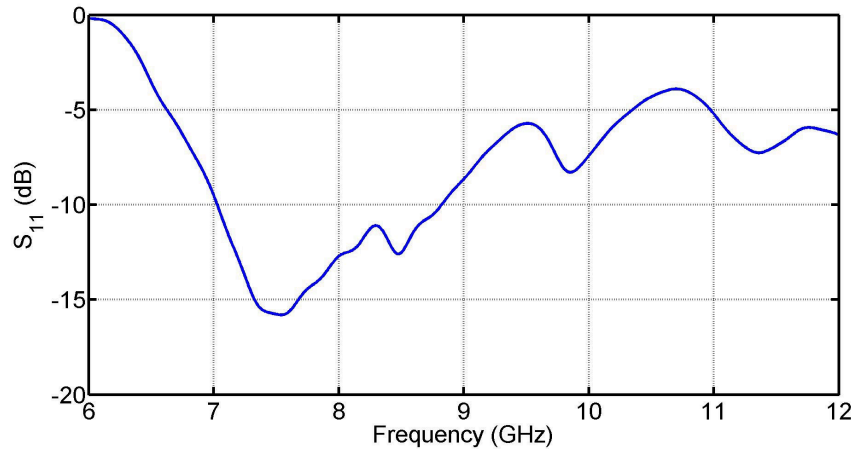


Figure C.11: Cross Polarisation of Γ Optimised Antenna

Figure C.12: Γ of Γ Optimised Antenna

C.4 Cross Polarisation Optimisation

To optimise cross polarisation, the error function was defined as the sum of the minimum of cross polarisations for $\phi = 0$ and $\phi = 90$. The optimisation function then minimises the sum and thus minimised both values. The optimised cross polarisation was similar to other cross polarisation results. The other results are acceptable.

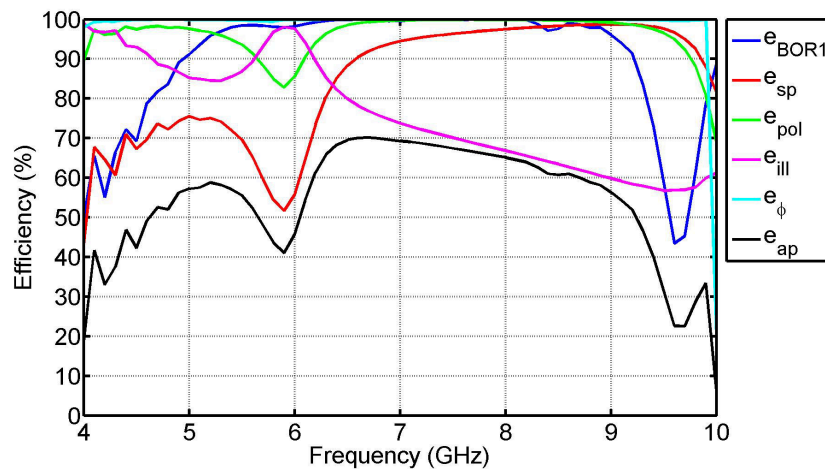


Figure C.13: Efficiencies of Cross Polarisation Optimised Antenna

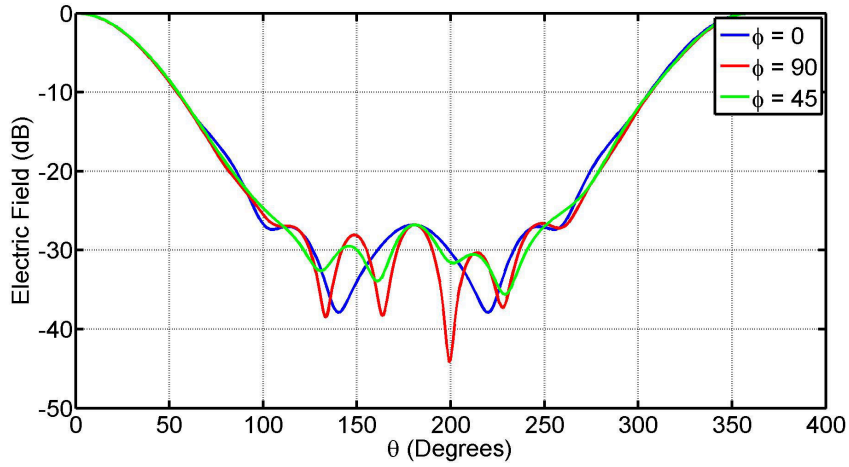


Figure C.14: Field Pattern of Cross Polarisation Optimised Antenna

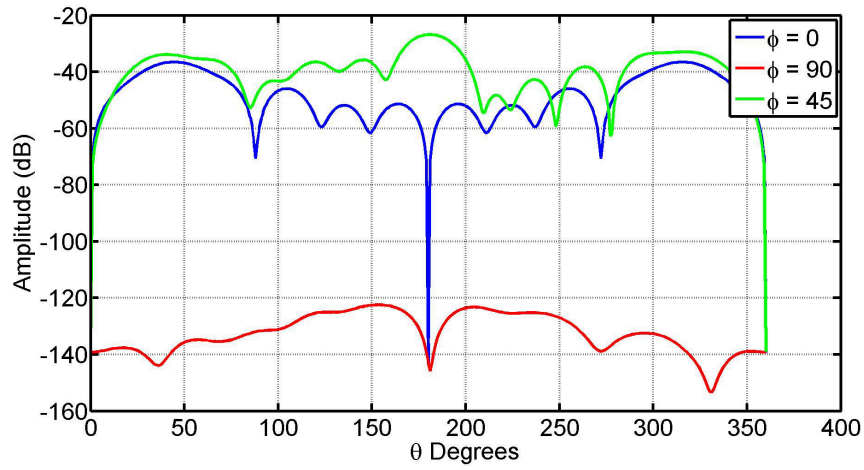
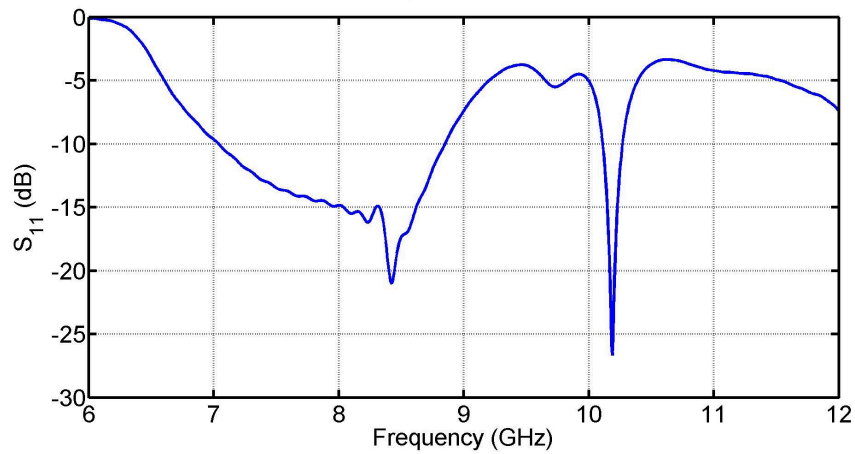


Figure C.15: Cross Polarisation of Cross Polarisation Optimised Antenna

Figure C.16: Γ of Cross Polarisation Optimised Antenna

Appendix D

TraX Specifications

TraX Interconnect (pty) ltd was used to manufacture the PCB's required for the LFP and LNA's. The specifications that need to be met by PCB designs are briefly summarised in Table D.1.

Specification	Value
Minimum Track	0.125 mm
Minimum Gap	0.125 mm
Smallest Mechanically Drilled Holes	0.25 mm
Final Cu Thickness for 0.15 mm Track Width	30 μm
Copper to Edge	0.3 mm
Chamfer Angles	30 degrees

Table D.1: TraX PCB Specifications

Appendix E

Components and PCB Layouts

The components that were used for the LPF and the LNA's are listed here. The PCB's that were designed are also shown. Figures are not to scale.

E.1 Low-Pass Filter

The components used in the lumped element design are a combination of inductors and capacitors.

Component	Value	Compromised Value
C_1	2.8 pF	3.7 pF
C_2	7.5 pF	8.3 pF
C_3	8.3 pF	8.3 pF
L_1	14.95 nH	16 nH
L_2	19.48 nH	20 nH
L_3	20.18 nH	20 nH

Table E.1: Low Pass Filter Ideal and Compromised Component Values

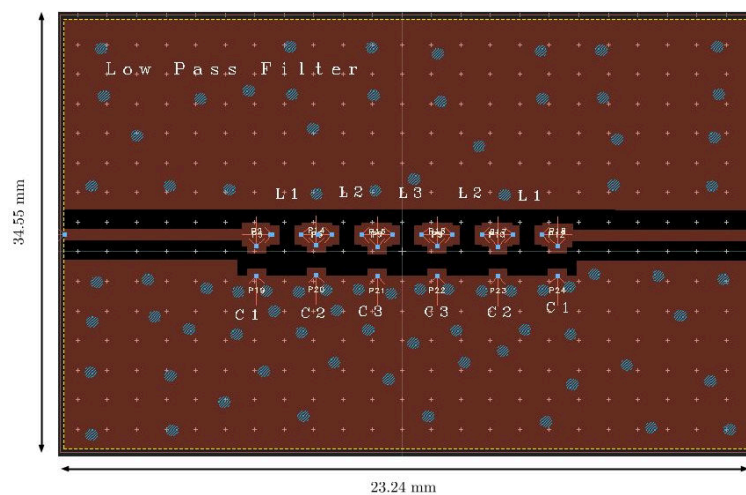


Figure E.1: Lumped Element Low Pass Filter PCB Design in ADS

E.2 IF LNA

The IF LNA required inductors and capacitors for its biasing network. A voltage regulator was added to ensure the supply voltage was precisely what was needed. This also help to reduce noise. A feed through capacitor was used to supply an external voltage to the LNA through the metallic enclosure.

Component	Value
$C_1 - C_3$	$0.1 \mu\text{F}$
C_4	$1 \mu\text{F}$
C_5	1.2 nF
C_6	68 pF
L_1	470 nH
LNA	Analog Devices - ADL5602
Voltage Regulator	Texas Instruments - LP3985-5
Feed Through Capacitor	Tusonix - 4403-040LF

Table E.2: IF LNA Component Values

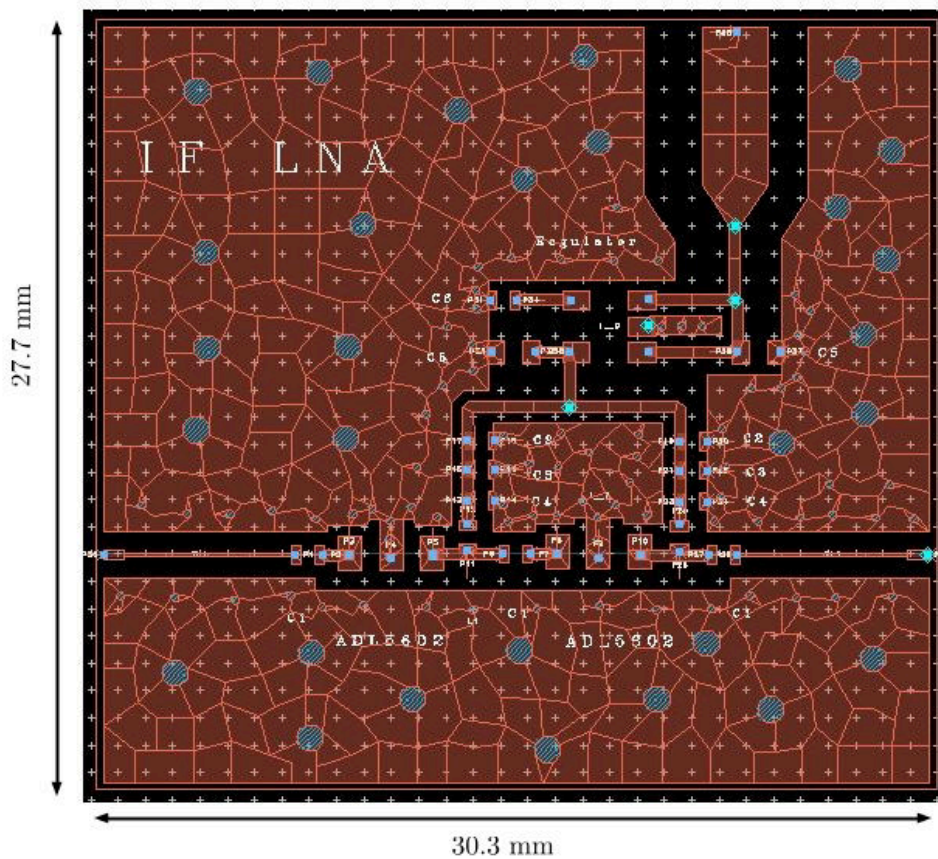


Figure E.2: PCB of IF Low Noise Amplifier Designed in ADS

E.3 RF LNA

The RF LNA works in a similar way to the IF LNA. A voltage regulator and feed through capacitor are also used.

Component	Value
$C_1 - C_2$	$0.1 \mu\text{F}$
$C_3 - C_6$	100 pF
L_1	6.8 nH
R_1	10 k Ω
LNA	Avago - VMMK-3803
Voltage Regulator	Texas Instruments - LP3985-3
Feed Through Capacitor	Tusonix - 4403-040LF

Table E.3: RF LNA Component Values

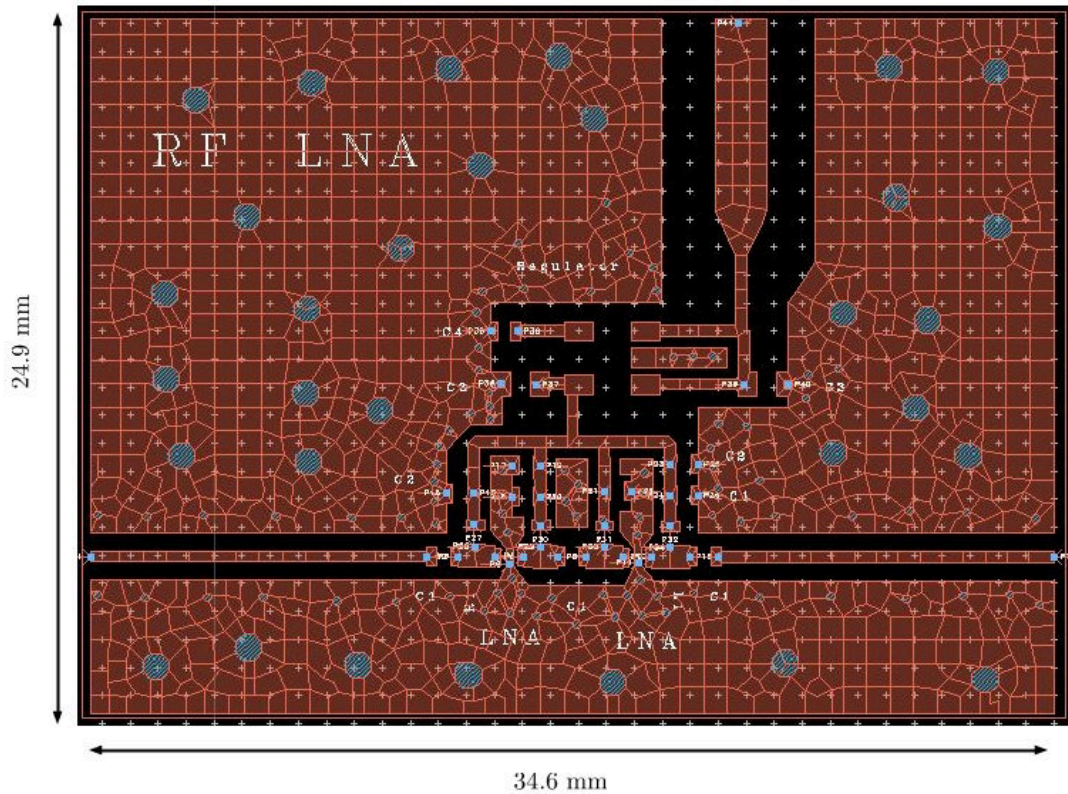


Figure E.3: PCB of RF Low Noise Amplifier Designed in ADS

Appendix F

Photos

Photographs of various system components are shown here.



Figure F.1: Photos of Conical Corrugated Horn Antenna

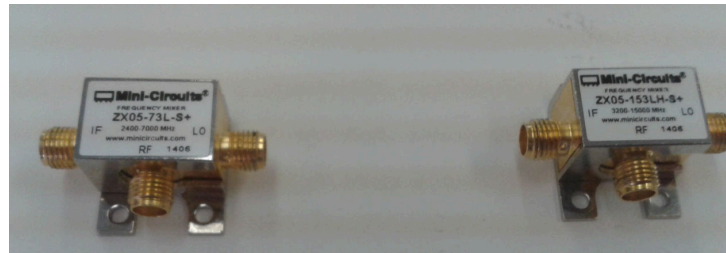


Figure F.2: Photo of Mixers

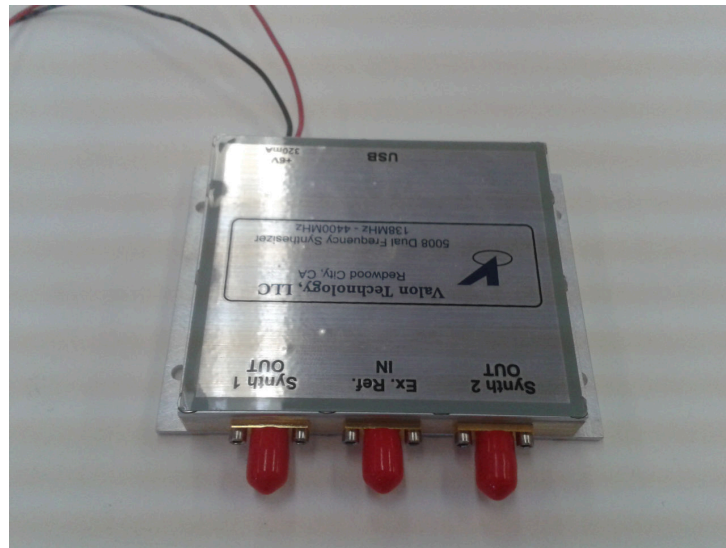


Figure F.3: Photo of Valon Frequency Synthesizer

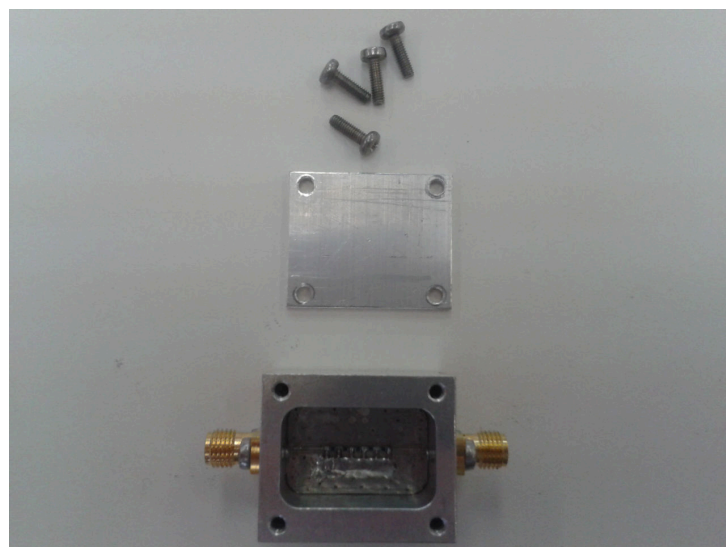


Figure F.4: Photo of Low-Pass Filter

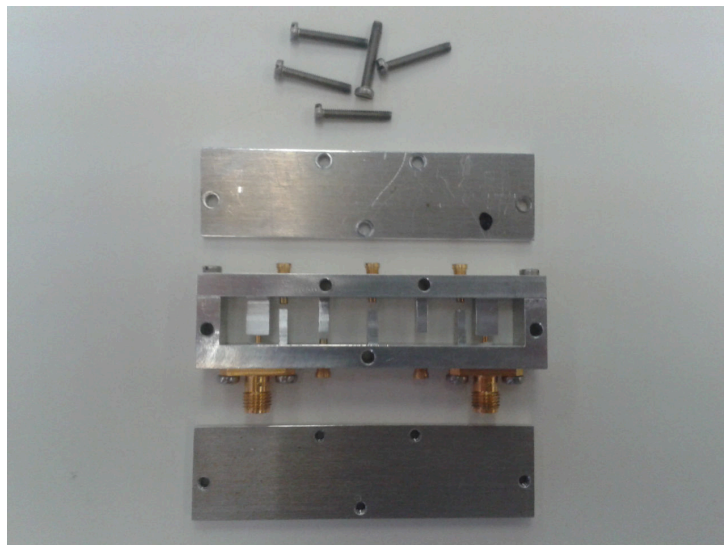


Figure F.5: Photo of RF Band-Pass Filter

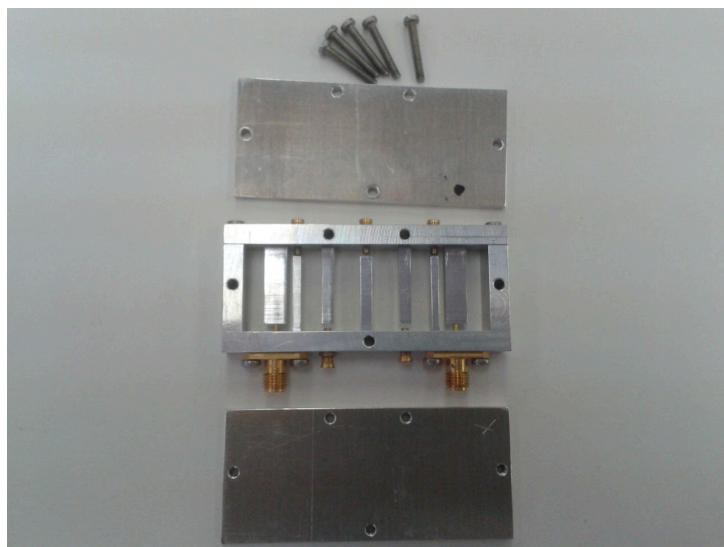


Figure F.6: Photo of IF Band-Pass Filter

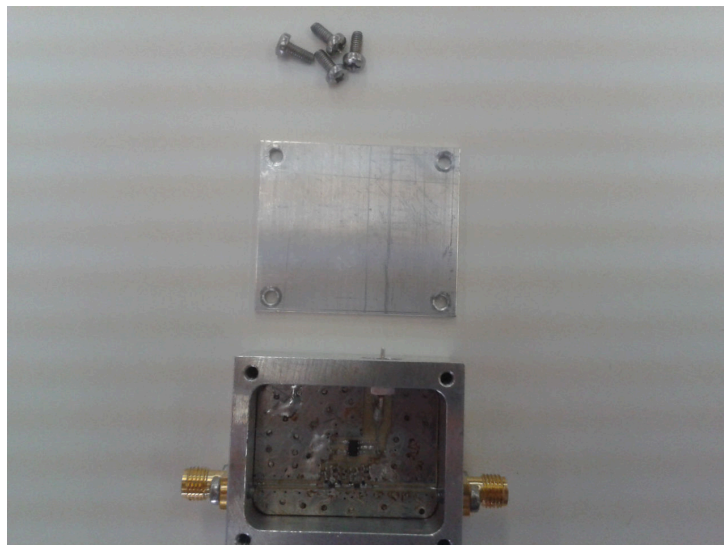


Figure F.7: Photo of RF Low Noise Amplifier

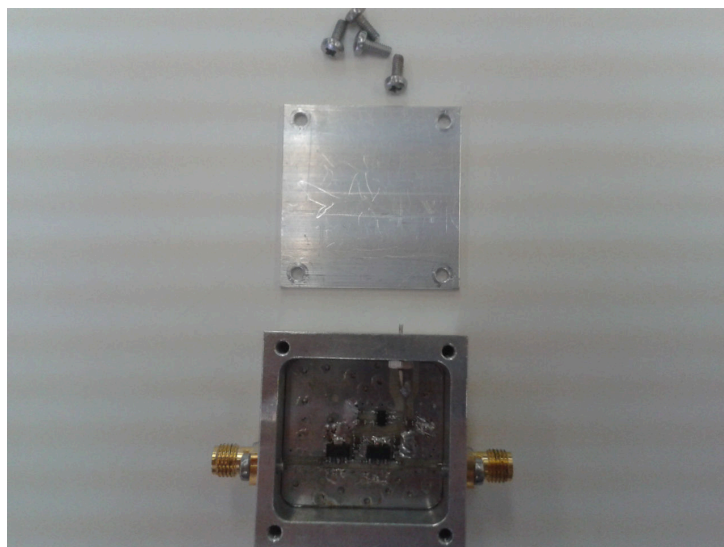


Figure F.8: Photo of IF Low Noise Amplifier



Figure F.9: Photos of Radio Frequency Over Fibre Link



Figure F.10: Photo of 30 m Fibre Optics Cable



Figure F.11: Photo of ROACH Board with Clock Synthesizer

Bibliography

- [1] C. Mihos and P. Harding. (2013, August) Astronomical coordinates. Department of Astronomy, CWRU. [Online]. Available: <http://burro.cwru.edu/Academics/Astr306/Coords/coords.html>
- [2] J. Kraus, *Radio Astronomy*, 2nd ed. Cynus-Quasar, 1986.
- [3] F. Bradaschia. (2013, August) What is amateur radio astronomy? Primaluce Lab. [Online]. Available: <http://www.primalucelab.com/radioastronomy/blog/amateur-radio-astronomy-radioastronomia-amatoriale>
- [4] T. Wilson. (2011, November) Techniques of Radio Astronomy. Cornell University. [Online]. Available: <http://arxiv.org/abs/1111.1183>
- [5] P. Kildal, "Combined E- and H-Plane Phase Centers of Antenna Feeds," *IEEE Transactions on Antennas and Propagation*, vol. 31, no. 1, pp. 199–202, 1983.
- [6] A. Magus. (2013) Waveguide-fed scalar corrugated conical horn. [Online]. Available: http://www.antennamagus.com/database/antennas/antenna_page.php?id=126
- [7] Proc Potter. antenna.cz. [Online]. Available: http://antenna.cz/nn-15_POTTER/aboutpotter/index.html
- [8] C. A. Balanis, *Modern Antenna Handbook*. Wiley. com, 2011.
- [9] D. M. Pozar, *Microwave and RF Design of Wireless Systems*. John Wiley & Sons, Inc., 2000.
- [10] *Avago Technologies - VMMK-3803*, 2014.
- [11] *Analog Devices - ADL5602*, 2013.
- [12] G. Matthaei, "Interdigital Band-Pass Filters," *Transactions on Microwave Theory and Techniques*, pp. 479–491, 1962.
- [13] W. Getsinger, "Coupled Rectangular Bars Between Parallel Plates," *IRE Transactions on Microwave Theory and Techniques*, pp. 65–72, 1962.
- [14] T. Ceramics. Microwave Tuning Elements. Temex Ceramics. [Online]. Available: <http://www.temex-ceramics.com/site/fichiers/DatasheetTuning.pdf>
- [15] I. Networks. (2009) Calculating fiber loss and distance. IMC. [Online]. Available: <http://www.bb-elec.com/Learning-Center/All-White-Papers/Fiber/Calculating-Fiber-Loss/Calculating-Fiber-Loss.pdf>

- [16] T. F. O. Association. Optical fiber. [Online]. Available: <http://www.thefoa.org/tech/ref/basic/fiber.html>
- [17] “General notice,” ICASA, Tech. Rep., 2004.
- [18] (2012, January) Radio astronomy frequency allocations. [Online]. Available: http://www.ukaranet.org.uk/basics/frequency_allocation.htm
- [19] (2003, November) Radio frequencies of the most important spectral lines. [Online]. Available: <http://www.craf.eu/iaulist.htm>
- [20] “MATLAB and Statistics Toolbox Release R2010a,” The Mathworks, Inc.
- [21] “CST Studio Suite 2013,” Computer Simulation Technology.
- [22] “Microwave Office 10,” AWR Corporation.
- [23] “Advanced Design System 2013,” Keysight.
- [24] Radio astronomy tutorial. MIT Haystack Observatory. [Online]. Available: <http://www.haystack.edu/edu/undergrad/materials/RadioAstronomy.html>
- [25] Administrator. (2013, August) Karl jansky: The father of radio astronomy. Astronotes. [Online]. Available: <http://www.armaghplanet.com/blog/karl-jansky-the-father-of-radio-astronomy.html>
- [26] E. Gregerson and D. Promeet. Radio source. Encyclopaedia Britannica. [Online]. Available: <http://www.britannica.com/EBchecked/topic/488960/radio-source>
- [27] (2014, March) Everything you wanted to know about the ska. Square Kilometre Array (SKA). [Online]. Available: <http://www.ska.ac.za/qa/index.php>
- [28] D. Davidson, “Radio astronomy lectures,” 2013.
- [29] P. J. Bevelacqua. (2014) Antenna Theory. [Online]. Available: <http://www.antenna-theory.com/basics/polarization.php>
- [30] L. M. Correia, *Mobile Broadband Multimedia Networks: Techniques, Models and Tools for 4G*. Academic Press, 2010.
- [31] P. J. Bevelacqua. (2014) Antenna Theory. [Online]. Available: <http://www.antenna-theory.com/basics/gain.php>
- [32] P. Kildal, “Factorization of the Feed Efficiency of Paraboloids and Cassegrain Antennas,” *IEEE Transactions on Antennas and Propagation*, vol. 33, no. 8, pp. 903–908, 1985.
- [33] P. Kildal and Z. Sipus, “Classification of Rotationally Symmetric Antennas as Types BOR0 and BOR1,” *IEEE Antennas and Propagation Magazine*, vol. 37, no. 6, pp. 114–117, 1995.
- [34] J. Yang, S. Pivnenko, and P.-S. Kildal, “Comparison of Two Decade-bandwidth Feeds for Reflector Antennas: The Eleven Antenna and Quadridge horn,” in *Antennas and Propagation (EuCAP), 2010 Proceedings of the Fourth European Conference on*. IEEE, 2010, pp. 1–5.

- [35] J. J. Z. J. Sanz Subirana and M. Hernández Pajares. (2011) Antenna Phase Centre. Technical University of Catalonia, Spain. [Online]. Available: http://www.navipedia.net/index.php/Antenna_Phase_Centrep
- [36] C. Balanis, *Modern Antenna Handbook*. Wiley, 2008. [Online]. Available: <http://books.google.co.za/books?id=t7HDEJDnjiQC>
- [37] C. A. Balanis, *Antenna Theory: Analysis and Design*, 3rd ed. John Wiley & Sons, 2005.
- [38] J. A. Nelder and R. Mead, "A simplex method for function minimization," *The Computer Journal*, vol. 7, no. 4, pp. 308–313, 1965. [Online]. Available: <http://comjnl.oxfordjournals.org/content/7/4/308.abstract>
- [39] I. Poole. Pll phase locked loop tutorial. Radio Electronics. [Online]. Available: <http://www.radio-electronics.com/info/rf-technology-design/pll-synthesizers/phase-locked-loop-tutorial.php>
- [40] Receiver architectures. [Online]. Available: <http://rf-circuits.info/radio/receiver-architectures/>
- [41] (1998) Superheterodyne receivers. [Online]. Available: <http://fas.org/man/dod-101/navy/docs/es310/superhet.htm>
- [42] I. Poole. Superheterodyne radio receiver tutorial. [Online]. Available: <http://www.radio-electronics.com/info/rf-technology-design/superheterodyne-radio-receiver/basics-tutorial.php>
- [43] J. Jansen van Rensburg, "The design of a two-element correlation interferometer operating at l-band," Master's thesis, Stellenbosch University, 2012.
- [44] D. Pozar, *Microwave Engineering, 4th Edition*. Wiley Global Education, 2011. [Online]. Available: <http://books.google.co.za/books?id=JegbAAAQBAJ>
- [45] (2001, July) Noise in antennas. Stanford University School of Engineering. [Online]. Available: http://web.stanford.edu/class/ee252/handouts/antenna_noise.pdf
- [46] Noise. Queen's University Department of Physics, Engineering Physics and Astronomy. [Online]. Available: <http://www.physics.queensu.ca/~phys352/lect04.pdf>
- [47] S. Turner. (2007, January) Johnson-nyquist noise. Wireless Systems Engineering Inc. [Online]. Available: <http://www.claysturner.com/dsp/Johnson-Nyquist%20Noise.pdf>
- [48] "Smith 3.1," University of Applied Science.
- [49] "TXLine 2003," AWR Corporation.
- [50] S. Maas, "Coaxial Resonator Filters," Master's thesis, Stellenbosch University, 2011.
- [51] D. Kajfez, "Q factor measurements, analog and digital," *University of Mississippi Dept. of EE, www.ee.olemiss.edu/darko/rfqmeas2b.pdf*, 2011.
- [52] P. Meyer, "Coupled TM Lines," *Mircowave Networks* 813.

- [53] G. Matthaei, "Design of Wide-Band (and Narrow-Band) Band-Pass Microwave Filters on the Insertion Loss Method," *Transactions on Microwave Theory and Techniques*, pp. 580–593, 1960.
- [54] C. Yao. (2012, June) What is radio over fiber? Complete Supply Solutions. [Online]. Available: <http://www.fiberoptics4sale.com/wordpress/what-is-radio-over-fiber/>
- [55] A. Zin, M. Bongsu, S. Idrus, and N. Zulkifli, "An overview of radio-over-fiber network technology," *ICP*, vol. 85, 2010.
- [56] I. Poole. Fibre optic communications tutorial. Radio Electronics. [Online]. Available: http://www.radio-electronics.com/info/telecommunications_networks/fiber-fibre-optics/communications-basics-tutorial.php
- [57] Mach-zehnder modulator. COMSOL. [Online]. Available: http://www.comsol.asia/model/download/187145/models.woptics.mach_zehnder_modulator.pdf
- [58] Multicom. Single mode vs. multi-mode fiber optic cable. Multicom. [Online]. Available: <http://www.multicominc.com/active/manufacture/multicom/Fiber%20Optics/singlemode-multimode.html>
- [59] analogreference(). Arduino. [Online]. Available: <http://arduino.cc/en/Reference/AnalogReference?from=Reference.AREF>
- [60] (2009) Casper. CASPER Group. [Online]. Available: <https://casper.berkeley.edu/>
- [61] T. L. Wilson, K. Rohlf, and S. Hüttemeister, *Tools of radio astronomy*. Springer, 2009, vol. 86.
- [62] T. Wilson, "Techniques of radio astronomy," Naval Research Laboratory, Tech. Rep., November 2011.
- [63] *CST Studio Suite 2013*, CST.